UNIVERSITÀ DI PISA

Scuola di Dottorato in Ingegneria "Leonardo da Vinci"

Corso di Dottorato di Ricerca in Telerilevamento

Tesi di Dottorato di Ricerca

Modeling microwave emission from snow covered soil

Autore:

Dr. Ing. Marco Brogioni *Firma*_____

Relatori:

Dr. Ing. Paolo Pampaloni *Firma*_____

Anno 2008

“Labor improbus omnia vincit”

To my family

ACKNOWLEDGMENTS

This work has been carried out in the frame of the research projects of the Microwave Remote Sensing Group of the Institute of Applied Physics (IFAC)-Italian National Research Council.

First of all, I want to thank Dr. Ing. Paolo Pampaloni, my tutor and pioneer of the microwave remote sensing in Italy, for introducing and leading me into this beautiful branch of scientific research. His lectures, advice, discussions and, above all, his rigorous ethics have been fundamental for my studies. Before I met him I barely knew what microwave remote sensing was, and now I am grateful to him for the discovery of this “new world”.

I would also like to thank Dr. Ing. Giovanni Macelloni, my officemate, Dr. Simonetta Paloscia, Dr. Ing. Emanuele Santi, Dr. Ing. Simone Pettinato, Mr. Roberto Ruisi and Dr. Pietro Poggi for their significant help and collaboration in my research and their friendship.

Part of my work in developing the IRIDE model was carried out at the Institute for Computational Earth System Science (ICESS) of the University of California-Santa Barbara under the supervision of Prof. Jiancheng Shi. I am very grateful to him for having hosted me at UCSB and spent his precious time discussing about electromagnetic models for natural surfaces.

Last, but not least, I must thank my family for supporting me during these harsh times, when the work of the people is considered only a hateful cost and the young researchers seem to be children who don’t want to grow up and stop playing.

SOMMARIO

Il ciclo idrologico rappresenta l'insieme di tutti i fenomeni legati alla circolazione e alla conservazione dell'acqua sulla Terra. Il monitoraggio su scala globale dei fattori che concorrono a produrre e modificare tale ciclo (umidità del terreno, copertura vegetale, estensione e caratteristiche del manto nevoso) risulta di estrema importanza per lo studio del clima e dei cambiamenti globali. Inoltre, l'osservazione sistematica di queste grandezze è importante per prevedere condizioni di rischio da alluvioni, frane e valanghe come pure fare stime delle risorse idriche. In questo contesto Il telerilevamento da satellite gioca un ruolo fondamentale per le sue caratteristiche di osservazioni continuative di tutto globo terrestre. I sensori a microonde permettono poi di effettuare misure indipendentemente dall'illuminazione solare e anche in condizioni meteorologiche avverse. I processi idrologici, ed in particolare quelli della criosfera (la porzione di superficie terrestre in cui l'acqua è presente in forma solida), sono fra quelli che meglio si possono investigare analizzando la radiazione elettromagnetica emessa o diffusa. Mediante l'utilizzo di modelli elettromagnetici che permettono di simulare l'emissione e lo scattering da superfici naturali è possibile interpretare le misure elettromagnetiche ed effettuare l'estrazione di quelle grandezze che caratterizzano i suoli e la loro copertura.

In questo lavoro di dottorato si è affrontato il problema della modellistica a microonde dei terreni coperti da neve, sia asciutta che umida. Dopo aver preso in considerazione i modelli analitici maggiormente utilizzati per simulare diffusione ed emissione a microonde dei suoli nudi e coperti da neve si è proceduto allo sviluppo e implementazione di due modelli di emissività. Il primo, basato sulla teoria delle fluttuazioni forti, è atto a descrivere il comportamento di un manto nevoso umido. Il secondo, basato sull'accoppiamento del modello di scattering superficiale AIEM (Advanced Integral Equation Method) con la teoria del trasferimento radiativo nei mezzi densi, è volto allo studio di uno strato di neve asciutta sovrastante un suolo rugoso. Tali modelli tengono conto degli effetti coerenti presenti nell'emissione del manto nevoso e non inclusi nella teoria del trasporto radiativo classico. Entrambi i codici sono stati validati con datasets numerici e sperimentali in parte derivati da archivi ed in parte ottenuti nel contesto di questo lavoro che ha previsto quindi anche una fase sperimentale. Quest'ultima è stata condotta con misure radiometriche multifrequenza su un'area di test situata sulle Alpi orientali. Le simulazioni ottenute con questi modelli e le conseguenti analisi hanno permesso di individuare la sensibilità della temperatura di brillanza ai parametri di interesse (spessore, equivalente in acqua e umidità del manto nevoso) in funzione di diverse configurazioni osservative (frequenza, polarizzazione ed angolo di incidenza). Questo ha consentito di migliorare la comprensione dei meccanismi di emissione dalle superfici innevate e di individuare le migliori condizioni osservative per un sistema di telerilevamento terrestre.

ABSTRACT

The hydrologic cycle represents the whole of the phenomena related to the circulation and preservation of the water on the Earth. The global scale monitoring of the factors involved in the production and modification of such cycle (e.g. soil moisture, vegetation cover, snow cover characteristics and extent) is extremely important for climatologic and global changes studies. Moreover, the systematic observation of such factors is important to forecast the risk of floods, landslides and avalanches as well as to estimate the water resources. In this context satellite remote sensing plays a fundamental role for its characteristic of systematic and continuous observation of the entire Earth's surface. Besides, microwave sensors allow performing measurements independently of solar illumination and weather conditions. The hydrological processes, especially the ones in the cryosphere (the part of Earth's surface in which the water is in solid form), are the ones which can be better investigated by analyzing the electromagnetic radiation emitted or scattered by natural surfaces. By using electromagnetic models, which simulate emission and scattering from natural surfaces it is possible to interpret the electromagnetic measurements and to perform the retrieval of the parameters that characterize the soil and its covers.

This thesis deals with the microwave modeling problem of soils covered by snow (both dry and wet). After a detailed review of the most used analytical models for simulating scattering and emission from soil (both bare and covered by snow), two emissivity models have been developed and implemented. The first one, based on the Strong Fluctuation Theory, is devoted to describe the wet snowpacks behavior. The second one, based on the Advanced Integral Equation Method surface scattering model coupled with the Dense Media Radiative Transfer Theory, is devoted to study a layer of dry snow overlying a rough soil. Both of these models account for the coherent effects that take place in the emission of snowpacks and which are not accounted for by the conventional radiative transfer theory. The two snow software have been validated against numerical and experimental datasets derived from archives and from experimental measurements carried out during this thesis work. This latter activity has been worked out by means of multifrequency radiometric measurements taken on a test area on the Eastern Italian Alps. The simulations performed by means of the two models allowed us to determine the sensitivity of the brightness temperature to the most interesting geophysical parameters (thickness, water equivalent and wetness of snow) as a function of different observation configurations (frequency, polarization and incidence angle). Such work made it possible to significantly improve the knowledge of the emission processes of snow covered areas and to determine the best observation configuration for an Earth remote sensing system.

Index

List of symbols

Re[..] and Im[..]	real and imaginary part of a complex number
J, i	imaginary unit
A	scalar quantities
$\overline{A}$, $\underline{A}$	vectors
$\overline{\overline{A}}$, $\underline{\underline{A}}$	matrices
"×" and "·"	vector and scalar products
$\nabla\times[..]$, $\nabla\cdot[..]$	rotor and divergence operators
<…>	ensemble average operator
$\underline{x}_0$, $\underline{y}_0$, $\underline{z}_0$	unit vectors for Cartesian coordinates
$\underline{r}_0$, $\underline{\theta}_0$, $\underline{\varphi}_0$	unit vectors for polar coordinates
$\underline{E}(\underline{r},t)$	electric field vector in the time domain [Volt/m]
$\underline{H}(\underline{r},t)$	magnetic field vector in the time domain
$\underline{E}(\underline{r})$	electric field vector in the frequency domain (ω is tacit) or electric field phasor
$\underline{H}(\underline{r})$	magnetic field vector in the frequency domain (ω is tacit) or magnetic field phasor
$\overline{\overline{G}}$	Dyadic Green's function
E_x, E_y, E_z	cartesian components of the electric field
E_r, E_θ, E_φ	polar components of the electric field
E_h, E_v	horizontal and vertical components of the electric field ($E_h=E_\varphi$; $E_v=E_\theta$)
ρ, ρ_m	electric and magnetic charge volumetric densities (charge densities)
K	effective propagation constant
$\underline{E}_i$ and $\underline{E}_s$	incident and scattered field in a scattering problem
$\underline{K}=\underline{\beta}-j\underline{\alpha}$	electromagnetic wave vector
k_x, k_y, k_z	cartesian coordinates of the wave vector
$e^{-j\underline{k}\cdot\underline{r}}e^{j\omega t}$	space and time dependence of a plane wave phasor (sign rule for Fourier transforming in the time and space domains)
F	Frequency or Fractional volume of ice crystals in snow
λ	wavelength
$K=2\pi/\lambda$	wavenumber
C	speed of light in vacuum
ε_0, μ_0, k_0	dielectric constant, magnetic constant and wavenumber of vacuum
$\varepsilon_c=\varepsilon'-j\varepsilon''$	complex dielectric constant of the medium (including conductive losses)
$\varepsilon_r=\varepsilon_r'-j\varepsilon_r''$	relative dielectric constant of the medium

ε_b	air permittivity
ε_s	permittivity of ice crystals
ε_g	auxiliary permittivity (in SFT)
ξ_i	susceptibility
$\underline{g(r)}$	pair distribution function
η	characteristic impedance of the medium
P_r	Power flux density at receiving point [Watt/m^2]
P_t	power flux density from transmitting antenna [Watt/m^2]
P_i	incident power flux density (on the target) [Watt/m^2]
P_s *or* w_R	scattered power flux density (from the target) [Watt/m^2]
A, w, t	absorbance, surface albedo and transmittance of a layer or a semi-infinite medium
k_e	extinction rate
e and e_λ	emissivity and spectral emissivity
W, ϖ	surface albedo or single scattering albedo (depending on the context)
B_λ or B_f	spectral radiance/brilliance [Watt/ster/m^2/μm or Watt/ster/m^2/Hz]
T_B	brightness temperature [K]
$\underline{I}$	incident direction unit vector (corresponding to direction in polar coordinates θ_i, φ_i)
$\underline{S}$	observation (scattered) direction unit vector (corresponding to direction in polar coordinates θ_s, φ_s)
R	distance between two points (i.e., observation point wrt source points)
R	distance of a point from origin of coordinate system
$\sigma(\theta_i, \varphi_i; \theta_s, \varphi_s; p_i,p_s) = \sigma(\underline{i}, \underline{s}; p_i,p_s)$	bistatic radar cross section for incidence direction θ_i, φ_i, polarization of incident wave p_i, observation direction θ_s, φ_s and observed polarization p_s.
$\sigma^\circ(\theta_i, \varphi_i; \theta_s, \varphi_s; p_i,p_s) = \sigma^\circ(\underline{i}, \underline{s}; p_i,p_s)$	bistatic scattering coefficient for incidence direction θ_i, φ_i, polarization of incident wave p_i, observation direction θ_s, φ_s and observed polarization p_s. (as defined in Ulaby *et al*., 1986)
$\gamma(\theta_i, \varphi_i; \theta_s, \varphi_s; p_i,p_s) = \gamma(\underline{i}, \underline{s}; p_i,p_s)$	As above, but following the definition by [Tsang *et al*., 2000].
$\underline{f}(\underline{I}, \underline{s})$	scattering amplitude, being $\underline{E_s}(\underline{r}) = \underline{f}(\underline{i}, \underline{s})\, e^{-jkr}/r$
σ_a, σ_s, σ_e	absorption, scattering and extinction sections [m^2]
ξ_s, ξ_a	scattering and absorption efficiencies
k_a, k_s, k_e	absorption, scattering and extinction volumetric coefficients [m^{-1}]
$\tau(r_1, r_2)$ and $t(r_1, r_2) = e^{-\tau}$	optical depth and path transmittance from range r_1 to range r_2
$R_h(\theta)$ and $R_v(\theta)$	Fresnel reflection coefficients for H and V polarization and incidence angle θ, respectively
$T_h(\theta)$ and $T_v(\theta)$	Fresnel transmission coefficients for H and V polarization

	and incidence angle θ, respectively
T	Stickiness of ice particles
$\overline{\overline{P}}(\theta,\phi,\theta',\phi')$	phase matrix
$\overline{\overline{T}}_{10}(\theta)$	transmissivity matrix
$\Gamma_H(\theta)$, $\Gamma_V(\theta)$	plane surface specular reflectivity for H and V polarization, respectively
θ_B	Brewster angle (or pseudo Brewster angle)
$\zeta(x,y)$	height of a rough surface above the mean plane (random function of coordinates x,y)
l_x	correlation length of a random function x (subscript can be omitted)
μ_x and $\underline{\mu}_x$	mean value of random variable x or of a random vector $\underline{x}$, respectively
σ_x and σ_x^2	standard deviation and variance of a random variable x (or random function)
$\rho_x(\Delta t)=\rho_x(\tau)$ and $\rho_x(\Delta\underline{r})$	autocorrelation function of a stationary random function x (of time t or space $\underline{r}$)
ρ_{xy}:	correlation coefficient between two random variables x and y
$S=\partial y/\partial x$	sensitivity of radiative quantity y (measured by the sensor) to geophysical quantity x.
m_v, m_g	volumetric and gravimetric soil moisture, respectively
SMC	soil moisture content (either m_v or m_g)

x

1. INTRODUCTION

In the recent years there has been a growing interest in the weather global changes and in the management of the natural resources. The attention paid by the media to the climate increases every day and raises the alertness of the common people to the environment care. Moreover, people have been further scared by natural disasters like the hurricane Katrina, the Indian Ocean tsunami and floods in central Europe. The demand of knowledge about “what is happening to our planet” and “how these changes could be avoided” pushes the researchers to deeply investigate the natural phenomena and understand how to minimize the impact of the humankind on the environment.

At the same time, the reasons to improve our knowledge about the Earth are also driven by other factors. Besides the noble spirit of understanding our planet, there are economic and politic motivations. For example, the possibility of predicting the precipitation rate during the crop growth seasons can influence the life of large areas of the world by adopting appropriate countermeasures against the famine and by the speculation of the economic lobbies. In addition, the knowledge of some hydrological variables such as soil moisture, vegetation cover and the quantity of snow deposed during the winter season on the mountains is important for the agriculture, to evaluate the risk of floods and avalanches and also to drive the energy choices of the electrical companies.

In this scenario, the understanding of the Earth dynamics is very important and the remote sensing (RS) can play a fundamental role due to its intrinsic characteristics, e.g. the possibility to investigate remote and inaccessible areas and perform analysis very often (on daily or weekly basis). The remote sensing is based on the analysis of the electromagnetic (e.m.) radiation scattered or emitted by the natural bodies. Depending on the characteristics of the e.m. waves measured it is possible to deduct some features of the observed objects. The possibility to understand the state of an object being far from it let the remote sensing very attractive.

There are several areas in which the RS can be applied successfully. Among the majors: weather forecasts, land classification, and study of the processes involved in the hydrological cycle. This latter topic is considered very important because it represent the basis to understand the climate and its changes.

The hydrological cycle (see Fig. 1) is made up by several components. The main ones are: precipitations (rainfall, snowfall and hail), soil moisture, accumulation of snow and ice, water run-off and evaporation. Among them, one which can be investigated using at most the characteristics of remote sensing is the cryosphere (the portions of the Earth's surface where water is in a solid form). Indeed, the areas with snow covers are very often inaccessible and dangerous but they need to be accurately monitored. For instance, let us considering Antarctica which contains more than 95% of the fresh water on Earth and which influences the world climate due to its high albedo. Monitoring the Antarctic environment is very difficult using classical techniques. In fact the mean annual temperature is far below -30°C letting Antarctica be one of the most impervious place where the man can

live and operate. Thus, the use of satellite remote sensing techniques can result very useful.

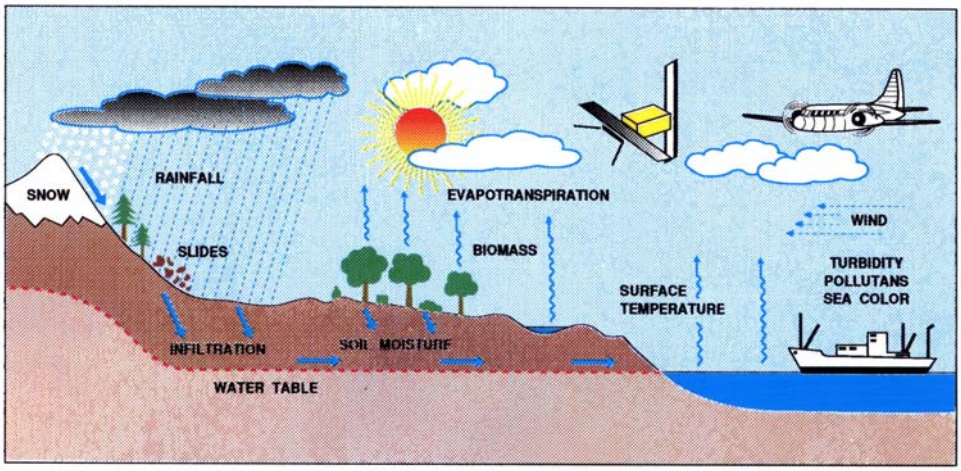

Fig. 1 - The hydrological cycle

Snow cover has the largest area extent of any component of the cryosphere and, except Antarctica, most of the Earth's snow-covered area is located in the Northern Hemisphere, where the mean snow-cover extent ranges from 46.5 million km^2 in January to 3.8 million km^2 in August [1]. The temporal variability is dominated by the seasonal cycle. However, changes in the annual spatial distribution of snow have been observed during the last decades related to the global warming [2]. The terrestrial cryosphere plays a significant role in the global climate, in climate response to global changes and as an indicator of change in the climate system. Moreover, remote sensing of the melting cycle of snow has proven to be crucial to forecast the snow-water runoffs, floods and avalanches, besides to manage water resources.

The remote sensing techniques are based on sensors that operate in different portions of the electromagnetic spectrum. For land applications, the researchers commonly use the optical part (which ranges from the far infrared to the ultraviolet) or the microwaves (electromagnetic waves with a frequency that span from 300 MHz to 300 GHz). The interaction of the e.m. waves with the natural bodies happens in two different ways which are strictly related one to the other. When the radiation impinges on a body, it can be both absorbed and scattered away (depending on the geometrical and physical properties the object). According to the Plank's law, in thermodynamic equilibrium the energy absorbed equals the one re-emitted. The two phenomena, absorption/emission and scattering are bound together by the principle of energy conservation. Microwave sensors can be either passive or active and can both operate on entire frequency spectrum. Passive sensors (radiometers) measure scattered radiation emitted by the sun in the optical range, or thermal emission emitted by the Earth's surface in the infrared and

microwave bands. Active sensors (lidar and radar) measure scattered radiation emitted by their own illuminating sources.

Remote sensing of snow has traditionally been carried out mostly by using optical sensors [3]. Several operational services have been established to obtain snow cover maps from the NOAA AVHRR sensors. These sensors have a poor resolution (1 km), but provide a reasonable temporal coverage (daily products) depending on cloud conditions. Indeed this is the biggest limitation to the use of optical instruments. The electromagnetic waves in the visible and infrared spectra cannot penetrate the clouds that let the optical sensors blind. Conversely, microwave sensors are almost insensitive to the weather phenomena. In general, there is an optimum sensor configuration (frequency range, polarization and incidence angle) for each observed target. For instance, the best frequency band to estimate soil moisture has been identified at L-band. Conversely, the observation of dry snow requires the use of higher frequencies that, at present are available in passive sensors only. Indeed, several experiments have documented the ability of C-band Synthetic Aperture Radar for mapping the extent of wet snow only by using both ERS and RADARSAT data [4]-[6]. Automated algorithms are available using change detection. However, due to its high transparency at C-band, dry snow cannot be separated from bare soil.

The sensitivity of microwave emission to snow type and water equivalent (SWE) has been pointed out in several theoretical [7]-[12] and experimental [13]-[22] studies which demonstrated the potential of microwave radiometers in monitoring snow parameters and seasonal variations in snow cover. Unfortunately, the rough spatial resolution of satellite sensors from satellite, such as the Special Sensor Microwave Imager (SSM/I), limited their effectiveness in operational use. The improved performance of the Advancing Microwave Scanning Radiometer (AMSR-E) on the Earth Observing (EOS) AQUA platform helps to partially overcome this drawback [23].

Radiation emitted at the lower frequencies of the microwave band (lower than about 10 GHz), by soil covered with a shallow layer of dry snow is mostly influenced by the soil conditions below the snow pack and by snow layering. At higher frequencies, however, the role played by volume scattering increases, and microwave emission becomes sensitive to snow cover [14],[15]. In general, high frequency microwave emission from dry snow decreases as snow depth (SD) increases, although SSM/I measurements taken within the former Soviet Union during the 1987–1988 winter period showed significant deviations from this pattern [21]. If snow melts, the presence of liquid water in the surface layer causes an increase in emission. The average spectra of the brightness temperature show that emission of dry and refrozen snow decreases with frequency, whereas emission from wet snow displays an opposite trend. Experiments carried out in the Swiss Alps by Hofer and Mätzler [15], by using ground-based sensors demonstrated that microwave radiometers can separate three snow conditions (winter, spring and summer) representative of the seasonal development of snow cover. These trends were interpreted by Schanda *et al*. [16], who pointed out the dominant role played by the Rayleigh scattering, and confirmed by other experiments (e.g. [18]). Further

investigations pointed out the importance of the snow crust, which can build up due to the night-time refreezing [24], [25].

The most important snow quantities to be monitored for applications are: extent of snow cover, snow liquid water content, and snow water equivalent. Regarding the liquid water content of snow (LWC) several retrieval algorithms have been developed. For instance, in [26] an algorithm based on polarimetric C-band SAR data is shown. Fully polarimetric information is needed to separate the effects of surface roughness from the effects of LWC. Since Envisat-ASAR only has dual polarization it has not been possible to study LWC solely from SAR. However, a combination of SAR and in situ measurements from synoptic weather measurements in Finland has revealed promising results.

The determination of the beginning of the snow melting is crucial in flood forecast and avalanche prevention. The potential of microwave radiometers in measuring snow wetness has been pointed out in [22]. Snow water equivalent (SWE) is the most important and highest valued snow parameter from a hydrological point of view. It is computed by the product between snow density and snow depth. Usually the SWE is defined for dry snowpack and it indicates the whole amount of water that will run-off to the valley during the spring season. As stated above, the retrieval of SWE from C-band SAR backscattering is very problematic, although some interesting result has been obtained over relatively smooth surfaces in cold regions [27]. A new approach to retrieve information on the changes in SWE from repeat pass interferometric phase changes was introduced by Guneriussen *et al*. [6] and tested in a drainage area in Norway. The method invokes advanced delta-k processes to avoid phase wrapping. Data were calibrated with corner reflectors not covered by snow.

To analyze experimental measurements and understand the interaction between electromagnetic waves and targets, models which describe the emission and scattering must be used. Depending on the degree of approximations of physical laws and on the method to calculate some parameters it is possible to obtain several kind of models which span from the empirical (the simplest but the less accurate to describe the observed medium) to the physical ones which are based on the electromagnetic theory and are the most complex.
To describe the electromagnetic emission or scattering from snow-covered surface, two models must be used: one for the soil and one for the snow. These models will be described in the following section.

This work is organized as follows: a comprehensive review of the state of the art for scattering and emission models for bare soil and snow is given in section two. Section three includes the description of the models developed to simulate the electromagnetic emission from Alpine snowpack, pointing out the improvements obtained in this work and the critical points. A comparison of model simulations with experimental data is outlined in section four.

2. STATE OF THE ART

A crucial problem of remote sensing is the retrieval of geophysical parameters from the measured electromagnetic radiation. This is an inversion problem that requires the use of appropriate direct models. In the last decades several models and techniques have been developed to analyze and simulate the interaction between microwaves and snow-covered surfaces. Depending on the approach followed to describe the electromagnetic behavior of the snowpack or to retrieve physical parameters, the models used to predict microwave emission and scattering can be divided in the following three groups: empirical, semi-empirical and theoretical. The choice of the method is closely related to the final application.

The empirical models are based on experimental relationships between remote sensing and ground data, and make use of regressions (or other kind of statistical analysis) to estimate soil and snow parameters [28]-[32]. The important matter is to have a large dataset of both electromagnetic measurements (or simulated data) and snow and soil physical parameters.

For instance in [33] the SD is estimated by

$$SD = 1.59\left(T_{18H} - T_{37H}\right) \quad (1)$$

Where T_{18H} and T_{37H} are respectively the 18 GHz and 37 GHz horizontally polarized brightness temperatures, and 1.59 is a constant obtained by a linear regression of the difference between 18GHz and 37GHz responses. If the 18GHz brightness temperature is less than the 37GHz one, no snow is assumed present.

The limits of these algorithms are the area over which they can give good predictions and the errors on the estimations which are relatively high. Considering that the electromagnetic emission depends simultaneously on several parameters of the snowpack but also on the ground features and on the vegetation coverage, it is easy to understand why the estimations can be different if they are made on the north European tundra or on the Asian desert.

Anyway, these algorithms are useful when the estimations are made on a global scale (tents or hundreds of squared kilometers). In this case, it is very difficult to have spatially detailed description of the surface, which, on the other hand, may include different types of coverage in the coarse spatial resolution elements of the spaceborne instruments. Thus, the use of methods that leave out detailed knowledge of the observed surfaces is very attractive and sometimes mandatory.

The procedure to develop an empirical algorithm is quite simple. The only need is two big datasets of conventional and electromagnetic measurements which will be split in two parts: the first half is used to establish the relationship and the other one to test the performance of the algorithm. Then, by using regressions (whether linear, quadratic, exponential, etc.) or artificial neural networks (ANN) relationships between the two kinds of data can be found and verified. It is possible to estimate snow physical parameters from electromagnetic measurements or also to predict the scattering and emission from conventional ones.

As stated before, the performances of these algorithms are not very good both because the study area are seldom homogeneous (and the electromagnetic signal of the snow is influenced by the one of the vegetation and other sources), and because the microwave emission/scattering strongly depends on several parameters (the retrieval of the geophysical parameters from the e.m. measurements is an ill-posed problem). Sometimes it is simpler to retrieve global parameters like the Snow Water Equivalent (which is defined as the integral of the snow density along the vertical profile of the snowpack) instead of snow depth and density separately. Anyway, in some cases the empirical algorithms have excellent performance. For instance, the retrieval of the snow temperature profile in Antarctica from AMSR-E radiometric measurements: the retrieval error has resulted to be lesser or equal than 1°C [31] because the structure of the snowpack remains almost unchanged year after year.

The semi-empirical models are based on physical laws (hence are more rigorous than the empirical ones) but, for the determination of some parameters they use experimental data. An example is the HUT (Helsinki University of Technology) model [34] which has been successfully used to simulate the microwave brightness temperature of a simplified snowpack configuration.

The approach used in the HUT snow emission model to estimate the brightness temperature of snow-covered soil relies on the following assumptions: the scattered microwave radiation is mostly concentrated in the forward direction and the snowpack is a single homogeneous layer overlying a semi-infinite half space (the ground). Thus, the brightness temperature inside a snowpack of depth d, just below the snow–air boundary, can be approximated as follows [34]:

$$T_b(d^-,\theta) = T_b(0^+,\theta)e^{-(k_e - q\,k_s)\sec\theta\, d} + \frac{k_a T_{snow}}{k_e - q\,k_s}\left(1 - e^{-(k_e - q\,k_s)\sec\theta\, d}\right) \equiv T_{B,g} + T_{B,s\uparrow} \qquad (2)$$

where θ is the observation angle, $T_b(0^+,\theta)$ is the soil brightness temperature just above the ground–snow interface, T_{snow} is the snowpack physical temperature, q is an empirical parameter (q = 0.96) describing the fraction of intensity scattered in the direction θ which is the same at all frequencies, and k_e, k_s, and k_a are, respectively, the extinction, scattering and absorption coefficients ($k_e = k_s + k_a$). It is easy to recognize in (2) that the first term of the right hand side is the ground contribution attenuated by the overlying layer while the second represents the contribution from the snow. The extinction properties of dry snow (i.e. k_e in (2)) as a function of snow grain size are modeled like in [35]. k_a is calculated from the complex dielectric constant of dry snow. The real part of the snow dielectric constant is determined by using the formulas given in [36] whereas the imaginary part is treated with a formula based on the Polder–Van Santen mixing model [37]. To calculate the imaginary part of snow permittivity, the ice dielectric properties are also required. These are computed using an empirical formula [36]. The effect of snow grain size is described through the extinction coefficient, as determined empirically in [35]

$$k_e = 0.0018 f^{2.8} \phi^2 \quad (3)$$

where k_e is in decibels, *f* is the frequency in gigahertz, and ϕ is the snow grain diameter in millimeters. Equation (3) was derived from observations on natural snowpack characterized by grain diameters ranging from 0.2 to1.6 mm.

Another example of semi-empirical model is the Microwave Emission Model of Layered Snowpacks (MEMSL) valid in the frequency range 5-100 GHz that has been developed by Wiesman and Mätzler [11] for dry winter snow and extended to wet snow by Mätzler and Wiesmann [12]. This model is based on multiple scattering radiative transfer theory, in which the scattering coefficient is determined from measurements of snow samples.

The theoretical models are, among the three categories, the most rigorous and are based on the solution of the Maxwell's equations. These models need an accurate characterization of the media interacting with the electromagnetic waves and are more useful to understand the phenomena which happen rather than estimate the physical properties of the target by inverting the experimental data. Indeed, the formulae describing the scattering or the emission are usually non-linear and very complex. Moreover the electromagnetic problem is multiparametric and ill-posed (different combination of input parameters give the same e.m. prediction), making almost impossible to invert the equations (theoretical methods).

The most used theoretical models for simulating surface scattering from soil are the Small Perturbation Method (SPM), the Kirchhoff Approach under the Physical and Geometrical Optics approximations (respectively KA-PO and KA-GO), the Integral Equation Method (IEM) and the Small Slope Approximation (SSA). For volume scattering from the snowpack the most advanced models are based on the Strong Fluctuation Theory (SFT) and the Dense Medium Radiative Transfer Theory (DMRT). All of these models have been successfully used within their limits of validity to simulate emission and scattering. A comprehensive description of these models is given in the following chapter.

Among the said models, the most used for the soil is the IEM, which has a wider validity domain than the SPM and the KA. In snow applications, the SFT and the DMRT use different approaches to model the snowpack (continuous for the SFT and discrete for the DMRT) but the results are similar; although, in recent years the DMRT has been improved and now, seems to reproduce experimental data better than the SFT over a wider range of frequencies.

The main problem with the theoretical models is the difficulty to solve exactly the Maxwell equations in the case of media with a complex structure such as the natural bodies. Usually several approximations can be made (see [38] for snow) leading to more or less wide validity ranges. Another issue, which is strictly bound to the complexity of the models, is the computational time. Until few years ago the computational power of the computers was quite lower than what it is now and this

led the researcher to obtain simpler models. In the recent times, these problems are less severe and it is possible to use more complicated methods.

It is worth noting also that with the advent of modern computers and the development of fast numerical methods, numerical simulations of the wave scattering problems have become an attractive alternative overcoming the limitations in regimes of validity of classical analytical models. An excellent treatment of various approaches can be found in the book by Tsang *et al*. [39]. A good review of the numerical methods is given also in the introduction of the paper by Li *et al*. [40].

2.1 Scattering and emission from soils

The electromagnetic scattering of the bare soils is usually modeled like surface scattering. This kind of scattering happens at the interface between two media that are homogeneous but with different electromagnetic properties. The former hypothesis is verified for the air but not exactly for the terrain, which is actually heterogeneous. Anyway, by considering the high density of the scatterers and the relatively high permittivity of its components, it is possible to compute an effective dielectric constant for the soil and to re-conduct the whole scattering problem to the classical surface one.

The problem of the scattering from a bare soil can be divided into three different sub-problems, which need to be solved:

- first of all, the soil can be modeled like a mixture of lime, clay, sand and water. Thus the effective permittivity of such mixture must be calculated on the basis of the percentage and the dielectric constant of each element.
- second, the roughness statistic of the interface must be determined through the shape of the autocorrelation function (ACF), and the related Height Standard Deviation (HStdD), (known also as Standard Deviation of Soil heights, SDS), and the correlation length. A different approach is the determination of the fractal features of the surface.
- finally, depending on the previous parameters, the electromagnetic problem must be solved by using appropriate approximations.

2.1.1 The dielectric constant of bare soils

Natural terrains can be regarded as mixtures of bulk material (sand, clay, loam, silt organic material, etc) and water, bounded by a rough surface. The determination of the electric properties of a mixture (the “homogenizations” problem) has been investigated since the nineteenth century [41]. Conversely, from the homogeneous media, the heterogeneous ones have electrical properties which depend on several factors: e.g. the percentage of the components, their permittivity and permeability, and the chemical bond between the molecules. A comprehensive description of the methods developed to obtain the effective dielectric constant of a mixture can be found in [41]. Usually mixing formulas that average the permittivity of each constituent by means of their percentage are used. However, when the differences between the electrical properties of the components are sensible, the models

become more complicated. This is the case of soils, in which the permittivity of dry material (usually close to 3) is much smaller than that of water.

The dielectric characteristics of water have been investigated in several textbooks and papers (e.g. [42]). The complex permittivity ε of pure free water can be described by the Debye equation:

$$\varepsilon = n^2 + \frac{\varepsilon_s - n^2}{1 + j2\pi f\tau} \tag{4}$$

where *n* is the refractive index, ε_s is the static dielectric constant, *f* is the frequency, and τ is the relaxation time. On the other hand, the permittivity of soil is also dependent on soil texture since the particle dimensions of soil components vary from less than 2 μm for clay to more than 1000 μm for sand. Thus, for the same volumetric moisture content, there is more free water in sand than in clay.

One of the most used models to calculate the dielectric constant of the terrain is semi-empirical and has been developed by Dobson *et al*. [43]. It assumes the soil made up by a four-component mixture and the resulting permittivity can be expressed as

$$\varepsilon_{soil}^{\alpha} = v_{ss}\varepsilon_{ss}^{\alpha} + v_a\varepsilon_a^{\alpha} + v_{fw}\varepsilon_{fw}^{\alpha} + v_{bw}\varepsilon_{bw}^{\alpha} \tag{5}$$

where the subscripts *ss*, *a*, *fw*, *bw* stand for solid soil, air, free water and bounded water and

$$\begin{aligned} &\varepsilon_{ss}^{\alpha} \cong 4.7 - j0 \\ &v_{ss} = 1 - v_{\phi} \\ &v_a = v_{\phi} - m_v \\ &m_v = v_{fw} + v_{bw} \\ &v_{\phi} = \frac{\rho_{ss} - \rho_b}{\rho_{ss}} \cong 1 - 0.38\rho_b \end{aligned} \tag{6}$$

In (6) v_{ϕ} is the soil porosity, $\rho_{ss} \cong 2.65$ gr/cm^3 is the density of the soil solid material and m_v is the total volumetric moisture content. To simplify the model but still retain a soil textural dependence it is possible to group together the water parameters as

$$v_{fw}\,\varepsilon_{fw}^{\alpha} + v_{bw}\,\varepsilon_{bw}^{\alpha} \cong m_v^{\beta}\varepsilon_{fw}^{\alpha} \tag{7}$$

where β is a parameter empirically determined.

Using (7) the soil permittivity can be written as

$$\varepsilon_{soil}^{\alpha} \cong 1 + \frac{\rho_b}{\rho_{ss}}\left(\varepsilon_{ss}^{\alpha} - 1\right) + m_v^{\beta}\left(\varepsilon_{fw}^{\alpha} - 1\right) \tag{8}$$

Dobson *et al*. [43] determined empirically the remained parameters α and β. They found that the value α=0.65 was the best compromise for all the soil types, whereas the magnitude of β can vary from 1.0 for sandy soil to 1.17 for silty clay. Generally, β can be estimated by

$$\beta = 1.09 - 0.11\ S + 0.18\ C \tag{9}$$

where *S* and *C* are respectively the weight fraction of the sand and the clay in the soil.

2.1.2 Characterization of soil roughness

2.1.2.1 Statistical description

A rough surface can be described by a height function *z = f(x,y)*. Direct assessment of roughness can be carried out by means of various experimental approaches able to reproduce the surface profile by using contact or laser probes. However, the exact characterization of natural surfaces is, in general, very difficult. The problem of defining optimal parameters for natural surface roughness has been investigated in many studies (e.g. [44]-[49]). In general, the analysis of scattering in remote sensing is performed by using random rough surface models, where the elevation of surface, with respect to the mean plane, is assumed to be a stationary stochastic process with a Gaussian height distribution. A different method of surface characterization is based on fractal description of surfaces [44].

An isotropically rough surface can be described by a one-dimensional random function z = *f* (ρ,ϕ) with zero mean, i.e. <*f* (ρ,ϕ)> = 0. For a stationary random process, we have:

$$\left\langle f(\rho_1,\phi_1) f(\rho_2,\phi_2) \right\rangle = \sigma_z^2 C(\rho_1 - \rho_2) \tag{10}$$

where σ_z is the height standard deviation and *C* is the autocorrelation function (ACF) which is a measure of the correlation of surface profile *f*(ρ) at two different locations ρ_1 and ρ_2.

The most common ACFs used in remote sensing of land surfaces are the Gaussian correlation function

$$C(\rho) = \exp(-\frac{\rho^2}{l^2}) \tag{11}$$

and the Exponential correlation function:

$$C(\rho) = \exp(-\frac{|\rho|}{l}) \tag{12}$$

where *l* is the correlation length.
The spectral densities are respectively:

$$W(k_\rho) = \frac{\sigma_z^2 l}{\pi\left(1 + k_\rho^2 l^2\right)} \tag{13}$$

for the exponential ACF and

$$W(k_\rho) = \frac{\sigma_z^2 l}{2\sqrt{\pi}} \exp\left(-\frac{k_\rho^2 l^2}{4}\right) \tag{14}$$

for the Gaussian one.

Besides these two functions, several other kinds of autocorrelation functions have been developed and applied. It is worth quoting the mixed-exponential and the 1.5-power which behave like an exponential for smooth surfaces and like a Gaussian for rough ones. In [50] several power ACF have been analyzed, pointing out that this type of functions shows the best performance in modeling the roughness of natural soils with respect to the Gaussian and exponential ones.

In addition to the height function $f(\rho)$, the slope function $\alpha(\rho) = f'(\rho)$ ($<\alpha(\rho)> = 0$) is also an important characterization of the rough surface. Given a stochastic process, its derivative is also a stochastic function. If a random surface $f(\rho)$ is generated by a Gaussian process its derivative $f'(\rho)$ is also Gaussian and its slope variance s^2 is related to the second derivative of its correlation at the origin i.e. [51]:

$$s^2 = \frac{2\sigma_z^2}{l^2} = -\sigma_z^2 C''(0) \tag{15}$$

For the exponential correlation function the rms slope does not exist. This implies that this kind of ACF does not work for very rough surfaces. On the other hand, several measurements on natural surfaces have shown that the exponential ACF best represents the soil roughness. These two facts are contradictory: some explanations could be that ground measurements are not much accurate (maybe due to the finite length of the instruments) or that more complex ACF types must be considered in the modeling. In [52] a multi-scale approach has been analyzed: the exponential-like correlation function was simulated by the sum of three X-power ACFs, which are differentiable and have physical insight. The results show that a possible reason of the exponential correlation of most natural surfaces is that they contain more than one scale of roughness and that a multi-scale ACF can represents better the natural roughness of soil.

2.1.2.2 Fractal description

An interesting alternative approach is to model the surface by a continuous fractal function [53]. This technique can provide a new description of natural soils, since fractals are suitable tools for describing mixtures of deterministic and random processes. A fractal analysis of perfectly conducting bi-dimensional profiles has been performed by Rouvier and Borderies [54], who pointed out the fractal nature of the scattered field. The characterization of soil roughness and backscattering in terms of fractal Brownian description has been studied by Zribi *et al*. [55], who also validated a model using experimental data. On the other hand, several scientists (e.g. [56]-[58]) have shown that the slope and intercept of the power spectrum of the soil profile can be additional significant descriptors of the topography of natural soils. Moreover, slope *S* of the power spectrum, computed in a log-log space, makes it possible to determine the fractal parameter *D* according to the relation: $D = (5 + S)/2$ [59].

Differently from the common descriptors of roughness (σ_x and l), the fractal dimension is a parameter which describes the scaling properties of a surface, i.e. it possesses the property of self similarity. The fractal dimension can be estimated by using the classical method of box counting or from the power spectrum of the surface profile.
A basic problem involves incorporating these roughness descriptions into existing scattering models to provide essentially the same information as the traditional parameters.

2.1.3 The electromagnetic models for bare soil

The most common analytical models of scattering by dielectric rough surfaces are the Small Perturbation Method (SPM) and the Kirchhoff Approach (KA) under both the Physical and Geometrical Optics solutions (respectively PO and GO). An updated comprehensive treatment of these two approaches is given in [51] and in [39]. Further advances include the small slope approximation (SSA) [60]-[63] and the Integral Equation Method [64],[65]. The starting point for all of these approaches is the Huygens principle, which expresses the field at an observation point in terms of fields at the boundary surface (e.g. [51]). The scattered intensities are usually decomposed into coherent and incoherent terms.
The limits of validity of these approaches have been frequently discussed in literature, but an exact criterion has not yet been exactly established. Anyway the plot in Fig. 2 show the commonly accepted validity range of SPM, PO, GO and IEM in the *ks-kl* plane [66].

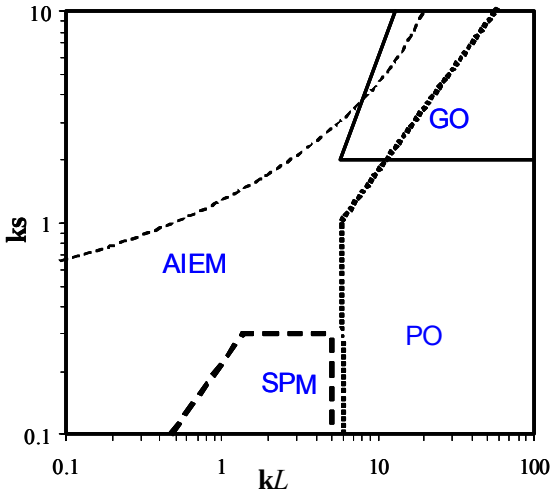

Fig. 2 - The validity range of the SPM, PO, GO and AIEM

From Fig. 2 it can be easily seen that the validity range of the AIEM cover both the SPM and the KA approximations letting it one of the most versatile models for the surface scattering.

2.1.3.1 The Small Perturbation Method (SPM)

The SPM, which is valid when the surface variations are much smaller than the electromagnetic wavelength and the slopes of the rough surface are relatively small, has found extensive applications in active and passive remote sensing of land surfaces. In this model, the random surface $z = f(x,y)$ is decomposed into its Fourier spectral components. The scattered wave consists of a spectrum of plane waves. The scattered fields can be solved by using the Extended Boundary Condition method with the perturbation method. In the EBC method the surface currents are calculated first by applying the extinction theorem. The scattered fields can then be calculated from the diffraction integral by making use of the calculated surface fields [51]. The solution for the one dimensional surface is given in [51]. The more complete analysis, carried out up to the second order solution of the three dimensional problem with two-dimensional dielectric rough surfaces assures energy conservation and can be found in [39]. In this approach the zero order solution consists of only a single spectral component, which is simply the Fresnel specular reflection from a flat surface at $z = 0$.

In the first order solution the incoherent bistatic scattering coefficient for a Gaussian correlation function assumes the form [67]:

$$\sigma_{qp}^{0}\left(\theta_s,\varphi_s,\theta_i,\varphi_i\right)=4\,k^4\sigma_\varsigma^2\,l^2\cos^2\theta_s\cos^2\theta_i\;f_{qp}\;e^{-\frac{k_{d\rho}^2\,l^2}{4}} \tag{16}$$

where θ_s, φ_s θ_i, φ_i are the incident and azimuth scattered and incident angles, $k_{d\rho}^2=k^2\left[\sin^2\theta_s+\sin^2\theta_i-2\sin\theta_s\sin\theta_i\cos(\phi_s-\phi_i)\right]$, and the f_{qp} terms are given in [67] as functions of the wave-numbers in free space and in the medium, the z components of incident and transmitted propagation vectors, and the incident and scattering angles.

The first order solution does not modify the coherent reflection coefficients and, to see the correction term for the coherent wave due to the rough surface, the second order solution must be calculated. In the second order solution, the bistatic scattering coefficients as given in [39] are the following:

$$\begin{aligned}\sigma^{\circ}_{hh}(\theta_s,\varphi_s;\pi-\theta_i,\phi_i)&=\\ &=4\pi k^2\cos^2\theta_s\int_{-\infty}^{\infty}W(\bar{k}_\perp-\bar{k}'_\perp)W(\bar{k}'_\perp-\bar{k}_{i\perp})\,\hat{f}_{ee}(\bar{k}_\perp,\bar{k}'_\perp,\bar{k}_{i\perp})\cdot\\ &\qquad\cdot\left[\hat{f}^{*}_{ee}(\bar{k}_\perp,\bar{k}'_\perp,\bar{k}_{i\perp}+\hat{f}^{*}_{ee}(\bar{k}_\perp,\bar{k}_\perp-\bar{k}'_\perp+\bar{k}_{i\perp},\bar{k}_{i\perp})\right]d\bar{k}'_\perp\end{aligned} \tag{17}$$

$$\begin{aligned}\sigma^{\circ}_{vh}(\theta_s,\varphi_s;\pi-\theta_i,\phi_i)&=\\ &=4\pi k^2\cos^2\theta_s\int_{-\infty}^{\infty}W(\bar{k}_\perp-\bar{k}'_\perp)W(\bar{k}'_\perp-\bar{k}_{i\perp})\,\hat{f}_{he}(\bar{k}_\perp,\bar{k}'_\perp,\bar{k}_{i\perp})\cdot\\ &\qquad\cdot\left[\hat{f}^{*}_{he}(\bar{k}_\perp,\bar{k}'_\perp,\bar{k}_{i\perp}+\hat{f}^{*}_{he}(\bar{k}_\perp,\bar{k}_\perp-\bar{k}'_\perp+\bar{k}_{i\perp},\bar{k}_{i\perp})\right]d\bar{k}'_\perp\end{aligned} \tag{18}$$

$$\sigma^{\circ}{}_{vv}(\theta_s,\varphi_s;\pi-\theta_i,\phi_i)=$$
$$=4\pi k^2\cos^2\theta_s\int_{-\infty}^{\infty}W(\bar{k}_\perp-\bar{k}'_\perp)W(\bar{k}'_\perp-\bar{k}_{i\perp})\hat{f}_{hh}(\bar{k}_\perp,\bar{k}'_\perp,\bar{k}_{i\perp})\cdot \quad (19)$$
$$\cdot\left[\hat{f}^*_{hh}(\bar{k}_\perp,\bar{k}'_\perp,\bar{k}_{i\perp}+\hat{f}^*_{hh}(\bar{k}_\perp,\bar{k}_\perp-\bar{k}'_\perp+\bar{k}_{i\perp},\bar{k}_{i\perp})\right]d\bar{k}'_\perp$$

$$\sigma^{\circ}{}_{hv}(\theta_s,\varphi_s;\pi-\theta_i,\phi_i)=$$
$$=4\pi k^2\cos^2\theta_s\int_{-\infty}^{\infty}W(\bar{k}_\perp-\bar{k}'_\perp)W(\bar{k}'_\perp-\bar{k}_{i\perp})\hat{f}_{eh}(\bar{k}_\perp,\bar{k}'_\perp,\bar{k}_{i\perp})\cdot \quad (20)$$
$$\cdot\left[\hat{f}^*_{eh}(\bar{k}_\perp,\bar{k}'_\perp,\bar{k}_{i\perp}+\hat{f}^*_{eh}(\bar{k}_\perp,\bar{k}_\perp-\bar{k}'_\perp+\bar{k}_{i\perp},\bar{k}_{i\perp})\right]d\bar{k}'_\perp$$

where:

- $\bar{k}_\perp,\bar{k}_{i\perp},\bar{k}'_\perp$, are wave vectors denoting scattering, incident and intermediate directions respectively
- $W(\bar{k}_\perp-\bar{k}'_\perp)$ is the spectral density of the rough surface

The functions f_{ee}, f_{he}, f_{hh}, f_{eh} are given in [39].

2.1.3.2 The Kirchhoff approach

Physical Optics (PO)

The Kirchhoff approximation, which is valid when the radius of curvature at every point on the surface is much larger than the wavelength, assumes that the fields at any point on the surface are equal to the fields that would be present on an infinite tangent plane at that point. Even with this approximation, no analytic solution has been obtained for the scattered field without further simplifications. The expression of the scattered field contains the integral of a function *F(α, β)* where *α* and *β* are the local slopes of the surface *f(x,y)*. In one case (physical optics PO), for surfaces with small height standard deviation σ, the integrand function *F(α, β)* is expanded about zero slope and only the first terms *F(0,0)* are kept.
The bistatic scattering coefficients can be decomposed into a coherent and an incoherent part. For a large illuminated area, the bistatic scattering coefficient for the coherent component, which only exists in the specular directions, is:

$$\sigma^0_{Cqp}=4\pi\left|R_{po}\right|^2\exp(-4k^2\sigma_\varsigma{}^2\cos^2\theta_i)\delta_{qp}(\theta_s-\theta_i)\delta_{qp}(\phi_s-\phi_i) \quad (21)$$

where:

- subscript *p* represent polarization of the incident wave and subscript *q* the polarization of the scattered wave
- R_{po} is the reflection coefficient (*b* is for vertical or horizontal polarization)
- δ_{qp} is the Kronecker delta

The bistatic scattering coefficient for the incoherent component is given by equation [67]:

$$\sigma^{\circ}_{qp} = \left(\frac{k^2}{4}\right) |q_s \cdot F_p(\alpha,\beta)|^2 \; l^2 \, e^{-\sigma^2 k_{dz}^2} \sum_{m=1}^{\infty} \frac{(\sigma k_{dz})^{2m}}{m(m!)} e^{(k_{dx}^2 + k_{dy}^2) l^2/(4m)} \qquad (22)$$

where:

- q_s = h_s or v_s (horizontal or vertical directions of the scattered field)
- k = $2\pi/\lambda$ = wave number
- λ = electromagnetic wavelength
- α , β = local slopes along x and y directions
- θ_i, ϕ_i, θ_s, ϕ_s = incident and scattering incident and azimuth angles
- R_h, R_v = Fresnel reflection coefficients
- l = surface correlation length
- σ = height standard deviation
- $F_q(\alpha,\beta) = f(\alpha,\beta,R_h,R_v,\theta_i,\theta_s,\phi_s,\phi_i)$
- $k_{dx} = k \cdot (\sin\theta_i \cdot \cos\phi_i - \sin\theta_s \cdot \cos\phi_s)$
- $k_{dy} = k \cdot (\sin\theta_i \cdot \sin\phi_i - \sin\theta_s \cdot \sin\phi_s)$
- $k_{dz} = k \cdot (\cos\theta_i + \cos\theta_s)$

Geometrical Optics (GO)

When the wavelength is much smaller than the surface height standard deviation, we can assume under the geometrical optics limit (GO) that scattering occurs only along directions for which there are specular points on the surface excluding local diffraction effects. The bistatic scattering coefficients are proportional to the probability of the occurrence of the slopes, which specularly reflect the incident wave into the observation directions. The asymptotic solutions to the vector scattering integrals can be obtained using the stationary-phase method. In this approach the coherent component vanishes and the cross-polarized backscattering coefficient is zero since the Fresnel coefficients are evaluated at normal incidence. The bistatic scattering coefficient is expressed by [39]:

$$\sigma^{\circ}_{qp} = \frac{k_d^4}{\left|\hat{k}_i \times \hat{k}_s\right|^4 k_{dz}^4 \, 2\sigma_\varsigma^2 \left|C''(0)\right|} \exp\left[-\frac{k_{dx}^2 + k_{dy}^2}{2k_{dz}^2 \sigma_\varsigma^2 \left|C''(0)\right|}\right] f_{ab} \qquad (23)$$

where:

- $f_{qp} = g\,(k_x, k_y, k_z, k_{sx}, k_{sy}, k_{sz}, \sigma, R_h, R_v, \theta_i, \theta_s, \varphi_i, \varphi_s)$
- (k_x, k_y, k_z) and (k_{sx}, k_{sy}, k_{sz}) = components of incidence (k_i) and scattered (k_s) wave vectors
- $k_d = k_i - k_s = \{k_{dx}, k_{dy}, k_{dz}\}$
- *C"(0)* = second derivative of the autocorrelation function computed in the origin

It should be noted that the bistatic scattering coefficients satisfy reciprocity but violate energy conservation i.e. by ignoring multiple scattering there is a loss of energy.
Moreover, at high incidence angle the shadowing effect, which is neglected in the previous formula, becomes important. To take this effect into account the bistatic coefficients can be modified by introducing a shadowing function derived by Smith [68] and Sancer [69] (see also [39]). The modified coefficients σ^{m}_{qp} become:

$$\sigma^{m}_{qp}\left(\hat{k}_s,\hat{k}_i\right)=\sigma_{qp}\left(\hat{k}_s,\hat{k}_i\right)S\left(\hat{k}_s,\hat{k}_i\right) \tag{24}$$

where:

$$S\left(\hat{k}_s,\hat{k}_s\right)=\begin{cases}\dfrac{1}{1+\Lambda\left(\mu_s\right)} & \phi_s=\phi_i+\pi,\theta_s\geq\vartheta_i\\ \dfrac{1}{1+\Lambda\left(\mu_i\right)} & \phi_s=\phi_i+\pi,\theta_i\geq\vartheta_s\\ \dfrac{1}{1+\Lambda\left(\mu_s\right)+\Lambda\left(\mu_i\right)} & otherwise\end{cases} \tag{25}$$

$$\Lambda(\mu)=\frac{1}{2}\left[\sqrt{\frac{2}{\pi}}\frac{s}{\mu}e^{-\frac{\mu^2}{2s^2}}-erfc\left(\frac{\mu}{\sqrt{2}s}\right)\right] \tag{26}$$

$$s=\sigma_{\varsigma}\sqrt{\left|C''(0)\right|}=\sqrt{2}\frac{h}{l} \tag{27}$$

In (25) and (26) μ=cot(θ). By adding this factor, the energy budget is improved, but the sum of reflected and transmitted energy is always less than unity and the difference is higher for H polarization [39].
An analytical theory for polarimetric scattering by 2D dimensional anisotropic Gaussian surface based on second order Kirchhoff approximation has been developed in [70]. The study was developed for any surface slope and height distributions assumed to be statistically even. The model is based on the geometric optics and takes into account the shadowing effect within the first- and second-order illumination functions. The computation of the incoherent scattering coefficient requires only threefold integrations allowing a relatively small computer time. It has been shown that the cross incoherent scattering coefficient is nil due to the shadow. The second-order incoherent scattering coefficient is proportional to the product of two surface slope probabilities for which the slopes would specularly reflect the rays in the double scattering process. In addition, the slope distributions are related to each other by a propagating term, equal to the modified characteristic function derived over the elevation difference where both reflections occur. This result generalizes the one obtained by Sancer [69] for any process in the case of single scattering.
Simulations performed with various versions of the model (first and second order), with and without shadowing were compared with numerical simulations in [71]. From the obtained results, a general conclusion of the applicability of the method

was the following. For rms slope equal to 1, the model can be applied for incident angles θ_i, greater than 40°, for which the higher order contributions vanish. This means that if the rms slope diminishes, then the lower limit θ_i, should decrease. From the simulations, this point was not verified since $k\sigma_\zeta$ is not large enough to use the geometric optics approximation. Thus, the first restriction of the model seems to be that $k\sigma_\zeta$ must be greater that 2π. According to the surface slope, the greater is the rms slope, the larger must be the incident angle in order to eliminate the higher order contributions. For a dielectric surface, θ_i, decreases when $|\varepsilon_r|$ decreases because a part of energy is transmitted in the lower medium leading to the higher order contributions vanishing more quickly.

2.1.3.3 The Small Slope Approximation

The Small Slope Approximation (SSA) is one of the "non classical" methods proposed to solve the problem of scattering of electromagnetic waves from a rough surface, bridging the gap between the ranges of applicability of "classical" methods, such as Kirchhoff approximation (valid in the high frequency limit) and the Small Perturbation Method (SPM) (valid in the low frequency limit). SSA has been proposed by Voronovich [62],[72] who demonstrated that, following an approach very similar to the SPM, it is possible to derive a solution for the scattered and transmitted fields which are valid for surface with small slopes. A comprehensive description of the model can be found in [73].The limit of applicability of SSA is:

$$\nabla\zeta << \frac{k_z}{k} \tag{28}$$

where $\nabla\zeta$ is the gradient of the surface height, k is the wavenumber and k_z is the vertical component of the propagation vector of the incident plane wave or any other plane wave generated by the scattering phenomena and sensibly different from zero. This condition basically requires the maximum slope of the surface being much smaller than the grazing angle (angle respect to the horizontal) of any wave involved in the process. The authors claim that this condition does not depend on the frequency of the incident wave, as opposed to the SPM which requires:

$$k_z\zeta << 1 \tag{29}$$

The mathematically formulation of SSA is quite involved, even if it basically follows the formulation of the SPM proposed by Rice [74]. The scattered field of arbitrary polarization (similar considerations apply to the transmitted one) is represented trough a plane wave expansion The amplitude $S(\underline{k}_i,\underline{k})$ of each plane wave component (named the Scattering Amplitude SA) with propagation vector $\underline{k}$ depends on the incident propagation vector $\underline{k}_i$ and incident and observed polarizations. A key point of the formulation is the representation chosen for SA in order to satisfy few symmetry conditions of the solution regarding arbitrary vertical and horizontal translations of the rough surface. The following generic representation is chosen:

$$S(\underline{\mathrm{k}},\underline{\mathrm{k}}_\mathrm{i}) = \int \frac{d\underline{\mathrm{r}}_\mathrm{t}}{(2\pi)^2} \exp\left[-j(\underline{\mathrm{k}}_\mathrm{t} - \underline{\mathrm{k}}_\mathrm{ti})\cdot\underline{\mathrm{r}}_\mathrm{t} + j(k_z + k_{zi})\zeta(\underline{\mathrm{r}}_\mathrm{t})\right] \varphi(\underline{\mathrm{k}},\underline{\mathrm{k}}_\mathrm{i};\underline{\mathrm{r}}_\mathrm{t};[\zeta])\, d\underline{\xi} \tag{30}$$

where subscript "*t*" indicates the horizontal component of vectors ($\underline{r}_t$ is the generic point on the *xy* plane where the height of the surface is ζ and $\underline{k}_t$ is the horizontal component of a wave propagation vector).
The Fourier transform representation is introduced for the functional $\varphi(\underline{k}_i,\underline{k};\underline{r}_t;[\zeta])$ of the rough height profile $\zeta(\underline{r}_t)$, so that the previous equation becomes:

$$S(\underline{k},\underline{k}_i)=\int \frac{d\underline{r}_t}{(2\pi)^2}\, e^{-j(\underline{k}_t-\underline{k}_{ti})\cdot\underline{r}_t+j(k_z+k_{zi})\zeta(\underline{r}_t)}\; e^{j\underline{\xi}\cdot\underline{r}_t}\; \Phi(\underline{k},\underline{k}_i;\underline{\xi};[\zeta])\, d\underline{\xi} \tag{31}$$

where

$$\varphi(\underline{k},\underline{k}_i;\underline{r}_t;[\zeta])=\int e^{j\underline{\xi}\cdot\underline{r}_t}\; \Phi(\underline{k},\underline{k}_i;\underline{\xi};[\zeta])\, d\underline{\xi} \tag{32}$$

and the bi-dimensional variable $\underline{\xi}$ is a generic point in the Fourier transform domain of variable $\underline{r}_t$, and function $\zeta(\underline{\xi})$ is the Fourier transform of the surface height. Similarly to the SPM formulation, a series expansion is introduced for the SA. In this case the series expansion is introduced for functional $\Phi(\underline{k},\underline{k}_i;\ \underline{\xi}:[\zeta])$ which depend on the surface profile or its Fourier transform $\zeta(\underline{\xi})$. For this purpose it is considered the integral-power series applicable to smooth functional of $\zeta(\underline{\xi})$, which is a generalization of the Taylor series of a function of variable *x*. Assuming again the transformational conditions mentioned before, introducing such expansion leads to the following formula (omitting the dependence on $\underline{k},\underline{k}_i$):

$$\begin{aligned}\Phi(\underline{\xi};[\zeta])=\delta(\underline{\xi})\Phi_0+\int\delta(\underline{\xi}-\underline{\xi}_1)\Phi_1(\underline{\xi}_1)\underline{\xi}_1\zeta(\underline{\xi}_1)d\underline{\xi}_1+\\ +\int\delta(\underline{\xi}-\underline{\xi}_1-\underline{\xi}_2)\Phi_2(\underline{\xi}_1,\underline{\xi}_2)\underline{\xi}_1\zeta(\underline{\xi}_1)\underline{\xi}_2\zeta(\underline{\xi}_2)d\underline{\xi}_1d\underline{\xi}_2+\cdots\end{aligned} \tag{33}$$

The key point is the observation that in the expression of SA the following integral has to be computed:

$$\int e^{j\underline{\xi}\cdot\underline{r}_t}\; \Phi(\underline{\xi};[\zeta])\, d\underline{\xi} \tag{34}$$

By substituting the above expansion in this integral, the *n*th order term can be estimated as follows (reported here up to the 2nd order for sake of simplicity):

$$\begin{aligned}\int e^{j\underline{\xi}\cdot\underline{r}_t}\delta(\underline{\xi}-\underline{\xi}_1-\underline{\xi}_2)\Phi_2(\underline{\xi}_1,\underline{\xi}_2)\underline{\xi}_1\zeta(\underline{\xi}_1)\underline{\xi}_2\zeta(\underline{\xi}_2)d\underline{\xi}_1d\underline{\xi}_2=\\ =\int\Phi_2(\underline{\xi}_1,\underline{\xi}_2)\underline{\xi}_1\zeta(\underline{\xi}_1)e^{j\underline{\xi}_1\cdot\underline{r}_t}\,\underline{\xi}_2\zeta(\underline{\xi}_2)e^{j\underline{\xi}_2\cdot\underline{r}_t}d\underline{\xi}_1d\underline{\xi}_2\end{aligned} \tag{35}$$

By considering the mean value of the integrand function Φ_2:

$$\begin{aligned}\int\Phi_2(\underline{\xi}_1,\underline{\xi}_2)\underline{\xi}_1\zeta(\underline{\xi}_1)e^{j\underline{\xi}_1\cdot\underline{r}_t}\,\underline{\xi}_2\zeta(\underline{\xi}_2)e^{j\underline{\xi}_2\cdot\underline{r}_t}d\underline{\xi}_1d\underline{\xi}_2\approx\\ \approx|\Phi_2|\int\underline{\xi}_1\zeta(\underline{\xi}_1)e^{j\underline{\xi}_1\cdot\underline{r}_t}d\underline{\xi}_1\int\underline{\xi}_2\zeta(\underline{\xi}_2)e^{j\underline{\xi}_2\cdot\underline{r}_t}d\underline{\xi}_2=|\Phi_2|\|\nabla\zeta|^2\end{aligned} \tag{36}$$

where a well known property of the Fourier transform of the derivative has been applied. More generally, the *n*th term of the expansion gives rise to a term whose order of magnitude is the *n*th power of the gradient of the surface profile. This shows that the series expansion of SA can be valid when $|\nabla\zeta|$ (i.e., the slope of the surface) is small enough, as stated at the beginning.

The mathematical formulation prosecutes in a very similar way to the SPM. Limiting the solution to the first term (the zero-order term is a plane wave propagating in the specular direction) a random surface is subsequently considered and the relevant statistical moments of the scattered field are computed. Considering a spatially homogeneous random function representing the surface height and with Gaussian statistics, as done in most of the formulations, the coherent component is associated to the specular wave, whilst the power density of the incoherent component is associated to the variance of the Scattering Amplitude (SA). In the far field zone the bistatic scattering coefficient is also computed for a generic pair of incident and observed polarizations *p* and *q*, leading to the following formula for the first order approximation in the SSA (it differs of a factor 4π from [62] to account for a different definition of the coefficient):

$$\sigma_{pq}{}^{\circ}(\underline{\mathrm{k}}_{\mathrm{i}},\underline{\mathrm{k}}) = \sigma_{pq}{}^{\circ}(\theta_i,\varphi_i;\theta_s,\varphi_s) = \\ = \frac{(2k_z k_{zi})^2}{\pi}\left|B_{pq}(\underline{\mathrm{k}}_{\mathrm{i}},\underline{\mathrm{k}})\right|^2 \int e^{-j(\underline{\mathrm{k}}_{\mathrm{t}}-\underline{\mathrm{k}}_{\mathrm{ti}})\cdot\underline{\mathrm{r}}_{\mathrm{t}}} \cdot e^{-(k_z+k_{zi})^2\sigma^2} \cdot \frac{e^{-(k_z+k_{zi})^2 B(\underline{\mathrm{r}}_{\mathrm{t}})}-1}{(k_z+k_{zi})^2} d^2\underline{\mathrm{r}}_{\mathrm{t}} \quad (37)$$

where σ^2 is the variance of the random function $\zeta(\mathrm{r_t})$ representing the surface height, and $B(\mathrm{r_t})$ is its covariance function equal to the expected value $B(\mathrm{r_t})=\langle\zeta(\rho_t)\zeta(\underline{\mathrm{r}}_t\rho_t)\rangle$ and related to the surface autocorrelation function ρ by $B(\mathrm{r_t})=\sigma^2\rho(\mathrm{r_t})$. The factor $B_{pq}(\mathrm{k_i},\mathrm{k})$ is function of both incident and scattered propagation vectors and permittivity of the medium underneath the surface in a way dependent on polarizations (see [61] for the complete expression of such factor).

It is worth to note that Plant [75] has demonstrated that for the backscattering case this equation for the backscattering coefficient yield to the same expression provided by the IEM when considering single scattering contributions only.

SSA has been extensively used to simulate the scattering behaviour of the sea surface, either alone or in the framework of a double scale approach in order to account the effect of steep waves (in this case SSA does not require to introduce arbitrary parameters, such as the separation among small scale and large scale sea wavenumber introduced when considering the SPM). In particular, SSA has been used to simulate the bistatic scattering originating from the sea surface illuminated by the GPS signal.

2.1.3.4 The IEM model and its evolutions (IEMM and AIEM)

The Integral Equation Method (IEM) was conceived by Fung and his collaborators in the middle of the 80's with the main purpose of extending the validity range of the classical asymptotic approaches. The model evaluates the scattering coefficients of a randomly rough dielectric surface by using relatively simple algebraic formulas. A first systematic version of the IEM was published in 1992 [64]. In the following fifteen years, the model was improved in various successive versions to better evaluate the scattering from natural surfaces for the various measurement configurations and types of roughness.

The IEM model (first version Fung 1992)

Assuming a plane wave impinging on a rough surface, the far-zone scattered field in the medium above the surface is calculated with the Stratton-Chu formula [64],[65]. To obtain an accurate estimate of the total tangential field, the basic idea is to solve the integral equation to which the tangential field on the surface must obey (for this reason it is named as an Integral Equation Method). The IEM add a complementary term (c) to the classical Kirchhoff (k) tangential field. Such as the tangential fields, the scattered fields are expressed as a combination of the Kirchhoff (superscript *k*) and the complementary (superscript *c*) term:

$$E_{qp}^{s} = E_{qp}^{k} + E_{qp}^{c} \tag{38}$$

where:

$$E_{qp}^{k} = CE_0 \int f_{qp}\, e^{j\left(\vec{k}_s - \vec{k}_i\right)\cdot\vec{r}}\, dxdy \tag{39}$$

$$E_{qp}^{c} = \frac{CE_0}{8\pi^2} \int F_{qp}\, e^{ju(x-x')+jv(y-y')+j\vec{k}_s\cdot\vec{r}-j\vec{k}_i\cdot\vec{r}'}\, dx\, dy\, du\, dv\, dx'\, dy' \tag{40}$$

$$C = -\frac{jk}{4\pi R} e^{-jkR} \tag{41}$$

p and *q* denote the incident and receiving polarization respectively, *R* is the range of the observation point, *k* is the wavenumber, E_0 is the amplitude of the incident field, *x,y,x',y'* are integration variable in the space domain and *u,v* are integration variables in the Fourier domain.

f_{qp} and F_{qp} are dimensionless, complicated functions which depend on spatial variables. Several approximations are made to make these functions independent of spatial variables. In particular:

1. it assumed that the surface slope is moderate
2. the terms in the tangential field expressions involving the sum of the Fresnel reflection coefficients are disregarded.
3. In the expression of f_{qp}, the Fresnel reflection coefficients are approximated as a function of the incident angle at low frequencies (surface with small or moderate scale roughness) and as a function of the specular angle at high frequencies (surface with large scale roughness). Instead, the incidence angle is considered for F_{pq}.
4. The complementary term is derived by inserting the scattered field derived by the Kirchhoff approximation into the integral equation to which the tangential field on the surface must obey. In other word, it is a sort of second iteration for the Kirchhoff solution.
5. In the spectral representations of Green's function and its gradient (introduced in the complementary fields), the phase term with the absolute sign can be dropped because if the surface points are close together then the difference $z - z'$ will be small. On the other hand, if the two surface points are far apart then they cannot be correlated and hence will not contribute to the average power.
6. In the spectral representation of the gradient of the Green's function, the last term of vector $\underline{g}=u\underline{x}_0+v\underline{y}_0\pm\underline{z}_0\sqrt{(k^2-u^2-v^2)}$ is neglected, since it tends to cancel

itself when the ensemble average is made for rough surfaces. In other words, it is assumed that the Green's function is constant along the vertical direction when the complementary tangent surface field is computed. These last two assumptions have been revised in the following versions by the authors.

7. Moreover, the spatial dependence of both functions through the slope terms is removed by performing integration by parts and then ignoring the edge terms.

Once the field coefficients, f_{qp} and F_{qp}, are made independent of spatial variables, it is possible to provide the expression of the incoherent scattered power. It is obtained subtracting the mean squared power from the total power:

$$\begin{aligned}\left\langle \left|E_{qp}^{s}\right|^{2}\right\rangle - \left|\left\langle E_{qp}^{s}\right\rangle\right|^{2} &= \left\langle E_{qp}^{s} {E_{qp}^{s}}^{*}\right\rangle - \left\langle E_{qp}^{s}\right\rangle \left\langle E_{qp}^{s}\right\rangle^{*} = \\ &= \left\langle E_{qp}^{k} {E_{qp}^{k}}^{*}\right\rangle - \left\langle E_{qp}^{k}\right\rangle \left\langle E_{qp}^{k}\right\rangle^{*} + \\ &\quad + 2\,\mathrm{Re}\left[\left\langle E_{qp}^{c} {E_{qp}^{k}}^{*}\right\rangle - \left\langle E_{qp}^{c}\right\rangle \left\langle E_{qp}^{k}\right\rangle^{*}\right] + \\ &\quad + \left\langle E_{qp}^{c} {E_{qp}^{c}}^{*}\right\rangle - \left\langle E_{qp}^{c}\right\rangle \left\langle E_{qp}^{c}\right\rangle^{*}\end{aligned} \tag{42}$$

The corresponding bistatic scattering coefficient is:

$$\sigma_{qp}^{o} = \sigma_{qp}^{k} + \sigma_{qp}^{kc} + \sigma_{qp}^{c} =$$

$$= \begin{cases} \dfrac{k^2}{2} e^{-2k^2\sigma_z^2} \displaystyle\sum_{n=1}^{\infty} \sigma^{2n} \frac{\left|I_{qp}^{n}\right|^2}{n!} W^{(n)}\left(k_x, k_y\right) & \textit{smooth} \\ \dfrac{k^2 \left|f_{qp}\right|^2}{2\sigma^2 (k_{sz}+k_z)^2 \sqrt{\left|\rho_{\xi\xi}(0)\right|\left|\rho_{\zeta\zeta}(0)\right| - \rho_{\xi\zeta}^2(0)}} \cdot & \\ \quad \cdot e^{-\frac{\left|\rho_{\zeta\zeta}(0)\right|(k_{sx}+k_x)^2 + \left|\rho_{\xi\xi}(0)\right|(k_{sy}+k_y)^2 - 2\left|\rho_{\xi\zeta}(0)\right|(k_{sx}+k_x)(k_{sy}+k_y)}{2\sigma^2 (k_{sz}+k_z)^2 \sqrt{\left|\rho_{\xi\xi}(0)\right|\left|\rho_{\zeta\zeta}(0)\right| - \rho_{\xi\zeta}^2(0)}}} & \textit{rough} \end{cases} \tag{43}$$

From the above expression, it follows that the scattering coefficient is given by the sum of three terms: the Kirchhoff, the complementary and the cross terms (superscript *kc*). To carry out the average operation a hypothesis about the type of surface height distribution is necessary. The assumption of a Gaussian height distribution simplifies the calculation of the incoherent power terms [64],[65]. The model that is obtained is expressed in terms of multiple integrals and can be represented in two different forms depending upon whether the surface height is moderate or large in terms of the incident wavelength ($k\sigma_\zeta$). A large normalized surface height may be interpreted as corresponding to high frequency.

In the case of moderate roughness, the exponential factor involving the surface correlation under the integral is expanded into series and some terms, which do not give significant contribution in the reduction of the integral, are disregarded. Instead, when the surface height is large, a stationary phase evaluation is carried out and it is necessary that the normalized surface correlation is close to unity otherwise the integrand functions present in the scattering coefficient are not appreciable. Moreover, for each case, in the expression of scattering coefficient it is possible to distinguish two types of terms: one representing single-scattering, and the other representing multiple-scattering. This division is important to identify weather single or multiple scattering is important for application. Formulas for bistatic scattering coefficient valid separately when $k\sigma_\zeta \leq 2$ and for large $k\sigma_\zeta$ are given in [65].
It is important to note that this model does not include the effect of shadowing due to the roughness of the incident and scattered intensities. Thus, an additional function is needed to account for this effect. Some shadowing functions have been derived to correct the single scattering coefficient. The method of correction is simply multiply the scattering coefficient by the shadowing function, which depends on the cotangent of the incident angle and the surface slope. While this multiplication is suitable for the single scattering, for multiple scattering it cannot represent shadowing of the surface for the re-scattered field. A possible way to include it into the multiple scattering coefficients is to consider two shadowing functions: one depends on the cotangent of the incident angle and the other on the cotangent of the incident angle of the re-scattered field. Since the scattering terms appear in the form of a two dimensional integration with respect to the spectral variables (with respect to the Fourier transform representation of the Green's function), the latter shadowing function should be integrated. In this way the re-scattered field along every direction is modified by a shadowing function evaluated along that direction. Instead the other function is placed outside to multiply the integrals [64].

The IEMM model (Hsieh et al., 1997, 2003)

Several tests of the IEM model have shown that neglecting the contribution from two surface points that are neither near nor far can be illegitimate. Thus an improved version of the model has been proposed, which removes the assumption in the spectral representation of the Green's function used in the scattered field to compute multiple scattering (single-scattering terms were left unchanged) [75].

The far-zone scattered field becomes:

$$E_{qp}^{k} = CE_0 \int f_{qp}\, e^{j\left(\vec{k}_s - \vec{k}_i\right)\cdot\vec{r}}\, dxdy \tag{44}$$

$$E_{qp}^{c} \approx \frac{CE_0}{8\pi^2} \int F_{qp}\, e^{ju(x-x')+jv(y-y')-jq|z-z'|+j\vec{k}_s\cdot\vec{r}-j\vec{k}_i\cdot\vec{r}'}\, dxdydudvd\,x'dy' \tag{45}$$

For the expressions of f_{qp} and F_{qp}, this model keeps the same as given by the IEM. This leads to another approximation, the validity of which is justified by comparisons with measurements taken on statistically known surface. As a consequence it is required a revaluation of the average power and the scattering

coefficients, but, the added phase term factor, $q|z-z'|$, only affects the cross and complementary terms of the averaged power, whilst the Kirchhoff term remains the same as the IEM model [76].
Moreover it was found that keeping of such a phase term is needed to identify upward and downward scattering intensities. To understand this necessity Fig. 3 shows the scattered radiation generated by single scattering. If *S* represents an applicable shadowing function for the randomly rough surface, after the impingement of the incident wave on the surface, only the fraction *S* of the upward scattered power leaves the surface permanently. The other fraction of the upward propagating power, 1-*S*, is intercepted by the surface and becomes a source of multiple scattering. In other words, 1-*S* of the total illuminated area is re-illuminated by the upward scattered power. Similarly, only an *S* fraction of the total illuminated area is re-illuminated by downward scattered power. These intercepted scattered powers represent a further contribution of the incident power on the surface in multiple scattering processes. Therefore, it is not possible to assign the correct shadowing effect to multiple scattering calculation without identifying the upward and downward scattered intensities. In case of bistatic scattering an appropriate amount of shadowing is included to the incident and scattered power [76].

Comparisons of bistatic single, multiple and total scattering predicted by the IEMM model with measurements taken on a statistically known perfectly conducting Gaussian distributed surfaces with Gaussian ACF have pointed out the significant contribution of multiple scattering on very rough surfaces. The agreement between model predictions and laboratory measurements was within a fraction of 1 dB at all scattering angles [77].

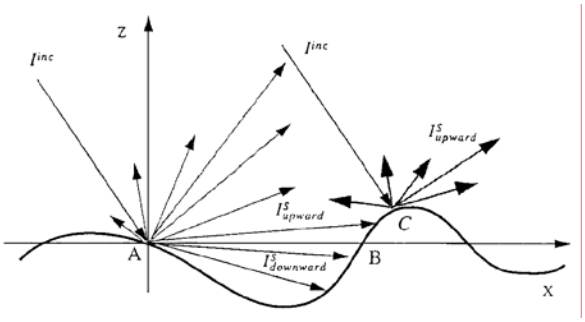

Fig. 3 - A surface scattering geometry showing single and multiple scattering rays. On average the upward scattered field will illuminate (1-S) portion of the total illuminated area and the downward scattered field will illuminate S portion of the total illuminated area (After [76])

A modification of the IEMM (Chen et al., 2000)

In the first version of the IEMM the complementary field coefficients F_{qp} are kept the same as in the IEM. In a further improvement [78], also these coefficients are modified to account for the absolute phase term within Green's function. So, these coefficients are re-derived based on new surface slope expressions and are

distinguished in $F_{qp,up}$ and $F_{qp,dn}$ to denote the upward and downward scattering parts. A comparison between the bistatic scattering coefficients computed with numerical simulations FDTD) for a conducting Gaussian surface with Gaussian ACF ($k\sigma_\zeta$ = 0.35, kl = 4.5) and the predictions of the re-derived IEMM model with and without multiple scattering has shown an overall good behavior of single scattering. However, in regions close to the minimum values of scattering the contribution of multiple scattering is significant (Fig. 4).

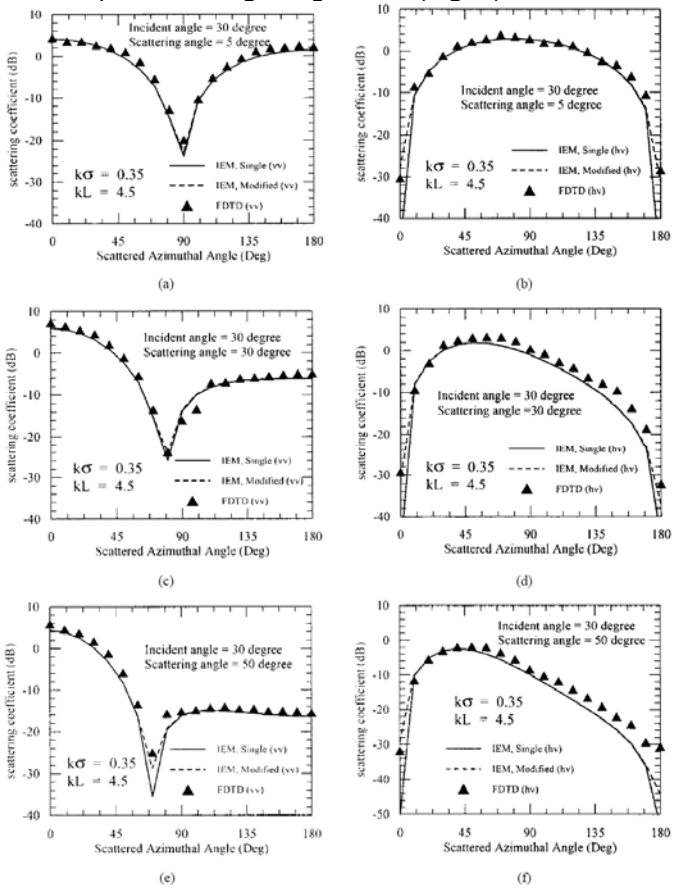

Fig. 4 - Comparisons of azimuthal angular behavior of scattering coefficient simulated with FDTD and IEMM with and without multiple scattering for co-polarization vv (a, c, e), and cross-polarization hv (b,d, f). Conducting Gaussian surface with Gaussian ACF (kσ = 0.35, kL = 4.5), θ_i = 30° incidence angle, θ_s = 5°, 30°, 50° scattering angles. (After [78]).

<u>*An update to the IEM (Wu, 2001; Fung, 2004)*</u>

In the IEM the spatial dependence of the Fresnel reflection coefficients is removed assuming that the local angle of incidence can be approximated as either the incident angle in the low frequency region (for slightly or moderate rough surfaces) or the specular angle in the high frequency region (for surface with large roughness

scale). The separation of these two regions leads to a discontinuity in the angular response reflection of the coefficients, and therefore to an unsatisfactory scattering behavior. This is particularly true for low dielectric constant or high loss surfaces because higher values of dielectric constant have fewer variations in the Fresnel reflection coefficients [79]. Another problem arises about the estimate of the Fresnel reflection coefficients in the intermediate region where both approximations fail.

For these reasons a transition model for the reflection coefficient was developed. Such model allowed the argument of the Fresnel reflection coefficients to change from the incident angle to the specular angle as the operating frequency and/or surface roughness changed from small to large values [79]. The Fresnel reflection coefficients, $R_v(\theta)$ and $R_h(\theta)$, that appear in the single scattering IEM, were then generalized by replacing them with new transition reflection coefficients, $R_v(T)$ and $R_h(T)$ [79],[80].

Comparisons of model results with numerical simulations using the Method of Moments were performed for surfaces with dielectric constant ε =3 - j0.1, surface rms height σ_z = 0.429 cm, correlation length l = 3 cm, and characterized by three different correlation functions (Gaussian, 1.5 Power, Two parameters). The comparisons, carried out for the backscattering as a function of frequency and incidence angle, with Fresnel reflections coefficients evaluated at θ_i, *0*, and *T*, showed that the difference between the three predictions was more appreciable at higher frequencies and higher incidence angles. In all cases, the analysis indicated that there was a region where neither $R_p(\theta_i)$, or $R_p(0)$ was applicable and where the use of the transition function in Fresnel reflection coefficient were in good agreement with simulations of both polarizations.

A further test of the validity of the transition function was carried out by comparing single scattering IEM simulations using the Fresnel reflection coefficients evaluated at θ_i, θ_s and *T* with experimental data acquired at the EMSL of the Joint Research Centre (JRC) in Italy on a Gaussian dielectric surface with Gaussian ACF (σ_z = 2.5 cm, l = *6* cm) [80]. Data were taken at 35° incidence angle in the frequency range 0.5-5 GHz The corresponding normalized rms height, $k\sigma_z$ changed from 0.26 to 2.6, making the scattering property changing from low frequency condition to a high frequency condition. The comparison showed that, simulation with $R_p(T)$ was able to well match experimental backscattering data in the transition region between 2.3 and 4 GHz making a link between simulations using $R_p(\theta_i)$, in the low frequency region and simulations using $R_p(0)$ above 4 GHz.

It should be noted that the transition model is demonstrated for the backscattering only. Its applicability to bistatic scattering remains the subject of further study.

The IEM2M model (Alvarez-Perez, 2001) and the Advanced Integral Equation (AIEM) (Chen, 2003a; Wu, 2004)

The last version of IEMM, with the modification on the complementary coefficients $F_{qp,}$ still contains an erroneous assumption for which terms corresponding to second-order scattering occurring through the medium below the surface are treated as occurring within the upper medium. Thus, the second-order scattering is not correctly described [81].

The main problem arises because the IEMM does not provide treatment to separate the medium in the spectral representation of Green's function and its gradient [81],[82]. That is, the phase term $e^{jq|z-z'|}$ is maintained, but no distinction is made between *q* in medium 1 and medium 2 for this phase term. Hence, second-order scattering within medium 1 is mixed inappropriately with second-order scattering through medium 2.
So both the IEM2M and the AIEM fully remove the two IEM assumptions of dropping the phase term with the absolute sign in the Green's function and its gradient, and cancelling the term with $\pm$ in the definition of the vector $\underline{g}$ when the ensemble averaging is made. Moreover, they express the complementary term of the scattering field as the sum of two contributions: one represents the interaction between two points on the surface that can take place through the incident medium and the other the interaction through the medium below the boundary (Fig. 5). For each case a difference is made between waves propagating upwards and downwards.

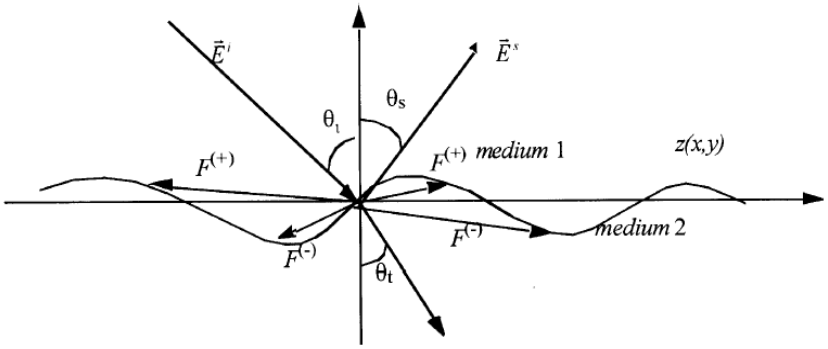

Fig. 5 - The geometry of scattering from a rough surface. $F^{(+)}$ represents the upward re-radiation, and $F^{(-)}$ represents the downward re-radiation. They may go through both the upper and lower medium.(After [82])

Although both approaches are based on the same concept for the complementary field, the mathematical representation is slightly different as also it is different the method of evaluation of the incoherent power and the assumption on the local angle of the Fresnel reflection coefficients.
The IEM2M re-derives the entire formulation of the model, for surfaces with small or moderate heights and for surfaces with large heights, with the Fresnel coefficients chosen in that way:

1. the first interaction of the incident wave with the surface in a second-order process contributes with a reflection coefficient characterized by the incident angle and transmitted polarization
2. a first-order term contributes with a reflection coefficient characterized by the scattering angle and receiving polarization [81].

Instead, the AIEM model, that represents a directed modification of the IEMM [78], expresses the above mentioned contributions for the complementary field in a simple way. It can be written as the sum of four terms, from which it is possible to recognize the terms related to the interaction between two points that happens through the incident medium ($E^c_{qp1,z>z'}$ and $E^c_{qp1,z<z'}$) and those related to the interaction through the medium below the boundary ($E^c_{qp2,z>z'}$ and $E^c_{qp2,z<z'}$) [82],[83]:

$$E^c_{qp} = E^c_{qp1,z>z'} + E^c_{qp2,z>z'} + E^c_{qp1,z<z'} + E^c_{qp2,z<z'} \quad (46)$$

$$E^c_{qp1,z>z'} = \frac{CE_0}{8\pi^2}\int_{z>z'} F^{(+)}_{qp1}\cdot e^{j\left[u(x-x')+v(y-y')-q_1(z-z')+k_1\left(\hat{k}_s\cdot\vec{r}-\hat{k}_i\cdot\vec{r}'\right)\right]} \quad (47)$$

$$E^c_{qp2,z>z'} = \frac{CE_0}{8\pi^2}\int_{z>z'} F^{(+)}_{qp2}\cdot e^{j\left[u(x-x')+v(y-y')-q_2(z-z')+k_1\left(\hat{k}_s\cdot\vec{r}-\hat{k}_i\cdot\vec{r}'\right)\right]} \quad (48)$$

$$E^c_{qp1,z<z'} = \frac{CE_0}{8\pi^2}\int_{z<z'} F^{(-)}_{qp1}\cdot e^{j\left[u(x-x')+v(y-y')-q_1(z-z')+k_1\left(\hat{k}_s\cdot\vec{r}-\hat{k}_i\cdot\vec{r}'\right)\right]} \quad (49)$$

$$E^c_{qp2,z<z'} = \frac{CE_0}{8\pi^2}\int_{z<z'} F^{(-)}_{qp2}\cdot e^{j\left[u(x-x')+v(y-y')-q_2(z-z')+k_1\left(\hat{k}_s\cdot\vec{r}-\hat{k}_i\cdot\vec{r}'\right)\right]} \quad (50)$$

The condition ***z*** > z' represents the upward propagation, while the opposite represents the downward propagation. It is noted that when dealing with complementary field coefficients, the reradiated fields can propagate through medium 1, denoted by $F^{(+)}_{qp1}$, $F^{(-)}_{qp1}$, and through medium 2, denoted by $F^{(+)}_{qp2}$, $F^{(-)}_{qp2}$, as shown in Fig. 5.

Once these scattering fields are obtained, the single scattering terms that in the IEMM were left the same as those present in the first IEM version, are re-derived since mathematically such terms should be modified according to the derivation keeping the absolute phase term within Green's function [82]. The multiple-scattering terms instead are left as the same formulated in the IEMM [78],[83].

The AIEM model has been validated comparing the prediction results for backscattering with numerical simulations and measured data in terms of angular, frequency and polarization dependence [83].

It has been shown that the difference between the results of the AIEM and the IEM, both using the transition model for the Fresnel reflection coefficient, is quite small on slightly rough surface (rms slope = 0.235) suggesting that the absolute phase term in the Green's function can be ignored. Instead, when the roughness increases to $k\sigma_z$ = 3.0, *kl* = 6.0, the difference between the two models becomes significant. It was also observed that the difference is larger for smaller dielectric constants. This indicates that the absolute phase term in the Green's function cannot be dropped out for surfaces with a large slope and a small dielectric constant [83].

We can remark that the refinement work carried out from the first IEM to the last AIEM consisted in removing some of the original approximations. This was done either to obtain a relatively simple (but efficient) scattering model and to limit the

computing time power of the 90's PC. It is worth to note that the computational time of the AIEM is much heavier than the first IEM, and in many practical cases the original formulation is fully acceptable. However, at the present state of the art, the AIEM represents perhaps the best model for simulating surface scattering. Indeed, it combines the high accuracy in evaluating the scattering coefficients with a high versatility in modeling the various statistics of the soil (Gaussian, Exponential, Two scale, etc.).

2.2 Scattering and emission from a snow layer

In microwave remote sensing the snow cover is in general modeled as a heterogeneous slab upon a semi-infinite medium. In such representation there are three main contributions to the total emission: the upward emission from the snowpack, the one of the soil attenuated by the overlying layer and the downward snow emission reflected by soil. In more sophisticated approaches the multi-layer nature of the snow cover and the coherent behavior of the e.m. waves in such complex media are also taken into consideration.
From the electromagnetic point of view, snow can be considered as a dense heterogeneous medium composed of ice particles, which occupy an appreciable volume fraction (of the order or bigger than 10 %), air, and, in the case of wet snow, liquid water. This latter can appear as a thin film around ice grain and as pockets among ice particles. In such a dense medium, where there is more than one scatterer within a wavelength distance and the dielectric properties of the particles are significantly different from those of the background, the assumption of independent scattering, and then the conventional radiative transfer (CRT), are not valid anymore.
The inhomogeneous layer of snow can be treated as a continuous random medium where scattering effects are taken into account by means of random fluctuations of permittivity described by a correlation function, or as a discrete scattering medium composed of scattering particles embedded in a host background. Both methods can address coherence effects and satisfy energy conservation [39],[67],[84].
The first theories of scattering from random media disregarded the singular nature of the dyadic Green's function (DGF) and were valid only for the case of weak fluctuations of dielectric constant (WFT). When dealing with remote sensing of snow cover the strong variations of the permittivity must be taken into account.

2.2.1 The Strong Fluctuation Theory

In the Strong Fluctuation Theory (SFT) the snow is modeled like a homogeneous medium with permittivity fluctuations described by a correlation function: the variance characterizes the strength of the permittivity function of the medium and correlation lengths corresponding to the scales of the fluctuation. The major features of SFT are:

- the singularity of the DGF is taken into account to evaluate the effective permittivity of the random medium
- the exclusion volume has the same shape of the correlation function (related to the shape of the scatterers)

An effective permittivity is used to characterize both absorption and scattering effects due to randomness of the medium. The scatterers (i.e. ice grains) embedded in the background are transformed into dipoles embedded in a medium with an auxiliary permittivity ε_g. The latter can be seen as a quasi-static permittivity taking into account absorption effects. The effective permittivity, which considers also the scattering effects, is computed from ε_g and from the correlation function describing permittivity fluctuations of the continuous random medium. Once the effective permittivity has been obtained, the brightness temperature can be computed from the coherent wave approach described in the following paragraph.

A first formulation of the SFT [85] represents the snow layer as an infinite half space (host) medium with permittivity ε_b (air) filled with scatterers with permittivity ε_s (ice grains). The fractional volume occupied by the scatterers is f and the one occupied by the host medium is (1-f). In [86] several correlation functions are assessed, for both isotropic and anisotropic cases. All of these functions satisfy the previous requirements and lead to an extension of the classic Weak Fluctuation Theory (WFT).

In [87] the authors extend the theory to the case of a three-component mixture. The components of the infinite half space are two types of scatterers (ice particles and water droplets with permittivity ε_{s1} and ε_{s2} and volume fraction f_{s1} and f_{s2} respectively) embedded in a background medium (air with permittivity ε_b). This representation is useful in modeling wet snow that is composed by ice grains, water and air. The expressions of effective permittivity and scattering coefficients remain in the same algebraic form of the two-component case with the addition of small correction coefficients (see Appendix 2).

The case of wet snow is treated by Stogryn [88] who reformulates the SFT by accounting for a medium with N-constituents and considers the case of ice grains covered by a thin film of water. Special attention is paid to the case of spherical inclusions for which the susceptibility ξ_i has a simple form. The scattering coefficients remain the same and only the effective permittivity is changed accounting for the N possible values ε_i (i=1..N) that $\varepsilon(\underline{r})$ can assume. In the model, wet snow is modeled as an isotropic random medium consisting of air, ice, and water (both as menisci between ice grains and as a thin film surrounding ice particles). The manner in which water is distributed in the snow has a major effect on the snow dielectric properties. At frequencies below 12 GHz, corrections due to the finite-ice-grain size is small so that ε_g is close to the true dielectric constant. The fraction of water present as a film f_f, which fits experimental data is independent of frequency to within experimental accuracy of the determination of the dielectric constant, and well fits data for both the real and the imaginary part of the dielectric constant. From the fitting of the experimental data, the author obtains f_f = 0.24 for all the frequencies between 8 and 12 GHz. It should be noted that the Polder-Van Santen theory (ε_g calculated as in [87]) corresponds to the limiting case of f_f = 0. It is shown that for a snowpack with density = 0.442 g/cm^{-3} and total water fraction = 2.5 %, the Polder-Van Santen formula underestimates Im(ε_g) by a factor of 13.1 at 8 GHz and by a factor of 8.9 at 12 GHz. The underestimate is less

pronounced for Re(ε_g) where the Polder-Van Santen theory is lower by a factor of about 1.05 at the two frequencies.
The permittivity of snow under various physical conditions has been subject of many theoretical and experimental investigations for a long time, and data are currently available at frequencies up to 90 GHz (e.g. [89],[90],[35],[36]). More recently, Arslan *et al*. [91] computed the effective permittivity of wet snow by using the SFT for a two phase (dry snow with nonsymmetrical inclusions of liquid water) and a three-phase (air, and spherical inclusions of ice and water) model. The results indicated that the shape and the size of inclusions are important. It should be noted that penetration in dry snow is very high up to frequencies of Ku band. A small quantity of liquid water (1-2%) can reduce penetration to a fraction of the observation wavelength.

2.2.1.1 Wave approach

As stated before, according to the Strong Fluctuation Theory the random medium is modeled like a homogeneous layer with a spatially fluctuation permittivity. By using the fluctuation-dissipation theorem the brightness temperature of a slab above a semi-infinite medium can be easily calculated. Moreover, using the wave approach is possible to extend the results to a multilayer snowpack [92].

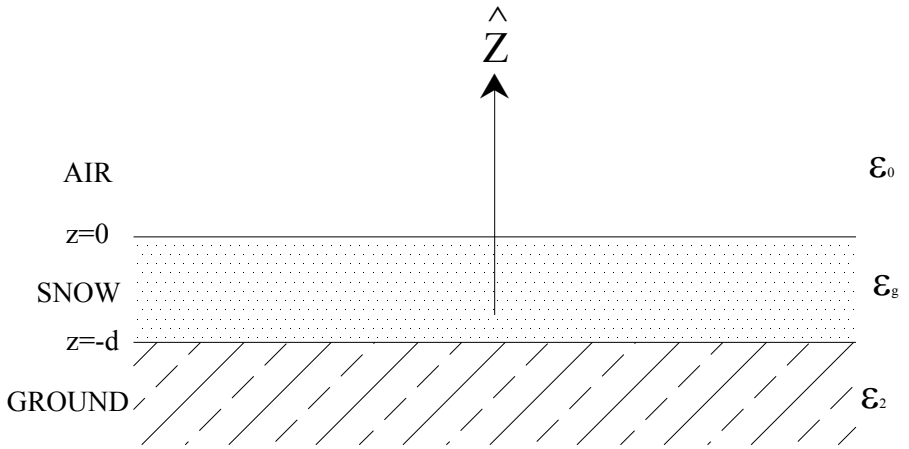

Fig. 6 – Structure of the simple snowpack modeled like in [92]: there is one layer of snow above a semi-infinite medium (the soil).

For a single layer of random scatterers overlying a semi-infinite medium (Fig. 6), the brightness temperature at the zeroth order is expressed by [51]

$$T_{Bh}^{(0)}(\theta)=\frac{k_0}{\cos\theta}\frac{\varepsilon_g''}{\varepsilon_0}T_1\frac{1}{2k_{1z}''}\left[\left|\frac{T_{h,01}}{D_2}\right|^2\left(1-e^{-2k_{1z}''d}\right)\left(1+\left|R_{h,12}\right|^2e^{-2k_{1z}''d}\right)\right] + \frac{k_0}{\cos\theta}\frac{\varepsilon_2''}{\varepsilon_0}T_2\frac{1}{2k_{2z}''}\left|\frac{T_{h,01}T_{h,12}}{D_2}\right|^2e^{-2k_{1z}''d} \quad (51)$$

$$T_{Bv}^{(0)}(\theta)=\frac{k_0}{\cos\theta}\frac{\varepsilon_g^{"}}{\varepsilon_0}T_1\frac{1}{2k_{1z}^{"}}\left[\left|\frac{k_0T_{v,01}}{k_1F_2}\right|^2\left(1-e^{-2k_{1z}^{"}d}\right)\left(1+\left|R_{v,12}\right|^2e^{-2k_{1z}^{"}d}\right)\right] \tag{52}$$

$$+\frac{k_0}{\cos\theta}\frac{\varepsilon_2^{"}}{\varepsilon_0}T_2\frac{1}{2k_{2z}^{"}}\left|\frac{k_0T_{v,01}T_{v,12}}{k_2F_2}\right|^2e^{-2k_{1z}^{"}d}$$

where T_1 and T_2 are respectively the snow and soil temperatures, $R_{p,mn}$ and $T_{p,mn}$ are the reflection and transmission coefficients (p=*v or h*, indicates polarization, mn = 01,12 indicates transition between layers) and the double apex stands for the imaginary part.

If the T_1=T_2 and $\varepsilon_{eff}\sim\varepsilon_g$ (the random medium is only absorptive, i.e. the scattering coefficient can be disregarded) the previous equations become

$$T_{Bh}^{(0)}(\theta)=T_1\left(1-\left|\frac{R_{h,01}+R_{h,12}\,e^{2ik_{1z}d}}{1+R_{h,01}R_{h,12}\,e^{2ik_{1z}d}}\right|^2\right) \tag{53}$$

$$T_{Bv}^{(0)}(\theta)=T_1\left(1-\left|\frac{R_{v,01}+R_{v,12}\,e^{2ik_{1z}d}}{1+R_{v,01}R_{v,12}\,e^{2ik_{1z}d}}\right|^2\right) \tag{54}$$

which are the well known brightness temperatures for an absorptive layer above a semi-infinite medium [8], [51],[84].

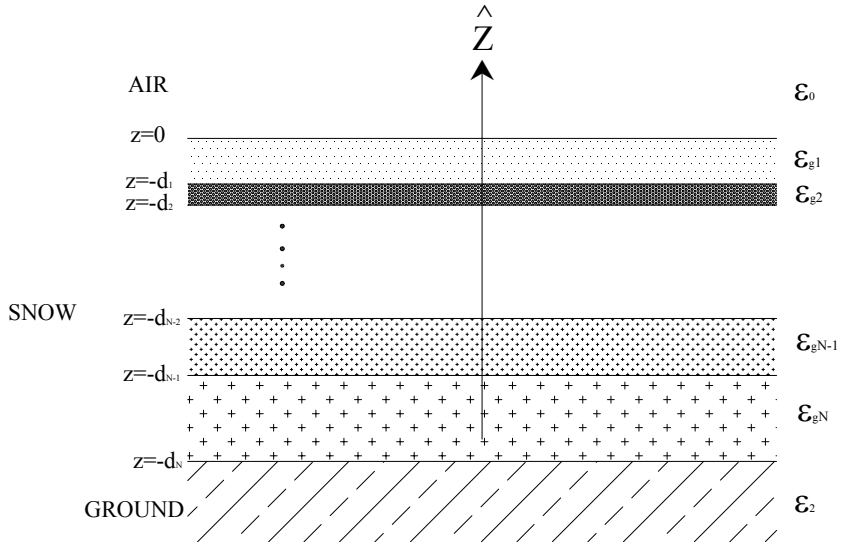

Fig. 7 – The structure of a multilayer snowpack overlying a half-space. The interfaces are considered as flat [51][83].

To account for the layered structure of natural media, it is also possible to extend (51)-(52) to a multi-layer case (Fig. 7). In [92] and [51] the fluctuation-dissipation theorem is applied to such complex media and the final expression of brightness temperature is

$$T_{Bh}^{(0)}(\theta) = \frac{k_0}{\cos\theta}\sum_{r=1}^{N}\frac{\varepsilon_r''}{\varepsilon_0}T_r\frac{1}{2k_{rz}''}\left[\,|A_r|^2\left(e^{2k_{rz}''d_r}-e^{2k_{rz}''d_{r-1}}\right)-|B_r|^2\left(e^{-2k_{rz}''d_r}-e^{-2k_{rz}''d_{r-1}}\right)\right] + \frac{k_0}{\cos\theta}\frac{\varepsilon_t''}{\varepsilon_0}T_t\frac{1}{2k_{tz}''}|T_h|^2 e^{-2k_{tz}''d_N} \quad (55)$$

$$T_{Bv}^{(0)}(\theta) = \frac{k_0}{\cos\theta}\sum_{r=1}^{N}\frac{\varepsilon_r''}{\varepsilon_0}T_r\frac{1}{2k_{rz}''}\left[\,|C_r|^2\left(e^{2k_{rz}''d_r}-e^{2k_{rz}''d_{r-1}}\right)-|D_r|^2\left(e^{-2k_{rz}''d_r}-e^{-2k_{rz}''d_{r-1}}\right)\right] + \frac{k_0}{\cos\theta}\frac{\varepsilon_t''}{\varepsilon_0}T_t\frac{1}{2k_{tz}''}|T_v|^2 e^{-2k_{tz}''d_N} \quad (56)$$

where the coefficients A_r, B_r, C_r, D_r, $r=1..N$, and transmissivity T_v, T_h can be calculated according [51].

2.2.2 Dense Medium Radiative Transfer Theory (DMRT)

The classical radiative transfer theory has been successfully used to predict the electromagnetic behavior of the discrete models where the scatterers are very sparse. Unfortunately, when the fractional volume occupied by the scattering particles is appreciable ($f > 0.1$) and the dielectric properties of the particles are significantly different from that of the background medium, such as in the case of snow, the particle positions become correlated. Thus, the assumption of independent scattering overestimates the scattering and the Conventional Radiative Transfer (CRT) cannot be used anymore. Indeed, if the particles scatter independently, the extinction rate is linearly proportional to the number of particles per unit volume n_o and to $f = n_o v_o$, where v_o is the volume of a single particle. However, physical intuition suggests that that the linear relation cannot be correct for arbitrary f, because when the entire volume is occupied by scatterers, the medium becomes homogeneous ($f = 1$) and scattering should be equal to zero. Experimental data taken on a slab containing densely distributed spherical particles overlying a homogeneous half-space confirmed that, in a dense medium with small particles, both the coherent attenuation rate and bistatic intensities first increase with the volume fraction of the particles until a maximum is reached, and then decrease when the volume fraction further increases [93],[94] (Fig. 8). Thus attenuation rates and bistatic scattering exhibit a peak as a function of the concentration of particles. The magnitudes of both are also less than those predicted by the independent scattering assumption and the conventional radiative transfer theory.

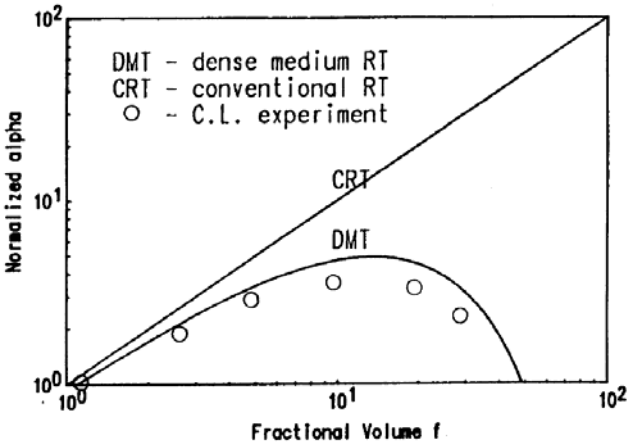

Fig. 8 - Theoretical results of normalized attenuation rates as a function of fractional volume compared with experimental data. Circles represent the experimental data. All the data have been normalized by the attenuation rate based on independent scattering at a fractional volume of 100 percent (After [94]).

Dense media scattering has been the subject of continual interest since the beginning of 80's because of the importance of the effects from the correlation of scatterers [95]-[97]. In Fig. 9 is depicted a comparison of the pair distribution functions *g(r)* of the scatterers for several volume fractions in a dense medium and in a sparse one, as a function of the distance between the particles. It is possible to see that, in a dense medium, the probability that two particles are at a certain distance decrease as the distance increase. Moreover, when the density increases (and the distance among the scatterers decreases) also the probability to find the particles closer each others increases. When the separation between the particles is 3-4 diameters, *g(r)*~1, which means that the probability of this spatial configuration is almost zero.

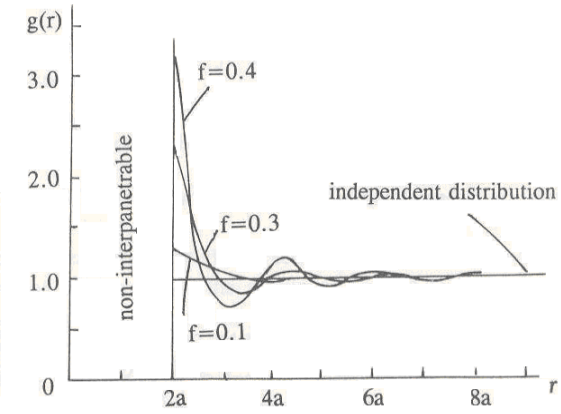

Fig. 9 - The pair distribution function of the scatterers in a dense medium with respect to a sparse one (represented by the independent distribution). (After [84])

The Dense Medium Radiative Transfer equations (DMRT) were derived from the wave theory under the quasi-crystalline approximation with coherent potential (QCA-CP) [98]-[100] on the first moment of the field, and the ladder approximation of correlated scatterers on the second moment of the field [67],[101],[102]. The basic physical idea is that because the particles are randomly distributed, the phases of the scattered fields are random, so that the products of scattered fields generally average to zero except those terms in the multiple scattering equations that result in constructive interference. The mathematical approach is to identify and retain only the constructive interference terms in the correlated ladder approximation. Putting these terms together gives the DMRT equation.

The ladder approximation is one of the common approximations used for the Bethe-Salpeter equation [102]. Detailed derivations can be found in [96]. The reason for choosing the combination of the QCA-CP and ladder approximation is that energy conservation is obeyed exactly. Sometimes the dense medium radiative transfer theory is called the radiative wave theory to emphasize its derivation from wave theory and that does not use conventional radiative transfer theory in any step of the derivations. In the ladder approximation of correlated scatterers, wave interactions between different particles (whether of far, near, or intermediate range) are weighted by the pair distribution function of particle positions; therefore the wave interactions of all ranges of distance separation are included. The extinction rate, albedo, and phase matrix of the DMRT equation are expressed in terms of the physical parameters of the medium [96],[103]. DMRT takes the following into account: 1) Scattering by correlated scatterers; 2) the pair distribution function of scatterer positions; and 3) the effective propagation constant of a dense medium. The improved equations also preserve the advantages of the conventional radiative transfer equations: a) Multiple scattering of the incoherent intensities is included; b) energy conservation and reciprocity are obeyed; and c) the form of the equations remains the same as the conventional radiative transfer equations so that numerical solutions are calculated in the same manner [96],[103].

In [94] the DMRT was applied to study the multiple scattering in a slab containing densely distributed particles smaller than a wavelength overlying a homogeneous half-space (Fig. 10). The theory was used to explain the phenomena observed in a controlled laboratory experiment [93],[104], performed in 1983. In this paper the DMRT equations, derived from the Dyson equation under the QCA-CP and the Bethe-Salpeter equation under the ladder approximation of correlated scatterers, were solved numerically by using the Fourier series expansion and discrete ordinate-eigenanalysis approaches [67],[105]. The extinction rate, albedo, and phase matrix were related to the physical parameters of the medium.

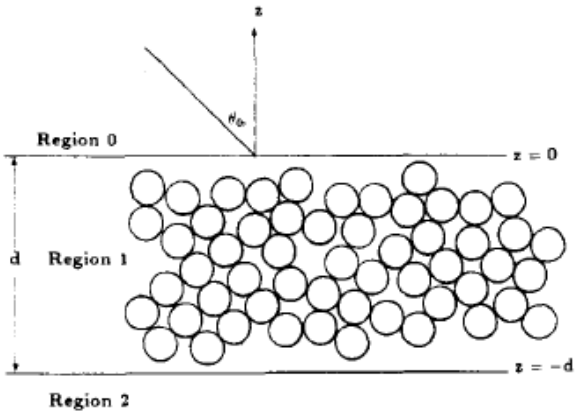

Fig. 10 - A polarized electromagnetic plane-wave incident upon a slab of densely distributed particles (region 1) overlying a homogeneous half-space (region 2). (After [94])

The study considers a slab of densely distributed spherical particles of radius *a* and permittivity $\varepsilon_s = \varepsilon_s' + i\varepsilon_s''$ embedded in a background of permittivity ε. The slab is of thickness *d* and lies above a homogeneous medium with a permittivity of $\varepsilon_2 = \varepsilon_2' + i\varepsilon_2''$. The DMRT is used to describe the propagation and scattering in the slab. The pair distribution function *g(r)* describes the correlation of particle positions and is dependent on the physical parameters of particle size *a* and fractional volume *f* occupied by the particles.

Two assumptions are inherent in deriving the effective propagation constant and albedo: 1) The particle size has to be small compared to the wavelength of interest; 2) the effective propagation constant *K* is assumed to have a small imaginary part compared with its real part; i.e., $K'' << K'$. Based on these two assumptions, minor modifications were made to the formulae when computing the effective propagation constant and albedo. K_0 introduced according to the assumption of small particle size, satisfies the relation

$$K_0^2 = k^2 + \frac{f(k_s^2 - k^2)}{1 + \frac{k_s^2 - k^2}{3K_0^2}(1-f)} \tag{57}$$

where $k = \sqrt{\mu\varepsilon}$ and $k_s = \sqrt{\mu\varepsilon_s}$ are, respectively, the wavenumbers of the background and the particles, μ is the permeability. The background medium is assumed as non-absorptive (i.e., air). $f = n_0 4\pi a^3/3$ is the fractional volume occupied by the particles, and n_o is the number density of particles in a unit volume.

Physically, K_0 indicates the propagation constant of coherent waves in a medium where the scattering effect is insignificant and can be ignored; mathematically, K_0 is regarded as the zeroth order solution of *K*. From (57), K_0, generally a complex number, is solved by using a quadratic formula. Nevertheless, in accordance with the second assumption, K^2 is approximately expressed as $K^2 = K'^2 + i2K'K''$, where K' and K'' represent the real and imaginary parts, respectively. With this approximation of K^2 it is:

$$K^2 = K'^2 + 2iK'K'' =$$

$$= k^2 + \frac{f(k_s^2 - k^2)}{1 + \frac{k_s^2 - k^2}{3K_0^2}(1-f)} \cdot \left\{ 1 + i\frac{2}{9}\frac{K_0 a^3 (k_s^2 - k^2)}{1 + \frac{k_s^2 - k^2}{3K_0^2}(1-f)} \left[1 + 4\pi n_0 \int_0^\infty dr r^2 (g(r) - 1)) \right] \right\} \quad (58)$$

where K_0 is now known from (57). Assuming that the particles are non-interpenetrable and that the intermolecular forces are zero [106] the pair distribution $g(r)$ function is computed using the Percus-Yevick approximation from the following equation [67],[96],

$$1 + 4\pi n_0 \int_0^\infty dr\, r^2 (g(r) - 1)) = \frac{(1-f)^4}{(1+2f)^2} \quad (59)$$

The imaginary part $2K$, representing the extinction rate k_e, is solved from (58) by balancing the real and imaginary parts separately. The albedo ϖ is

$$\widetilde{\omega} = \frac{2}{9}\frac{a^3 f}{k_e} \left| \frac{k_s^2 - k^2}{1 + \frac{k_s^2 - k^2}{3K_0^2}(1-f)} \right|^2 \frac{(1-f)^4}{(1+2f)^2} \quad (60)$$

In region 1, for $\pi \geq \theta \geq 0$, the dense medium radiative transfer equation assumes a form which resembles the conventional radiative transfer equation.

$$\cos\theta \frac{\partial \bar{I}(z;\theta,\phi)}{\partial z} = -k_e \bar{I}(z;\theta,\phi) + k_a CT + \int_0^\pi d\theta' \sin\theta' \int_0^{2\pi} \overline{\overline{P}}(\theta,\phi;\theta'\phi')\, d\phi' \cdot \bar{I}(z;\theta',\phi') \quad (61)$$

where the 4x4 phase matrix $\overline{\overline{P}}(\theta,\phi,\theta',\phi')$, is dependent on k_e and ϖ . $\bar{I}(z;\theta,\phi)$ is column vector containing the four Stokes parameters.

Equation 61 is derived from the Bethe-Salpeter equation under the ladder approximation of correlated scatterers. In the Bethe-Salpeter equation, the phase information is maintained through the covariance of the incoherent and coherent fields. In the ladder approximation of correlated scatterers the effects of near, intermediate, and far field are included and weighted in a consistent manner.

The phase matrix in (61), $\overline{\overline{P}}(\theta,\phi,\theta',\phi')$, is identical to the Rayleigh phase matrix of Rayleigh scatterers. To obtain (61) the coherent and the incoherent parts of the intensity were added together to form the total Stokes vector. The real part K' of the effective propagation constant K is generally much larger than the imaginary part K''. The angles of reflection and transmission at the boundary between region 0 and region 1 obey Snell's law by using the real part of the effective propagation constant in region 1. Hence, $k_o \sin\theta_o = K' \sin\theta$, where θ_o and θ are angles in region 0 and region 1, respectively.

Once the dense medium radiative transfer equations are solved subject to the boundary conditions, the scattered Stokes vector in the direction (θ_{os} ,ϕ_{os}) region 0 is:

$$\bar{I}_o(\theta_{os},\phi_{os};z=0)=\overline{\overline{T}}_{10}(\theta_s)\cdot\bar{I}(\theta_s,\phi_s;z=0) \tag{62}$$

where:

$$\bar{I}_o(\theta_{os},\phi_{os};z=0)=\begin{bmatrix} I_{vs} \\ I_{hs} \\ U_s \\ V_s \end{bmatrix} \tag{63}$$

and $\overline{\overline{T}}_{10}(\theta)$ is the transmissivity matrix of the Stokes vector from region 1 to region 0.

In [94] the dense medium radiative transfer equations were solved numerically by using Fourier series expansion and discrete eigen-analysis approaches. As an example of the results Fig. 11 shows a comparison of computed bistatic intensities with experimental data taken in laboratory.

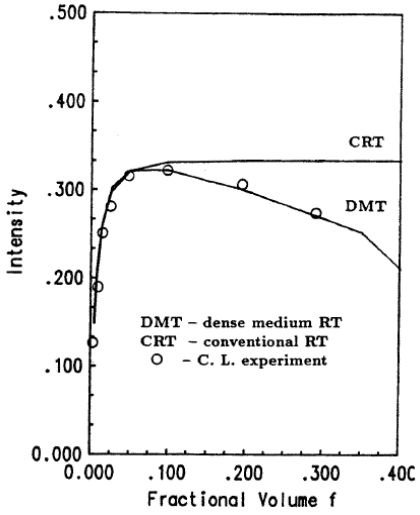

Fig. 11 - Computed normalized bi-static intensities as a function of fractional volume f are compared with a controlled laboratory experiment. DMT and CRT denote the results of dense medium theory and conventional theory, respectively, and circles represent the experimental data for particle concentration from 0.302 to 28.95 percent (After [94])

2.2.2.1 Approximation of multiple scattering equations (Quasi-Crystalline Approximation, QCA, and QCA with Coherent Potential, QCA-CP)

Multiple scattering from a collection of discrete scatterers can be studied by using the Foldy-Lax equations and taking configurational averages that lead to a

hierarchy of equations. However, to solve the equations, approximations need to be made. The most used approximations in modeling scattering from snow pack are the effective field approximation (EFA) and the quasi-crystalline approximation (QCA). Coherent potential (CP) is frequently introduced to impose self-consistent approximations.

For a half space of N particles in regions $V_1, V_2, \ldots V_N$ (the j^{th} particle is centered at r_j, has permittivity ε_j, permeability μ, and wavenumber k_j) the Foldy-Lax multiple scattering equations in operator form can be written as follows [39]:

$$\overline{\overline{G}} = \overline{\overline{G_o}} + \sum_{l=1}^{N} \overline{\overline{G_o}}\,\overline{\overline{T_l}}\,\overline{\overline{G_l}}$$

$$\overline{\overline{G_j}} = \overline{\overline{G_o}} + \overline{\overline{G_o}} \sum_{l=1, l\neq j}^{N} \overline{\overline{T_l}}\,\overline{\overline{G_l}} \qquad (64)$$

where the Green's functions $\overline{\overline{G}}$ and $\overline{\overline{G_l}}$ l = 1,2, ..,N are functions of all the particles and $\overline{\overline{T_l}}$ is the transition operator defined in [39] function of the l^{th} particle .
To calculate the coherent and incoherent fields ensemble averages of multiple scattering equations must be taken. By using the concept of configurational averaging and the Bayes' rule we obtain from (64) [39]:

$$E\,(\overline{\overline{G}}\,) = \overline{\overline{G_o}} + N\overline{\overline{G_o}}\,E(\overline{\overline{T_j}}\;\overline{\overline{E_j}}(\overline{\overline{G_l}})) \qquad (65)$$

where E is the expectation value.
Similarly, by fixing the particle l we obtain from (65)

$$E_l(\overline{\overline{G_l}}) = \overline{\overline{G_o}} + \overline{\overline{G_o}} \sum_{l=!, l\neq j}^{N} E_l\,\overline{\overline{T_j}}\;\overline{\overline{G_j}} \qquad (66)$$

On averaging the summation in (66) can be replaced by (N-1). Thus:

$$E_l(\overline{\overline{G_l}}) = \overline{\overline{G_o}} + \overline{\overline{G_o}}\;(N-1)E_l\;(\overline{\overline{T}}_j\;E_{jl}(\overline{\overline{G_j}})) \qquad (67)$$

The equations (65) to (67) indicate that the total average is given in terms of the conditional average with one particle fixed, and the conditional average with one particle fixed is given in terms of the conditional average with two particle fixed. In similar manner, we can express the conditional average with n particles in terms of n+1 particles fixed. A hierarchy of equations is generated.
In the Effective Field Approximation (EFA, Foldy's approximation), truncation is carried out at the first equation of the hierarchy. It is assumed

$$E_j(\overline{\overline{G_j}}) \cong E(\overline{\overline{G}}) \qquad (68)$$

The approximation is valid for sparse concentration of particles.

The quasi-crystalline approximation (QCA) is a higher order approximation than the effective field approximation. Truncation is made at the second stage of the hierarchy of equations. The operator equation is [39]:

$$E(\overline{\overline{G}}) = \overline{\overline{G_o}} + n_o \overline{\overline{G_o}} \int d\bar{r}_j \overline{\overline{C_j}}\, E(\overline{\overline{G}}) \tag{69}$$

where $n_o \int d\bar{r}_j \overline{\overline{C_j}}$ is the mass operator for discrete scatterers under the QCA.

The idea of coherent potential originates from the observation that in the derivation of multiple scattering equations, the background medium dyadic Green's operator is used. The potential operator $\overline{\overline{U}}$ is proportional to $k_p^2 - k^2$ and is a measure of the difference in permittivity from the background medium. However, as the concentration of particles increases, the coherent wave propagates in an effective medium *K*, and the scattering potential is a result of the difference in wavenumber from *K* rather than from *k*. The idea of coherent potential is to introduce the Green's operator with wavenumber *K* [39].

In the low frequency limit of the QCA-CP is:

$$K^2 = \frac{3 f k^2 y}{1 - fy}\left\{1 + i\frac{2}{3}\frac{(ka)^3 y}{1 - fy}\left[1 + 4\pi n_o \int_0^\infty dr\, r^2 \big(g(r) - 1\big)\right]\right\} \tag{70}$$

where:

- $y = \dfrac{\varepsilon_s - \varepsilon}{\varepsilon_s + 2\varepsilon}$
- *g(r)* is the pair distribution function

In the QCA-CP the relationship governing *K* is non-linear. When the scattering attenuation term that is dependent on particle size can be neglected (very low frequency limit), the mixture formula for the effective permittivity $\varepsilon_{eff} = K^2/\omega\mu_o$ is :

$$\varepsilon_{eff} = \frac{\varepsilon(1 - f) + f\varepsilon_s + f\dfrac{(\varepsilon - \varepsilon_s)\varepsilon_s}{3\varepsilon_{eff} - \varepsilon + \varepsilon_s}}{1 + f\dfrac{(\varepsilon - \varepsilon_s)}{3\varepsilon_{eff} + \varepsilon_s - \varepsilon}} \tag{71}$$

The QCA-CP has been extended to multiple species of particles different in [39].

It is worth noting that for a long time the QCA approximation has not been used because, conversely than QCA-CP, it didn't obey the energy conservation. In [107] a new approach to calculate the propagation constants of a dense medium under QCA has been proposed which obey energy conservation.

The main difference between the QCA and QCA-CP resides in their validity range. It has been demonstrated [107] that the solution of the radiative transfer under QCA-CP is limited to small particles compared to the wavelength and the phase matrix obtained is equivalent to the Rayleigh one. Instead, when only QCA is used, higher order multipole effects can be accounted for, hence the model is applicable to moderate-size particles (i.e. the validity range is the same of the Mie scattering). Actually, the DMRT-QCA can be regarded as a correction to the classical Mie

scattering [38]. It is also worth noting that the QCA solution is close to the QCA-CP when the scatterer size is small.

To better understand the difference in applications between the two approximations, it is useful to consider the frequencies used in the microwave remote sensing of snow. The dimensions of the ice crystals can range from tenths to few millimeters. At C-band, the wavelength is 5-6 cm and at Ka band is 8 mm. So, the QCA-CP could not be very appropriate to simulate the snow emission at higher frequencies because the gain size is comparable to the wavelengths.

2.2.2.2 Effects of size distribution

The effects of a size distribution were analyzed in [108] by considering a scattering medium containing particles of multiple sizes. The particle sizes were distributed according to a Rayleigh probability density function, with the large size tail truncated at a radius of 1 cm. Fig. 12 shows how the effective extinction rate k_e varies as a function of fractional volume for four different cases. We can see that, for each kind of scattering particle used, the extinction rate calculated using the size distribution is much larger than the corresponding extinction rate calculated using single size particles. The effective albedo is also much larger when a truncated Rayleigh distribution is used. These two effects combine to give an increase of over 10 db in the backscattered cross-section when a size distribution is substituted for single sized particles. This effect occurs because the truncated Rayleigh size distribution includes some snow grains that are quite a bit larger than the mode size, although at much lower concentration. These large snow grains are responsible for most of the radar cross-section. This does not mean, however, that the medium is acting like a sparse distribution of large particles alone. In a dense medium, the collective behavior of all the particles determines the scattering and absorption characteristics of the medium. The positions, and therefore the scattering of each particle, are also constrained by the location and size of all the other particles. DMRT incorporates the collective behavior and correlated scattering effects into the effective extinction rate, albedo, and phase matrix in a rigorous and consistent way.

In [108] the DMRT was applied to a three-layer model consisting of two Scattering layers overlying a homogeneous half space with a Rayleigh size distribution for particle size in each layer (Fig. 13). Results from this model were compared with results from a model that uses a single scattering layer containing single sized particles whose size matches the mode size of the Rayleigh distribution. It was found that the model that used a size distribution gave higher cross-sections than the model with single sized particles. A peak in extinction rate as a function of fractional volume for lossless particles was eliminated introducing a small loss. When two scattering layers were examined, the layer with the largest particles determined most of the cross-section. This occurs because larger particles scatter more than small particles. The case with two scattering layers also indicated that higher frequencies are needed to see volume scattering in thin snow cover.

The three-layer model was extended to the multilayer case in [109] and used to investigate the relationship between the electromagnetic sensor response and the snow-cover changes under time-varying environmental conditions. Within each snow layer the constituent ice particles were random clusters of small primary spherical particles. The stickiness τ was applied to parameterize the clustering

nature of snow grains**.** The aggregated ice particles are randomly distributed in a background medium of complex permittivity.

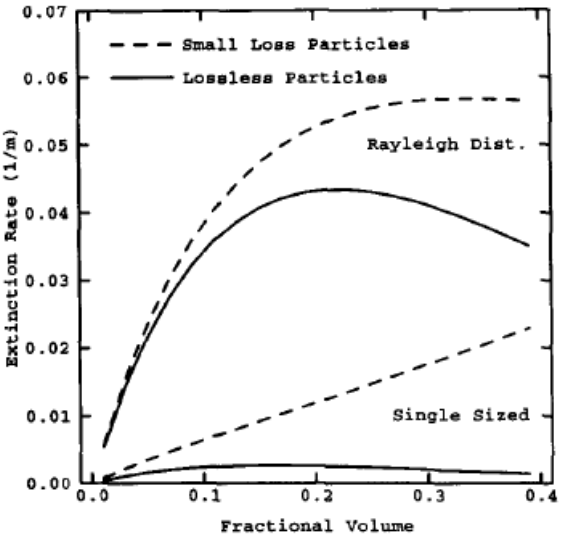

Fig. 12 - The extinction rate as a function of the fractional volume of scattering particles for 4 different cases using a single scattering layer. 1) small loss particles with ε_{1s} = (3.2 + i0.001) and a Rayleigh probability density function for particle size with a mode snow grain radius of 1 mm. 2) lossless particles with ε_{1s} = 3.2 and a Rayleigh probability density function for particle size with a mode snow grain radius of 1 mm. 3) and 4) are like cases 1) and 2) except that a single snow grain size of 1 mm is used (no size distribution). The other parameters are: Layer depth = 0.5 m, frequency = 5 GHz. (After [108])

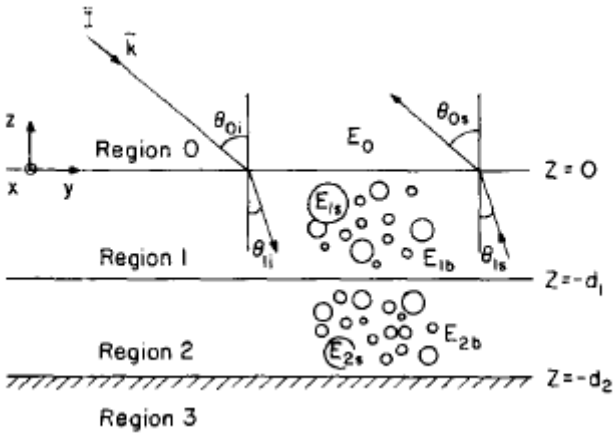

Fig. 13 - The layered scattering medium. The upper half space (region 0) is assumed to be air. The two scattering layers (regions and 2) contain dense distributions of ice particles. The lower half space (region 3) is assumed to be soil (After [108]).

In [110] volume 3-D pair distribution functions were calculated from the 2-D stereological data by solving Hanisch's integral equation. Monte Carlo simulations were first used for multisize particles to verify the procedure. Next, the procedure was applied to available planar snow sections. A log-normal distribution of particle sizes was assumed for the ice grains in snow. To derive multisize pair functions, a least squares fit was used to recover pair functions for particles with sufficient number density and the hole correction approximation was assumed for the larger particles. A family of 3-D pair distribution functions were derived. These were then substituted into DMRT to calculate scattering. It was found that the computed scattering rates were comparable to those calculated under the Percus–Yevick approximation of pair distribution functions of multiple sizes.
An approach to eliminate the assumption of small particles *(ka*<<1) was developed in [107] with a model based on QCA-DMRT applicable to moderate sized particles. The extension is important for microwave remote sensing because for frequencies above 10 GHz, the particle sizes in some geophysical media are comparable to the wavelength. Cases of particles with and without interparticle forces were studied. It was shown that particles with interparticle forces (sticky particle model) can better represent the observed frequency dependence in the snow covered terrains. Cases for coated particles were also studied.
In [111] the snow medium was treated as densely packed sticky ice particles following a size distribution. The quasi-crystalline approximation (QCA) dense medium theory was applied to calculate the absorption, scattering and emission of snow at multiple frequencies. The correlation of particle position is taken into account by using the Percus-Yevick approximation that can accommodate particles of multiple sizes. The size distribution is discretized so that it can be applied to the Percus-Yevick approximation for the cross pair distribution function of particles with different sizes. The model was extended to sticky particles of moderate size in [112],[113]. In this work the rough surface scattering was modeled by the Numerical Maxwell Model of 3D simulations (NMM3D), which is accelerated by fast computation method known as with Sparse-Matrix Canonical Grid method (SMCG). The bistatic scattering coefficients of rough surfaces were used as the boundary conditions for the DMRT.

2.2.3 Frequency behavior of snow models

A systematic analysis of the models in terms of their performances as a function of observation frequency and geometry was not found in literature. In most cases the low frequency limit (correlation length << electromagnetic wavelength) was assumed to be valid up to about 18 GHz for both SFT and DMRT, while no significant constraints in the observation angle were noted. The range of validity of the dry snow effective permittivity modeled with the strong fluctuation theory was examined by Huining *et al*. [114] by comparing model predictions with experimental data-based values. The results showed that the SFT provides reasonable accurate estimates for the imaginary part of the effective permittivity in the 1- to 100-GHz range except for large grain sizes at high frequencies (60 - 90GHz). More recently, the frequency dependence of scattering and extinction of dense media for frequencies higher than 18 GHz was studied by Chen *et al*. [115] using Monte Carlo simulations of the three-dimensional solutions of Maxwell's equations. The

particle positions were generated by deposition and bonding techniques. Monte Carlo simulations were performed for various frequencies, particle sizes, and particle permittivities. The extinction, scattering, and absorption properties of snow were calculated for non-sticky and sticky particles with different stickiness parameters. Numerical solutions of Maxwell's equations compared well with QCA/DMRT results indicate that the frequency dependence of densely packed sticky small particles is much weaker than that of independent scattering and better match the observed data.

3. MODELING THE EMISSION FROM SNOW COVERED SOIL

The models developed in this work aim to simulate the electromagnetic emission of continental dry and wet snowpacks. Even if the two kinds of snow are similar, the presence of liquid water strongly affects the e.m. emission behavior. Thus, two different models have been used to simulate the brightness temperature.
The dry snowpack can be represented like one layer of snow above the soil. To this end, two electromagnetic models have been coupled, the Advanced Integral Equation Method (AIEM) and the Dense Media Radiative Transfer under the Quasi-Crystalline Approximation (DMRT-QCA). The first model has been chosen due to its wide range of validity and flexibility. For instance, it is possible to change the autocorrelation function very easily disregarding if the ACF is azimuthally isotropic or not. The DMRT-QCA has been selected because it represents one of the most advanced models for the snow. It could account for a wide range of particle size and for the adhesive properties of the ice crystals. Moreover, it has been developed for the Mie scattering (which occurs when the scatterers have dimensions comparable to the wavelength) instead of the Rayleigh approximation like most of the model available in literature. This feature is very important because it extends the validity range of the model up to the Ka band, which usually is the highest frequency used to monitor snow covers. The obtained model has been called IRIDE (IFAC RadiatIve Dry snow Emission) Model.
Wet snow is characterized by the presence of liquid water among the ice particles. The electric properties of liquid water are very different from the ones of the ice crystals: the imaginary part of the water permittivity is very high and this lead to a high emission and to a high extinction of the radiation coming from bottom. The SFT can model different kind of scatterers and it is easy to use in a multilayer model with the wave approach. Moreover, because wet snow with only a few percents of LWC is able to mask the contribution of the soil, this latter can be modeled as a flat plane. With this choice, the computational time can be strongly reduced. These are the reasons because the Strong Fluctuation Theory has been chosen to simulate the brightness temperature of wet snow.

In Fig. 14 the structure of the model for dry snow is outlined. θ is the observation angle, ε_s is the permittivity of the spherical ice grains and ε_0 is the one of the bulk (air), ε_2 is the dielectric constant of the ground that is modeled as a semi-infinite medium, d is the thickness of the snowpack.

In the following paragraphs, the description of the emission model obtained by properly coupling the AIEM and DMRT-QCA will be given. The errors found in literature and corrected during this research will be pointed out as well as all the critical points.

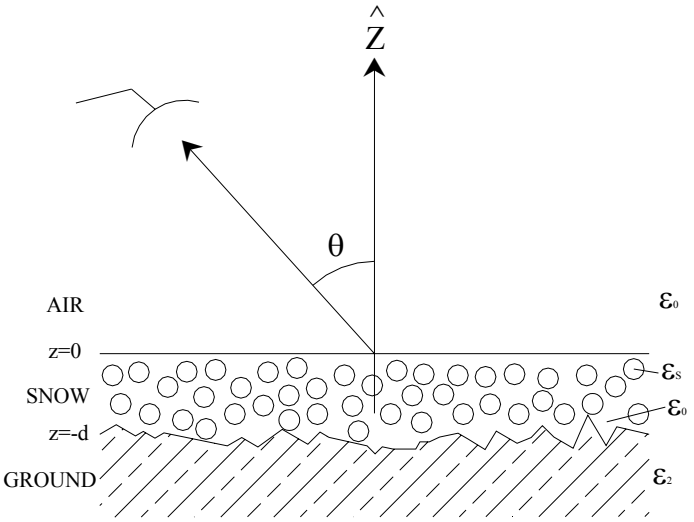

Fig. 14 - Structure of the model for dry snowpacks

3.1 Bistatic scattering from soil: the Advanced Integral Equation Method (AIEM)

3.1.1 The model

In simulating emission from snow covered soil both the direct contribution from soil and the downward snow emission scattered from soil can be very significant (Fig. 15). Thus, it is important to have available a good model to simulate scattering from soil in the backward and forward directions. To this end a bistatic polarimetric version of the Advanced Integral Equation Method has been developed, implemented and validated with numerical and experimental data.

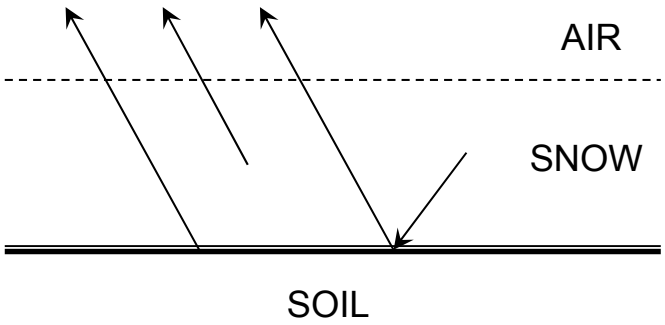

Fig. 15 – The three contributions to the total emission

As stated in the previous chapter, the first systematic version of the Integral Equation Method was published in 1992 [64]. The IEM adds a complementary term to the classical Kirchhoff tangential field, and the scattered fields are expressed as a combination of the Kirchhoff and the complementary term. In the first paper [64] only the single scattering was developed. Multiple scattering terms were added by [76],[77] in the IEMM, while the Advanced Integral Equation Method (AIEM) was formulated by Chen *et al.* [82] and Wu *et al.* [83]. In this latter version the complementary field was written as the sum of four terms: two of them related to the downward radiation ($E^c_{qp1,z>z'}$ and $E^c_{qp2,z>z'}$) and two representing upward one ($E^c_{qp1,z<z'}$ and $E^c_{qp2,z<z'}$) [82],[83]:

$$E^c_{qp} = E^c_{qp1,z>z'} + E^c_{qp2,z>z'} + E^c_{qp1,z<z'} + E^c_{qp2,z<z'} \tag{72}$$

This has been obtained by keeping the absolute phase term within Green's function [82]. Thus, the single scattering terms were re-derived and modified. The multiple-scattering terms instead were the same as in the formulation of the IEMM [78],[83].

We can remark that the refinement work carried out from the first IEM to the last AIEM consisted in removing some of the original approximations. It is worth to note that the computational time of the AIEM is much heavier than in the first IEM, and in many practical cases the original formulation is fully acceptable. However, at the present state of the art, the AIEM represents perhaps the best model for simulating surface scattering. Indeed, it combines the high accuracy in evaluating the scattering coefficients with a high versatility in modeling the surface statistics of soils (Gaussian, Exponential, Two-scale, etc.).

The reference system (also called principal frame) of the Advanced Integral Equation Method is depicted in Fig. 16.

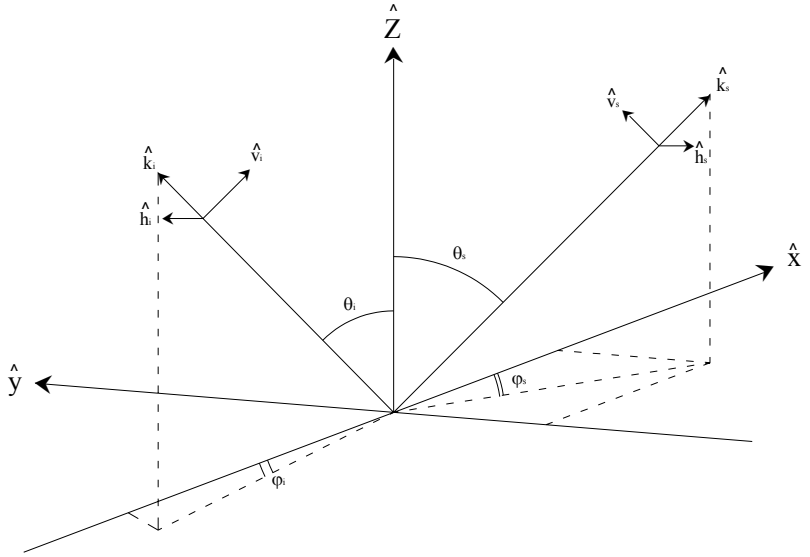

Fig. 16 - The reference system of the Advanced Integral Equation Method

The AIEM model can be written as sum of single and multiple scattering terms:

$$\sigma^0_{qp} = \sigma^0_{qp}(S) + \sigma^0_{qp}(M) \tag{73}$$

The single scattering terms account for the electromagnetic waves that impinge upon the surface and are scattered in the upper or in the lower medium without further interaction with the surface. Instead the multiple terms account for the waves, which interact with the surface two or more times.
The normalized scattering coefficient is composed of three terms, namely the Kirchhoff, the cross and the complementary terms. The expression for the single scattering term is:

$$\begin{aligned}\sigma^o{}_{qp}(S) &= \sigma^k{}_{qp}(S) + \sigma^{kc}{}_{qp}(S) + \sigma^c{}_{qp}(S) = \\ &= \frac{k_1{}^2}{2} e^{-\sigma^2(k_z^2 + k_{sz}^2)} \cdot \sum_{n=1}^{\infty} \frac{\sigma^{2n}}{n!} \left| I^n_{qp} \right|^2 W^{(n)}(k_{sx} - k_x, k_{sy} - k_y)\end{aligned} \tag{74}$$

where k_1 is the wavenumber in the upper medium, σ is the height standard deviation of the surface roughness and $W^{(n)}$ is the Fourier transform of the nth power of the normalized surface correlation function. The transmitted polarization is p and q is the received one.
The difference between the IEM and the AIEM resides in the expression of the function I^n_{qp}. For the IEM model it has the following expression:

$$I^n_{qp} = (k_z + k_{sz})^n \; f_{qp} \; e^{-\sigma^2 k_z k_{sz}} + \frac{(k_{sz})^n F_{qp}(-k_x, -k_y) + (k_z)^n F_{qp}(-k_{sx}, -k_{sy})}{2} \tag{75}$$

where the coefficients $F_{qp}(-k_x, -k_y)$ and $F_{qp}(-k_{sx}, -k_{sy})$ can be found in (Fung, 1994). In the AIEM, which accounts for the scattered waves in various directions by means of the $q_{1,2}$ functions, I^n_{qp} is different from the previous equation and is expressed by

$$
\begin{aligned}
I_{qp}^{n} \;=\;& (k_z + k_{sz})^n \;\; f_{qp} \;\; e^{-\sigma^2 k_z k_{sz}} \\
&+\frac{1}{4}\Big\{(k_{sz} - q_1)^n \;\; F_{qp1}^{(+)} \;\; e^{-\sigma^2 (q_1^2 - q_1 k_{sz} + q_1 k_z)} \\
&\quad +(k_{sz} - q_2)^n \;\; F_{qp2}^{(+)} \;\; e^{-\sigma^2 (q_2^2 - q_2 k_{sz} + q_2 k_z)} \\
&\quad +(k_{sz} + q_1)^n \;\; F_{qp1}^{(-)} \;\; e^{-\sigma^2 (q_1^2 + q_1 k_{sz} - q_1 k_z)} \\
&\quad +(k_{sz} + q_2)^n \;\; F_{qp2}^{(-)} \;\; e^{-\sigma^2 (q_2^2 + q_2 k_{sz} - q_2 k_z)} \;\; \Big\}_{u,v=-k_x,-k_y} \\
&+\frac{1}{4}\Big\{(k_z + q_1)^n \;\; F_{qp1}^{(+)} \;\; e^{-\sigma^2 (q_1^2 - q_1 k_{sz} + q_1 k_z)} \\
&\quad +(k_z + q_2)^n \;\; F_{qp2}^{(+)} \;\; e^{-\sigma^2 (q_2^2 - q_2 k_{sz} + q_2 k_z)} \\
&\quad +(k_z - q_1)^n \;\; F_{qp1}^{(-)} \;\; e^{-\sigma^2 (q_1^2 + q_1 k_{sz} - q_1 k_z)} \\
&\quad +(k_z - q_2)^n \;\; F_{qp2}^{(-)} \;\; e^{-\sigma^2 (q_2^2 + q_2 k_{sz} - q_2 k_z)} \;\; \Big\}_{u,v=-k_{sx},-k_{sy}}
\end{aligned}
\tag{76}
$$

with $q_m = \sqrt{k_m^2 - u^2 - v^2} \qquad m = 1,2$

In (76) f_{qp} accounts for the Kirchhoff field and $F_{qp1,2}^{(\pm)}$ accounts for the complementary scattered intensities in the upward (+) and downward (-) directions both in the upper (1) and lower (2) media. We have fully rederived these latter coefficients because all the papers available in the open literature are affected by many typographical errors. As an example, the original expression of coefficient $F_{hh2}^{(-)}$ has two signs reversed. The correct expressions for these coefficients are:

$$
\begin{aligned}
F_{vv1}^{(+)} \;=\;& -\left(\frac{1-R_v}{q_1}\right)(1+R_v) \;\; C_1 + \left(\frac{1-R_v}{q_1}\right)(1-R_v) \;\; C_2 + \left(\frac{1-R_v}{q_1}\right)(1+R_v) \;\; C_3 \\
&+\left(\frac{1+R_v}{q_1}\right)(1-R_v) \;\; C_4 + \left(\frac{1+R_v}{q_1}\right)(1+R_v) \;\; C_5 + \left(\frac{1+R_v}{q_1}\right)(1-R_v) \;\; C_6
\end{aligned}
$$

$$
\begin{aligned}
F_{vv2}^{(+)} \;=\;& \left(\frac{(1+R_v)\mu_r}{q_2}\right)(1+R_v) \;\; C_{1t} - \left(\frac{1+R_v}{q_2}\right)(1-R_v) \;\; C_{2t} - \left(\frac{1+R_v}{q_2 \;\; \varepsilon_r}\right)(1+R_v) \;\; C_{3t} \\
&-\left(\frac{(1-R_v)\varepsilon_r}{q_2}\right)(1-R_v) \;\; C_{4t} - \left(\frac{1+R_v}{q_2}\right)(1+R_v) \;\; C_{5t} - \left(\frac{1-R_v}{q_2 \;\; \mu_r}\right)(1-R_v) \;\; C_{6t}
\end{aligned}
$$

$$
\begin{aligned}
F_{hh1}^{(+)} &= \left(\frac{1-R_h}{q_1}\right)(1+R_h)\ C_1 - \left(\frac{1-R_h}{q_1}\right)(1-R_h)\ C_2 - \left(\frac{1-R_h}{q_1}\right)(1+R_h)\ C_3 \\
&\quad - \left(\frac{1+R_h}{q_1}\right)(1-R_h)\ C_4 - \left(\frac{1+R_h}{q_1}\right)(1+R_h)\ C_5 - \left(\frac{1+R_h}{q_1}\right)(1-R_h)\ C_6
\end{aligned}
$$

$$
\begin{aligned}
F_{hh2}^{(+)} &= -\left(\frac{(1+R_h)\varepsilon_r}{q_2}\right)(1+R_h)\ C_{1t} + \left(\frac{1+R_h}{q_2}\right)(1-R_h)\ C_{2t} + \left(\frac{1+R_h}{q_2\ \mu_r}\right)(1+R_h)\ C_{3t} \\
&\quad + \left(\frac{(1-R_h)\mu_r}{q_2}\right)(1-R_h)\ C_{4t} + \left(\frac{1-R_h}{q_2}\right)(1+R_h)\ C_{5t} + \left(\frac{1-R_h}{q_2\ \varepsilon_r}\right)(1-R_h)\ C_{6t}
\end{aligned}
\qquad (77)
$$

$$
\begin{aligned}
F_{hv1}^{(+)} &= +\left(\frac{1-R}{q_1}\right)(1+R\ )\ B_1 - \left(\frac{1-R}{q_1}\right)(1-R\ )\ B_2 - \left(\frac{1-R}{q_1}\right)(1+R\ )\ B_3 \\
&\quad + \left(\frac{1+R}{q_1}\right)(1-R\ )\ B_4 + \left(\frac{1+R}{q_1}\right)(1+R\ )\ B_5 + \left(\frac{1+R}{q_1}\right)(1-R\ )\ B_6
\end{aligned}
$$

$$
\begin{aligned}
F_{hv2}^{(+)} &= -\left(\frac{(1+R\ )\mu_r}{q_2}\right)(1+R\ )\ B_{1t} + \left(\frac{1+R}{q_2}\right)(1-R\ )\ B_{2t} + \left(\frac{1+R}{q_2\ \varepsilon_r}\right)(1+R\ )\ B_{3t} \\
&\quad - \left(\frac{(1-R\ )\varepsilon_r}{q_2}\right)(1-R\ )\ B_{4t} - \left(\frac{1-R}{q_2}\right)(1+R\ )\ B_{5t} - \left(\frac{1-R}{q_2\ \mu_r}\right)(1-R\ )\ B_{6t}
\end{aligned}
$$

$$
\begin{aligned}
F_{vh1}^{(+)} &= +\left(\frac{1+R}{q_1}\right)(1-R\ )\ B_1 - \left(\frac{1+R}{q_1}\right)(1+R\ )\ B_2 - \left(\frac{1+R}{q_1}\right)(1-R\ )\ B_3 \\
&\quad + \left(\frac{1-R}{q_1}\right)(1+R\ )\ B_4 + \left(\frac{1-R}{q_1}\right)(1-R\ )\ B_5 + \left(\frac{1-R}{q_1}\right)(1+R\ )\ B_6
\end{aligned}
$$

$$
\begin{aligned}
F_{vh2}^{(+)} &= -\left(\frac{(1-R\ )\varepsilon_r}{q_2}\right)(1-R\ )\ B_{1t} + \left(\frac{1-R}{q_2}\right)(1+R\ )\ B_{2t} + \left(\frac{1-R}{q_2\ \mu_r}\right)(1-R\ )\ B_{3t} \\
&\quad - \left(\frac{(1+R\ )\mu_r}{q_2}\right)(1+R\ )\ B_{4t} - \left(\frac{1+R}{q_2}\right)(1-R\ )\ B_{5t} - \left(\frac{1+R}{q_2\ \varepsilon_r}\right)(1+R\ )\ B_{6t}
\end{aligned}
$$

The previous $F_{qp1,2}^{(\pm)}$ coefficients depend on six functions C_1-C_6 for the co-polar scattering coefficients and on six functions B_1-B_6 for the cross-polar ones. These terms too, affected by many errors in literature (e.g. in (78) the k_1 factor is missing in C_1, C_4, B_1, B_4), have been re-derived. The right expressions are:

$$C_1 = k_1\left\{\cos\phi_s\left[1-\frac{(k_{sx}+u)(k_x+u)}{(k_{sz}-q_1)(k_z+q_1)}\right]-\sin\phi_s\left[\frac{(k_{sy}+v)(k_x+u)}{(k_{sz}-q_1)(k_z+q_1)}\right]\right\}$$

$$\begin{aligned}C_2 = & -\cos\phi_s\left[-q_1\cos\theta_i+u\ \cos\theta_i\frac{(k_{sx}+u)}{(k_{sz}-q_1)}-q_1\sin\theta_i\frac{(k_x+u)}{(k_z+q_1)}+u\sin\theta_i\frac{(k_{sx}+u)(k_x+u)}{(k_{sz}-q_1)(k_z+q_1)}\right.\\ & \left.-v\cos\theta_i\frac{(k_y+v)}{(k_z+q_1)}+v\ \sin\theta_i\frac{(k_{sx}+u)(k_y+v)}{(k_{sz}-q_1)(k_z+q_1)}\right]\\ & +\sin\phi_s\left[-u\ \cos\theta_i\frac{(k_{sy}+v)}{(k_{sz}-q_1)}-u\ \sin\theta_i\frac{(k_{sy}+v)(k_x+u)}{(k_{sz}-q_1)(k_z+q_1)}+q_1\sin\theta_i\frac{(k_y+v)}{(k_z+q_1)}\right.\\ & \left.-u\ \cos\theta_i\frac{(k_y+v)}{(k_z+q_1)}-v\ \sin\theta_i\frac{(k_{sy}+v)(k_y+v)}{(k_{sz}-q_1)(k_z+q_1)}\right]\end{aligned} \tag{78}$$

$$\begin{aligned}C_3 = & \frac{1}{(k_{sz}-q_1)(k_z+q_1)}\left\{\left[-(k_z+q_1)\sin\theta_i+(k_x+u)\cos\theta_i\right]\cdot\right.\\ & \left.\left[k_{sx}\ q_1\cos\phi_s+k_{sy}\ q_1\sin\phi_s+k_{sz}\ u\ \cos\phi_s+k_{sz}\ v\ \sin\phi_s\right]\right\}\end{aligned}$$

$$\begin{aligned}C_4 = & k_1\left\{\cos\theta_s\sin\phi_s\left[\sin\theta_i\frac{(k_y+v)}{(k_z+q_1)}+\cos\theta_i\frac{(k_{sx}+u)(k_y+v)}{(k_{sz}-q_1)(k_z+q_1)}\right]\right.\\ & +\cos\theta_s\cos\phi_s\left[\cos\theta_i+\sin\theta_i\frac{(k_x+u)}{(k_z+q_1)}-\cos\theta_i\frac{(k_{sy}+v)(k_y+v)}{(k_{sz}-q_1)(k_z+q_1)}\right]\\ & \left.+\sin\theta_s\left[\cos\theta_i\frac{(k_{sx}+u)}{(k_{sz}-q_1)}+\sin\theta_i\frac{(k_{sx}+u)(k_x+u)}{(k_{sz}-q_1)(k_z+q_1)}+\sin\theta_i\frac{(k_{sy}+v)(k_y+v)}{(k_{sz}-q_1)(k_z+q_1)}\right]\right\}\end{aligned}$$

$$\begin{aligned}C_5 = & -\cos\theta_s\sin\phi_s\left[v\frac{(k_{sx}+u)}{(k_{sz}-q_1)}+v\frac{(k_x+u)}{(k_z+q_1)}\right]\\ & -\cos\theta_s\cos\phi_s\left[q_1+u\frac{(k_x+u)}{(k_z+q_1)}-v\frac{(k_{sy}+v)}{(k_{sz}-q_1)}\right]\\ & \left.-\sin\theta_s\left[q_1\frac{(k_{sx}+u)}{(k_{sz}-q_1)}+u\frac{(k_{sx}+u)(k_x+u)}{(k_{sz}-q_1)(k_z+q_1)}+v\frac{(k_{sy}+v)(k_x+u)}{(k_{sz}-q_1)(k_z+q_1)}\right]\right\}\end{aligned}$$

$$
\begin{aligned}
C_6 \;=\;& \cos\theta_s \sin\phi_s \left[q_1 \frac{(k_{sx}+u)(k_y+v)}{(k_{sz}-q_1)(k_z+q_1)} + u \frac{(k_y+v)}{(k_z+q_1)} \right] \\
& - \cos\theta_s \cos\phi_s \left[q_1 \frac{(k_{sy}+v)(k_y+v)}{(k_{sz}-q_1)(k_z+q_1)} + v \frac{(k_y+v)}{(k_z+q_1)} \right] \\
& + \sin\theta_s \left[u \frac{(k_{sy}+v)(k_y+v)}{(k_{sz}-q_1)(k_z+q_1)} - v \frac{(k_{sx}+u)(k_y+v)}{(k_{sz}-q_1)(k_z+q_1)} \right] \Bigg\}
\end{aligned}
$$

$$
\begin{aligned}
B_1 \;=\;& k_1 \Bigg\{ \cos\theta_s \sin\phi_s \left[1 - \frac{(k_{sx}+u)(k_x+u)}{(k_{sz}-q_1)(k_z+q_1)} \right] \\
& + \cos\theta_s \cos\phi_s \left[\frac{(k_{sy}+v)(k_x+u)}{(k_{sz}-q_1)(k_z+q_1)} \right] + \sin\theta_s \left[\frac{(k_{sy}+v)}{(k_{sz}-q_1)} \right] \Bigg\}
\end{aligned}
$$

$$
\begin{aligned}
B_2 \;=\;& \cos\theta_s \sin\phi_s \Bigg[q_1 \cos\theta_i - u \;\cos\theta_i \frac{(k_{sx}+u)}{(k_{sz}-q_1)} + q_1 \sin\theta_i \frac{(k_x+u)}{(k_z+q_1)} - u \sin\theta_i \frac{(k_{sx}+u)(k_x+u)}{(k_{sz}-q_1)(k_z+q_1)} \\
& + v \cos\theta_i \frac{(k_y+v)}{(k_z+q_1)} - v \;\sin\theta_i \frac{(k_{sx}+u)(k_y+v)}{(k_{sz}-q_1)(k_z+q_1)} \Bigg] \\
& + \sin\theta_s \Bigg[q_1 \cos\theta_i \frac{(k_{sy}+v)}{(k_{sz}-q_1)} + q_1 \sin\theta_i \frac{(k_{sy}+v)(k_x+u)}{(k_{sz}-q_1)(k_z+q_1)} + q_1 \sin\theta_i \frac{(k_{sx}+u)(k_y+v)}{(k_{sz}-q_1)(k_z+q_1)} \\
& + u \;\cos\theta_i \frac{(k_{sx}+u)(k_y+v)}{(k_{sz}-q_1)(k_z+q_1)} + v \;\cos\theta_i \frac{(k_{sy}+v)(k_y+v)}{(k_{sz}-q_1)(k_z+q_1)} \Bigg] \\
& + \cos\theta_s \cos\phi_s \Bigg[u \;\cos\theta_i \frac{(k_{sy}+v)}{(k_{sz}-q_1)} + u \;\sin\theta_i \frac{(k_{sy}+v)(k_x+u)}{(k_{sz}-q_1)(k_z+q_1)} - q_1 \sin\theta_i \frac{(k_y+v)}{(k_z+q_1)} \\
& + u \;\cos\theta_i \frac{(k_y+v)}{(k_z+q_1)} + v \;\sin\theta_i \frac{(k_{sy}+v)(k_y+v)}{(k_{sz}-q_1)(k_z+q_1)} \Bigg]
\end{aligned}
$$

$$
\begin{aligned}
B_3 \;=\;& - \cos\theta_s \sin\phi_s \left[q_1 \sin\theta_i \frac{(k_{sx}+u)}{(k_{sz}-q_1)} + u \;\sin\theta_i - q_1 \cos\theta_i \frac{(k_{sx}+u)(k_x+u)}{(k_{sz}-q_1)(k_z+q_1)} - u \;\cos\theta_i \frac{(k_x+u)}{(k_z+q_1)} \right] \\
& - \sin\theta_s \left[u \;\sin\theta_i \frac{(k_{sy}+v)}{(k_{sz}-q_1)} - u \;\cos\theta_i \frac{(k_{sy}+v)(k_x+u)}{(k_{sz}-q_1)(k_z+q_1)} - v \;\sin\theta_i \frac{(k_{sx}+u)}{(k_{sz}-q_1)} + v \cos\theta_i \frac{(k_{sx}+u)(k_x+u)}{(k_{sz}-q_1)(k_z+q_1)} \right] \\
& + \cos\theta_s \cos\phi_s \left[q_1 \sin\theta_i \frac{(k_{sy}+v)}{(k_{sz}-q_1)} + v \;\sin\theta_i - q_1 \cos\theta_i \frac{(k_{sy}+v)(k_x+u)}{(k_{sz}-q_1)(k_z+q_1)} - v \;\cos\theta_i \frac{(k_v+u)}{(k_z+q_1)} \right]
\end{aligned}
\tag{79}
$$

$$
\begin{aligned}
B_4 \;=\;& k_1 \Bigg\{ \cos\phi_s \left[\sin\theta_i \frac{(k_y+v)}{(k_z+q_1)} + \cos\theta_i \frac{(k_{sx}+u)(k_y+v)}{(k_{sz}-q_1)(k_z+q_1)} \right] \\
& - \sin\phi_s \left[\cos\theta_i + \sin\theta_i \frac{(k_x+u)}{(k_z+q_1)} - \cos\theta_i \frac{(k_{sy}+v)(k_y+v)}{(k_{sz}-q_1)(k_z+q_1)} \right] \Bigg\}
\end{aligned}
$$

$$B_5 = -\cos\phi_s\left[v\ \frac{(k_{sx}+u)}{(k_{sz}-q_1)}+v\ \frac{(k_x+u)}{(k_z+q_1)}\right]+\sin\phi_s\left[q_1-v\ \frac{(k_{sy}+v)}{(k_{sz}-q_1)}+u\ \frac{(k_x+u)}{(k_z+q_1)}\right]$$

$$B_6 = \cos\phi_s\left[q_1\frac{(k_{sx}+u)(k_y+v)}{(k_{sz}-q_1)(k_z+q_1)}+u\ \frac{(k_y+v)}{(k_z+q_1)}\right]+\sin\phi_s\left[q_1\frac{(k_{sy}+v)(k_y+v)}{(k_{sz}-q_1)(k_z+q_1)}+v\ \frac{(k_y+v)}{(k_z+q_1)}\right]$$

As the Kirchhoff terms of the σ^o accounts for single scattering only, the multiple scattering coefficients (IEMM, [78]) are added to the complementary field. It can be useful to write the $\sigma^0(M)$ as the sum of three terms: the cross-term *kc* related to the interaction of the Kirchhoff and complementary fields, and the terms *c1*, *c2* which are due to the complementary field only

$$\sigma^0_{qp}(M)=\sigma^{kc}_{qp}(M)+\sigma^{c1}_{qp}(M)+\sigma^{c2}_{qp}(M) \tag{80}$$

At the present state of the art [78] the three terms of the IEMM can be expressed by the following formula

$$\sigma^{kc}_{qp}(M) = \frac{k_1^2}{8\pi}S(\theta_i)\ S(\theta_s)\ \mathrm{Re}\Big\{\ f^*_{qp}\ \iint\Big(F^{(+)}_{qp}(u,v)\cdot G^{kc}(u,v,q_1)\cdot[1-S(u,v)] + F^{(-)}_{qp}(u,v)\cdot G^{kc}(u,v,-q_1)\cdot S(u,v)\Big)\ du\ dv\ \Big\} \tag{81}$$

$$\begin{aligned}\sigma^{c1}_{qp}(M) = \frac{k_1^2}{64\pi}S(\theta_i)\ S(\theta_s)\ \iint\Big(& F^{(+)}_{qp}(u,v)\cdot {F^{(+)}_{qp}}^*(u,v)\cdot G^{c1}(u,v,q_1,q_1')\cdot[1-S(u,v)] \\ & + F^{(+)}_{qp}(u,v)\cdot {F^{(-)}_{qp}}^*(u,v)\cdot G^{c1}(u,v,q_1,-q_1')\cdot[1-S(u,v)] \\ & + F^{(-)}_{qp}(u,v)\cdot {F^{(+)}_{qp}}^*(u,v)\cdot G^{c1}(u,v,q_1,-q_1')\cdot S(u,v) \\ & + F^{(-)}_{qp}(u,v)\cdot {F^{(-)}_{qp}}^*(u,v)\cdot G^{c1}(u,v,-q_1,-q_1')\cdot S(u,v)\Big)\ du\ dv\end{aligned} \tag{82}$$

$$\begin{aligned}\sigma^{c2}_{qp}(M) = \frac{k_1^2}{64\pi}S(\theta_i)\ S(\theta_s)\ \iint\Big(& F^{(+)}_{qp}(u,v)\cdot {F^{(+)}_{qp}}^*(u',v')\cdot G^{c2}(u,v,q_1,q_1')\cdot[1-S(u,v)] \\ & + F^{(+)}_{qp}(u,v)\cdot {F^{(-)}_{qp}}^*(u',v')\cdot G^{c2}(u,v,q_1,-q_1')\cdot[1-S(u,v)] \\ & + F^{(-)}_{qp}(u,v)\cdot {F^{(+)}_{qp}}^*(u',v')\cdot G^{c2}(u,v,q_1,-q_1')\cdot S(u,v) \\ & + F^{(-)}_{qp}(u,v)\cdot {F^{(-)}_{qp}}^*(u',v')\cdot G^{c2}(u,v,-q_1,-q_1')\cdot S(u,v)\Big)\ du\ dv\end{aligned} \tag{83}$$

with

$$u' = -u-k_{sx}-k_x \qquad v' = -v-k_{sy}-k_y \qquad q' = \sqrt{k_1^2-u'^2-v'^2}$$

In the previous equations the *G* functions are

$$G^{kc}(u,v,q_1) = e^{-\sigma^2(k_{sz}^2+k_z^2+k_{sz}\ k_z+q_1^2-k_{sz}\ q_1+k_z\ q_1)}$$
$$\cdot\sum_{m=1}^{\infty}\frac{[\sigma^2(k_z+q_1)(k_{sz}+k_z)]^m}{m!}W^{(m)}(k_x+u,k_y+v) \tag{84}$$
$$\cdot\sum_{n=1}^{\infty}\frac{[\sigma^2(k_{sz}+q_1)(k_{sz}+k_z)]^n}{n!}W^{(n)}(k_{sx}+u,k_{sy}+v)$$

$$G^{c1}(u,v,q_1,q_1') = e^{-\sigma^2(k_{sz}^2+k_z^2+q_1^2(k_z-k_{sz})(q_1+q_1')+q_1'^2)}$$
$$\cdot\sum_{m=1}^{\infty}\frac{[\sigma^2(k_z+q_1)(k_z+q_1')]^m}{m!}W^{(m)}(k_x+u,k_y+v) \tag{85}$$
$$\cdot\sum_{n=1}^{\infty}\frac{[\sigma^2(k_{sz}-q_1)(k_{sz}-q_1')]^n}{n!}W^{(n)}(k_{sx}+u,k_{sy}+v)$$

$$G^{c2}(u,v,q_1,q_1') = e^{-\sigma^2(k_{sz}^2+k_z^2+q_1^2(k_z-k_{sz})(q_1+q_1')+q_1'^2)}$$
$$\cdot\sum_{m=1}^{\infty}\frac{[\sigma^2(k_{sz}-q_1)(k_z+q_1')]^m}{m!}W^{(m)}(k_x+u,k_y+v) \tag{86}$$
$$\cdot\sum_{n=1}^{\infty}\frac{[\sigma^2(k_s+q_1)(k_{sz}-q_1')]^n}{n!}W^{(n)}(k_{sx}+u,k_{sy}+v)$$

It is worth noting that the formulation of the AIEM is subsequent to that of the IEMM. The F_{qp} functions used in the IEMM differ from the ones of the AIEM because the formulation of [78] does not distinguish between waves which propagate in the upper or in the lower medium, but only upperward and downward. The following relation exists between the previous coefficients

$$F_{qp}^{(\pm)}(IEMM) = F_{qp,1}^{(\pm)}(AIEM) + F_{qp,2}^{(\pm)}(AIEM) \tag{87}$$

All the numerical evaluations of the multiple scattering coefficients must satisfy the following conditions required to limit the integrals to the radiation modes

$$k_z - q_1 > 0 \quad k_{sz} - q_1 > 0 \quad k_z - q_1' > 0 \quad k_{sz} - q_1' > 0$$

3.1.2 The reflection coefficients

All the f_{qp} and F_{qp} functions depend on the vertical or horizontal reflection coefficients. These coefficients are related to the local incidence angle (the angle formed by the incidence direction and the normal to the surface) and hence they are strongly dependent on the surface roughness. In the original formulation of the IEM these coefficients were calculated at the incidence angle (for smooth surfaces) or at the specular angle (for rough surfaces) for the Kirchhoff component. The bound between the two regions has been established in [65] as follows:

$$R_{v,h} = \begin{cases} R(\theta_i) & k^2\sigma L < 1.2\sqrt{\varepsilon_r} \\ R(\theta_{spec}) & kL > 5 \end{cases} \tag{88}$$

However, the separation between the two regions is not well defined, and methods to remove empirical approximations have been investigated. In [79] a transition function to connect the reflection coefficient from one region to the other has been developed. This function is based on the ratio between the σ^c and σ^o. The reflection coefficient is expressed by :

$$R_p(T) = R_p(\theta_i) + [R_p(\theta_{spec}) - R_p(\theta_i)] \cdot \gamma_p \tag{89}$$

where the transition function γ_p is $\gamma_p = 1 - S_p / S_0$. In the case of backscattering it is θ_{spec} = 0 and the S_p and S_0 functions are expressed in a simply way by:

$$S_p = \frac{|F_p|^2 \sum_{n=1}^{\infty} \frac{(k\ \sigma\ \cos\theta)^{2n}}{n!}\ W^{(n)}(2k\ \sin\theta)}{\sum_{n=1}^{\infty} \frac{(k\ \sigma\ \cos\theta)^{2n}}{n!} \left| F_p + \frac{2^{n+2}\ R_p(0)}{e^{(k\ \sigma\ \cos\theta)^2} \cos\theta} \right| W^{(n)}(2k\ \sin\theta)} \tag{90}$$

$$S_0 = \frac{1}{\left| 1 + \frac{8\ R_p(0)}{F_p\ \cos\theta} \right|^2} \tag{91}$$

with:

$$F_v = 8\ R_v^2(0)\ \sin^2\theta \left(\frac{\cos\theta + \sqrt{\varepsilon_r - \sin^2\theta}}{\cos\theta\ \sqrt{\varepsilon_r - \sin^2\theta}} \right) \tag{92}$$

$$F_h = -8\ R_h^2(0)\ \sin^2\theta \left(\frac{\cos\theta + \sqrt{\varepsilon_r - \sin^2\theta}}{\cos\theta\ \sqrt{\varepsilon_r - \sin^2\theta}} \right) \tag{93}$$

For the more general case of bistatic scattering the transition function is still under investigation. In this work the reflection coefficient has been selected after some comparisons with the FDTD simulations in the most critical conditions (see Appendix 1) which led us to assume the following rule:

$$R_{v,h} = \begin{cases} R(\theta_i) & k^2\sigma L < 1.2\sqrt{\varepsilon_r} \\ R(\theta_{spec}) & k^2\sigma L > 1.2\sqrt{\varepsilon_r} \end{cases} \tag{94}$$

In computing the complementary field, the reflection coefficients are always calculated at the incidence angle. The justification for this approximation relies on the fact that the complementary term is dominant for smooth surfaces where the Kirchhoff field is negligible. On the contrary, for very rough surfaces, is the

contribution of the complementary components that can be disregarded and the reradiated field is correctly expressed by the Kirchhoff term only.

3.1.3 The shadowing effects

When the roughness becomes appreciable (i.e. $k^2\sigma L > 1.2\sqrt{\varepsilon_r}$) there is a fraction of surface that is not more completely illuminated by the incidence plane wave. This shadowing effect affects the reradiated fields. To account for this effect the scattering coefficients must be multiplied by two functions, which account respectively for the incidence and scattered direction. In [39] the shadowing function is expressed by

$$S(\hat{k}_s,\hat{k}_i) = \frac{1}{\Lambda(\theta_s)+\Lambda(\theta_i)+1} \tag{95}$$

where the lambda function is

$$\Lambda(\mu) = \frac{1}{2}\left[\sqrt{\frac{2}{\pi}}\frac{s}{\cot(\mu)}e^{-\frac{\cot(\mu)^2}{2s^2}} - erfc\left(\frac{\cot(\mu)}{s\sqrt{2}}\right)\right] \tag{96}$$

For the multiple scattering Chen *et al*. [78] introduced a slightly different *S* function (whereas the lambda function remained the same):

$$S(\hat{k}_s,\hat{k}_i) = \frac{1-\frac{1}{2}erfc\left(\frac{\cot(\theta_i)}{s\sqrt{2}}\right)}{1+\Lambda(\theta_i)}\cdot\frac{1-\frac{1}{2}erfc\left(\frac{\cot(\theta_s)}{s\sqrt{2}}\right)}{1+\Lambda(\theta_s)} \tag{97}$$

3.1.4 The autocorrelation functions

In (74) the $W^{(n)}$ function represents the Fourier transform of the *n*-th power of the surface correlation function. Along with the roughness Height Standard Deviation, the correlation function is an important parameter to characterize rough surfaces. The most used correlation functions are the exponential, the Gaussian and the x-power (1<x<2). The function which best fits the experimental measured spectra is the exponential one, but the main problem with it is that the exponential function is not derivable in the origin and so it has not physical insight.
The power spectral densities corresponding to the six types of surface correlation functions implemented in the model (which are the most used in microwave remote sensing) are listed below:

- 1D Gaussian

$$W^{(n)}(k_x) \equiv \int \rho^n(x)e^{jk_x x}dx = L\sqrt{\frac{\pi}{n}}e^{-\frac{k_x{}^2L^2}{4n}} \tag{98}$$

- 1D exponential

$$W^{(n)}(k_x) = \frac{2\ L\ n}{n^2 + {k_x}^2 L^2} \tag{99}$$

- 2D Gaussian isotropic in the azimuth plane

$$W^{(n)}(k_x, k_y) \equiv \frac{1}{2\pi}\iint \rho^n(x,y) e^{jk_x x + jk_y y}\, dxdy = \frac{L^2}{2n} e^{-\frac{[{k_x}^2 + {k_y}^2]L^2}{4n}} \tag{100}$$

- 2D exponential isotropic in the azimuth plane

$$W^{(n)}(k_x, k_y) = \left(\frac{L}{n}\right)^2 \left(1 + \frac{[{k_x}^2 + {k_y}^2]L^2}{n^2}\right)^{-1.5} \tag{101}$$

- 1.5-power isotropic in the azimuth plane

$$W^{(n)}(k_x, k_y) = L^2 \left(\frac{KL}{2}\right)^{1.5n+1} \frac{\mathrm{K}_{-(1.5n+1)}\left([{k_x}^2 + {k_y}^2]L^2\right)}{\Gamma(1.5n)} \tag{102}$$

- 2D mixed-exponential isotropic in the azimuth plane

$$W^{(n)}(k_x, k_y) = \int_0^\infty e^{-\frac{n\rho^2}{\sqrt{1^4 + L^2\rho^2}}} J_0(K\rho)\ \rho\, d\rho \tag{103}$$

In this latter case the integral must be evaluated numerically because a close form does not exist. It is worth pointing out that the mono-dimensional correlation function models a surface which has an infinite correlation length in the transverse direction, whereas the bi-dimensional one accounts for surfaces which are isotropic in the azimuth plane. As a consequence, the 1-D spectra have to be divided by 2*k* to perform 1-D simulations, while the factor 2π is present in the definition of the 2-D transform only. Other autocorrelation functions accounting for surfaces with different correlation lengths in the *x* and *y* directions or for multi-scale ones are not taken into consideration in this work.

3.1.5 Polarimetric version of the AIEM

In recent years there has been a growing interest in studying the full polarimetric features of the observed surfaces. Indeed, this approach increases the potential of microwave sensors in detecting land characteristics. Unfortunately, almost all the available electromagnetic models for surface scattering deal with the linear polarizations only, or have a very narrow range of validity. Thus, an extended version of AIEM, which can simulate the four Stokes parameters, has been developed.

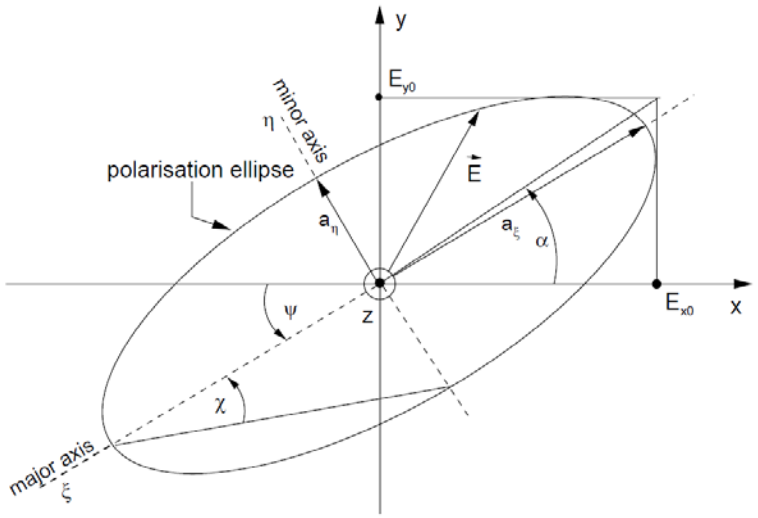

Fig. 17 - Polarization ellipse in x-y plane for a wave travelling in the z direction. ψ, η, α are respectively the rotation, the ellipticity and the auxiliary angles. (After [116])

Following [117] the scattering coefficient for arbitrary transmitted and received polarizations can be written as

$$\sigma^0_{RT}(\psi_r,\chi_r,\psi_t,\chi_t)=\frac{4\pi}{a}\underline{A}_R^T\ \underline{\underline{M}}\ \underline{A}_T \tag{104}$$

where:

- A_R and A_T are the modified Stokes vectors for the received and transmitted polarizations
- M is the average Stokes scattering operator
- a is the illuminated area
- ψ and χ are respectively the rotation and the ellipticity angles.

The A vector can be expressed as

$$\underline{A}=\begin{pmatrix}1\\ \cos 2\psi\ \cos 2\chi\\ \sin 2\psi\ \cos 2\chi\\ \sin 2\chi\end{pmatrix} \tag{105}$$

The ψ and χ parameters are depicted in Fig. 17. By appropriately setting these two terms it is possible to obtain all the possible polarizations (Fig. 18). The principal ones are

- Right → 2 χ = -90°
- Left → 2 χ = 90°
- Vertical → 2 χ = 0° and 2 ψ = 0°

- Horizontal → 2 χ = 0° and 2 ψ = 180°

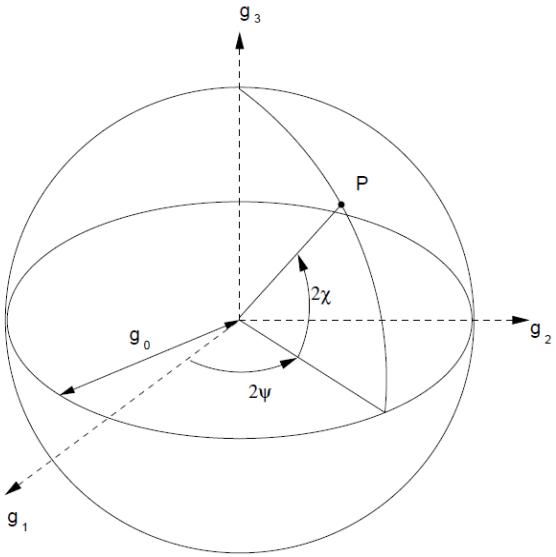

Fig. 18 - Poincaré sphere of polarization states. The linear polarizations are along the equator and the circular ones at the poles. The upper and lower hemisphere represents all the possible elliptical polarizations. (After [116])

In (104) the *M* matrix is expressed by

$$\underline{\underline{M}} = \underline{\underline{R}}^{T\,-1} \left\langle \underline{\underline{W}} \right\rangle \underline{\underline{R}}^{-1} \tag{106}$$

where

$$\underline{\underline{W}} = \begin{pmatrix} S_{VV}S_{VV}^* & S_{VH}S_{VH}^* & S_{VH}S_{VV}^* & S_{VV}S_{VH}^* \\ S_{HV}S_{HV}^* & S_{HH}S_{HH}^* & S_{HH}S_{HV}^* & S_{HV}S_{HH}^* \\ S_{HV}S_{VV}^* & S_{HH}S_{VH}^* & S_{HH}S_{VV}^* & S_{HV}S_{VH}^* \\ S_{VV}S_{HV}^* & S_{VH}S_{HH}^* & S_{VH}S_{HV}^* & S_{VV}S_{HH}^* \end{pmatrix} \quad \underline{\underline{R}} = \begin{pmatrix} 1 & 1 & 0 & 0 \\ 1 & -1 & 0 & 0 \\ 0 & 0 & 1 & 1 \\ 0 & 0 & -i & i \end{pmatrix} \tag{107}$$

Each element of the *W* matrix represents the correlation product of the electromagnetic fields. For the Small Perturbation Method, the components of *W* can be expressed by

$$\left\langle S_{qp} S_{mn}^* \right\rangle = \frac{r^2 P}{\left|E_0\right|^2} = A\, k_1^2 \cos^2\theta_s \; f_{qp} f_{mn}^* \; W(\left|\mathrm{k}_\perp - \mathrm{k}_{\perp i}\right|) \tag{108}$$

and, for the Geometrical Optic (in the case of a Gaussian surface)

$$\left\langle S_{qp} S_{mn}^{*} \right\rangle = \frac{r^2 P}{\left|E_0\right|^2} = \frac{A \left|k_1\right|^2 q^2}{8\pi\, q_z^4 m^2} U_{qp} U_{mn}^{*}\; e^{-\frac{q_x^2+q_y^2}{2\, q_z^2 m^2}} \tag{109}$$

Each model depends on a factor like $a_{qp}a_{mn}^{*}$. In the case of linear polarization $qp=mn$ and $a_{qp}a_{mn}^{*}=|a_{qp}|^2$, thus we can easily obtain the expression for the scattering written in chapter 2.

According to the AIEM model the bistatic scattering coefficient can be expressed by

$$\sigma^{o}{}_{qp}(S) = \frac{k_1^{\,2}}{2} e^{-\sigma^2 (k_z^2 + k_{sz}^2)} \cdot \sum_{n=1}^{\infty} \frac{\sigma^{2n}}{n!} \left| I_{qp}^{n} \right|^2 W^{(n)}(k_{sx} - k_x, k_{sy} - k_y) \tag{110}$$

If the term $\left|I_{qp}^{n}\right|^2$ is written as $I_{qp}^{n} \cdot I_{qp}^{n*}$, it is possible to obtain an expression for the bistatic scattering coefficient very similar to (108) and (109).

Moreover it can be written a new matrix *Q* that act like <*W*>

$$\begin{aligned} \sigma_{RT}^{0}(\psi_r, \chi_r, \psi_t, \chi_t) &= \frac{4\pi}{a} \underline{A}_R^{-1} \underline{\underline{R}}^{T\,-1} \left\langle \underline{\underline{W}} \right\rangle \underline{\underline{R}}^{-1} \underline{A}_T \\ &= \underline{A}_R^{-1} \underline{\underline{R}}^{T\,-1} \underline{\underline{Q}} \underline{\underline{R}}^{-1} \underline{A}_T \end{aligned} \tag{111}$$

from which

$$\frac{4\pi}{a} \left\langle S_{qp} S_{mn}^{*} \right\rangle = \left\langle \widetilde{S}_{qp} \widetilde{S}_{mn}^{*} \right\rangle \tag{112}$$

The elements of the new *Q* matrix are written as

$$\left\langle \widetilde{S}_{qp} \widetilde{S}_{mn}^{*} \right\rangle = \frac{k_1^{\,2}}{2} e^{-\sigma^2 (k_z^2 + k_{sz}^2)} \cdot \sum_{n=1}^{\infty} \frac{\sigma^{2n}}{n!} I_{qp}^{n}\; I_{mn}^{n*} W^{(n)}(k_{sx} - k_x, k_{sy} - k_y) \tag{113}$$

which represents the kernel of the polarimetric AIEM.

Because there are no polarimetric datasets like the ones used in the validation of the AIEM model, the SPM has been used to make a validation of the P-AIEM.

In Fig. 19 is depicted a comparison of the SPM and the AIEM models for two rough surfaces. It is possible to see that there is an excellent agreement between the predictions of two models on the entire range of observation angles for both the two degrees of roughness.

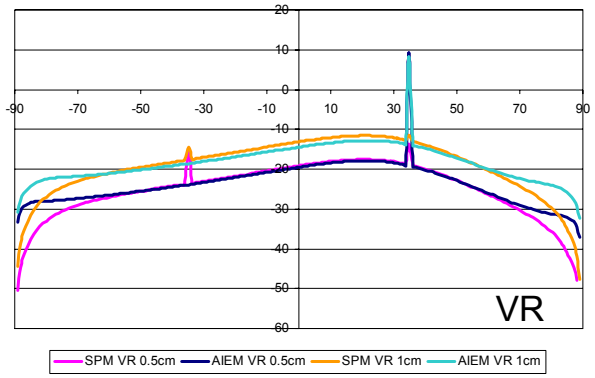

Fig. 19 - Comparison between the bistatic scattering coefficient γ in VR polarization simulated with the AIEM (dark and light blue) and the SPM (pink and orange) models for two different surface HStdD (0.5 cm pink and dark blue, 1cm orange and light blue). The other parameters are θ_i=35°, L=6 cm, exponential ACF, mv=5%.

3.1.6 Validation of the AIEM

During the analysis of the state of the art it emerged that the validity range of the Advanced Integral Equation Method hadn't been properly investigated. The authors claim that the AIEM is able to simulate a very wide range of rough surfaces but it was almost impossible to find clear limits in literature. In the framework of the ESA project "Use of Bi-Static Microwave Measurements for Earth Observation" a huge number of bistatic scattering simulations from rough surfaces made with the Finite Difference Time Domain (FDTD) model have been available and they have been used to validate the developed AIEM model and investigate its validity ranges. The parameters of the numerical dataset are shown in Tab. 1.

Table 1 - s = Surface Height Standard Deviation, l = correlation length

Parameters	*Values*
Autocorrelations function (ACF)	*Gaussian and Exponential*
Permittivity	*5.00 + j 0.6, 8.5 + j 1.2, 24.0 + j 3.19, 27 + j 4 at L- band*
	4.06 + j 0.3, 7.0 + j 0.8, 24.0 + j 3.19 at C-band
Normalized Height Standard Deviation ks	*0.12, 0.23, 0.35, 0.47, 0.82 at L- band*
	0.50, 1.0, 1.5, 2.0, 3.5, 4.0 at C-band
Normalized Correlations length kl	*1.48, 2.96, 5.48 at L-band*
	6.28, 12.57 at C-band

The surfaces modeled were all mono-dimensional (i.e. the surface was anisotropic with an infinite correlation length in a direction) and ranged from the very smooth case, *ks*=0.12, to the very rough ones, *ks*=4 for several values of permittivity (which represent the soil from the dry to the water saturated condition).

3.1.6.1 Gaussian ACF L-band

In this case simulations have been performed with *ks* = 0.12, *kl* = 5.48 and for two values of permittivity (5 + j0.6 and 24 + j 3.19), and for incidence angles of 30° and 50°. These values correspond to roughness conditions intermediate between SPM and PO approximations (see Fig. 2). In all the cases considered there is a good agreement between analytical and numerical simulations for scattering angles higher than the backscattered direction. For scattering angles lower than backscattering direction, the numerical solution presents higher values and a marked separation of two polarizations. A discrepancy can also be observed at extreme scattering angles (absolute values larger than 70-80 degrees), which can be justified by the criticality of modeling those situation both by numerical FDTD and closed form simulators. As an example Fig. 20 presents the results obtained on a surface with permittivity 5 + j 0.6 at the incidence angle θ_i = 30° (a), and θ_i = 50° (b).

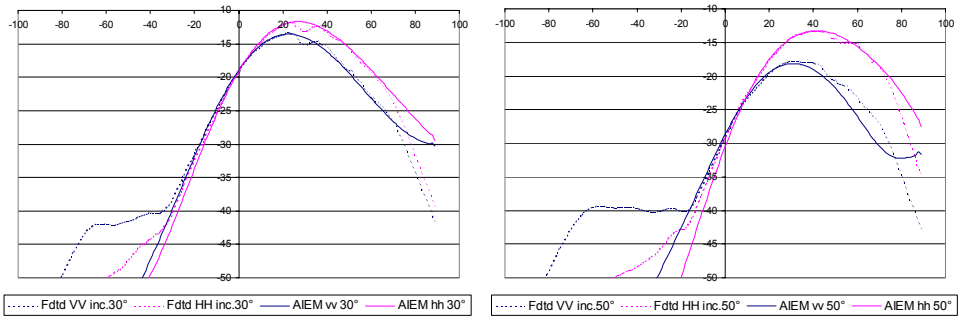

(a) (b)

Fig. 20 - Bistatic scattering coefficient at L-band as a function of scattering angle for a surface with Gaussian ACF, ks = 0.12 and kl = 5.48). a) incidence angle θ_i = 30° and permittivity ε =5 + j 0.6, b) incidence angle θ_i = 50° and permittivity ε =24 + j 3.19

3.1.6.2 Gaussian ACF C-band

At C-band, simulations have been performed with *ks* = 2.0 and 3.5, *kl* = 12.56, for three values of permittivity (4.06+j0.3, 7.0+j0.8 and 24+j3.19), and for incidence angles between 10° and 60° at 10° steps. The rougher surface falls within the GO approximation range, whilst the smoother one may be considered both in the GO and PO applicability limits (intersection area in Fig. 2). Some examples are reported in Fig. 21. In all the mentioned cases, there is in general a good agreement between analytical and numerical simulations up to a *ks*=3.5. On the

smoother surface (*ks* = 2) some deviation exists only at the highest incident angles and for scattering angles lower than backscattering direction, where the numerical solution presents higher values and a noticeable separation of two polarizations, as in the previous Gaussian case at L band. As expected, the angular distribution of scattered power becomes flatter as the roughness increases. The dip at Vertical polarization at the highest incidence angle appears to be related to the Brewster angle.

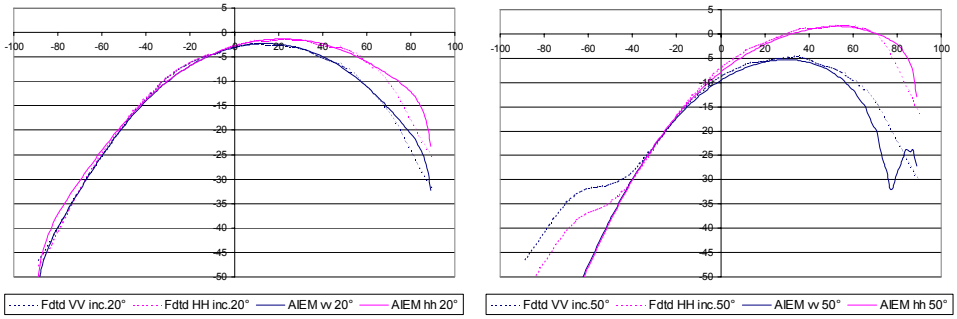

ε =4.06 + j 0.3 ; ks = 2.0

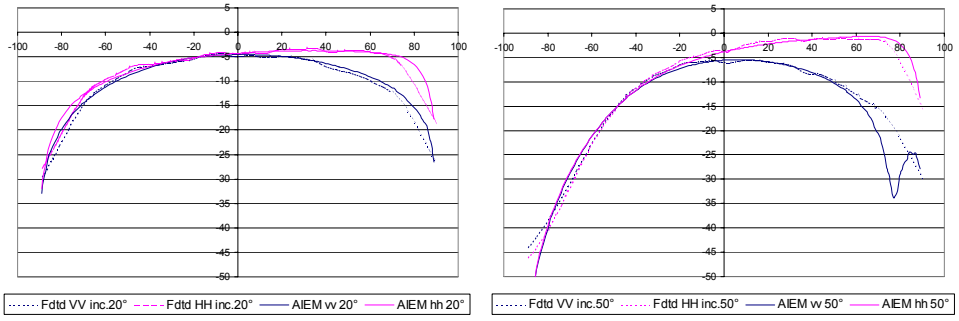

ε =4.06 + j 0.3 ; ks = 3.5

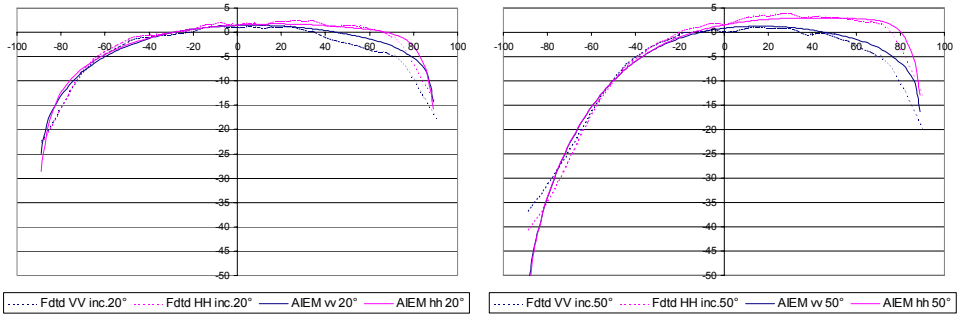

ε =24.6 + j 3.19 ; ks = 3.5

Fig. 21 - Bistatic scattering coefficient at C-band as a function of scattering angle for a surface with Gaussian ACF and kl = 12.56.

3.1.6.3 Exponential ACF L-band

At L-band, simulations have been performed with *ks* from 0.12 to 0.82, *kl* from 1.48 to 2.96, and for 2 values of permittivity (8.5 +j1.2 and 27.0 +4.0). As for other cases, incidence angles ranged between 10° and 60° at 10° steps. Some examples are reported in Fig. 22. There is, in general, a good agreement between analytical and numerical simulations. Some overestimation of the AIEM is evident at the extreme negative scattering angles for *ks* = 3.5 especially for the horizontal component at negative scattering angles. This overestimation increases as the roughness increases.

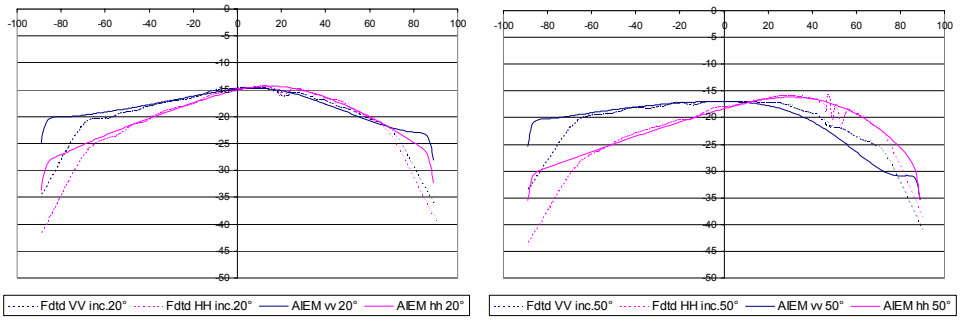

ks=0.12 kl=1.48 eps=8.5+j1.2

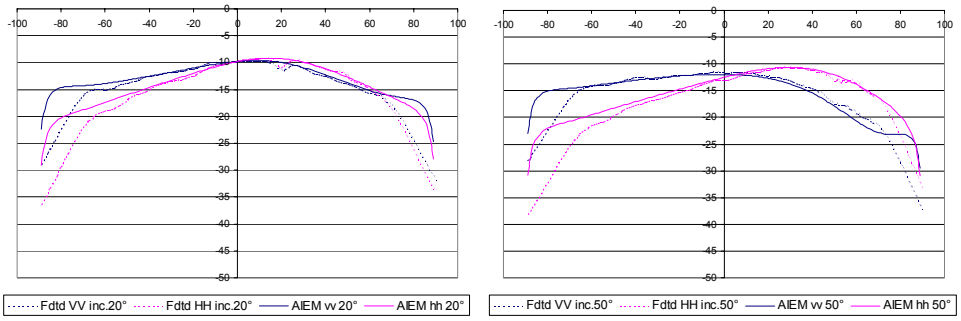

ks = 0.23 kl = 1.48 ε = 8.5+j1.2

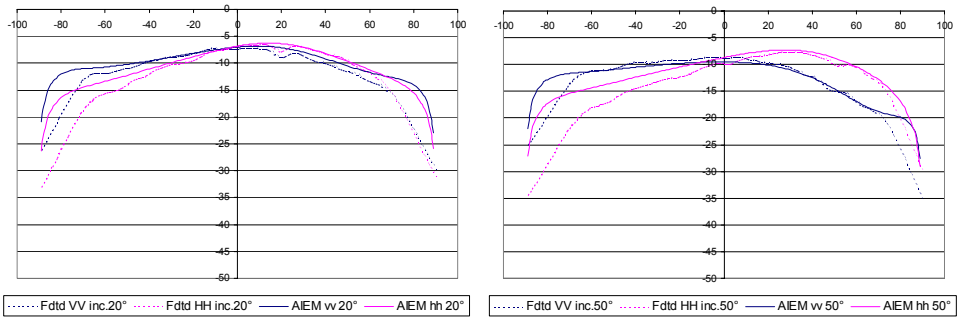

ks = 0.35 kl = 1.48 ε = 8.5+j1.2

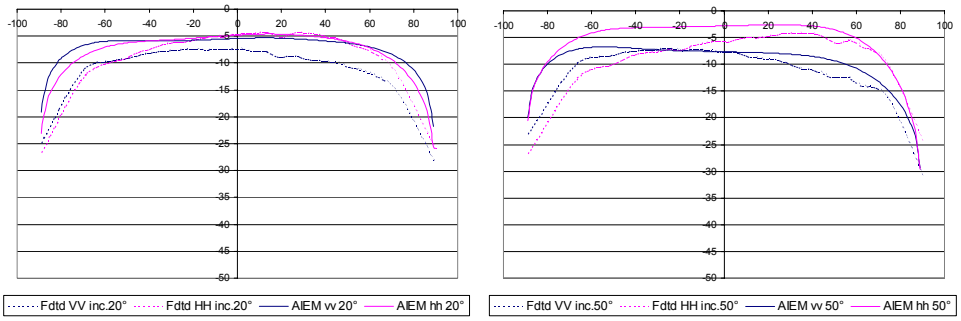

ks = 0.82 kl = 1.48 ε = 8.5+j1.2

Fig. 22 - Bistatic scattering coefficient at L-band as a function of scattering angle for a surface with Exponential ACF

3.1.6.4 Exponential ACF C-band

At C-band simulations have been performed with *ks* from 0.5 to 4.0, *kl* = 6.28 and 12.57, and 3 values of permittivity (4.06 + j0.3, 7.0 + j0.8 and 24 + j 3.19). As for other cases, incidence angles ranged between 10^o and 60^o at 10^o steps. Some examples are reported in Fig. 23. In all cases, there is, in general, a good agreement between analytical and numerical simulations until *ks*=2 (and *kl*=12.57). As the roughness increases (*ks* $\geq$ 3) a significant overestimation of the AIEM appears, mainly at vertical polarization. It is noticeable that in these cases the roughness should fall within the GO approximation limits, which predict same backscattering at vertical and horizontal polarization, as done by the AIEM simulations. Conversely, the FDTD simulations predicts higher scattering at horizontal polarization in all directions for those cases.

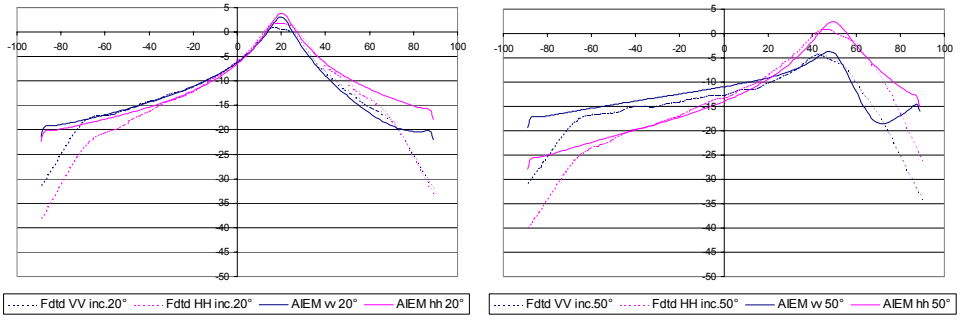

ks = 0.5 kl = 12.57 ε = 7.0+j0.8

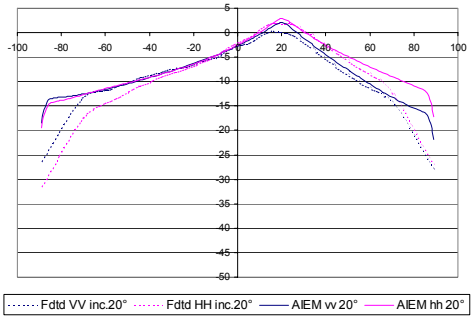

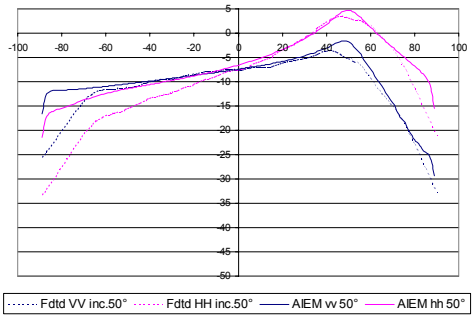

ks = 1.0 kl = 12.57 ε = 7.0+j0.8

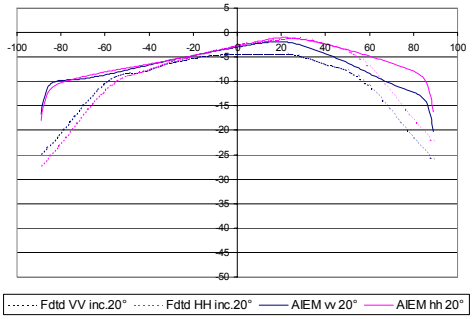

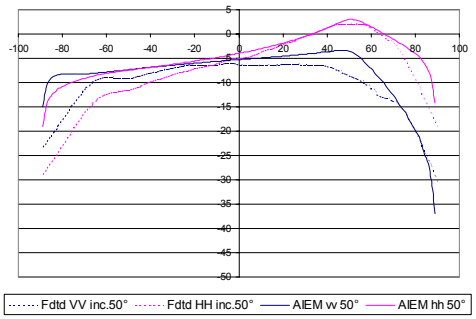

ks= 1.5 kl = 12.57 ε = 7.0+j0.8

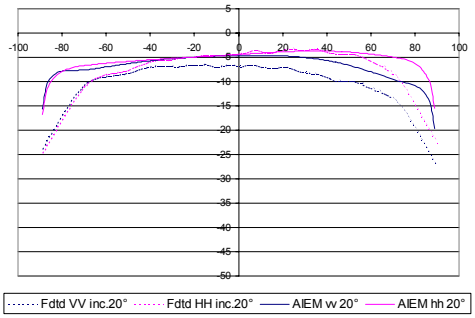

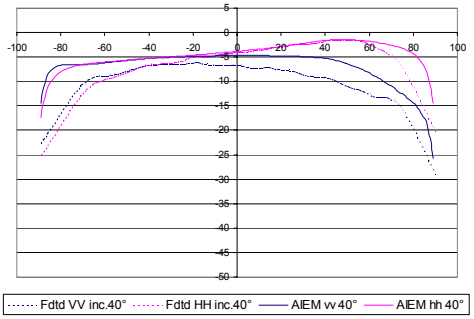

ks = 2.0 kl = 12.57 ε = 7.0 + j 0.8

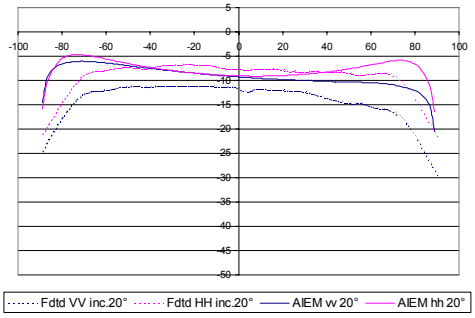

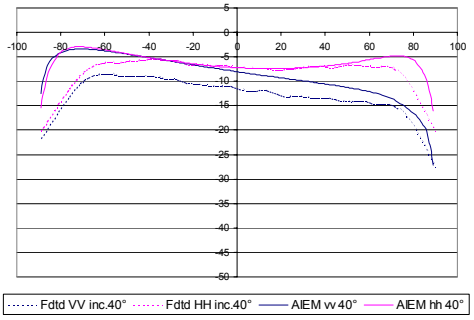

ks = 3.5 kl = 12.57 ε = 7.0 + j 0.8

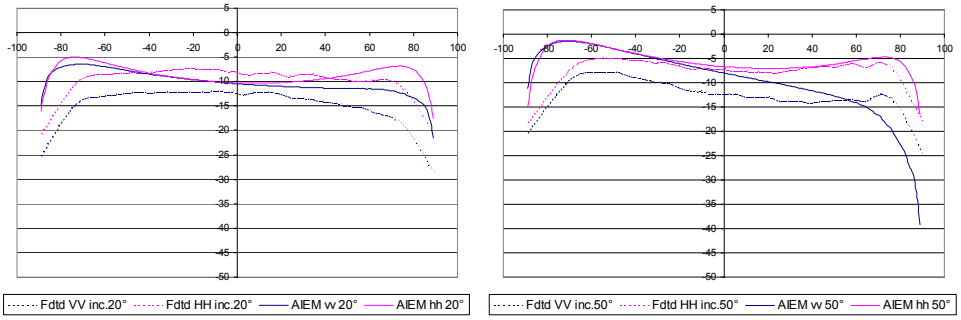

ks = 4.0 kl = 12.57 ε = 7.0+j0.8

Fig. 23 – Bistatic scattering coefficient at C-band as a function of scattering angle for a surface with Exponential ACF

3.1.7 Comparison between AIEM simulations and experimental data

All the comparisons made in the AIEM validation phase have been done against numerical data. In order to better test the performances of the Advanced Integral Equation Method to simulate the bistatic scattering from natural surfaces it is worth to extend the validation to experimental datasets. Between 1995 and 1996, an experiment aimed to investigate the bistatic scattering signature of non-vegetated surfaces took place at the ElectroMagnetic Signature Laboratory of the European Joint Research Center (EMSL-JRC) in Ispra (Italy). Three different soil targets, composed by an artificial homogeneous dielectric shaped with a suitable mold, were used [118]). The dielectric material was a combination of sand, water, and ethanediol. The latter component, which attracts water, was added to guarantee a good stability in time (15–20 days) of the model dielectric properties. The permittivity was measured using a coaxial probe directly applied on the surface. The sample under test was contained in a cylinder of 2 m in diameter and 0.4 m height. The roughness of the models had a Gaussian height distribution but, on the azimuthal plane, two of them were characterized by a Gaussian autocorrelation function while a third model had a mixed Gaussian-exponential ACF.

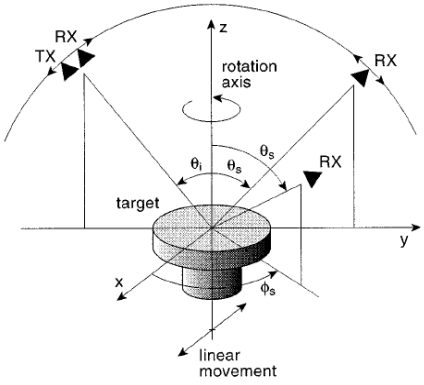

Fig. 24 - The scattering measurements configuration of the EMSL-JRC anechoic chamber (After [66])

The surface characteristics of the three soil models and their values of permittivity are summarized respectively in Tabs 2 and 3.

Table 2 - Summary of surface characteristics

surface type	***ACF***	***S (cm)***	***ACL (cm)***
Smooth	Gaussian	0.4	6
Medium rough	mixed Gaussian/ exponential	0.9	*l* = 1.8 L = 3.0
Rough	Gaussian	2.5	6

Table 3 - The permittivity of target material

Frequency (GHz)	***Gaussian smooth/rough***	***Medium rough***
2	8.7 + i 2.8	5.0 + i 1.4
5	6.8 + i 2.8	4.5 + i 1.4
6.8	6.0 + i 2.6	4.1 + i 1.4
10	5.5 + i 2.2	3.9 + i 1.1
18	5.2 + i 1.6	3.8 + i 0.9

The polarimetric scattering measurements were carried out on the sample placed in the centre of the EMSL anechoic chamber (radius 10 m) at various incidence and scattering angles between 10 and 50 degrees (the arrangement is depicted in Fig. 24). A frequency stepped CW mode (step =11.25 MHz) in the range 1.5 - 18.5 GHz was used, applying a full polarimetric calibration in the monostatic configuration and a simple “Response & Isolation” correction in the bistatic case. The absolute calibration accuracy was better than +/- 0.5 dB and the system noise level for typical measurement settings (averaging factor =128, time window span = 10 ns) ranges from -50 dBsm at 2 GHz to -40 dBsm at 18 GHz [118].
The scattering matrix of the target was measured in the plane of incidence (vertical polarization plane) both in monostatic and bistatic mode for different incidence and scattering angles. Independent samples were obtained by rotating the target in azimuth to obtain uncorrelated data at a given frequency and averaging in the frequency domain over a window larger than one correlation length. It should be noted that, the contribution of the coherent term (which is important for a smooth surface at low frequency) has been subtracted from the experimental data used in this section, so that only the AIEM model for incoherent component has been considered here. The procedure used for subtracting the coherent component from the data can be affected by significant errors which can explain some discrepancy we observe hereafter in specular direction.
For this comparison the AIEM and SPM models have been run for 2-D surfaces. It should be noted that, in the case of SPM and for the frequency range of interest,

the validity conditions of the model can be satisfied for the Gaussian “smooth” surface only.

3.1.7.1 Gaussian ACF: Smooth surface

Fig. 25 represents a comparison of backscattering coefficient measured and simulated as a function of frequency at H polarization for three values of incidence angle and for a surface with Gaussian autocorrelation function. We see that the AIEM well reproduces co-polarized experimental data on the entire frequency range at steep incidence angle. At higher incident angles the trend of backscattering as a function of frequency shows that, as the frequency increases, experimental data tend to a constant value, whereas the model predicts a decrease of backscattering. Very similar results have been obtained at VV polarization.

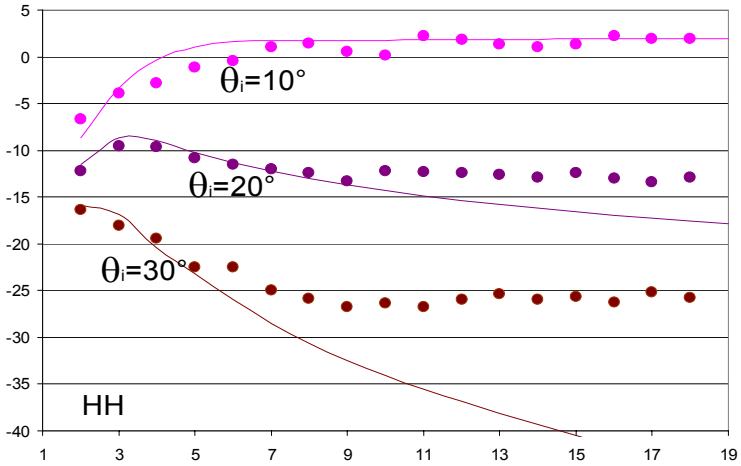

Fig. 25 – Simulated (continuous line and measured (points) backscattering coefficient from a “smooth” surface (s =0.4cm l =6cm) with a Gaussian ACF as a function of frequency

Fig. 26 represent the comparison of measured and simulated bistatic scattering coefficient carried out as function of scattering angle on the “smooth” surface at L-band (2 GHz). We can see that the model reproduces experimental data in the backscattering regions quite well, whereas a discrepancy (higher than 5 dB) appears in the region of specular forward scattering. However, it should be noted that the model does not include the coherent term (which is important for a smooth surface at low frequency). As said before, the latter contribution has been subtracted from the experimental data via a procedure that can be affected by significant errors.

The results for the comparison carried out on the same surface at C (5 GHz) and X (10 GHz) bands are shown in Figs. 27 and 28. We see that, at 5 GHz, the AIEM fits experimental data on the entire range of tested scattering angles very well. The same trend is observed at 10 GHz for HH polarization and scattering angle higher than -20 degrees, whereas, for high negative scattering angles, the model tends to underestimate experimental data especially at VV polarization.

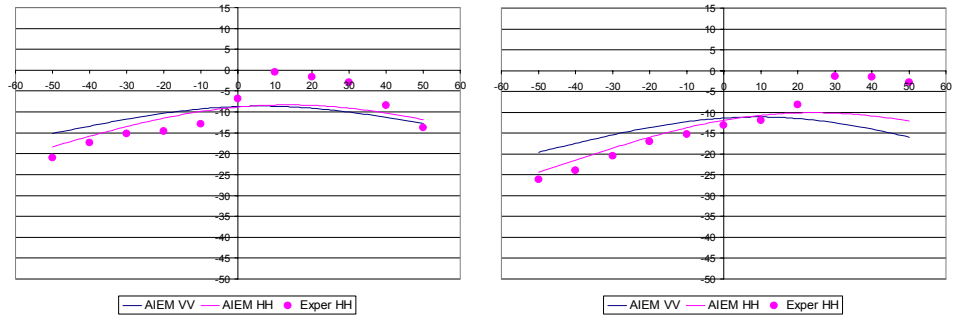

Fig. 25 - Measured and simulated bistatic scattering coefficient as function of scattering angle on the "smooth" surface (s = 0.4cm l=6cm ε = 8.7+j2.8) at L-band (2 GHz) (a: θ_i = 20° b: θ_i =40°),

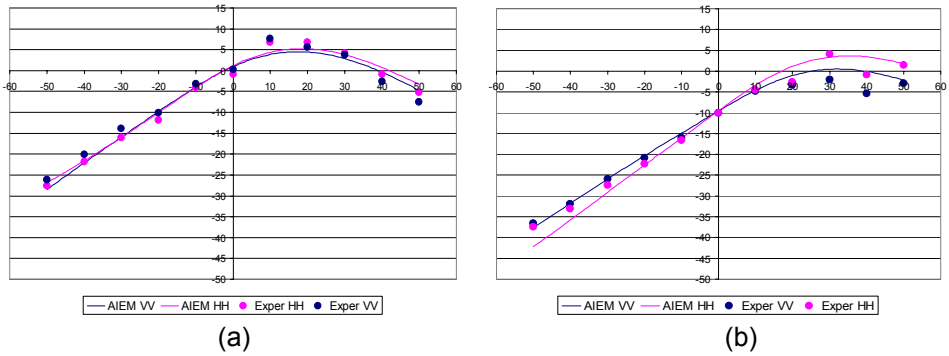

Fig. 26 - Measured and simulated bistatic scattering coefficient as function of scattering angle on the "smooth" surface (s=0.4cm l=6cm) at C-band (ε = 6.8 +j2.8) (a: θ_i =20° b: θ_i =40°),

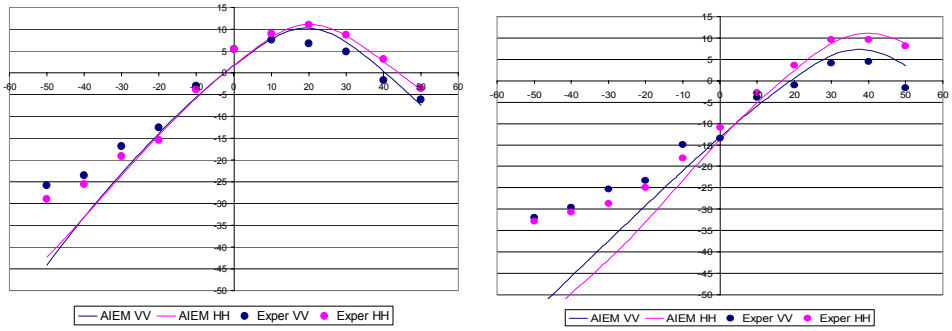

Fig. 27 - Measured and simulated bistatic scattering coefficient as function of scattering angle on the "smooth" surface (s=0.4cm l=6cm ε = 5.5+j2.2) at X-band (10 GHz) (a: θ_i =20° b: θ_i =40°)

3.1.7.2 Gaussian ACF: "Rough" surface

For the "Rough" surface experimental data are very well reproduced at all frequencies between 2 and 10 GHz, As an example Fig. 29 (a, b) shows the bistatic scattering coefficient at 10 GHz as a function of scattering angle for incidence angles equal to -20 and -40 degrees respectively.

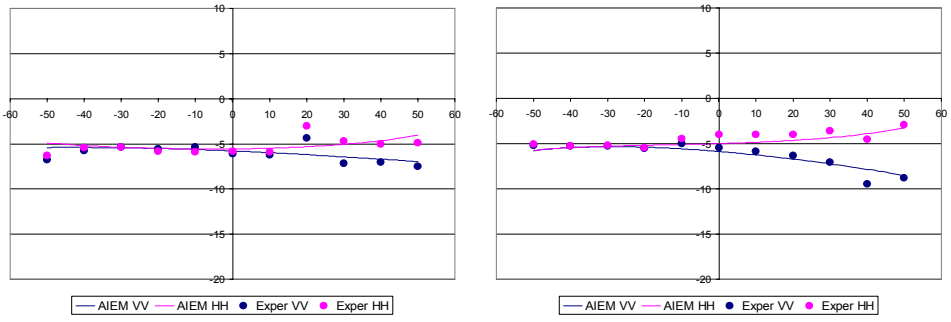

Fig. 29 - Measured and simulated bistatic scattering coefficient as function of scattering angle on the "Rough" surface (s=2.5cm l = 6cm) at X-band (ε = 5.5+j2.2) (a: θ_i =20°; b: θ_i =40°)

3.1.7.3 "Medium rough" mixed ACF surface

On the "Medium Rough" surface, which has a mixed Gaussian-Exponential correlation function, two approximations to the local angle θ_l can be considered: the

flat surface approximation, obtained by replacing θ_i with the incidence angle and the specular incidence approximation (θ_i =0). The first approximation is valid in the low frequency limit while the second one is for high frequencies. The bound between the two regions has been determined by measurements [65]. Therefore, the reflection coefficients are expressed by (94):

$$R_{v,h} = \begin{cases} R(\theta_i) & k^2 sL < 1.2\sqrt{\varepsilon_r} \\ R(\theta_{spec}) & k^2 sL > 1.2\sqrt{\varepsilon_r} \end{cases}$$

As for the smooth surface, the comparison of the model with experimental data at low frequency (2 GHz), not represented here, shows good agreement except in the region of coherent scattering, but at higher frequencies, this discrepancy disappears. Fig. 30 shows the results obtained at 5 GHz, for an incidence angle equal to - 40 degrees. At a higher frequency (10 GHz), experimental data are much better reproduced by the AIEM.

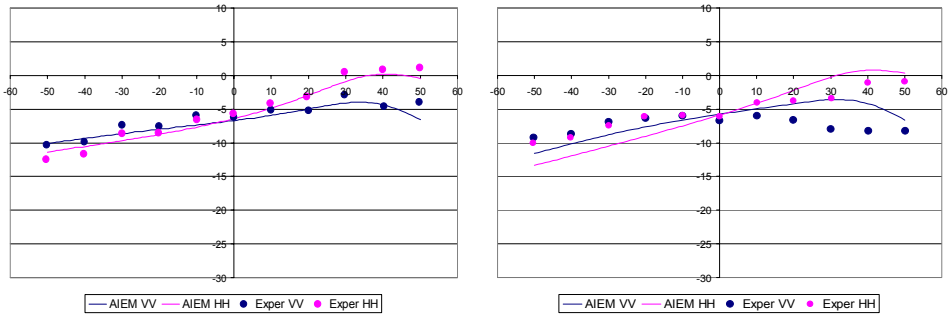

Fig. 30 - Measured and simulated bistatic scattering coefficient as function of scattering angle on the "Medium Rough" (mixed-exponential ACF) surface at θ_i =40° (s=0.9cm l=1.8cm L=3cm ε=4.5+j1.4) a = 5 GHz, b = 10 GHz

3.2 Electromagnetic properties of a dry snowpack: the Dense Media Radiative Transfer model (DMRT)

As stated in the "State of the art", the DMRT radiative transfer equation is formally the same of the classical one except for the characteristics of the medium, which are computed in a different way. The electromagnetic properties of a dense medium must be described by specifying how the statistics of the spatial configuration of scatterers is influenced by the high density and by the stickiness property of the ice grains. The function that expresses this collective behavior under the quasi-crystalline approximation is the pair distribution function.

3.2.1 The pair distribution function for sticky particles

Let us consider a collection of spherical identical particles which tend to adhere one another (just like the snow crystals) and denote the particle radius with ***a***, the factional volume occupied by the scatterers with *f* and the stickiness parameters with τ. Stickiness is a physical parameter used in molecular physics to describe the potential energy of adhesiveness between particles. In [51],[39] the sticky parameter is adopted to better describe the correlated distribution of ice crystal in the snowpack. The particle positions are determined by inter-particle potential energy: given the potential energy, the Percus Yevick equation can be soled to calculate the pair distribution function, which is proportional to the joint probability density functions of two particles. Usually, the value τ=0.1 is chosen because in this case the frequency dependence of extinction coefficient is 2.8 (for the independent scattering is 4), which is the best frequency dependence value tested through experiments [35].

The first function that must be calculated is the pair distribution function and the related structure factor. In [38] were found several typographic errors that have been detected and corrected in this work. The pair distribution function describes the probability that two particles can be at a certain distance. The scatterers are considered not penetrable.

The pair distribution function is defined as

$$g(r) = \begin{cases} 0 & r < 2a \\ 1 + h(r) & r \geq 2a \end{cases} \tag{114}$$

where h(r) is the structure factor expressed by

$$h(r) = \frac{1}{(2\pi)^3} \frac{4\pi}{r\, n_0} \frac{1}{a^2} \int_0^\infty \left[\frac{n_0 \widetilde{C}(p)}{1 - n_0 \widetilde{C}(p)} \right] X \ \sin\left(\frac{r}{a} X \right) dX \tag{115}$$

$$X = pa \tag{116}$$

The above integral is not numerically convergent as $p \to \infty$ and an asymptotic evaluation must be performed. Thus, h(r) must be divided into two parts

$$h(r) = h_{reg}(r) + h_{sing}(r) \tag{117}$$

where h(r) is separated into a regular part (which is convergent) and into an asymptotic part

$$h_{reg}(r) = \frac{1}{(2\pi)^3} \frac{4\pi}{r\, n_0} \frac{1}{a^2} \int_0^\infty \left\{ \left[\frac{n_0 \widetilde{C}(p)}{1 - n_0 \widetilde{C}(p)} \right] - \left[\frac{n_0 \widetilde{C}(p)}{1 - n_0 \widetilde{C}(p)} \right]_{asy} \right\} X \ \sin\left(\frac{r}{a} X \right) dX \tag{118}$$

$$h_{sing}(r) = \frac{t\ a}{6} \delta(r - 2a) \tag{119}$$

In (118) $n_0 \widetilde{C}(p)$ can be obtained from [39]

$$n_0\widetilde{C}(p)=1-\left\{\frac{f}{1-f}\left[\left(1-t\ f+\frac{3f}{1-f}\right)\Phi(X)+\left[3-t(1-f)\right]\ \Psi(X)\right]+\cos X\right\}^2+$$
$$-\left\{\frac{f}{1-f}X\ \Phi(X)+\sin X\right\}^2 \tag{120}$$

where

$$\Psi(X)=\frac{\sin X}{X} \tag{121}$$

$$\Phi(X)=3\left[\frac{\sin X}{X^3}-\frac{\cos X}{X^2}\right] \tag{122}$$

$$t=\frac{6}{f}\left[\tau+\frac{f}{1-f}-\sqrt{\left(\tau+\frac{f}{1-f}\right)^2-\frac{f\left(1+f/2\right)}{3(1-f)^2}}\right] \tag{123}$$

and

$$\left[\frac{n_0\widetilde{C}(p)}{1-n_0\widetilde{C}(p)}\right]_{asy}=\frac{2\ t\ f\ \sin X\cos X}{X} \tag{124}$$

The pair distribution function is not regular and has very sharp peaks. Anyway, it usually converges to one when the distance between the particles is greater than 2-3 diameters. This means that in a dense medium the particles cannot assume arbitrary positions but are closely packed together.

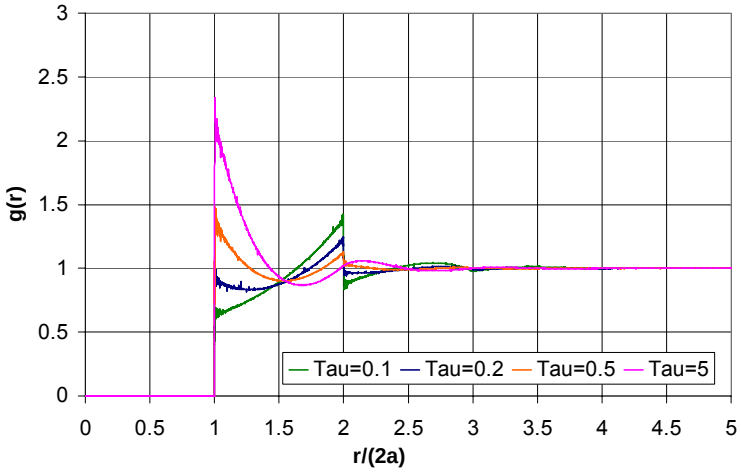

Fig. 31 - The Percus-Yevick pair distribution function for sticky spherical scatterers. The distance between the particles is normalized to the diameter. The volume fraction is 0.3.

In Fig. 31 the pair distribution function is represented for several values of stickiness. The sharp peak for r=2a clearly show the tendency of the scatterers to adhere one another.

Once the pair distribution function has been computed it is possible to find the other two relevant parameters for the radiative transfer equation: the effective permittivity and the extinction coefficient.

3.2.2 The effective permittivity and the extinction coefficient

The parameters used in the radiative transfer equation and that characterize the propagation medium are the effective permittivity and the extinction coefficient. Considering a medium composed by *N* particles centered in $\bar{r}_1,\ \bar{r}_2,\ \bar{r}_3,...,\bar{r}_N$ and the incident wave impinging along k_i, the Foldy-Lax multiple scattering equation describes the electromagnetic field in a dense medium and can be written as in [39], [51]

$$\bar{\bar{w}}^{(j)} = \sum_{\substack{l=1 \\ l\neq j}}^{N} \bar{\bar{\sigma}}(k\ \bar{r}_l \bar{r}_j)\ \bar{\bar{T}}^{(l)} \bar{\bar{w}}^{(l)} + e^{i(\bar{k}_i \bullet \bar{r}_j)}\ \bar{a}_{inc} \tag{125}$$

where $\bar{\bar{w}}^{(j)}$ and $\bar{\bar{w}}^{(l)}$ are respectively the exciting field coefficients of the *j*-th and *l*-th particles, $\bar{\bar{T}}^{(l)}$ is the T-matrix of the l-th particle, $\bar{a}_{inc}$ is the coefficient of the incident field and the matrix $\bar{\bar{\sigma}}(k\ \bar{r}_l \bar{r}_j)$ describes the vector translation formula transforming spherical waves centered at $\bar{r}_j$ to spherical waves centered at $\bar{r}_l$. Equation (125) can be easily interpreted: the field exciting the *j*-th particle is the sum of the waves scattered by all the other particles (except the considered one) and the incident wave.

The (125) holds for a fixed spatial configuration of the *N* particles. To perform a statistical configuration analysis of (125) the conditional average must be used. Denoting with $p\left(\bar{r}_1,\bar{r}_2,...,\bar{r}_{j-1},\bar{r}_{j+1},...\bar{r}_N \mid \bar{r}_j\right)$ the conditional probability density function, it is

$$\bar{w}(\bar{r}_j) = E_j[\bar{\bar{w}}^{(j)}] = \int \bar{\bar{w}}^{(j)}\, p\left(\bar{r}_1,\bar{r}_2,...,\bar{r}_{j-1},\bar{r}_{j+1},...\bar{r}_N \mid \bar{r}_j\right) d\bar{r}_1 d\bar{r}_2 ... d\bar{r}_{j-1} d\bar{r}_{j+1} ... d\bar{r}_N \tag{126}$$

where all $\bar{r}_x$ become dummy variables excepted $\bar{r}_j$. (126) represents the *j*-th particle mean exciting field and can be written as

$$\bar{\bar{w}}(\bar{r}_j) = \sum_{\substack{l=1 \\ l\neq j}}^{N} \int \bar{\bar{\sigma}}(k\ \bar{r}_l \bar{r}_j)\ \bar{\bar{T}}^{(l)} \bar{\bar{w}}^{(l)}\ p\left(\bar{r}_1, \bar{r}_2, ..., \bar{r}_{j-1}, \bar{r}_{j+1}, ... \bar{r}_N \mid \bar{r}_j\right) d\bar{r}_1 d\bar{r}_2 ... d\bar{r}_{j-1} d\bar{r}_{j+1} ... d\bar{r}_N + e^{i(\bar{k}_i \bullet \bar{r}_j)}\ \bar{a}_{inc} \tag{127}$$

Since $\bar{\bar{\sigma}}(k\ \bar{r}_l \bar{r}_j)$ depends on both $\bar{r}_l$ and $\bar{r}_j$ it is useful to apply another time the Bayes' rule to (127)

$$\bar{\bar{w}}(\bar{r}_j) = \sum_{\substack{l=1 \\ l\neq j}}^{N} \int \bar{\bar{\sigma}}(k\ \bar{r}_l \bar{r}_j)\ \bar{\bar{T}}^{(l)} \bar{\bar{w}}^{(l)}\ p\left(\bar{r}_1, \bar{r}_2, ..., \bar{r}_{l-1}, \bar{r}_{l+1}, ..., \bar{r}_{j-1}, \bar{r}_{j+1}, ... \bar{r}_N \mid \bar{r}_l, \bar{r}_j\right) p\left(\bar{r}_l \mid \bar{r}_j\right) d\bar{r}_1 d\bar{r}_2 ... d\bar{r}_{j-1} d\bar{r}_{j+1} ... d\bar{r}_N + e^{i(\bar{k}_i \bullet \bar{r}_j)}\ \bar{a}_{inc} \tag{128}$$

Then (128) becomes

$$\bar{\bar{w}}(\bar{r}_j) = E_j\left[\bar{\bar{w}}^{(j)}\right] = \sum_{\substack{l=1 \\ l\neq j}}^{N} \int \bar{\bar{\sigma}}(k\ \bar{r}_l \bar{r}_j)\ p(\bar{r}_l \mid \bar{r}_j)\ \bar{\bar{T}}^{(l)} E_{lj}\left[\bar{\bar{w}}^{(l)}\right] d\bar{r}_l + e^{i(\bar{k}_i \bullet \bar{r}_j)}\ \bar{a}_{inc} \tag{129}$$

where E_j is the conditional average given the position of the *j*-th particle, $p(\bar{r}_l \mid \bar{r}_j)$ is the conditional probability of finding the *l*-th particles in $\bar{r}_l$ when the *j*-th one is in $\bar{r}_j$, and E_{lj} is the conditional average given the position of the *j*- and *l*-th particles.

Based in the QuasiCrystalline Approximation (QCA),

$$E_{lj}\left(\bar{\bar{w}}^{(l)}\right) \approx E_l\left(\bar{\bar{w}}^{(l)}\right) \equiv \bar{\bar{w}}(\bar{r}_l) \tag{130}$$

The previous equation means that the average field computed by holding fixed two particles is approximated by the one holding fixed only one particle. Since $\bar{r}_j$ has become a dummy variable, it is possible to replace the summation by N-1. Hence it is possible to made the following substitution

$$(N-1)\, p(\bar{r}_l \mid \bar{r}_j) = n_0\ g(\bar{r}_l - \bar{r}_j) \tag{131}$$

The average exciting field of the *l*-th particle under the quasi-crystalline approximation can be eventually written as

$$\bar{\bar{w}}(\bar{r}_j) = n_0 \int \bar{\bar{\sigma}}(k\ \bar{r}_l \bar{r}_j)\ g(\bar{r}_l - \bar{r}_j)\ \bar{\bar{T}}^{(l)} \bar{\bar{w}}(\bar{r}_l)\ d\bar{r}_l + e^{i(\bar{k}_i \bullet \bar{r}_j)}\ \bar{a}_{inc} \tag{132}$$

where $g(\bar{r}_l - \bar{r}_j)$ is the pair distribution function described in the previous paragraph.

The integral equation (132) could be solved by means of a vector spherical wave expansion truncated at multipole N_{max}. Its value is chosen according to the following rule [38]

$$N_{\max} = \lfloor k\ 2a \rfloor + 1 \tag{133}$$

In remote sensing of snow, this value is at most 3. This expansion leads to a set of $2N_{max}$ equations, the Lorentz-Lorentz law (L-L law) and to the Ewald-Oseen (E-O) theorem.

The L-L law is [39,eq. 6.1.46a-b]

$$X_v^{(M)} = -2\pi n_0 \sum_{n=1}^{N_{\max}} \sum_{p=|n-v|}^{n+v} (2n+1)\left[L_p(k,K \mid 2a) + M_p(k,K \mid 2a)\right] \cdot \left\{ \begin{array}{l} T_n^{(M)} X_n^{(M)} a(1,n \mid -1,v \mid p) A(n,v,p) \\ \quad + T_n^{(N)} X_n^{(N)} a(1,n \mid -1,v \mid p,p-1) B(n,v,p) \end{array} \right\}$$

$$X_v^{(N)} = -2\pi n_0 \sum_{n=1}^{N_{\max}} \sum_{p=|n-v|}^{n+v} (2n+1)\left[L_p(k,K \mid 2a) + M_p(k,K \mid 2a)\right] \cdot \left\{ \begin{array}{l} T_n^{(M)} X_n^{(M)} a(1,n \mid -1,v \mid p,p-1) B(n,v,p) \\ \quad + T_n^{(N)} X_n^{(N)} a(1,n \mid -1,v \mid p) A(n,v,p) \end{array} \right\} \quad (134)$$

$$v = 1,2,3,\ldots N_{\max}$$

where M_p and L_p are [39,eqs. 6.1.34 and 6.1.39]

$$M_p(k,K \mid 2a) = \int_{2a}^{\infty} [g(r)-1]\ h_p(kr)\ \ j_p(Kr)\ r^2 dr \quad (135)$$

$$L_p(k,K \mid 2a) = -\frac{(2a)^2}{K^2-k^2}\left[k\ h_p'(k2a)\ \ j_p(K2a) - K\ h_p(k2a)\ \ j_p'(K2a)\right] \quad (136)$$

In the previous equations k is the wavenumber in the vacuum, K is the effective wavenumber in the dense medium, h_p is the Bessel function of p order, j_p is the Hankel function and n_0 is the particle number density that can be obtained from

$$n_0 = \frac{6f}{\pi(2a)^3} \quad (137)$$

The functions $A(n,v,p)$, $B(n,v,p)$ [39, eqs. 6.1.44a-b], $a(1,n \mid -1,v \mid p)$ and $a(1,n \mid -1,v \mid p,p-1)$ [120, eqs. 10.4.14 and 10.4.15] are

$$A(n,v,p) = \frac{v(v+1)+n(n+1)-p(p+1)}{n(n+1)} \quad (138)$$

$$B(n,v,p) = \frac{1}{n(n+1)}\sqrt{(n+v+p+1)(v+p-n)(n+p-v)(n+v-p+1)} \quad (139)$$

$$a(m,n\,|\,\mu,\nu\,|\,p)=(-1)^{m+\mu}(2p+1)\sqrt{\frac{(n+m)!\;(\nu+\mu)!\;(p-m-\mu)!}{(n-m)!\;(\nu-\mu)!\;(p+m+\mu)!}}\cdot \cdot\begin{pmatrix} n & \nu & p \\ m & \mu & -m-\mu \end{pmatrix}\begin{pmatrix} n & \nu & p \\ 0 & 0 & 0 \end{pmatrix} \tag{140}$$

$$a(m,n\,|\,\mu,\nu\,|\,p,q)=(-1)^{m+\mu}(2p+1)\sqrt{\frac{(n+m)!\;(\nu+\mu)!\;(p-m-\mu)!}{(n-m)!\;(\nu-\mu)!\;(p+m+\mu)!}}\cdot \cdot\begin{pmatrix} n & \nu & p \\ m & \mu & -m-\mu \end{pmatrix}\begin{pmatrix} n & \nu & q \\ 0 & 0 & 0 \end{pmatrix} \tag{141}$$

where

$$\begin{pmatrix} j_1 & j_2 & j_3 \\ m_1 & m_2 & -m_1-m_2 \end{pmatrix} \tag{142}$$

represents the Wigner 3j symbol which can be found in [120, pag. 536].

In (134) $T_n^{(M)}$ and $T_n^{(N)}$ are the T matrix coefficients used in the expansion [51, eqs. 1.6.14b and 1.6.15b]

$$T_n^{(N)}=-\frac{k_p^2\;a^2\;j_n(k_pa)[k\;a\;j_n(k\;a)]'-k^2\;a^2\;j_n(k\;a)[k_pa\;j_n(k_pa)]'}{k_p^2\;a^2\;j_n(k_pa)[k\;a\;h_n(k\;a)]'-k^2\;a^2\;h_n(k\;a)[k_pa\;j_n(k_pa)]'} \tag{143}$$

$$T_n^{(M)}=-\frac{j_n(k_pa)[k\;a\;j_n(k\;a)]'-j_n(k\;a)[k_pa\;j_n(k_pa)]'}{j_n(k_pa)[k\;a\;h_n(k\;a)]'-h_n(k\;a)[k_pa\;j_n(k_pa)]'} \tag{144}$$

The L-L law (134) can be rearranged to give a system of $2N_{max}$ homogeneous equations for the $2N_{max}$ unknown amplitudes $X_1^{(M)}, X_2^{(M)},\ldots, X_{N\max}^{(M)}$ and $X_1^{(N)}, X_2^{(N)},\ldots X_{N\max}^{(N)}$. By imposing the determinant of (134) to vanish, it is possible to obtain the solution for the effective propagation constant *K*. The equation could be solved numerically by using the Muller's Method to search the root *K*. Anyway, bearing in mind that *K* is complex, *K=K' + j K"*, and *K"<<K'*, the final value of *K* will be determined by the convergence of the real part only and the imaginary one could not have the enough accuracy. In addition *K"* depends strongly on the pair distribution function which have very sharp peaks and which are difficult to be taken into account with this technique.

It is worth outlining that the quasi-crystalline approximation combined with the distorted Born approximation, may not conserve energy. To impose it, a different procedure must be followed.

From equations (134) only the real part of the obtained effective propagation constant *K* will be retained. After that, one of the equations of the L-L law must be substituted with the E-O theorem which is a single equation given by [39, 6.1.49]

$$K - k = -\frac{\pi\, i\, n_0}{k^2} \sum_{n=1}^{N_{\max}} \left(T_n^{(M)} X_n^{(M)} + T_n^{(N)} X_n^{(N)} \right) (2n+1) \tag{145}$$

The resulting set of equations is non-homogenous and the amplitudes $X_i^{(M)}, X_i^{(N)}$ *i=1,..,N_{max}* can be determined by solving the system.

Now it is possible to determine the absorption coefficient k_a which can be calculated by

$$k_a = \frac{k}{K_r} \frac{2\pi}{k^2 \left| 1 - R \right|^2} n_0 \sum_{n=1}^{N_{\max}} (2n+1) \left[\left| X_n^{(M)} \right|^2 + \left(-\operatorname{Re} T_n^{(M)} - \left| T_n^{(M)} \right|^2 \right) + \left| X_n^{(N)} \right|^2 + \left(-\operatorname{Re} T_n^{(N)} - \left| T_n^{(N)} \right|^2 \right) \right] \tag{146}$$

where K_r is the real part of *K* and

$$R = \frac{\pi\, i\, n_0}{k^2 (k + K_r)} \sum_{n=1}^{N_{\max}} (-1)^n \left[-T_n^{(M)} X_n^{(M)} + T_n^{(N)} X_n^{(N)} \right] (2n+1) \tag{147}$$

Bearing in mind that $k_e = k_a + k_s$, the first part extinction coefficient and of the effective permittivity of the snow is now calculated. To obtain the scattering coefficient we must compute before the phase matrix, which describe how the intensity impinging on an infinitesimal volume is distributed over all the other directions.

3.2.3 The DMRT-QCA phase matrix

The procedure to obtain the phase matrix for a dense medium under the quasi-crystalline approximation is well established in literature but it is very complicated due to the system of reference used. In [38] a new method has been shown which makes use of rotation matrices to switch between different frames.

Due to the spherical symmetry of the scatterers it is useful to obtain the phase matrix in the 1-2 system [51] (Fig. 32) and then switch to the principal one (depicted in Fig. 16).

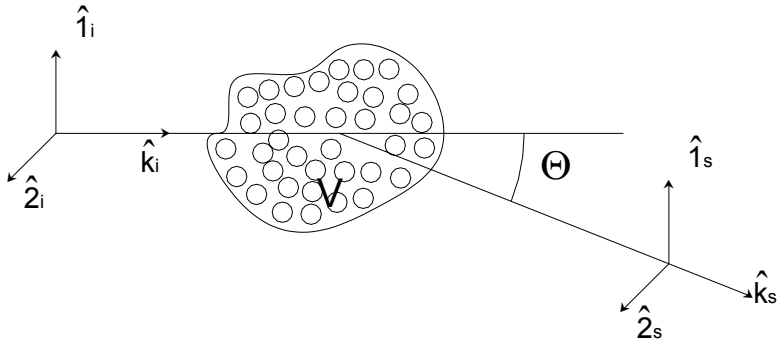

Fig. 32 - Geometry of the 1-2 frame based on the scattering plane.

The 1-2 scattering plane contains the incident k_i and scattering k_s vectors. The angle between them is Θ. The expressions for the 1_i, 2_i, 1_s and 2_s versors can be found in [51, eqs. 1.1.34-1.1.36] .

The phase matrix relates the Stokes parameters of the scattered wave to the one of the incident wave and, in the 1-2 frame, can be written as

$$\begin{bmatrix} I_{1s} \\ I_{2s} \\ U_{12s} \\ V_{12s} \end{bmatrix} = \begin{bmatrix} P_{11}(\Theta) & 0 & 0 & 0 \\ 0 & P_{22}(\Theta) & 0 & 0 \\ 0 & 0 & P_{33}(\Theta) & P_{34}(\Theta) \\ 0 & 0 & P_{43}(\Theta) & P_{44}(\Theta) \end{bmatrix} \cdot \begin{bmatrix} I_{1i} \\ I_{2i} \\ U_{12i} \\ V_{12i} \end{bmatrix} \tag{148}$$

Because of the spherical shape of the scatterers, the cross-polarization terms $P_{12}(\Theta)$ and $P_{21}(\Theta)$ are zero.

The phase matrix components are

$$\begin{aligned} P_{11}(\Theta) &= \left|f_{11}(\Theta)\right|^2 q(\Theta) \\ P_{22}(\Theta) &= \left|f_{22}(\Theta)\right|^2 q(\Theta) \\ P_{33}(\Theta) &= \mathrm{Re}\left(f_{11}(\Theta) f_{22}^*(\Theta)\right) q(\Theta) \\ P_{33}(\Theta) &= P_{44}(\Theta) \\ P_{34}(\Theta) &= -\mathrm{Im}\left(f_{11}(\Theta) f_{22}^*(\Theta)\right) q(\Theta) \\ P_{43}(\Theta) &= -P_{34}(\Theta) \end{aligned} \tag{149}$$

where the f_{ii} terms are expressed by

$$f_{11}(\Theta) = -\frac{i}{(1-R)}\sqrt{\frac{1}{k\,K_r}}\sum_{n=1}^{N_{\max}}\frac{2n+1}{n(n+1)}\left[T_n^{(M)} X_n^{(M)} \tau_n(\cos\Theta) + T_n^{(N)} X_n^{(N)} \pi_n(\cos\Theta)\right] \tag{150}$$

$$f_{22}(\Theta) = -\frac{i}{(1-R)}\sqrt{\frac{1}{k\ K_r}}\sum_{n=1}^{N_{\max}}\frac{2n+1}{n(n+1)}\left[T_n^{(M)}X_n^{(M)}\pi_n(\cos\Theta) + T_n^{(N)}X_n^{(N)}\tau_n(\cos\Theta)\right] \quad (151)$$

The term *q(Θ)* is a correction factor related to the structure factor by

$$q(\Theta) = n_0\left(1 + n_0(2\pi)^3 H(\Theta)\right) \quad (152)$$

We recall that the expression of the structure factor is

$$H(\Theta) = \frac{1}{2\pi^2 p}\int_0^{\infty}(g(r)-1)\ \sin(p\ r)\ r\ dr \quad (153)$$

where

$$p = \sqrt{\mathrm{Re}(K)^2 + k^2 - 2k\,\mathrm{Re}(K)\cos\Theta} \quad (154)$$

The functions $\tau_n(\cos\Theta)$ and $\pi_n(\cos\Theta)$ can be found in [121]

Once the phase matrix has been calculated, it is possible to obtain the second part of the extinction coefficient. The expression of the scattering coefficient in the 1-2 frame is

$$k_s = \pi\int_0^{\pi}\left(P_{11}(\Theta) + P_{22}(\Theta)\right)\ \sin\Theta\ d\Theta \quad (155)$$

Eventually the effective permittivity of the snow and the extinction coefficient are obtained

$$k_e = k_s + k_a \quad (156)$$

$$\varepsilon_{eff} = \frac{K' + i\,k_e/2}{k} \quad (157)$$

It is possible to make a useful comparison between the phase matrices of the DMRT-QCA and Mie. In the classical Mie phase matrix, the scattering amplitudes are

$$f_{11}(\Theta) = -\frac{i}{k}\sum_{n=1}^{N_{\max}}\frac{2n+1}{n(n+1)}\left[T_n^{(M)}\tau_n(\cos\Theta) + T_n^{(N)}\pi_n(\cos\Theta)\right] \quad (158)$$

$$f_{22}(\Theta) = -\frac{i}{k}\sum_{n=1}^{N_{\max}}\frac{2n+1}{n(n+1)}\left[T_n^{(M)}\pi_n(\cos\Theta) + T_n^{(N)}\tau_n(\cos\Theta)\right] \quad (159)$$

and the phase matrix components

$$P_{11}(\Theta) = \left|f_{11}(\Theta)\right|^2 n_0 \quad (160)$$

$$P_{22}(\Theta) = \left|f_{22}(\Theta)\right|^2 n_0 \quad (161)$$

Hence, it is possible to see the DMRT-QCA like a correction to the classical Mie scattering. Indeed there is a modification in the $f_{ii}(\Theta)$ terms made by the average multipole amplitudes $X_n^{(M)}$ and $X_n^{(N)}$ which depends on the pair distribution functions and account for the dense medium properties. Moreover also the $P_{ii}(\Theta)$ components are corrected by a term proportional to the structure factor $h(\Theta)$ which accounts for the adhesive features of the scatterers.

By using the previous procedure, the phase matrix obtained is expressed in terms of the 1-2 system of reference. To solve the vector radiative transfer equations it needs to express $P_{ii}(\Theta)$ in the principal frame. The procedure to transform the phase matrix is the following. Let α_i be the angle which rotates anticlockwise $\hat{v}_i$ (the incidence vertical versor) to $\hat{1}_i$ and α_s the angle which rotates anticlockwise $\hat{v}_s$ (the scattering vertical versor) to $\hat{1}_s$. The transformation between the two systems of reference can be seen as a rotation around the axis [105, pp.35-36]. Thus, the transformation of the phase matrix can be obtained by

$$P(\theta_s,\varphi_s,\theta_i,\varphi_i) = \begin{bmatrix} \cos^2\alpha_s & \sin^2\alpha_s & -\frac{\sin 2\alpha_s}{2} & 0 \\ \sin^2\alpha_s & \cos^2\alpha_s & \frac{\sin 2\alpha_s}{2} & 0 \\ \sin 2\alpha_s & -\sin 2\alpha_s & \cos 2\alpha_s & 0 \\ 0 & 0 & 0 & 1 \end{bmatrix} \bullet \begin{bmatrix} P_{11}(\Theta) & 0 & 0 & 0 \\ 0 & P_{22}(\Theta) & 0 & 0 \\ 0 & 0 & P_{33}(\Theta) & P_{34}(\Theta) \\ 0 & 0 & P_{43}(\Theta) & P_{44}(\Theta) \end{bmatrix} \bullet \begin{bmatrix} \cos^2\alpha_i & \sin^2\alpha_i & \frac{\sin 2\alpha_i}{2} & 0 \\ \sin^2\alpha_i & \cos^2\alpha_i & -\frac{\sin 2\alpha_i}{2} & 0 \\ -\sin 2\alpha_i & \sin 2\alpha_i & \cos 2\alpha_i & 0 \\ 0 & 0 & 0 & 1 \end{bmatrix} \quad (162)$$

In Fig. 33 (a,b,c) a comparison between the scattering components of the DMRT-QCA for sticky particles and the Mie scattering is shown.

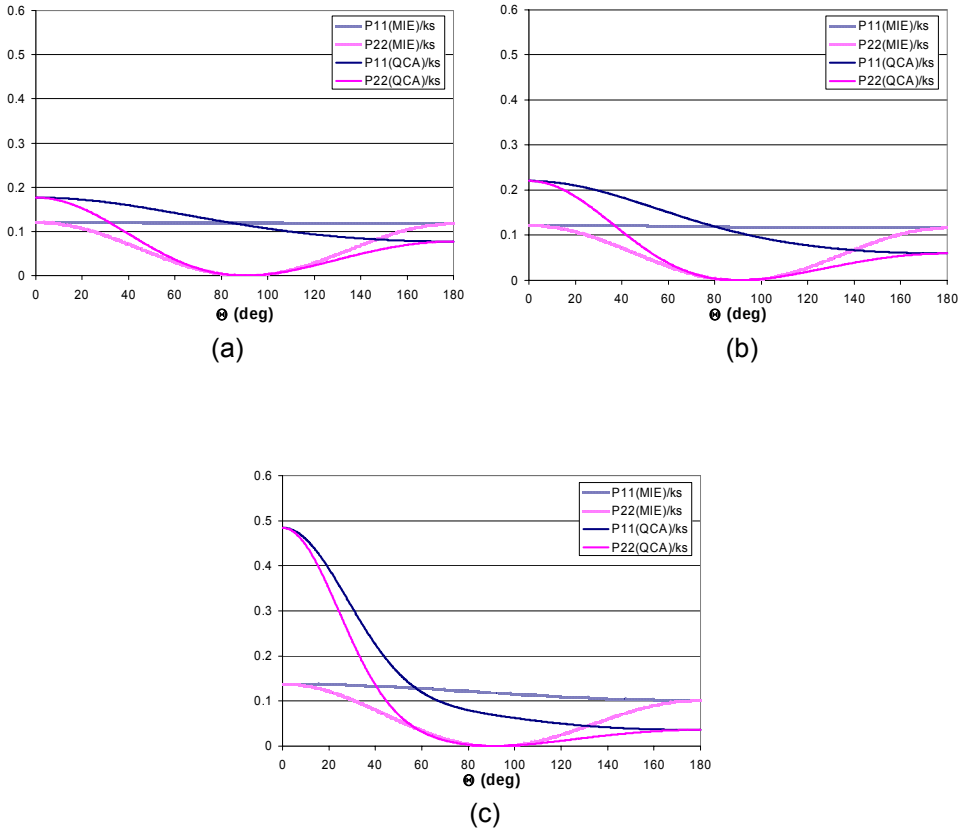

Fig. 33 – Comparison I of normalized phase scattering components for the DMRT-QCA and Mie scatterers as a function of Θ at (a) 13.4 GHz, (b) 17.5 GHz and (c) 37 GHz. The other parameters are f=0.25, grain radius=0.7mm, τ =0.1, ice permittivity=3.15+j0.001

It is clearly shown that the scattering predicted by the DMRT-QCA is mostly forward (Θ = 0°) at all frequency, especially at 37 GHz, whereas the Mie scattering is almost symmetrical.

3.3 Emission from a dry snow layer upon a rough soil

As stated in the previous sections, following a discrete approach dry snow can be modeled as a slab of random discrete spherical particles embedded in air upon a semi-infinite medium (the soil). The upper interface of the layer will be considered flat whereas the roughness of the snow-ground interface will be taken into consideration bistatic scattering coefficients. The procedure to obtain these terms will be outlined in the next paragraph. The rationale to consider flat the upper boundary is the following: at the air-snow interface, the roughness is extremely low and moreover the dielectric discontinuity is weak.

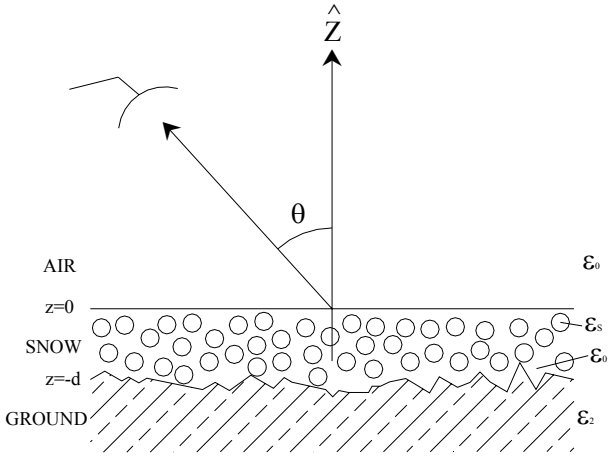

The structure of the model is depicted in Fig. 13 but for sake of convenience is also reported here. The observation angle is θ, ε_s is the permittivity of the spherical ice scatterers and ε_0 is the one of the host (air), ε_2 is the dielectric constant of the ground which is modeled as a semi-infinite medium, *d* is the thickness of the snowpack.

To calculate the brightness temperature of the snow, the radiative transfer equations have to be solved by imposing the boundary condition at the top and the bottom interfaces of the layer. In the following, the solution of the radiative transfer equations will be obtained by using the discrete ordinate-eigenanalysis technique.

For the media with a laminar structure, the scattering couples the specific intensity only in two directions: upwards (denoted by $I(\theta,z)$) and specularly downward at the same angle θ (denoted by $I(\pi-\theta,z)$). The general Vector Radiative Transfer (VRT) equations for one layer of scatterers can be written as [51][84].

$$\cos\theta\frac{d\vec{I}(\theta,\phi,z)}{dz}=-\overline{\overline{k_e}}(\theta,\phi)\vec{I}(\theta,\phi,z)+k_aC\vec{T}_1+ \\ +\int_0^{\pi/2}d\theta'\sin\theta'\int_0^{2\pi}d\phi'\cdot[\overline{\overline{P}}(\theta,\phi;\theta',\phi')\vec{I}(\theta',\phi',z)+ \\ +\overline{\overline{P}}(\theta,\phi;\pi-\theta',\phi')\vec{I}(\pi-\theta',\phi',z)] \tag{163}$$

$$-\cos\theta\frac{d\vec{I}(\pi-\theta,\phi,z)}{dz}=-\overline{\overline{k_e}}(\pi-\theta,\phi)\vec{I}(\pi-\theta,\phi,z)+k_aC\vec{T}_1+ \\ +\int_0^{\pi/2}d\theta'\sin\theta'\int_0^{2\pi}d\phi'\cdot[\overline{\overline{P}}(\pi-\theta,\phi;\theta',\phi')\vec{I}(\theta',\phi',z)+ \\ +\overline{\overline{P}}(\pi-\theta,\phi;\pi-\theta',\phi')\vec{I}(\pi-\theta',\phi',z)] \tag{164}$$

where $\bar{I}(\theta,\phi,z)$ is the specific intensity, k_e is the extinction coefficient, k_a is the absorption coefficient, T_1 is the thermodynamic temperature of the snow layer, P is the phase matrix of the discrete random medium. The first equation stands for the upward intensity and the latter is for the downward one. The procedure to compute k_e, k_a and P has been shown previously.

To solve equations (163)-(164) two boundary conditions must be imposed. They are:

$$\vec{I}(\pi-\theta,\phi,z=0)=\overline{\overline{R_{10}}}(\theta)\vec{I}(\theta,\phi,z=0) \quad \text{at z=0} \tag{165}$$

$$\vec{I}(\pi,\phi,z=-d)=\overline{\overline{R_{12}}}(\theta)\vec{I}_{oi}(\pi-\theta\ ,\phi\ ,z=-d)+\overline{\overline{T_{21}}}(\theta)C\vec{T}_2 \quad \text{at z=-d} \tag{166}$$

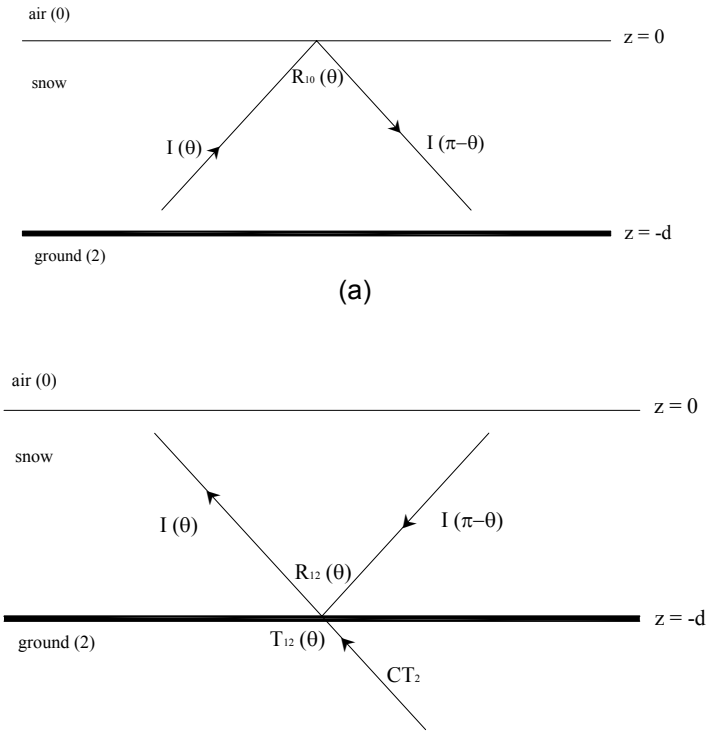

Fig. 34 - The boundary conditions at the upper (a) and lower interfaces (b)

In (165) $\overline{\overline{R_{10}}}(\theta)$ is the reflection coefficients matrix at the snow-air interface and in (166) $\overline{\overline{R_{12}}}(\theta)$ and $\overline{\overline{T_{21}}}(\theta)$ are respectively the snow-ground reflection and the ground-snow transmission matrices at the snow-ground boundary. The two

boundary conditions are depicted in Fig. 34. As stated before, the transmission and reflection matrices at the upper boundary are calculated via the Fresnel law whereas the ones at the bottom interface are calculate by integration of the bistatic scattering coefficients, computed through the AIEM, to account for the soil roughness.

To solve the previous set of equations it is useful to expand the Specific Intensity and the Phase matrix into a Fourier series as a function of the ϕ coordinate. The representations of these two quantities are

$$\vec{I}(z,\theta,\phi) = \bar{I}_0(\theta,z) + \sum_{m=1}^{\infty}[\bar{I}_{mc}(\theta,z)\cos m(\phi-\phi_{inc}) + \bar{I}_{ms}(\theta,z)\sin m(\phi-\phi_{inc})] \tag{167}$$

$$\bar{\bar{P}}(\theta,\phi,\theta',\phi') = \bar{\bar{P}}_0(\theta,\theta') + \sum_{m=1}^{\infty}[\bar{\bar{P}}_{mc}(\theta,\theta')\cos m(\phi-\phi_{inc}) + \bar{\bar{P}}_{ms}(\theta,\theta')\sin m(\phi-\phi_{inc})] \tag{168}$$

In the case of passive remote sensing of a layer composed by spherical scatterers overlying a soil with an azimuthal isotropic roughness autocorrelation function, the intensity vector has no ϕ dependence. Thus only the first terms of the (167) and (168) Fourier expansions (the 0th order solution) can be calculated by a simple integration

$$\bar{I}_0(\theta,z) = \frac{1}{2\pi}\int_{-\pi}^{\pi}\vec{I}(z,\theta,\phi)\ d\phi \tag{169}$$

$$\bar{\bar{P}}_0(\theta,\theta') = \frac{1}{2\pi}\int_{-\pi}^{\pi}\bar{\bar{P}}(\theta,\theta',\phi-\phi')\ d\phi-\phi' \tag{170}$$

Because we have supposed the soil to be azimuthal isotropic, in (170) the phase matrix depends on the angle ϕ-ϕ' instead of ϕ and ϕ' separately. Moreover, due to this kind of symmetry, the 3rd and the 4th components of the specific intensity vector are zero [51], hence the terms $\bar{I}_0(\theta,z)$ and $\bar{\bar{P}}_0(\theta,\theta')$ could be simply written as

$$\bar{I}_0(\theta,z) = \begin{bmatrix} I_v(\theta,z) \\ I_h(\theta,z) \end{bmatrix} \tag{171}$$

$$\bar{\bar{P}}_0(\theta,\theta') = \begin{bmatrix} P_{vv}(\theta,\theta') & P_{vh}(\theta,\theta') \\ P_{hv}(\theta,\theta') & P_{hh}(\theta,\theta') \end{bmatrix} \tag{172}$$

The VRT equations can be rearranged as

$$\cos\theta\frac{d\bar{I}_0(\theta,z)}{dz} = -\bar{\bar{k}}_e\ \bar{I}_0(\theta,z) + k_a C\vec{T}_1 + \int_0^{\pi/2} d\theta'\sin\theta'[\bar{\bar{P}}_0(\theta,\theta')\bar{I}_0(\theta',z) + \bar{\bar{P}}_0(\theta,\pi-\theta')\bar{I}_0(\pi-\theta',z)] \tag{173}$$

$$-\cos\theta\frac{d\bar{I}_0(\pi-\theta,z)}{dz}=-\bar{\bar{k}}_e\,\bar{I}_0(\pi-\theta,z)+k_a C\vec{T}_1+\int_0^{\pi/2}d\theta'\sin\theta'[\bar{\bar{P}}_0(\pi-\theta,\theta')\bar{I}_0(\pi-\theta',z)+ \quad (174)$$

$$+\bar{\bar{P}}(\pi-\theta,\pi-\theta')\bar{I}_0(\pi-\theta',z)]$$

(173)-(174) represent a set of four integral equations which can be solved analytically only in a few cases. There are two numerical methods applied successfully: the matrix doubling [65],[51] and the discrete order-eigenanalysis solution [51]. This latter is very simple, especially for the single layer case. However, the random medium must be “homogeneous” with only one type of pair distribution functions and without gradients inside the snowpack. Conversely, the matrix doubling allows one considering the vertical profiles of all the snow parameters (temperature, grain radius, fractional volume, etc) but it is more complicated.

In order to solve the (173)-(174) equations with the discrete order method it is mandatory to discretized the integrals and obtain a new set of 2n independent equations which will be solved by means of the eigenvalues analysis. An *n*-point Gaussian quadrature rule, is a quadrature rule constructed to yield an exact result for polynomials of degree 2*n* − 1, by a suitable choice of the *n* points x_i and *n* weights w_i. The domain of integration for such a rule is conventionally taken as [−1, 1], and the integral could be approximated by

$$\int_{-1}^{1} f(x)\ dx \approx \sum_{i=1}^{n} w_i f(x_i) \quad (175)$$

Because the limits of the integrals in (169)-(170) are not 1 and -1, the previous equation must be rewritten as

$$\int_a^b f(x)\ dx=\frac{b-a}{2}\int_{-1}^{1} f\left(\frac{b-a}{2}x+\frac{a+b}{2}\right)dx\approx\frac{b-a}{2}\sum_{i=1}^{n} w_i f\left(\frac{b-a}{2}x_i+\frac{a+b}{2}\right) \quad (176)$$

For the Gaussian quadrature rule, the associated polynomials are Legendre polynomials, $P_n(x)$. With the n^{th} polynomial normalized to give $P_n(1) = 1$, the i^{th} Gauss node, x_i, is the i^{th} root of P_n; its weight is given by (Abramowitz & Stegun 1972, p. 887)

$$w_i=\frac{2}{(1-x_1^2)(P'_n(x_i))^2} \quad (177)$$

Let μ_j be the 2*n* zeroes of the even order Legendre polynomial function $P_{2n}(\mu)$ and a_j are the weighting coefficients. Thus there are a total of 2*n* values both for μ_j and a_j which obey the relations

$$\begin{aligned} a_j &= a_{-j} \\ \mu_j &= -\mu_j \end{aligned} \qquad j=\pm1,\ \pm2,\ \pm3,....,\ \pm n \quad (178)$$

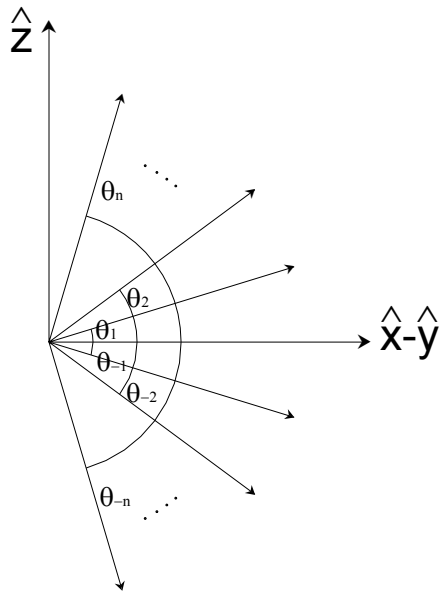

Fig. 35 - The quadrature angles represented in the principal frame

By letting μ'=cosθ' (the θ' angles are depicted in Fig. 35) the integral equations can be approximated by means of the quadrature formula giving a set of 2*n* equations. The (173) can be rewritten as

$$\mu_i \frac{d}{dz}\begin{bmatrix} I_{vi}(z) \\ I_{hi}(z) \end{bmatrix}_{\theta} = -k_{ei}\begin{bmatrix} I_{vi}(z) \\ I_{hi}(z) \end{bmatrix} + \sum_{j=-N}^{N} a_j \begin{bmatrix} (v_i, v_j) & (v_i, h_j) \\ (h_i, v_j) & (h_i, h_j) \end{bmatrix}\begin{bmatrix} I_{vj}(z) \\ I_{hj}(z) \end{bmatrix} + k_a CT_1 \begin{bmatrix} 1 \\ 1 \end{bmatrix} \qquad (179)$$

$$j = \pm 1,\ \pm 2,\ \pm 3, ..., \pm n$$

where

$$I_{\beta i}(z) = I_{\beta}(\mu_i, z) \qquad (180)$$

$$(\alpha_i, \beta_j) = P_{\alpha\beta}(\theta_i, \theta_j) \qquad \alpha, \beta = v, h \qquad (181)$$

The choice of the order *n* of the quadrature formula is intrinsically related to the rate of angular variation of the phase matrix. The smoother the variations are the lower the order that must be chosen. For instance, in the case of Rayleigh scattering, *n*=8 is a good choice [51].

The use of Gaussian quadrature is essential because it makes phase function renormalization unnecessary, implying that energy is conserved in the computation [39]. The (179) represents a set of 4*n* equations: 2*n* to account for the up-going and down-going intensities and 2*n* to account for the V and H polarizations.

To solve (179) for the homogeneous solution let

$$I_{\beta\, i}(z) = I_{\beta\, i} e^{\alpha\, z} \tag{182}$$

Substituting the previous equation in (179) it is easy to obtain 4*n* equations useful to determine the 4*n* eigenvalues of α and the corresponding eigenvectors. In a matrix formulation it is:

$$\begin{cases} \alpha \overline{\overline{\mu}} \cdot \bar{I}_u = -\overline{\overline{k}}_e \cdot \bar{I}_u + \overline{\overline{F}} \cdot \overline{\overline{a}} \cdot \bar{I}_u + \overline{\overline{B}} \cdot \overline{\overline{a}} \cdot \bar{I}_d \\ -\alpha \overline{\overline{\mu}} \cdot \bar{I}_d = -\overline{\overline{k}}_e \cdot \bar{I}_d + \overline{\overline{B}} \cdot \overline{\overline{a}} \cdot \bar{I}_u + \overline{\overline{F}} \cdot \overline{\overline{a}} \cdot \bar{I}_d \end{cases} \tag{183}$$

Where $\bar{I}_u$ and $\bar{I}_d$ represent respectively the upward and downward specific intensities and are vectors of rank 2*n*

$$\bar{I}_u = \begin{bmatrix} I_{v1} \\ \vdots \\ I_{vn} \\ I_{h1} \\ \vdots \\ I_{hn} \end{bmatrix} \quad ; \quad \bar{I}_u = \begin{bmatrix} I_{v1} \\ \vdots \\ I_{vn} \\ I_{h1} \\ \vdots \\ I_{hn} \end{bmatrix} \tag{184}$$

Both $\overline{\overline{\mu}}$, $\overline{\overline{k}}_e$ and $\overline{\overline{a}}$ are diagonal 2*n* x 2*n* matrices represented by

$$\overline{\overline{\mu}} = \begin{bmatrix} \mu_1 & 0 & 0 & 0 & 0 & 0 \\ 0 & \ddots & 0 & 0 & 0 & 0 \\ 0 & 0 & \mu_n & 0 & 0 & 0 \\ 0 & 0 & 0 & \mu_1 & 0 & 0 \\ 0 & 0 & 0 & 0 & \ddots & 0 \\ 0 & 0 & 0 & 0 & 0 & \mu_n \end{bmatrix} \tag{185}$$

$$\overline{\overline{k}}_e = \begin{bmatrix} k_{ev1} & 0 & 0 & 0 & 0 & 0 \\ 0 & \ddots & 0 & 0 & 0 & 0 \\ 0 & 0 & k_{evn} & 0 & 0 & 0 \\ 0 & 0 & 0 & k_{eh1} & 0 & 0 \\ 0 & 0 & 0 & 0 & \ddots & 0 \\ 0 & 0 & 0 & 0 & 0 & k_{ehn} \end{bmatrix} \tag{186}$$

$$\overline{\overline{a}} = \begin{bmatrix} a_1 & 0 & 0 & 0 & 0 & 0 \\ 0 & \ddots & 0 & 0 & 0 & 0 \\ 0 & 0 & a_n & 0 & 0 & 0 \\ 0 & 0 & 0 & a_1 & 0 & 0 \\ 0 & 0 & 0 & 0 & \ddots & 0 \\ 0 & 0 & 0 & 0 & 0 & a_n \end{bmatrix} \tag{187}$$

The matrices $\overline{\overline{F}}$ and $\overline{\overline{B}}$ are the forward and backward scattering phase matrices and are expressed by

$$\overline{\overline{F}} = \begin{bmatrix} (v_1, v_1) & \cdots & (v_1, v_n) & (v_1, h_1) & \cdots & (v_1, h_n) \\ \vdots & & \vdots & \vdots & & \vdots \\ (v_n, v_1) & \cdots & (v_n, v_n) & (v_n, h_1) & \cdots & (v_n, h_n) \\ (h_1, v_1) & \cdots & (h_1, v_n) & (h_1, h_1) & \cdots & (h_1, h_n) \\ \vdots & & \vdots & \vdots & & \vdots \\ (h_n, v_1) & \cdots & (h_n, v_n) & (h_n, h_1) & \cdots & (h_n, h_n) \end{bmatrix} \tag{188}$$

$$\overline{\overline{B}} = \begin{bmatrix} (v_1, v_{-1}) & \cdots & (v_1, v_{-n}) & (v_1, h_{-1}) & \cdots & (v_1, h_{-n}) \\ \vdots & & \vdots & \vdots & & \vdots \\ (v_n, v_{-1}) & \cdots & (v_n, v_{-n}) & (v_n, h_{-1}) & \cdots & (v_n, h_{-n}) \\ (h_1, v_{-1}) & \cdots & (h_1, v_{-n}) & (h_1, h_{-1}) & \cdots & (h_1, h_{-n}) \\ \vdots & & \vdots & \vdots & & \vdots \\ (h_n, v_{-1}) & \cdots & (h_n, v_{-n}) & (h_n, h_{-1}) & \cdots & (h_n, h_{-n}) \end{bmatrix} \tag{189}$$

Due to the spherical symmetry of the scatterers, also the phase functions are symmetrical and

$$(\alpha_i, \beta_j) = (\alpha_{-i}, \beta_{-j}) \qquad \alpha, \beta = v, h \tag{190}$$

Hence both $\overline{\overline{F}}$ and $\overline{\overline{B}}$ are symmetric matrices.

For a numerical solution of the problem, it could be useful to reduce the number of equations and this could be done by letting

$$\begin{aligned} \overline{I}_+ &= \overline{I}_u + \overline{I}_d \\ \overline{I}_- &= \overline{I}_u - \overline{I}_d \end{aligned} \tag{191}$$

By adding and subtracting (183) we obtain

$$\begin{aligned}\alpha\overline{\overline{\mu}}\cdot\overline{I}_{-} &= \overline{\overline{A}}\cdot\overline{I}_{+}\\ \alpha\overline{\overline{\mu}}\cdot\overline{I}_{+} &= \overline{\overline{W}}\cdot\overline{I}_{-}\end{aligned} \tag{192}$$

Where

$$\begin{aligned}\overline{\overline{A}} &= -\overline{\overline{k}}_e + \overline{\overline{F}}\cdot\overline{\overline{a}} + \overline{\overline{B}}\cdot\overline{\overline{a}}\\ \overline{\overline{W}} &= -\overline{\overline{k}}_e + \overline{\overline{F}}\cdot\overline{\overline{a}} - \overline{\overline{B}}\cdot\overline{\overline{a}}\end{aligned} \tag{193}$$

Combining the displayed equation in (192) it is possible to obtain the following equation which must be solved by the eigenanalysis

$$(\overline{\overline{\mu}}^{-1}\cdot\overline{\overline{W}}\cdot\overline{\overline{\mu}}^{-1}\cdot\overline{\overline{A}} - \alpha^2)\cdot\overline{I}_{+} = 0 \tag{194}$$

The previous equation has 2*n* eigenvalues $\alpha_1^2, \alpha_2^2, ..., \alpha_{2n}^2$ and 2*n* eigenvectors $\overline{I}_{1+}, \overline{I}_{2+}, ..., \overline{I}_{2n+}$. The final solution is written as

$$\overline{I}_{+} = \sum_{l=1}^{2n}\left\{ P_l\overline{I}_{+l}\ e^{\alpha_l z} + P_{-l}\overline{I}_{+l}\ e^{-\alpha_l(z+d)}\right\} \tag{195}$$

The constants P_l and P_{-l} must be determined by imposing the boundary conditions. Also $\overline{I}_{-}$ can be determined by (192). Denoting the homogenous solution with “H” it has

$$\overline{I}_u^H = \frac{1}{2}\sum_{l=1}^{2n}\left\{ P_l\left(1+\frac{1}{\alpha_l}\overline{\overline{\mu}}^{-1}\cdot\overline{\overline{A}}\right)\overline{I}_{+l}\ e^{\alpha_l z} + P_{-l}\left(1-\frac{1}{\alpha_l}\overline{\overline{\mu}}^{-1}\cdot\overline{\overline{A}}\right)\overline{I}_{+l}\ e^{-\alpha_l(z+d)}\right\} \tag{196}$$

$$\overline{I}_d^H = \frac{1}{2}\sum_{l=1}^{2n}\left\{ P_l\left(1-\frac{1}{\alpha_l}\overline{\overline{\mu}}^{-1}\cdot\overline{\overline{A}}\right)\overline{I}_{+l}\ e^{\alpha_l z} + P_{-l}\left(1+\frac{1}{\alpha_l}\overline{\overline{\mu}}^{-1}\cdot\overline{\overline{A}}\right)\overline{I}_{+l}\ e^{-\alpha_l(z+d)}\right\}$$

The particular solutions for equations (179) is denoted by the superscript P and is

$$\overline{I}_u^p = \overline{I}_d^p = C\overline{T}_1 \tag{197}$$

where $\overline{T}_1$ is a vector of rank 2*n* in which each component is equal to the snow thermodynamic temperature T_1.

As stated before, to obtain the constants P_l and P_{-l}, l=1,2,..2n, the boundary conditions must be imposed. For sake of convenience they are reported also here

$$\overline{I}_d(z=0) = \overline{I}(\pi-\theta,\phi,z=0) = \overline{\overline{R}}_{10}(\theta)\overline{I}(\theta,\phi,z=0) = \overline{\overline{R}}_{10}\cdot\overline{I}_u(z=0) \tag{198}$$

$$\bar{I}_u(z=-d)=\bar{I}(\pi,\phi,z=-d)=\bar{\bar{R}}_{12}(\theta)\bar{I}(\pi-\theta\ ,\phi\ ,z=-d)$$
$$+\bar{\bar{T}}_{12}(\theta)C\bar{T}_2=\bar{\bar{R}}_{12}\cdot\bar{I}_d(z=-d)+\bar{\bar{T}}_{12}\cdot C\bar{T}_2 \quad (199)$$

where

$$\bar{\bar{R}}_{10}=diag[r_{v10_1},\ r_{v10_2},\ ....,r_{v10_n},\ r_{h10_1},\ r_{h10_2},\ ....,r_{h10_n}]$$
$$\bar{\bar{R}}_{12}=diag[r_{v12_1},\ r_{v12_2},\ ....,r_{v12_n},\ r_{h12_1},\ r_{h12_2},\ ....,r_{h12_n}] \quad (200)$$
$$\bar{\bar{T}}_{12}=diag[t_{v12_1},\ t_{v12_2},\ ....,t_{v12_n},\ t_{h12_1},\ t_{h12_2},\ ....,t_{h12_n}]$$

The vector $\bar{T}_2$ is like $\bar{T}_1$ but with the temperature of the soil. Each component $r_{\alpha pq_i}$ of the (200) matrices must be read as: reflection coefficient (*r*) , from medium *q* to medium *p*, i^{th} quadrature angle. *t* denotes the transmission coefficient.

The brightness temperature $\bar{T}_B$ observed in region 0 can be eventually obtained from:

$$\bar{T}_B(\theta_{i0})=\frac{1}{C}\bar{\bar{T}}_{10}\cdot\bar{I}_u(z=0)=\frac{1}{C}\bar{\bar{T}}_{10}\cdot\left\{\bar{I}_u^H(z=0)+C\bar{T}_1\right\} \quad (201)$$

3.3.4 Computation of the reflection coefficients

To solve the vector radiative transfer equations, boundary conditions at the upper and lower interfaces must be imposed. They are

$$\bar{I}_d(z=0)=\bar{I}(\pi-\theta,\phi,z=0)=\bar{\bar{R}}_{10}(\theta)\bar{I}(\theta,\phi,z=0)=\bar{\bar{R}}_{10}\cdot\bar{I}_u(z=0) \quad (202)$$

$$\bar{I}_u(z=-d)=\bar{I}(\pi,\phi,z=-d)=\bar{\bar{R}}_{12}(\theta)\bar{I}(\pi-\theta\ ,\phi\ ,z=-d)$$
$$+\bar{\bar{T}}_{12}(\theta)C\bar{T}_2=\bar{\bar{R}}_{12}\cdot\bar{I}_d(z=-d)+\bar{\bar{T}}_{12}\cdot C\bar{T}_2 \quad (203)$$

Each component of $\bar{\bar{R}}_{ab}$ and $\bar{\bar{T}}_{ab}$ is a reflection coefficient or a transmit one which must be calculated depending on the roughness of the surface. As stated previously, in the present model we have supposed that, as frequently happens in alpine regions the interface at the air-snow boundary is flat, whereas the interface between the snow and the ground is rough.

The Fresnel reflection coefficients for V and H polarizations are expressed by

$$R_v=\frac{\eta_2\cos\theta_1-\eta_1\cos\theta_2}{\eta_2\cos\theta_1+\eta_1\cos\theta_2} \quad (204)$$

$$R_h=\frac{\eta_1\cos\theta_1-\eta_2\cos\theta_2}{\eta_1\cos\theta_1+\eta_2\cos\theta_2} \quad (205)$$

where η_a, θ_a, a=1,2 are the refractive index and the angle in the a medium. θ_1 and θ_2 are related by the Snell's law.

To calculate the reflection coefficients taking into account the soil roughness the equivalent reflectivity must be computed by means of

$$\Gamma_r(\theta,\phi) = \frac{1}{4\pi}\int_0^{2\pi}\int_0^{\frac{\pi}{2}}\left[\gamma_{rr}(\theta_s,\phi_s,\theta,\phi)+\gamma_{tr}(\theta_s,\phi_s,\theta,\phi)\right]\sin\theta_s\, d\theta_s d\phi_s \qquad (206)$$

$$t,r = v,h$$

where the scattering coefficients γ_{rr} and γ_{tr} are obtained from the AIEM model and, considering azimuthally isotropic surfaces, ϕ can be set to zero.

Eventually, the R reflection coefficient is the square root of the reflectivity.

3.4 Modeling snow containing free liquid water (wet snow)

To study the microwave emission of wet snow (i.e. a snowpack which contains free liquid water), it is almost useless to adopt a sophisticated model like the DMRT coupled with the AIEM because the penetration depth of e.m. waves in such medium is very shallow (of the order of a few centimeters at C-band). Moreover, the DMRT equations for a multi-species medium (like water droplets and ice crystals embedded in the air) are very difficult to solve and the computational time required can be too high. Another issue to be considered is the physical process involved in the melting/refreezing of snow (Fig. 36). Usually snow starts to melt when the temperature of the air is above 0°C and the sunlight impinges on the snowpack. In these conditions the thermal wave starts to slowly propagate into the medium and the snow starts to melt from the top to the bottom (Fig. 36 (a)). The refreezing phase happens when the air temperature is below 0°C (usually from dusk to dawn, Fig. 36 (b)), and the liquid water return to solid state. It should be noted that the refreezing can be complete or not: e.g. it is possible that the deepest layers of the snowpack remain moist because the air has not been enough cold during the night. Considering that the emission of a cloud of water particles can be very high (even close to that of a black-body) it is plain how the microwave brightness temperature of wet snow is driven by the LWC.

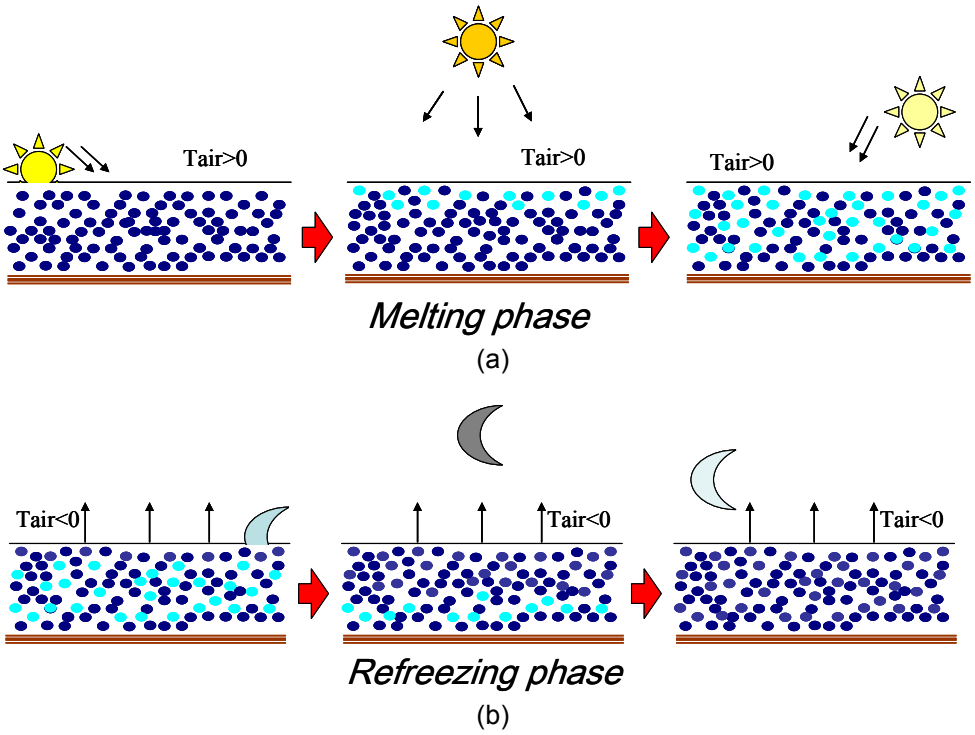

Fig. 36 - The melting and refreezing processes of snow. Ice crystals are depicted in dark blue while liquid water droplets are in light blue. (a) represents the melting phase from sunrise (on the left) to sunset (on the right). (b) represents the refreezing phase during the night. The arrows indicate the thermal flux.

The Strong Fluctuation Theory has proved to be very good in modeling the e.m. behavior of wet snow and represents a good trade-off between accuracy and computational time. Moreover, to model the "layered" behavior of the melting/refreezing processes, a multilayer method like the one in chapter 2 can be used.

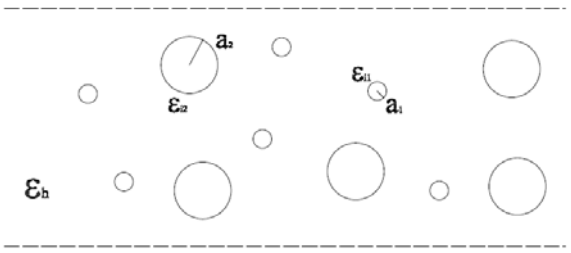

Fig. 37 - The structure of wet snow like modeled in the SFT

As stated previously, the SFT let the dense medium to be homogeneous and consider the scatterers like fluctuation of the permittivity. In the Weak Fluctuation Theory the permittivity is written as

$$\begin{aligned}
&\varepsilon(\underline{r}) = \varepsilon_m + \varepsilon_f(\underline{r}) \\
&\varepsilon_m = \left\langle \varepsilon(\underline{r}) \right\rangle \\
&\left\langle \varepsilon_f(\underline{r}) \right\rangle = 0 \\
&\left\langle \varepsilon_f(\underline{r}) \varepsilon_f(\underline{r}') \right\rangle = \delta\, \varepsilon_m^2\, R(\underline{r} - \underline{r}')
\end{aligned} \tag{207}$$

where the angular brackets stands for spatial average, δ is the normalized variance and *R* is the normalized correlation function of the dielectric constant. Instead the SFT use a different (and more effective) approach to represent the permittivity

$$\varepsilon(\underline{r}) = \varepsilon_g + \varepsilon'_f(\underline{r}) \tag{208}$$

where ε_g is the auxiliary permittivity which is valid in the low-frequency limit (where the e.m. interactions between two particles is negligible) and $\varepsilon'_f(\underline{r})$ is the random fluctuation.

By using this decomposition, the wave equation can be written as

$$\underline{\nabla} \times \underline{\nabla} \times \underline{E} - k_0^2 \frac{\varepsilon_g}{\varepsilon_0} \underline{E} = k_0^2 \left(\frac{\varepsilon(\underline{r}) - \varepsilon_g}{\varepsilon_0} \right) \underline{E} \tag{209}$$

Solving (209) (the procedure is outlined in appendix 2) it is possible to obtain the effective permittivity of the snow medium

$$\varepsilon_{eff} \cong \varepsilon_g + j\, k_g\, k_0^2\, \varepsilon_0\, 2 \left(\frac{\varepsilon_g}{\varepsilon_0} \right)^2 \left\{ \left(f_{s1} r_{s1}^2 + f_{s2} r_{s2}^2 + f_b r_b^2 \right) a_1^3 + r_{s2}^2\, f_{s2} \left(1 + f_{s2} \right) \left(a_2^3 - a_1^3 \right) \right\} \tag{210}$$

where

$$r_{ice} = \frac{\varepsilon_{ice} - \varepsilon_g}{\varepsilon_{ice} + 2\varepsilon_g}; \quad r_{water} = \frac{\varepsilon_{water} - \varepsilon_g}{\varepsilon_{water} + 2\varepsilon_g}; \quad r_{host} = \frac{\varepsilon_{host} - \varepsilon_g}{\varepsilon_{host} + 2\varepsilon_g} \tag{211}$$

and f_{ice}, f_{water}, f_{host} are bounded together by $f_{ice} + f_{water} + f_{host} = 1$

The auxiliary permittivity can be obtained by solving

$$\sum_{p=1}^{n} \frac{\varepsilon_{ice} - \varepsilon_g}{\varepsilon_{ice} + 2\varepsilon_g} f_p = 0 \tag{212}$$

which is equivalent to the Polder-Van Santen mixing formula.

4. EXPERIMENTAL RESULTS AND COMPARISON WITH SIMULATIONS

The description of the interaction between electromagnetic waves and natural targets is one of the most difficult tasks of the research. The main reason resides in the intrinsic randomness of natural environment. While it can be simple to describe artificial targets (which usually have a well-defined geometry and electric properties), Earth surfaces are quite difficult to characterize. The best way to check the performances of the models is to compare the analytical estimations with measurements taken on natural (or semi-natural) targets.

In [122] a large dataset of radar measurements taken on snowcovers on the Swiss Alps is published. In [18] fields measurements of microwave emission from snow covered soil taken on several test sites in Italy are shown. Macelloni *et al*. [22] [123] investigated the melting-freezing processes of the snow by means of long time series of the brightness temperature at several frequencies. Some measurements have been taken also on artificial targets to simulate soils with a pre-determined surface roughness [66]. In [124] is presented a long time series of measurements taken on dry snow during the 2006/2007 winter season by the Microwave Remote Sensing Group of the IFAC. These measurements have been used during the codification of the dry snow model for a preliminary validation.

4.1 Comparison of the snow emission model with experimental data

The Microwave Remote Sensing Group of the Institute for Applied Physics of the Italian National Research Council (IFAC-CNR) has performed several experiments on the snow cover surfaces under the most common conditions. The aims of these investigations were to understand the relationships between the microwave emission and the physical properties of terrains covered by snow with or without vegetation. The datasets obtained are very extensive and includes both electromagnetic and synoptic direct measurements of the media parameters (e.g. height, density, temperature and crystal characteristics of the snowpack).

It is worth pointing out that, conversely from the surface scattering, it is very difficult to validate the volume scattering models (like the DMRT-QCA or SFT) against numerical datasets. Indeed, the only way to obtain such dataset is to perform a Montecarlo analysis: numerically solve the Maxwell equations for a huge number of scatterers configurations. This technique requires a computer with a very high computational power and for this reason has been rarely used. Thus, the use of experimental dataset is almost mandatory.

4.1.1 The IFAC remote sensing equipment and experiments

The remote sensing data were collected by means of a Radiometer set measuring thermal emission at several different microwave frequencies: from 1.413 GHz up to 37 GHz and in the thermal infrared (8-14 μm) band. The microwave sensors measured the horizontal and vertical polarization components of brightness temperature with an accuracy of ±0.5 K, at incidence angles between 30 and 70 degrees. The instruments were portable, self-calibrated systems with a dual

polarization horn antenna for each frequency channel and an internal calibration based on two loads at different temperatures (250 K ±0.2 K and 370 K ± 0.2 K). The calibrated output digital signals were recorded on a notebook computer together with temperatures of calibrating loads. Calibration checks in the range 30 K - 300 K are always carried out during the field experiments by means of absorbing panels of known emissivity and temperature (Eccosorb AN74 and VHP8), and observing clear sky with a calibrated noise source coupled to the antenna. Background emission is periodically measured by means of a reflecting plate placed above the target and subtracted from the total emission. The achieved measurement accuracy (repeatability) has proven to be better than ±1.0 K, with an integration time of 1 sec. The beamwidth of the corrugated conical horns is 20° at -3 dB and 56° at -20 dB for both frequencies and both polarizations. The sensors were installed on a shelter placed directly on the snow (Fig. 38) or on a snowmobile. The observation geometry (distance between antenna and target) is arranged to meet the conditions of far field operation at an observation angle θ = 30° from a minimum height of 140 cm. The FOV ranged from 0.6x0.6 m^2 at θ = 30° incidence angle to 2x2 m^2 at θ = 70°. The infrared sensor, a commercial type hand-held radiometer with accuracy (repeatability) of ± 0.5 K, is placed on the same boresight of microwave radiometers. Microwave emissivity is approximated by normalizing the brightness temperature to the thermometric temperature at 10 cm depth.

Fig. 38 – The microwave instruments shelter placed on the Mount Cherz test site during the 2002/2003 winter season. In the foreground it is possible to see a profilometer for the roughness measurements

4.1.2 The Morsex (Microwave and Optical Remote Sensing experiment) dataset

Field measurements of microwave emission from soil covered with snow were carried out from 1996 until 1999 on the Italian Alps and Apennines on various test

sites at different elevations in order to represent situations of varying snow cover conditions including dry snow at high density with rounded polycrystals, low density fresh/dry snow, and finally a typical spring situation of wet snow with rounded particles, high surface density and a very low consistence. In each test site the composition of the strongly stratified snow pack was analyzed according to the standards of the International Commission on Snow and Ice [125].
The test sites (depicted in Fig. 39) were selected in order to have a flat surface with sufficient extension, homogeneity and horizon free to guarantee the same conditions for the antenna footprints at all the observation angles.

(a)

(b)

Fig. 39 - The locations of the three test sites on the Eastern Italian Alps. In (a) is depicted the Campolongo pass and in (b) the passo Valles and Zingari alti test sites. (from Google Earth)

4.1.2.1 Comparison between the snow model and the Morsex dataset of dry snow

The Morsex radiometric dataset was used to validate the IRIDE snow model and to test his capability to simulate the microwave emission before use it for a sensitivity analysis and to better understand the interaction between the electromagnetic waves and the snow medium.

The first comparison between measured and simulated data was made as a function of the observation angle. Three different snowpacks were taken into consideration corresponding to three different alpine test sites. The measurements were carried out at 6.8, 10 and 37 GHz. The input parameters of the model are depicted in Tab. 4. As outlined previously, the snow data were derived from ground measurements except for the grain size, which was used as a fitting parameter, while the soil parameters were obtained from fitting the C-band radiometric data. The 1.5-power autocorrelation function was chosen because it better represents the soil roughness over such large scale of roughness.

Tab. 4 – Input parameters to the IRIDE model for the simulation of the Morsex dataset

Input parameters

	Campolongo Pass	Valles	Zingari Alti
Snow			
Temperature (K)	266	266	266
Depth (m)	0.67	1.19	1.16
Fractional volume	0.3	0.3	0.3
Particle diameter (mm)	0.8 @ 6.8,10 GHz 0.45 @ 37 GHz	0.7 @ 6.8,10 GHz 0.4 @ 37 GHz	0.7 @ 6.8,10 GHz 0.4 @ 37 GHz
Stickiness	0.1	0.1	0.1
Soil			
Permittivity	4+j1	6+j2	5+j1
HSdtD (cm)	0.7	0.5	0.5
Correlation length (cm)	12	12	12
ACF	1.5 power		

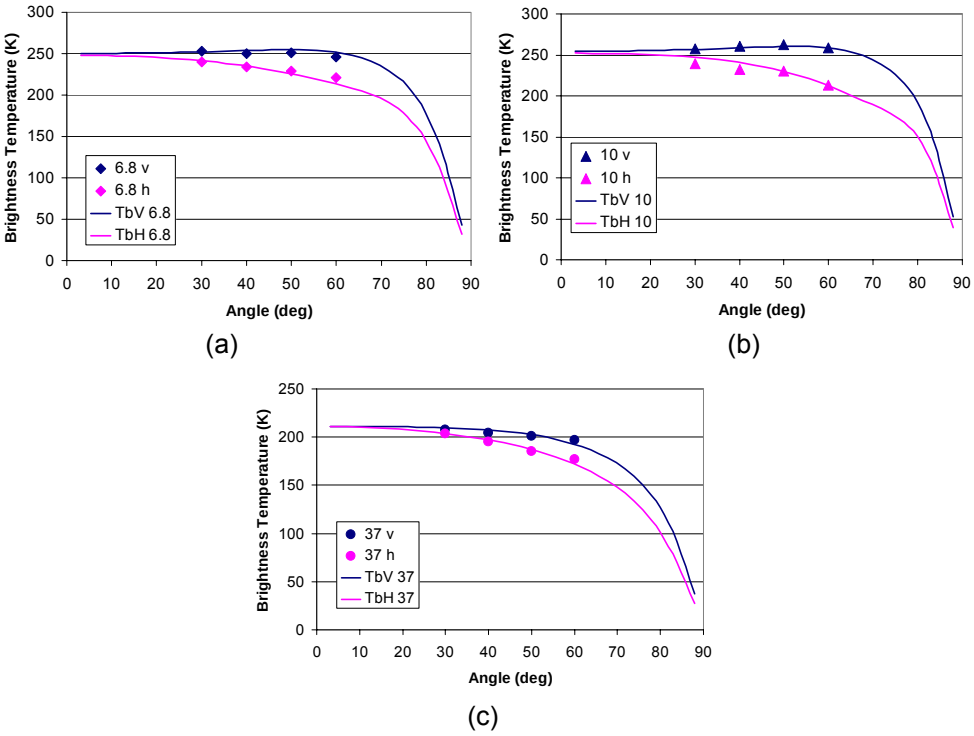

Fig. 40 - Comparison between simulated (continuous line) and measured (dots) brightness temperatures of dry snow at (a) 6.8 GHz, (b) 10 GHz and (c) 37 GHz. Experimental data are taken on the Campolongo Pass test site. Input parameters for the snow model are shown in Tab. 4

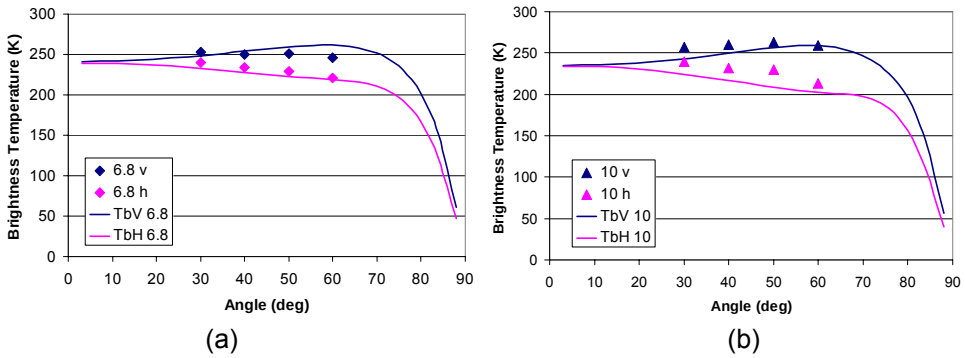

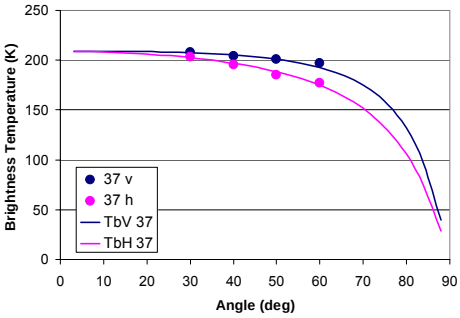

(c)

Fig. 41 - Comparison between simulated (continuous line) and measured (dots) brightness temperatures of dry snow at (a) 6.8 GHz, (b) 10 GHz and (c) 37 GHz. Experimental data are taken on the Valles test site. Input parameters for the snow model are shown in Tab. 4.

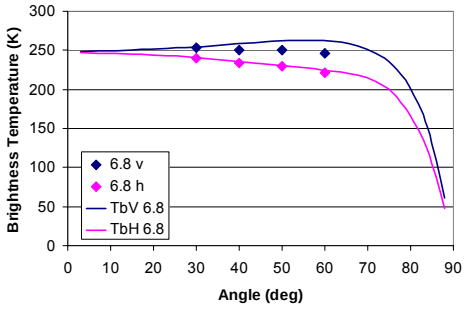

(a)

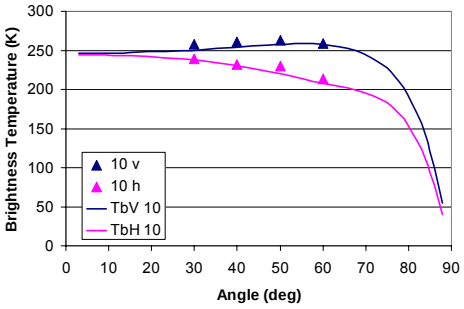

(b)

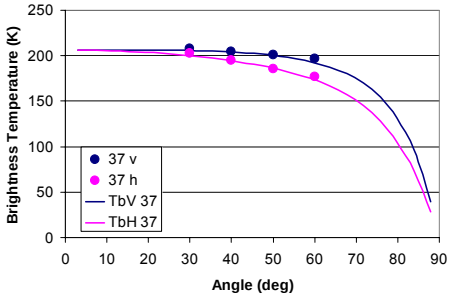

(c)

Fig. 42 - Comparison between simulated (continuous line) and measured (dots) brightness temperatures of dry snow at (a) 6.8 GHz, (b) 10 GHz and (c) 37 GHz. Experimental data are taken on the Zingari alti test site. Input parameters for the snow model are shown in Tab. 4

Figures 40-42 show the comparisons between snow model simulations and microwave measurements taken on Campolongo, Passo Valles and Zingari Alti test sites. The snow was everywhere dry thick and quite stratified, even if this latter feature does not affect very much the brightness temperature of alpine dry snow at C- and X-band. The agreement between the measured and simulated data is very good for the three test sites and improved with respect to other models [18]. It is worth pointing out that for the lowest frequency, the emission of the soil is predominant.

In addition to the measurements as a function of the observation angle, the relationship between brightness temperature and the snow water equivalent (SWE) was investigated. The SWE is defined by

$$SWE = \int_0^d \rho(z)\, dz \approx \overline{\rho}\, z \qquad (213)$$

where $\overline{\rho}$ is the mean density. The last part of the equation holds exactly only for homogeneous snowpack.

The relationship between measured and simulated brightness temperatures as a function of SWE is represented in Fig. 43. The two frequencies considered are the 10 and 37 GHz at V polarization and the observations are made at 40 deg incidence angle. The inputs for the model were the same as used in the previous simulations (see Tab. 4). Also in this case the agreement is very good over a wide range of SWE.

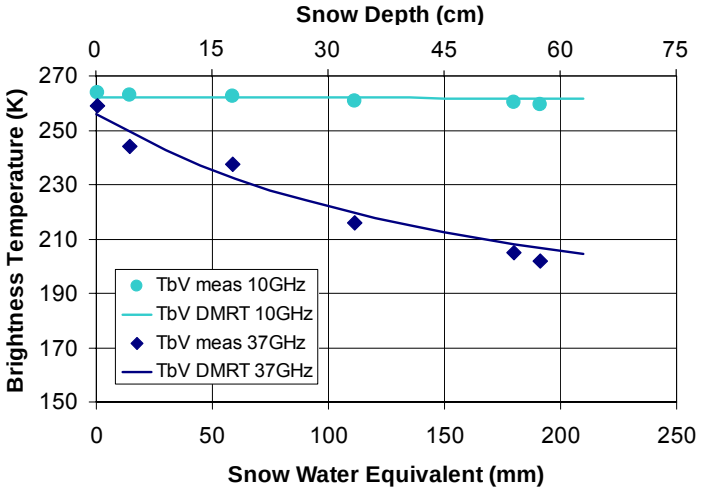

Fig. 43 - Comparison between measured (dots) and simulated (lines) brightness temperature as a function of snow water equivalent and snow depth at 40° observation angle for a mean fractional volume of 0.3. The experimental data are taken on the Campolongo Pass test sites.

4.2 The effect of the liquid water on the emission of snow

During the 2002/2003 winter season, the Microwave Remote Sensing Group of the IFAC carried out a long-term experiment [22] aiming to investigate how the electromagnetic emission is affected by the melting/refreezing processes of snow. The experiment was called the MASMEX 02/03 (Microwave Snow Melting Experiment) and was carried out on the Mount Cherz test site. In order to have detailed data on the condition of the snowpack a physically-based hydrological model developed by the University of Brescia was used to estimate the time evolution of snow depth and wetness. Moreover, conventional measurements of snow parameters were carried out along vertical profiles at each significant change during the daily cycles of snow melting and refreezing (the majority daily or several time in a day). These measurements included, for each characteristic layer: grain shape and size, volumetric liquid water content (VLWC), snow density, temperature, and hardness. They were used also to calibrate the hydrological model and test its performances, and the measurement of liquid water content was carried out using standard empirical methods and two electromagnetic probes: the Snow Fork (TOIKKA- Finland) and a probe built by IFAC-CNR.

To simulate the emission of wet snow, a two-layer model based on the wave approach was used. The permittivity of the snow was computed by means of the SFT, modeling the free water like spherical droplets among the ice crystals. The input parameters were derived from the hydrological model except the correlation length of the permittivity fluctuations. This latter was determined by the fitting of the experimental measurements on a melting/refreezing cycle and used to estimate the emission for the following days. It should be noted that the electromagnetic snow model considers flat interfaces between the air, the snow layers and the ground.

The first model activity in the Masmex framework was to asses the capability of the SFT to simulate the emission of snow for long time series and to reproduce the fluctuations of the brightness temperature. In Tab. 5 are shown the inputs of the model derived from ground and simulated hydrological data. Both correlation length of the permittivity fluctuation and soil permittivity were kept constant for the entire simulations.

	Depth (cm)	Volume Fraction (%)	Temperature (°C)	VLWC (%)	Correlation Length (mm)	Permittivity
Upper layer min/max	10	38/53	- 4.2 /0	0 /2.9	0.6	
Lower layer min/max	9/ 48	33/48	-1.8 /0	0 /3.1	0.9	
Soil			0			6+ j 0.5

Tab. 5 - Input parameters of the SFT model used in the simulation of the MASMEX 02/03 data

Fig. 44 shows the measured brightness temperature at 37 GHz V polarization of one day, along with the simulated one and the LWC of the upper (10 cm) and lower layers of the snow. We can see that the model is able to reproduce very well the emission for the entire cycle. The comparison with liquid water content shows that the brightness temperature is better correlated to LWC of the first layer in the melting phase while, in the refreezing one, the e.m. emission process is driven by the LWC of the lower layer. As pointed out in paragraph 3.4, the brightness temperature of snow rises immediately just from the beginning of the melting phase. During the refreezing, T_b gently decreases because the wet snow emission is attenuated by the overlying dry snow layers (see Fig. 44). As the refreezing phase proceeds, the wet snow is hidden by a dry layer which increases with the time and attenuates the microwave emission coming from the bottom.

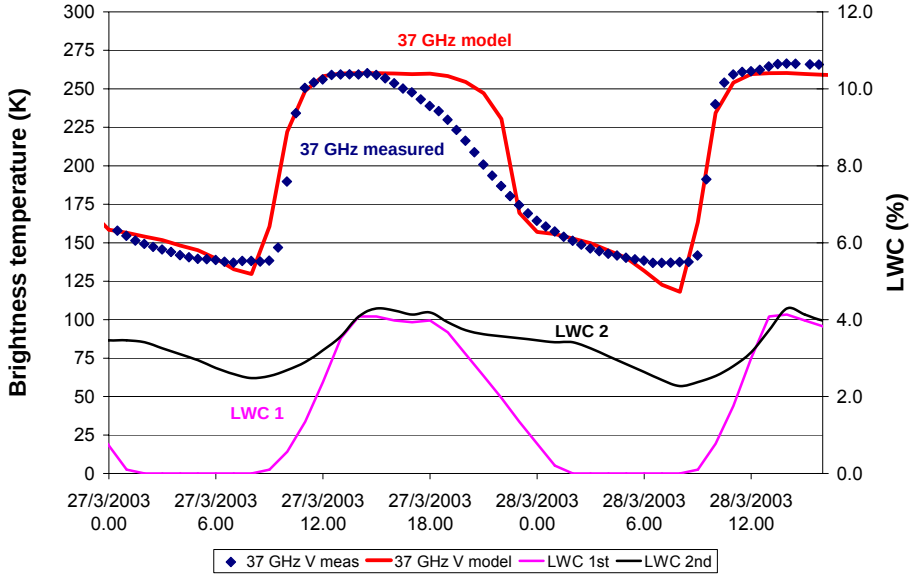

Fig. 44 - Time series of measured and simulated brightness temperatures Tb at 37 GHz vertical polarization. Lower lines (pink and black) represent respectively the liquid water content of the upper and lower layers.

The comparison of measured and simulated brightness temperatures at 19 GHz and 37 GHz for a long sequence of data are represented in Fig. 45 and 46. The investigated period was eleven days long at the end of March and four days in April. It is possible to see that the brightness temperature at 19 GHz has, in both cases, an appreciable overestimation of experimental data, which can be due to the various approximations made in the model and also to a slight overestimation of the snow temperature. Anyway, the model reproduces well the trend of experimental data.

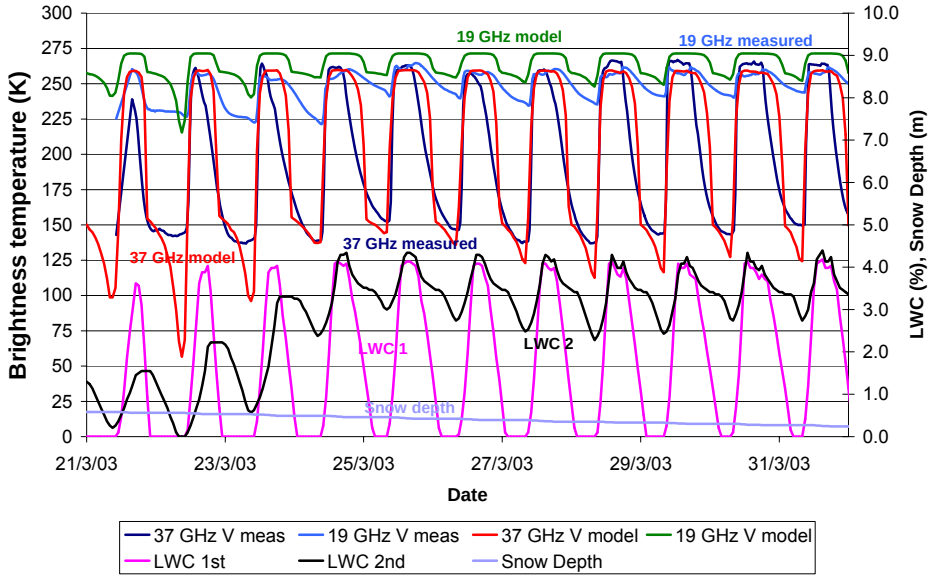

Fig. 45 - Experimental and simulated brightness temperatures at 19 and 37 GHz (Vertical polarization) together with simulated volumetric liquid water content of the two snow layers as a function of time. Inputs to the e.m. model were obtained from hydrological simulations except for correlation length and soil permittivity which were derived from ground measurements

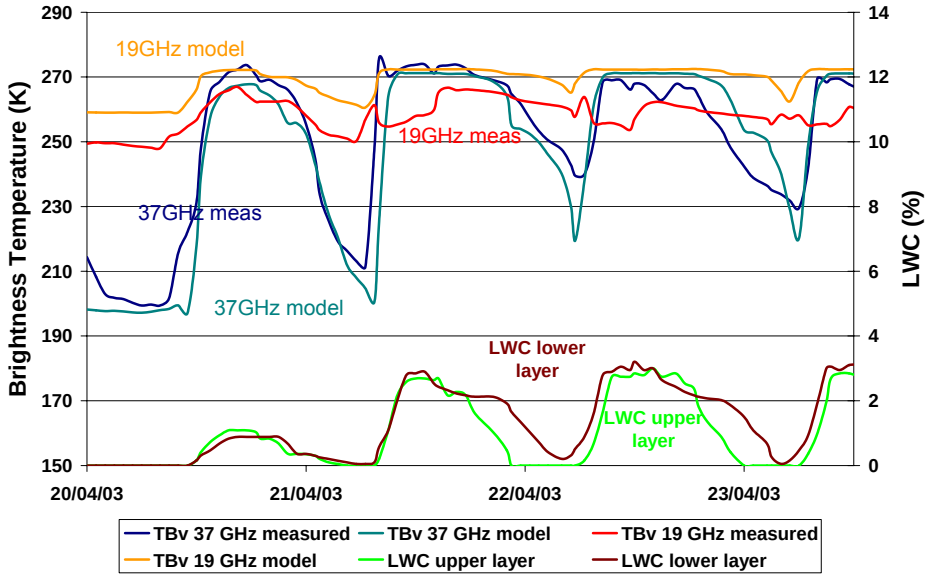

Fig. 46 - Experimental and simulated brightness temperatures at 19 and 37 GHz (Vertical polarization) together with simulated volumetric liquid water content of the two snow layers as a function of time. Inputs to the e.m. model were obtained from hydrological simulations except for correlation length and soil permittivity which were derived from ground measurements

To better understand how the various layers affect the emission of the snowpack a model analysis carried out to separate the terms that contribute to total emission was made. These contributions are: emission from soil attenuated by the two snow layers, emission from the lower layer of snow attenuated by the overlying layer, and the emission of the upper layer. Also in this case the frequencies investigated were 19 and 37 GHz. Fig. 47 shows that the upper layer controls emission in the melting phase, while the lower layer mostly influences brightness in the refreezing phase. The soil contribution is appreciable on relatively thin layers of refrozen snow only, and, as expected, it is higher at 19 GHz than at 37 GHz. It is appreciable only when the overlying layers of snow are both completely frozen (e.g. in the night of March, 22nd). After this date, the soil contribution disappears as soon as the snow wetness increases, and it remains undetectable because the LWC didn't drop to zero anymore.

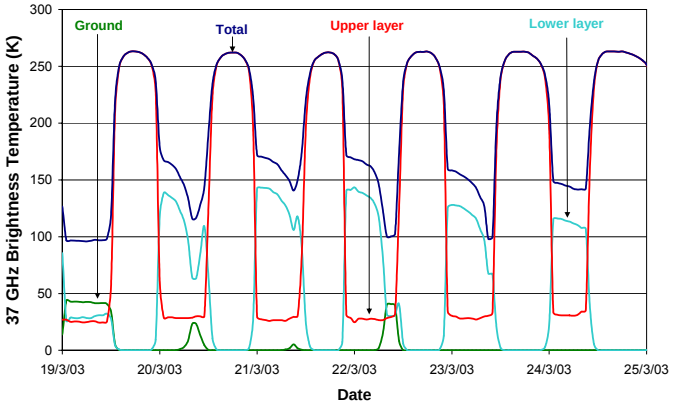

(a)

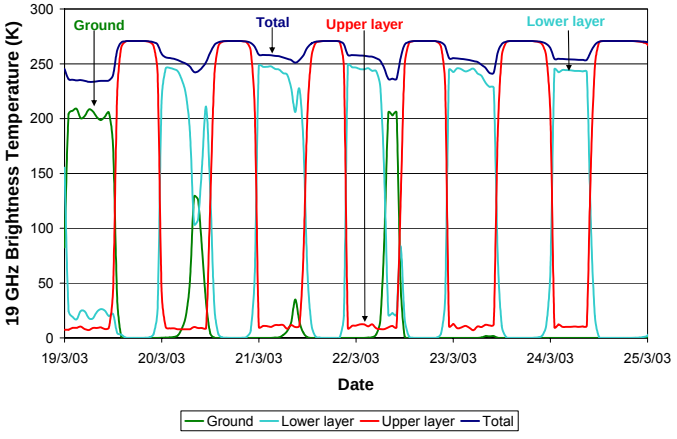

(b)

Fig. 47- Contribution of emission from soil and from the two snow layers to total brightness temperature (a: 37 GHz, b: 19 GHz)

5. SENSITIVITY ANALYSIS OF THE DMRT MODEL

Theoretical models are very useful to check and understand the relationships between the physical parameters of natural media and their electromagnetic behavior. Usually, these kinds of investigations are carried out by means of sensitivity analysis. The behavior of Strong Fluctuation Theory has been studied in [126] and will not be repeated here. Instead, the new IRIDE model for dry snow based on DMRT and the AIEM will be used to understand how the geophysical parameters of dry snow can affect the electromagnetic emission. As stated before, the main parameters that characterized the snow are the thickness, the density and the grain radius. Thus, the analysis has been focused on these variables for several frequencies and polarizations. When the results for the V and H pol. are similar, only one will be shown.

The sensitivities of the brightness temperature as a function of the snow depth (SD) for the Ku and Ka bands for the two polarizations) are depicted In Figs. 48-49 (a)-(b). In this analysis the soil has been modeled as flat with a permittivity ε= 3.2 like in [107]. The snow inputs (Tab. 6) were set to typical values for the North European snow covers: fractional volume=0.3, stickiness τ =0.1, the grain size is indicated in the figures close to each curve. At 19 GHz, V polarization there is a good sensitivity (nearly linear) of the emission to the snow depth for almost every particle size. It should be noted that only for tiny crystals (in case of diameters smaller than 0.2mm) the sensitivity is almost zero. In the other cases, it ranges from -25.1 K/m for small particles up to -107 K/m for big one. At 37 GHz the sensitivity is higher with a saturation at relatively low thicknesses. For shallow snowpacks the sensitivity is almost constant and range from 32 K/m up to 40 K/m respectively for grain radius from 0.2 to 0.5 mm.

Table 7 - Input parameters to the dry snow model for the preliminary sensitivity analysis

parameter	*value*
Fractional volume	0.2
Grain radius	0.1-0.5mm
Scatterers permittivity	3.2+j0.002 @ 19 GHz 3.2+j0.01 @ 37 GHz
Stickiness τ	0.1
Snow temperature	260 K
Soil temperature	260 K
Ground permittivity	3.2

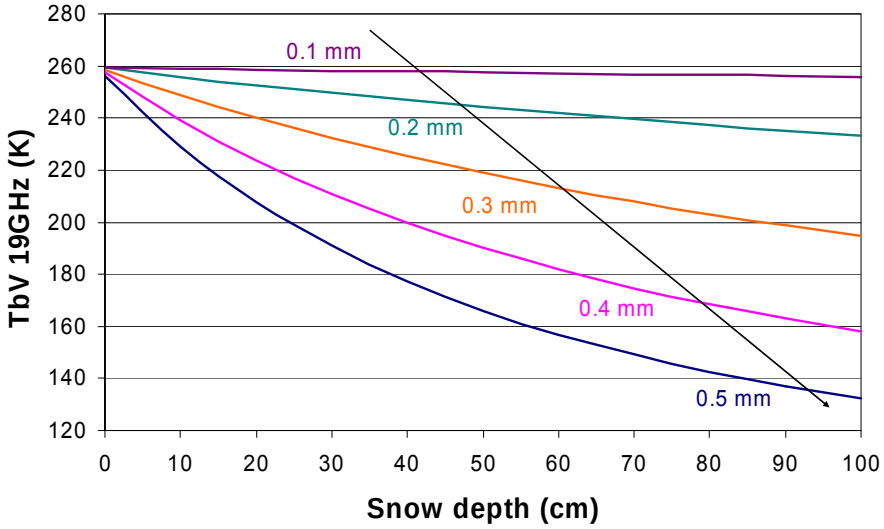

(a)

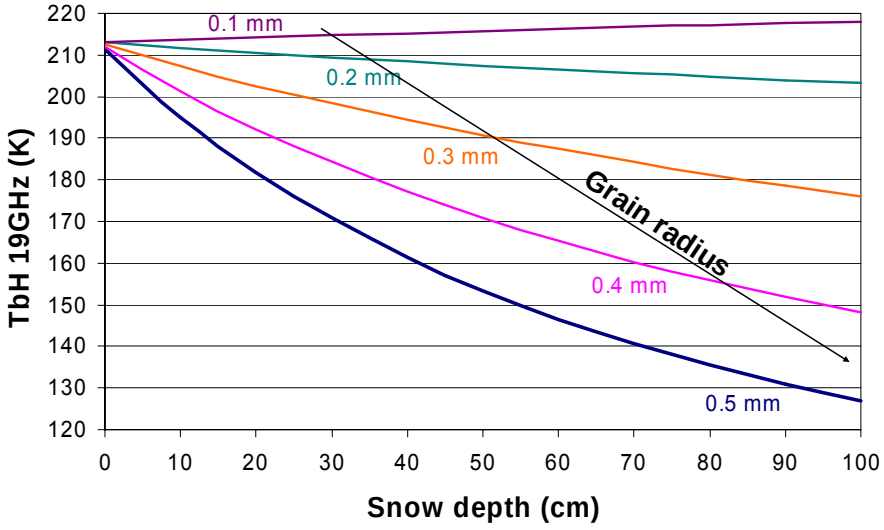

(b)

Fig. 48 – The brightness temperature at 19 GHz (a) V and (b) H polarizations as a function of snow depth for several values of grain size. The model parameters can be found in Tab. 7

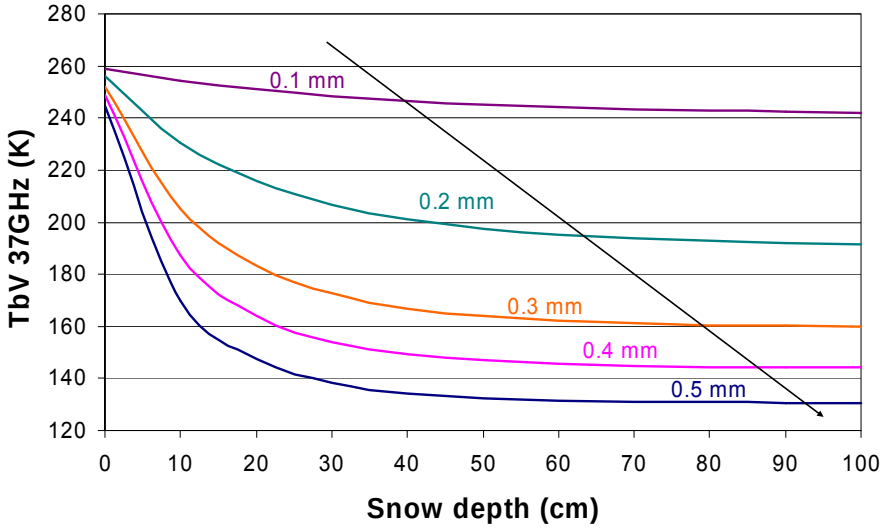

(a)

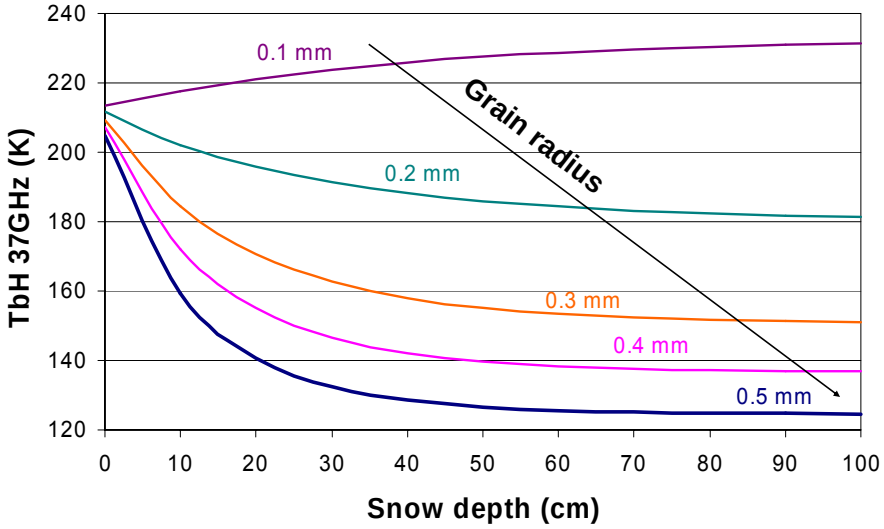

(b)

Fig. 49 – The brightness temperature at 37 GHz (a) V and (b) H polarizations as a function of snow depth for several values of grain size. The model parameters can be found in Tab. 7

Fig. 50 shows an attempt to investigate the behavior of the Chang's algorithms [33]. It is useful to recall that such method is based on the difference between the brightness temperature measured at Ku band and the one at Ka band. The

coefficients of the linear regression described in the state of the art can be obtained by the fitting of experimental measurements and are disregarded in this analysis.

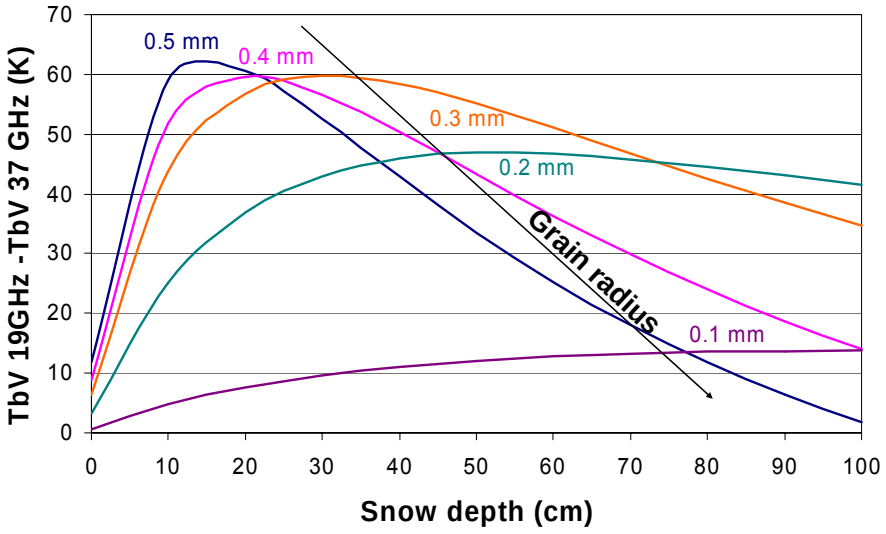

(a)

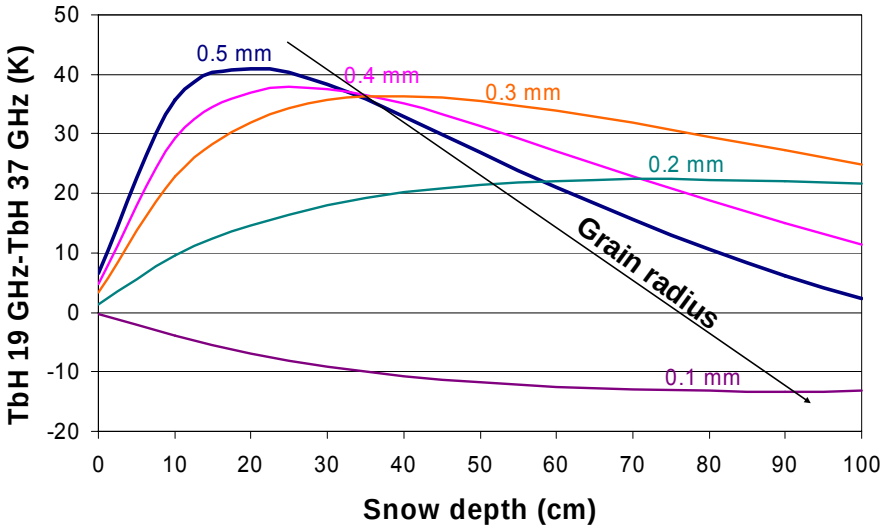

(b)

Fig. 50 – The brightness temperature difference ΔT_b at (a) V and (b) H polarizations as a function of snow depth for several values of grain size. The model parameters can be found in Tab. 7

For small grain size the difference ΔT_b between the two frequencies increases almost linearly at least up to a depth of 1m. As the grain radius increases ΔT_b presents a maximum (which happens at smaller snow depth as bigger is the grain size) and the algorithm can fail. This is due to the saturation showed by the emission at 37 GHz. From these considerations, it is possible to understand why the empirical algorithms can give acceptable predictions only if applied to large areas, where the variability of the snow parameters as grain size is larger and this can help to smooth the sharp transition outlined in Fig. 50.

Fig. 51 shows a similar analysis as in Fig. 43. The emission as a function of SD is investigated for four values of frequency. It should be noted that, since the density is kept fixed, the results hold also for the SWE that range from 0 to 27.5 cm. At the lowest frequencies, as pointed out previously, the emission depends mainly on soil and is influenced very few by the snow cover. If the frequency rises at Ku and Ka bands, the extinction properties of the ice crystals become appreciable and heavy affect the brightness temperature. At 37 GHz the plot clearly shows saturation for a snow depth of 20-30 cm (SWE ≅ 9cm). Beyond these values, snow masks completely the soil emission and the measured brightness is only due to the snow.

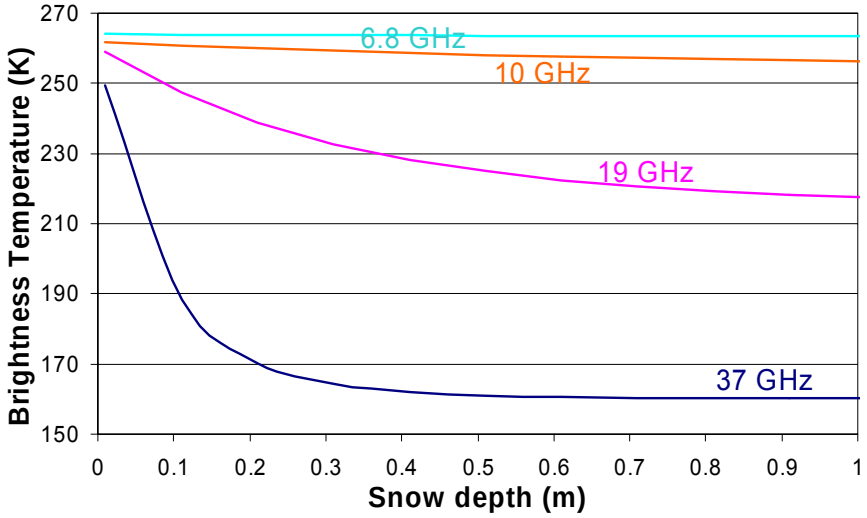

Fig. 51 – Sensitivity analysis of brightness temperature as a function of the snow depth for four frequencies. The input parameters to the model are summarized in Tab. 8

Tab. 8 – Input parameters for the simulation depicted in Fig. 51

parameter	*value*
Frequency	6.8,10,19,37 GHz
Observation angle	55 deg
Fractional volume	0.3
Grain radius	0.5mm
Scatterers permittivity	Hufford model
Stickiness τ	0.1
Snow temperature	266 K
Soil temperature	271 K
Soil HStdD	0.5 cm
Soil Corr. Length	20 cm
ACF	1.5 Power
Ground permittivity	8+j2

The last analysis is devoted to study the effect of the snow density on the emission. In a dense medium the brightness temperature is affected, in opposite ways, by the absorption and scattering processes. It is possible to see in Fig. 52 that for small particles the absorption is the main phenomena but if the scatterers size get bigger, the scattering become predominant. To this aim, the snowpack analyzed was 1 m thick and the grain radius considered were 0.3 and 0.5 mm. The entire set of parameters for the analysis is depicted in Table 9.

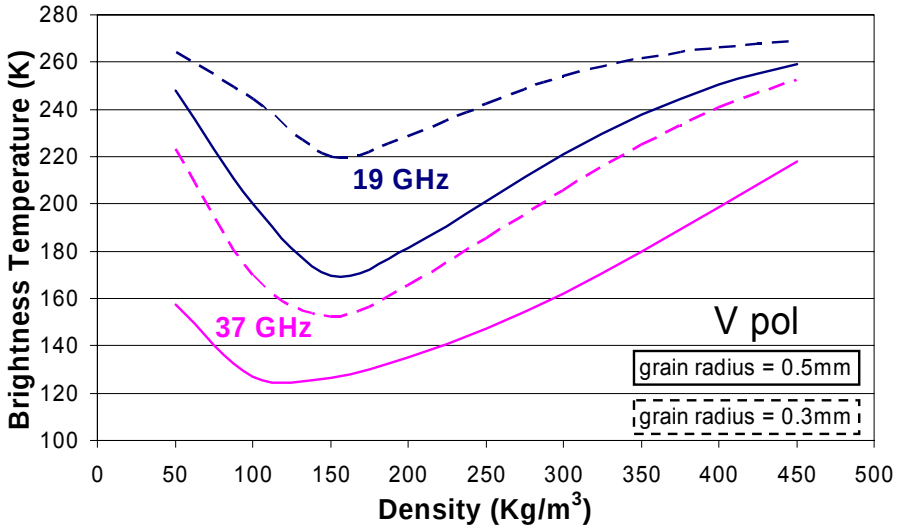

Fig. 52 – Sensitivity analysis of brightness temperature to snow density for two frequencies and two different grain radius. Even if the absolute values of the lines are different the trend is essentially the same for each curve. The input parameters are shown in Tab. 9

Tab. 9 – Input parameters for the simulation depicted in Fig. 52

parameter	*value*
Frequency	19,37 GHz
Observation angle	55 deg
Density	0.05-0.45 Kg/m^3
Grain radius	0.3, 0.5 mm
Scatterers permittivity	Hufford model
Snow depth	1 m
Stickiness τ	0.1
Snow temperature	266 K
Soil temperature	271 K
Ground permittivity	8+j2

For both the four cases considered, the trend of the diagrams is the same: for very tenuous snow the scattering is predominant and the brightness temperature decreases almost linearly, after a minimum is reached (for density around 150 Kg/m^3) the absorption/emission processes become predominant and the T_b start to rise. This behavior is typical of dense medium in which there is a strong interaction of the electromagnetic waves with the scatterers.

CONCLUSIONS

In this thesis, the problems of modeling the electromagnetic microwave emission from soils covered by snow have been discussed. Both dry and wet snowpacks have been considered. A comprehensive review of the state of the art of the electromagnetic theoretical models for simulating soil and snow microwave emission has been given. The characteristics of each model have been analyzed in-depth and discussed with respects to the measurement systems features and the parameters of the observed media. Moreover, special attention has been paid to identify the validity limits of the models. The e.m. models taken into consideration to simulate surface scattering have been: the Small Perturbation Method, the Kirchhoff Approach under the Physical and Geometrical Optics, the Small Slope Approximation, and the Advanced Integral Equation Method. Emission from snow has been studied by using the Dense Media Radiative Transfer Theory under the Quasi-Crystalline Approximation with or without Coherent Potentials and the Strong Fluctuations Theory.

From the literature analysis, the DMRT under the Quasi-Crystalline Approximation was found to be, at the state of the art, the best theoretical model for simulating dry snow, while the AIEM was the more suitable in modeling soil. For wet snow, the best performances have been shown by the SFT.

During the study of the models available in literature, many severe errors have been detected for both the DMRT and AIEM. Hence, the two models have been thoroughly revised and the errors corrected. Moreover, the AIEM was extended to the polarimetric case, which was not yet available in literature.
Subsequently, an advanced model for simulating emission from soils covered by dry snow (called IRIDE IFAC RadiatIve Dry snow Emission model) has been developed by coupling the DMRT with the AIEM. Since radiation from wet snow is practically not affected by soil contribution, the model for simulating wet snow was based on the SFT and the wave approach for multilayered media, by disregarding surface scattering from soil.

In order to check and test the performances of the developed software, an extensive validation has been successfully carried out by means of numerical and experimental data. The two models have also been used to give a physical insight to the microwave measurements collected by the IFAC Microwave Remote Sensing Group on some test sites in the Italian Alps and to enlighten the experimental relationships found between microwave emission and snow parameters.

Finally, an extensive sensitivity analysis of the IRIDE model has been carried out, in order to understand how the electromagnetic emission depends on the physical characteristics of snow and on the observing parameters. It has been found that both IRIDE and SFT models predict a sensitivity to snow depth and volume fraction well in agreement with experimental data, whereas the extremely high sensitivity to ice crystal dimensions still needs to be confirmed by measurements. For instance, the sensitivity of brightness temperature to the snow depth predicted by the IRIDE

model ranges from -4 up to -123 K/m at 19 GHz, in V pol., respectively for 0.2 and 1 mm grain diameter, and from -35 up to -354 K/m at 37 GHz, in V pol. The sensitivity of the emission simulated by IRIDE to snow density shows a non-monotonic behavior both for Ku and Ka bands and for the two grain sizes considered: up to 120-150 Kg/m^3, the emission is inversely proportional to the density, while, after such a value, the emission increases as the density increases. A further study has been carried out to check the empirical Chang's algorithm used for the retrieval of snow depth or of SWE. This analysis pointed out that the performances of the algorithm are strongly affected by the snow characteristics, in particular by the grain size, and this high dependence causes a relative big error in estimate the snow depth.

Further advancements in the IRIDE model will take into account the multilayer structure of dry snow, a different solution of the radiative transfer equation to consider the vertical profiles of snow parameters, and the non-spherical (ellipsoidal) shape of the ice grains. Moreover, another consideration emerged during the progress of the thesis is that the techniques used for estimating the soil characteristics, in particular the shape of the autocorrelation function, are not adequate for the description of the surface roughness and should be improved.

BIBLIOGRAPHY

[1] Robinson D.A., K.F. Dewey, and R.R. Heim, “Global snow cover monitoring: an update”, *Bulletin of American Meteorological Society*, Vol. 74, 1993, pp. 1689-1696

[2] Serreze M.C., J. E. Walsh, F. S. Chapin III, T. Osterkamp, M. Dyurgerov, V. Romanovsky, W. C. Oechel, J. Morison, T. Zhang And R. G. Barry, “Observational evidence of recent change in the northern high-latitude”, *Climatic Change*, Vol. 46 , no. 1-2, 2000, pp. 159-207

[3] Solberg R., D. Hiltbrunner, J. Koskinen, T. Guneriussen, K. Rautiainen and M. Hallikainen, "High-level earth observation snow products. Review of current products and methodology - requirements for and specification of new products and methodology," *SNOWTOOLS Technical Report from WP 410*, CEC Contract No. ENV4-CT96-0304, 1997

[4] Koskinen, J., J. Pulliainen, , and M. Hallikainen, “The Use of ERS-1 SAR Data in Snow Melt Monitoring”, *IEEE Transactions on Geoscience and Remote Sensing*, Vol. 35, no. 3, 1997, pp 601-610

[5] Nagler T. and H. Rott, “Retrieval of wet snow by means of multitemporal SAR data”, *IEEE Transactions on Geoscience and Remote Sensing*, Vol. 38, no. 2, 2000, pp. 754-765

[6] Guneriussen T., Hogda K. A., Johnsen H., Lauknes I., “InSAR for estimation of changes in snow water equivalent of dry snow”, Proceedings of IEEE Geoscience and Remote Sensing Symposium, IGARSS 2000 IEEE International Volume 2, pp.463-466

[7] Tsang L. and J. Kong, “Scattering of electromagnetic waves from a half space of densely distributed dielectric scatterers”, *Radio Science*, Vol. 18, 1983, pp. 1260–1272

[8] Ulaby F. T., R. K. Moore, and A. K. Fung, **Microwave Remote Sensing: Active and Passive**, Artech House, Vol. 3, 1986

[9] Jin Y. Q. and J.A. Kong, “Strong fluctuation theory of electromagnetic wave scattering by a layer of random discrete scatterers”, *Journal of Applied Physics*, Vol. 55, 1984, pp. 1364–1369

[10] Pulliainen J. and M.T. Hallikainen, “Estimation of snow water equivalent from SSM/I data by using a physical model-based inversion algorithm”, Proceedings of IEEE Geoscience and Remote Sensing Symposium, IGARSS 1998, IEEE International Vol.3, pp.1541-1543

[11] Wiesman A. and C. Mätzler, “Microwave emission model of layered snowpacks”, *Remote Sensing of Environment*, Vol. 70, 1999, pp. 307–316

[12] Mätzler C. and A. Wiesmann, “Extension of the microwave emission model of layered snowpacks to coarse-grained snow”, *Remote Sensing of Environment*, Vol. 70, 1999, pp. 317–325

[13] Kunzi K. F., A. D. Fisher, D. H. Staelin and J.W. Waters, “Snow and ice surfaces measured by the Nimbus 5 microwave spectrometer”, *Journal of Geophysical Research*, Vol. 81, no. 27, 1976, pp. 4965–4980

[14] Hofer R. and E. Schanda, “Signatures of snow in the 5 to 94 GHz range”, *Radio Science*, Vol. 13, 1978, pp. 365–369

[15] Hofer R. and C. Mätzler, “Investigation of snow parameters by radiometry in the 3- to 60-mm wavelength region”, *Journal of Geophysical Research*, Vol. 85, 1980, pp. 453–460

[16] Schanda E., C. Mätzler and K. Künzi, “Microwave remote sensing of snow cover”, *International Journal of Remote Sensing*, Vol. 4, 1983, pp. 149–158

[17] Rott H. and K. Sturm, “Microwave signature measurements of Antarctic and alpine snow,” in Proceedings of 11th EARSeL Symposium, Graz, Austria, 1991, pp. 140–151

[18] Macelloni G., S. Paloscia, P. Pampaloni and M. Tedesco, “Microwave emission from dry snow: A comparison of experimental and model results”, *IEEE Transactions on Geoscience and Remote Sensing*, Vol. 39, no. 12, 2001, pp.2649–2656

[19] Walker E. and B. E. Goodison, “Discrimination of a wet snow cover using passive microwave satellite data,” Annals of Glaciology, Vol. 17, 1993, pp. 307–311

[20] Grody N. C. and A. N. Basist, “Global identification of snowcover using SSM/I measurements”, *IEEE Transactions on Geoscience and Remote Sensing*, Vol. 34, no. 1, 1996, pp. 237–249

[21] Rosenfeld S. and N. C. Grody, “Metamorphic signature of snowrevealed in SSM/I Measurements”, *IEEE Transactions on Geoscience and Remote Sensing*, Vol. 38, no. 1, 2000, pp. 53–63

[22] Macelloni G., S. Paloscia, P. Pampaloni, M. Brogioni, R. Ranzi and A. Crepaz, “Monitoring of melting refreezing cycles of snow with microwave radiometers: the Microwave Alpine Snow Melting Experiment (MASMEx 2002-2003) ”, *IEEE Transactions on Geoscience and Remote Sensing*, Vol. 43, no. 11, 2005, pp. 2431-2442

[23] Kelly R. E., A. T. Chang, L. Tsang and J. L. Foster, “A prototype AMSR-E global snow area and snow depth algorithm”, *IEEE Transactions on Geoscience and Remote Sensing*, Vol. 41, no. 2, 2003, pp. 230–242

[24] Reber B., C. Mätzler, and E. Schanda, “Microwave signatures of snow crusts. Modeling and measurements”, *International Journal of Remote Sensing*, Vol. 8, 1987, pp. 1649-1665

[25] Mätzler C. , “Applications of the interaction of microwaves with the natural snow cover,” *Remote Sensing Review*, Vol. 1, 1987, pp. 1-129

[26] Shi J. and J. Dozier, “Inferring Snow Wetness Using C-band Data from SIR-C's Polarimetric Synthetic Aperture Radar”, *IEEE Transactions on Geoscience and Remote Sensing*, Vol. 33, no. 4, 1995, pp. 905-914

[27] Bernier, M., Fortin, JP., Gauthier, Y., Gauthier, R., Roy, R., Vincent, P., "Determination of snow water equivalent using RADARSAT SAR data in eastern Canada", *Hydrological Processes*, Vol. 13, no. 18, 1999, pp. 3041-3051

[28] Hallikainen M.T. and P.A. Jolma "Comparison of algorithms for retrieval of snow water equivalent from Nimbus-7 SMMR data in Finland", *IEEE Transactions on Geoscience and Remote Sensing*, Vol. 30, no. 1, 1992, pp.124-131

[29] Hallikainen M.T., P. Halme, M. Takala and J. Pulliainen, "Combined active and passive microwave remote sensing of snow in Finland", Proceedings of IEEE Geoscience and Remote Sensing Symposium, IGARSS 2003 IEEE International Volume 2, pp. 830 - 832

[30] Brogioni M., G. Macelloni, S. Paloscia, P. Pampaloni, S. Pettinato and E. Santi, "Estimating Snow water equivalent from satellite passive and active microwave sensors", Proceedings of IEEE Geoscience and Remote Sensing Symposium, IGARSS 2006, pp.3659 – 3660

[31] Macelloni G., M. Brogioni, P. Pampaloni and A. Cagnati, "Multifrequency Microwave Emission Fromthe Dome-C Area on the East Antarctic Plateau: Temporal and Spatial Variability", *IEEE Transactions on Geoscience and Remote Sensing*, Vol. 45, no. 7-1, 2007, pp. 2029-2039

[32] Oh Y., K. Sarabandi and F.T. Ulaby, "An empirical model and an inversion technique for radar scattering from bare soil surfaces", *IEEE Transactions on Geoscience and Remote Sensing*, Vol. 30, no. 2, 1992, pp. 370-381

[33] Chang, A.T.C., J.L. Foster and D.K. Hall, "Nimbus-7 SMMR derived global snow cover parameters", *Annals of Glaciology*, Vol. 9, 1987, pp. 39-44

[34] Pulliainen J.T., J. Grandell, and M. T. Hallikainen, "HUT Snow Emission Model and its Applicability to Snow Water Equivalent Retrieval", *IEEE Transactions on Geoscience and Remote Sensing*, Vol. 37, no. 3, 1999, pp. 1378-1390

[35] Hallikainen M. T., F. T. Ulaby and T. E. Van Deventer, "Extinction behavior of dry snow in the 18- to 90-GHz range", *IEEE Transactions on Geoscience and Remote Sensing*, Vol. 25, no. 6, 1987, pp. 737-745

[36] Mätzler C., "Applications of the interaction of microwaves with the natural snow cover", *Remote Sensing Reviews,* vol. 2, 1987, pp. 259–387

[37] Hallikainen M. T., F. Ulaby and M. Abdelrazik, "Dielectric properties of snow in the 3 to 37 GHz range", *IEEE Transaction on Antennas and Propagation,* Vol. 34, no. 11, 1986, pp. 1329–1340

[38] Tsang L., J. Pan, D. Liang, Z. Li, D.W. Cline and Y. Tan , "Modeling Active Microwave Remote Sensing of Snow Using Dense Media Radiative Transfer (DMRT) Theory With Multiple-Scattering Effects", *IEEE Transactions on Geoscience and Remote Sensing*, Vol. 45, no.4, 2007, pp. 990-1004

[39] Tsang L. and J.A. Kong, "**Scattering of electromagnetic waves – Advanced topics**", *John Wiley and Sons*, New York, 2001

[40] Li Q., L. Tsang, K.S. Pak, and C.H. Chan, "Bistatic Scattering and Emissivities of Random Rough Dielectric Lossy Surfaces with the Physics-Based Two-Grid Method in Conjunction with the Sparse-Matrix Canonical Grid Method", *IEEE Transactions on Antennas and Propagation*, Vol. 48, no. 1, 2000, pp. 1-11

[41] Sihvola A., "**Electromagnetic mixing formulas and applications**", *The Institution of Electrical Engineers*, 1999

[42] Hasted J.B., "**Aqueous Dielectrics**", Studies in Chemical Physics, Chapman and Hall, 1973

[43] Dobson M.C., F.T. Ulaby, M.T. Hallikainen and M.A. El-Rayes, "Microwave Dielectric Behavior of Wet Soil-Part II: Dielectric Mixing Models", *IEEE Transactions on Geoscience and Remote Sensing*, Vol. 23, no. 1, 1985, pp. 35-46

[44] Church E.L., "Fractal surface finish*", Applied Optics*, vol. 27, 1988, pp. 1518-1526

[45] Bennet J.M. and L. Mattsson, "**Introduction to surface roughness and scattering**", Optical Society of America, Washington D.C., 1989

[46] Bennet J.M., "Recent developments in surface roughness characterization", *Measurement Science and Technology,* vol. 3, 1992, pp. 1119-1127

[47] Dong W.P., P.J. Sullivan and K.J. Stout, "Comprehensive study of parameters for characterizing three-dimensional surface topography I: Some inherent properties of parameter variation", *Wear*, vol. 159, 1992, pp. 161-171

[48] Dong W.P., P.J. Sullivan, and K.J. Stout, "Comprehensive study of parameters for characterizing three-dimensional surface topography II: Statistical properties of parameter variation", *Wear*, vol. 167, 1993, pp. 9-21

[49] Dong W.P., P.J. Sullivan, and K.J. Stout, "Comprehensive study of parameters for characterizing three-dimensional surface topography III: Parameters for characterizing amplitude and some functional properties", *Wear*, vol. 178, 1994, pp. 29-43

[50] Li Q., J.C. Shi and K.S. Chen, "A Generalized Power Law Spectrum and its Applications to the Backscattering of Soil Surfaces Based on the Integral Equation Model", *IEEE Transactions on Geoscience and Remote Sensing*, Vol. 40, No. 2, 2002, pp. 271-280

[51] Tsang, L., J.A. Kong and K.H. Ding, "**Scattering of Electromagnetic Waves - Theories and Applications***", John Wiley and Sons*, New York, 2000

[52] Fung, A.K. and N.C. Kuo, “Backscattering from Multi-Scale and Exponentially Correlated Surfaces”, *Journal of Electromagnetic Waves and Applications*, Vol. 20, no. 1, 2006, pp. 3-11

[53] Jaggard D.L. and X. Sun, “Scattering from fractally corrugated surfaces”, *Journal of Optical Society of America*, *A*, no. 7, 1990, pp. 1131-1139

[54] Rouvier S. and P. Borderies, “Ultra wide band electromagnetic scattering of a fractal profile”, *Radio Science*, no. 32, 1997, pp. 285-293

[55] Zribi M., J. Paille, V. Ciarletti, O. Taconet, P. Boissard, M. Chapron and B. Rabin, “Modelisation of Roughness and Microwave Scattering of Bare Soil Surfaces Based on Fractal Brownian Geometry”, *Proceedings of IEEE Geoscience and Remote Sensing Symposium, IGARSS 1998*, IEEE International Volume 3, pp. 1213-1215

[56] Nayak P., “Random Process Model of Rough Surfaces”, *Journal of Lubrification Science*., no. 93, 1971, pp. 398-407

[57] Adler R. J. and D. Firman, “A non Gaussian model for random surfaces”, *Philosophical Transactions of the Royal Society of London,* Series A, 1981, pp. 433-462

[58] Greenwood J. A., “A unified theory of surface roughness *Proceedings of the Royal Society of London*, Series A, 1984, pp. 133-157

[59] Brown S. R. and C. H. Scholz, “Broad bandwidth study of the topography of natural rock surfaces”, *Journal of Geophysical Research*, No. 90, B14, 1985, pp. 11575-11582

[60] Broschat S. L., “The small slope approximation reflection coefficient for scattering from a “Pierson-Moskowitz” sea surface”, *IEEE Transactions on Geoscience and Remote Sensing*, Vol. 31, 1993, pp. 1112-1114

[61] Voronovich A.G., “**Wave Scattering from Rough Surfaces**”, Springer Series on Wave Phenomena, Berlin, Springer, 1994a

[62] Voronovich A.G., “Small-slope approximation for electromagnetic wave scattering at a rough interface of two dielectric half-spaces”, *Waves in Random Media*, No. 4, 1994, pp. 337–367

[63] Thorsos E.I. and S.L. Broschat, “An investigation of the small-slope approximation for scattering from rough surfaces: part I. Theory”, *Journal of Acoustic Society of America*, vol. 97, 1995, pp. 2082–2093

[64] Fung A. K., Z. Li and K. S. Chen, “Backscattering from a Randomly Rough Dielectric Surface”, *IEEE Transactions on Geoscience and Remote Sensing*, Vol. 30, no. 2, 1992, pp. 356-369

[65] Fung A.K., “**Microwave scattering and emission models and their applications**”, *Artech House Inc.*, Boston, 1994

[66] Macelloni G., G. Nesti, P. Pampaloni, S. Sigismondi, D. Tarchi, and S. Lolli, “Experimental validation of surface scattering and emission models”,

IEEE Transactions on Geoscience and Remote Sensing, Vol. 38, no. 1 (Part: II), 2000, pp. 459-469

[67] Tsang L., J.A. Kong and R.T. Shin, "**Theory of Microwave Remote Sensing**", *Wiley Interscience*, New York, 1985

[68] Smith B., "Geometrical shadowing of a random rough surface", *IEEE Transactions on Antennas and Propagation*, Vol. 15, no. 5, 1967, pp. 668-671

[69] Sancer, M., "Shadow-corrected electromagnetic scattering from a randomly rough surface", *IEEE Transactions on Antennas and Propagation*, Vol.17, no. 5, 1969, pp. 577-585

[70] Bourlier C. and G. Berginc, "Multiple scattering in the high-frequency limit with second-order shadowing function from 2D anisotropic rough dielectric surfaces: I. Theoretical study", *Waves in Random Media*, no. 14, 2004, pp. 229-252

[71] Bourlier C. and G. Berginc, "Multiple scattering in the high-frequency limit with second-order shadowing function from 2D anisotropic rough dielectric surfaces: II. Comparison with numerical results", *Waves in Random Media*, no. 14, 2004, pp. 253-276

[72] Voronovich A.G., "Non-local small-slope approximation for wave scattering from rough surfaces", *Waves Random Media*, vol. 6, pp. 151–167, 1996

[73] Report "State of the Art on Bistatic Microwave Measurements for Earth Observation", Use of Bi-Static Microwave Measurements for Earth Observation project, European Space Agency (ESA) Contract ESTEC 19173/05/NL/GLC, IFAC-CNR, Università "La Sapienza" – Rome, Universitá "Tor Vergata" – Rome, Space Engineering

[74] Rice S.O., "Reflection of electromagnetic waves from slightly rough surfaces", *Communications on Pure and Applied Mathematics,* 4, 1951, pp.351–378

[75] Plant W. J., "A stochastic, multiscale model of microwave backscatter from the ocean", *Journal of Geophysical Research*, Vol. 107, no. C9, 2002, pp. 3-1/3-21

[76] Hsieh C.-Y., A.K. Fung, G. Nesti, A.J. Sieber and P. Coppo, "A Further Study of the IEM Surface Scattering Model", *IEEE Transactions on Geoscience and Remote Sensing*, Vol. 35, no. 4, 1997, pp. 901-909

[77] Hsieh C.-Y. and A.K. Fung, "Bistatic multiple scattering from randomly rough surfaces", *IEE Proceedings - Microwaves, Antennas and Propagation*, Vol. 150, No. 4, 2003, pp. 214-218

[78] Chen K.S., T.D. Wu, M.K. Tsay and A.K. Fung, "A Note on the Multiple Scattering in an IEM Model", *IEEE Transactions on Geoscience and Remote Sensing*, Vol. 38, no. 1, 2000, pp. 249-256

[79] Wu T.-D., K.S. Chen, J.C. Shi and A.K. Fung, “A Transition Model for the Reflection Coefficient in Surface Scattering”, *IEEE Transactions on Geoscience and Remote Sensing*, Vol. 39, no. 9, 2001, pp. 2040-2050

[80] Fung A.K. and K.S. Chen, “An Update on the IEM Surface Backscattering Model”, *IEEE Geoscience and Remote Sensing Letters*, Vol. 1, no. 2, 2004, pp. 75-77

[81] Álvarez-Pérez J. L., “An extension of the IEM/IEMM surface scattering model”, *Waves in Random Media*, no. 11, 2001, pp. 307-329

[82] Chen K.S., T.D. Wu, L. Tsang, Q. Li, J. Shi and A. K. Fung, “Emission of Rough Surfaces Calculated by the Integral Equation Method With Comparison to Three-Dimensional Moment Method Simulations”, *IEEE Transactions on Geoscience and Remote Sensing*, Vol. 41, No. 1, 2003, pp. 90-101

[83] Wu T.D. and K.S. Chen, “A Reappraisal of the Validity of the IEM Model for Backscattering From Rough Surfaces”, *IEEE Transactions on Geoscience and Remote Sensing*, Vol. 42, no. 4, 2004, pp. 743-753

[84] Jin, Y.Q., “**Electromagnetic scattering models for quantitative remote sensing**”, World Scientific, Singapore, 1993

[85] Tsang L. and J.A. Kong, “Application of strong fluctuation random medium theory to scattering from a vegetation-like half space”, *IEEE Transactions on Geoscience and Remote Sensing*, Vol. 19, no.1, 1981, pp. 62-69

[86] Tsang L. and J.A. Kong, “Scattering of electromagnetic waves from random media with strong permittivity fluctuations”, *Radio Science*, 1981, Vol. 16, no. 3, pp. 303-320

[87] Tsang L., J.A. Kong and R.W. Newton, “Application of Strong Fluctuation Random Medium Theory to Scattering of Electromagnetic Waves from a Half-Space of Dielectric Mixture”, *IEEE Transactions on Antennas and Propagation*, Vol. 30, no. 2, 1982, pp. 292-302

[88] Stogryn A., “Strong Fluctuations Theory for moist granular media”, *IEEE Transactions On Geoscience And Remote Sensing*, Vol. 23, no. 2, 1985, pp. 78-83

[89] Evans S., “Dielectric properties of ice and snow. A review,” *Journal of Glaciology*, Vol. 5, 1965, pp. 773-792

[90] Walford M. E. R., “Field measurements of dielectric absorption in Antarctic ice and snow at very high frequencies”, *Journal of Glaciology* , 1968, pp. 789-794

[91] Arslan N., H. Wang, J. Pulliainen and M. Hallikainen, “Effective permittivity of wet snow using strong fluctuation theory”, *Progress in Electromagnetic Research*, Vol. 31, 2001, pp. 273–290

[92] Jin, Y.Q. and J.A. Kong, “Strong fluctuation theory of electromagnetic wave scattering by a layer of random discrete scatterers”, *Journal of Applied Physics*, Vol. 55, no. 5, 1984, pp. 1364-1369

[93] Ishimaru A. and Y. Kuga, “Attenuation constant of a coherent field in a dense distribution of particles,” *Journal of Optical Society of America,* Vol. 72, 1982, pp.1317–1320

[94] Wen B., L. Tsang, D. Winebrenner and A. Ishimaru, “Dense medium radiative transfer theory: comparison with experiment and application to microwave remote sensing and polarimetry”, *IEEE Transactions on Geoscience and Remote Sensing*, Vol. 28, no. 1, 1990, pp. 46-59

[95] Tsang L. and J.A. Kong, “Scattering of electromagnetic waves from a half space of densely distributed dielectric scatterers”, *Radio Science*, Vol. 18, 1983, pp. 1260-1272

[96] Tsang L. and A. Ishimaru, “Radiative wave equations for vector electromagnetic propagation in dense non-tenuous media”, *Journal of Electromagnetic Waves and Applications*, vol. 1, no. 1, 1987, pp. 52-72

[97] Ding K.H. and L. Tsang, “Effective propagation constants of dense nontenuous media with multi-species of particles”, *Journal of Electromagnetic Waves and Applications*, Vol. 2, no. 8, 1988, pp. 757-777

[98] Tsang L. and J.A. Kong, “Multiple scattering of electromagnetic waves by random distribution of discrete scatterers with coherent potential and quantum mechanical formulism”, *Journal of Applied Physics*, vol. 15, 1980, pp. 3465-3485

[99] Soven P., “Coherent-potential model of substitutional disordered alloys”, *Physical Review*, vol. 156, 1967, pp. 809-813

[100] Kohler W. E. and G. C. Papanicolaou, “Some applications of the coherent potential approximation”, *Multiple Scattering and Waves in Random Media*,: North Holland, 1981, pp. 199-223

[101] Tsolakis A. I., I. M. Besieris, and W. E. Kohler, “Two-frequency radiative transfer equation for scalar wave in a random distribution of discrete scatterers with pair correlations”, *Radio Science*, Vol. 20, 1985, pp. 1037-1052

[102] Frisch V., “**Wave propagation in random medium**’’, Probabilistic Methods in Applied Mathematics, New York: Academic, 1968

[103] Tsang L., “Passive remote sensing of dense nontenuous media”, *Journal of Electromagnetic Waves and Applications*, vol. 1, no. 2, 1987, pp. 159-173

[104] Kuga Y. and A. Ishimaru, “Retroreflectance from a dense distribution of particles”, *Journal of Optical Society of America,* vol. 1, 1984, pp. 831-835

[105] Ishimaru A., “**Wave Propagation and Scattering in Random Media, vol. I: Single Scattering and Transport Theory**”, Academic Press, New York, 1978.

[106] Percus J . K. and G. J. Yevick, “Analysis of classical statistical mechanics by means of collective coordinates”, *Physical Review*, vol. 110, 1958, pp. 1-13

[107] Tsang L., C.T. Chen, A.T.C. Chang, J. Guo and K.H. Ding, "Dense Media Radiative Transfer Theory Based on Quasicrystalline Approximation with Application to Passive Microwave Remote Sensing of Snow", *Radio Science*, Vol.35, no.3, 2000, pp.731-49

[108] West R., L. Tsang and D.P. Winebrenner, "Dense medium radiative transfer theory for two scattering layers with a Rayleigh distribution of particle sizes", *IEEE Transactions on Geoscience and Remote Sensing*, Vol. 31, no. 2, 1993, pp. 426-437

[109] Ding K.H., Y.E. Yang, S.E. Shih, J.A. Kong and R.E. Davis, "Modeling of electromagnetic wave scattering from time-varying snowcover", *Proceedings of IEEE Geoscience and Remote Sensing Symposium, IGARSS 1996*, International Volume 1, pp. 757 – 759

[110] Zurk L.M., L. Tsang, J.C. Shi and R.E. Davis, "Electromagnetic scattering calculated from pair distribution functions retrieved from planar snow sections", *IEEE Transactions on Geoscience and Remote Sensing*, Vol. 35, no. 6, 1997, pp. 1419-1428

[111] Tsang L., K.-H. Ding and A.T.C. Chang, "Scattering by densely packed sticky particles with size distributions and applications to microwave emission and scattering from snow", *Proceedings of IEEE Geoscience and Remote Sensing Symposium, IGARSS 2003*, IEEE International Volume 4, pp. 2844-2846

[112] Tan Y., Z. Li, L. Tsang; A.T.C. Chang and Q. Li, "Modeling passive and active microwave remote sensing of snow using DMRT theory with rough surface boundary conditions", *Proceedings of IEEE Geoscience and Remote Sensing Symposium, IGARSS 2004*, IEEE International Volume 3, pp. 1842–1844

[113] Tan Y., Z. Li, K.K. Tse and L. Tsang, "Microwave model of remote sensing of snow based on dense media radiative transfer theory with numerical Maxwell model of 3D simulations (NMM3D)", *Proceedings of IEEE Geoscience and Remote Sensing Symposium, IGARSS 2005*, IEEE International Volume 1, pp. 578 – 581

[114] Huining W., J. Pulliainen and M. Hallikainen, Effective Permittivity of Dry Snow in the 18 to 90 GHz Range, *Progress In Electromagnetics Research*, PIER 24, 1999, 119-138

[115] Chen C.T., L. Tsang, J. Guo, A.T. C. Chang and K.H. Ding, "Frequency Dependence of Scattering and Extinction of Dense Media Based on Three-Dimensional Simulations of Maxwell's Equations with Applications to Snow", *IEEE Transactions on Geoscience and Remote Sensing*, Vol. 41, no. 8, 2003, pp. 1844 - 1852

[116] Hellmann M., "SAR polarimetry tutorial", 2002, available at http://epsilon.nought.de/

[117] Ulaby F.T. and C. Elachi, "**Radar Polarimetry for Geoscience Applications**", Artech House Publishers, 1990

[118] Nesti G., P. Pampaloni, P. Coppo, M. Hallikainen, M. Mancini, P. Troch, and M. von Shonermark, “Experimental research at EMSL on scattering properties of non vegetated terrains”, *Proceedings of IEEE Geoscience and Remote Sensing Symposium, IGARSS 1995*, T. Stein, Ed., Firenze, Italy, 1995, pp. 2020–2022

[119] Abramowitz M. and I.A. Stegun, “**Handbook of Mathematical Functions**”, Dover, New York, 1972

[120] Tsang, L., J.A. Kong and K.H. Ding, “**Scattering of Electromagnetic Waves – Numerical dimulations***”, John Wiley and Sons*, New York, 2000

[121] Van de Hulst H. C., “**Light Scattering by Small Particles***”,* New York:Dover, 1957.

[122] Strozzi, T. "Active microwave signature catalogue of snowcovers at 5.3 and 35 GHz", Res. Report 96-6, Institute of Applied Physics, University of Bern, 1996

[123] Macelloni G., P.Pampaloni, M.Brogioni, E.Santi, A.Cagnati, M.Drinkwater, “DOMEX 2004: an experimental campaign at dome-C Antarctica for the calibration of space-borne low-frequency microwave radiometers”, *IEEE Transactions on Geoscience and Remote Sensing*, Vol.44, no.10, 2006, pp. 2642 – 2653

[124] Brogioni M., G. Macelloni, S. Paloscia, P. Pampaloni, S. Pettinato , E. Santi, S. Zecchetto, “Monitoring Snow Cover in Alpine Regions with Multi-Frequency Microwave Sensors”, *Proceedings of IEEE Geoscience and Remote Sensing Symposium, IGARSS 2007, in press*

[125] Colbeck S., E. Akitaya, R. Armstrong, H. Gubler, J. Lafeuille, K. Lied, D. McClung and E. Morris, “The International Classification for Seasonal Snow on the Ground. International association of scientific hydrology”, In: *International Commission of Snow and Ice. Working group on Snow Classification*, 1990

[126] Tedesco M., “Microwave remote sensing of snow”, PhD Thesis, University of Potenza, 2003

Appendix 1: Validation of the AIEM model

In this chapter, the comparisons made in the validation phase between the AIEM simulations and the FDTD data provided by ESA will be shown. These latter are considered as data truth. All the comparisons are made for surfaces with mono-dimensional correlation function. The validation of the model for bi-dimensional surface has been carried out by means of the ISPRA-JRC experimental data.

For sake of convenience the labels over the axes are omitted. This has been done for improve the readability of the diagrams. The horizontal axe represents the scattering angle (degrees) and the vertical one represents the bistatic scattering coefficient γ (dB). The incidence angle is indicated in the legend of the graphs. The continuous lines indicate the AIEM data while the dashed ones represent the FDTD reference data. The horizontal polarization is depicted in pink and the vertical polarization is depicted in blue.

The simulations at L and C band are carried out respectively at 1.25 GHz and 5 GHz.

Exponential correlated surfaces

- Land L ks=0.12 kl=1.48 eps=8.5+j1.2

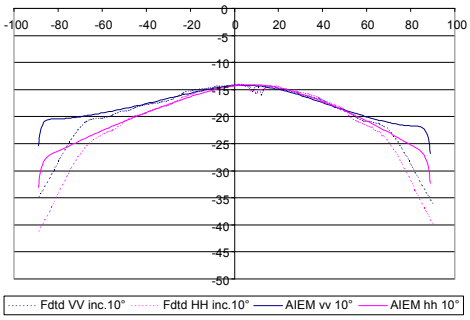

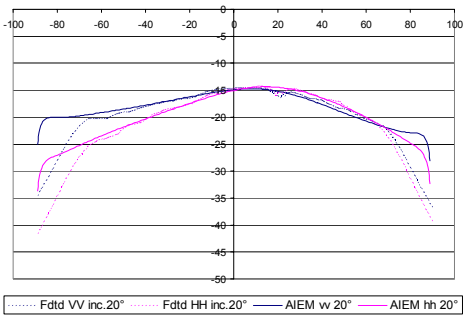

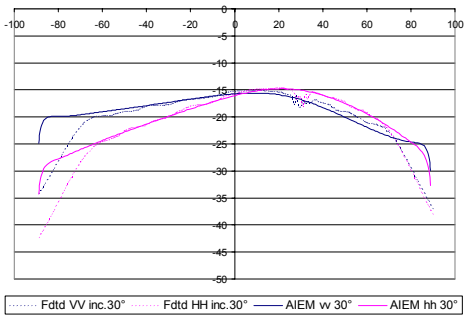

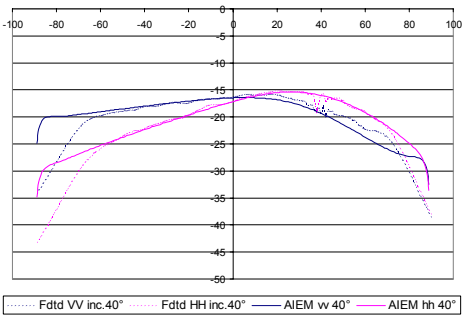

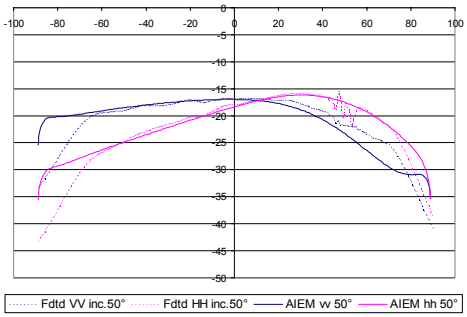

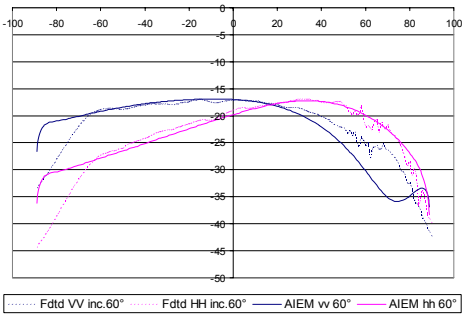

- Land L ks=0.12 kl=1.48 eps=27+j4

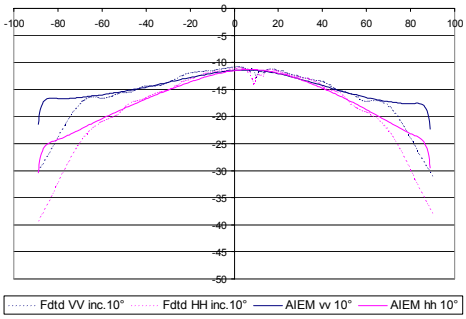

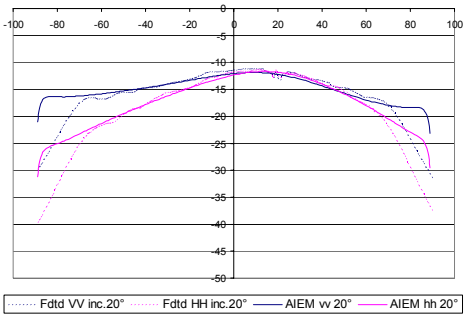

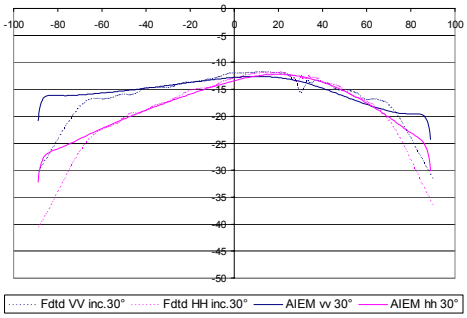

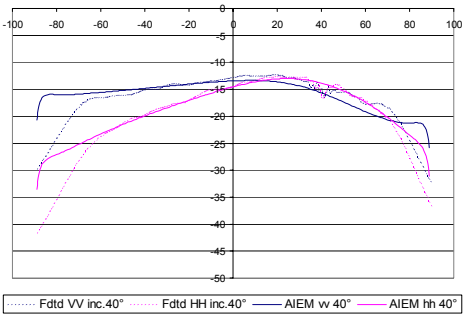

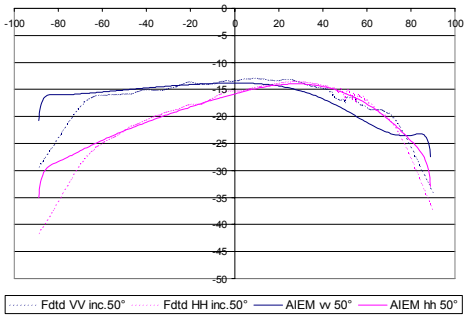

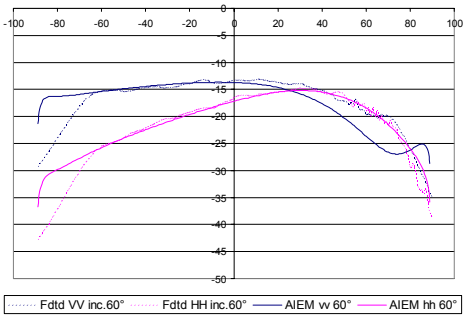

- Land L ks=0.12 kl=2.96 eps=8.5+j1.2

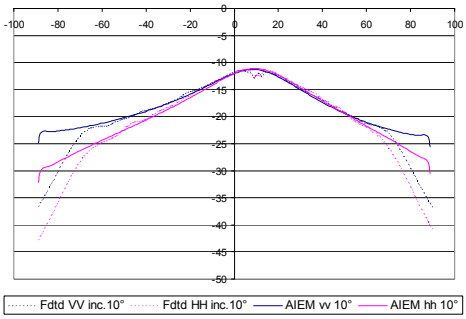

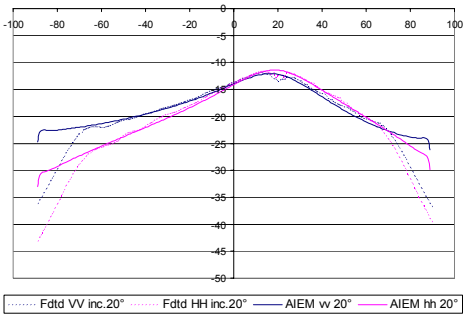

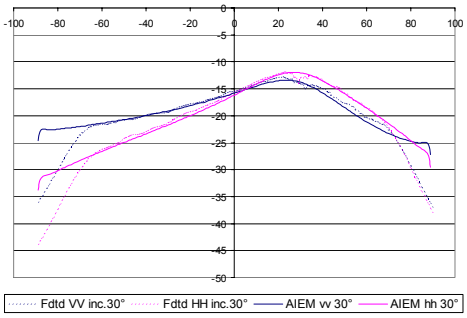

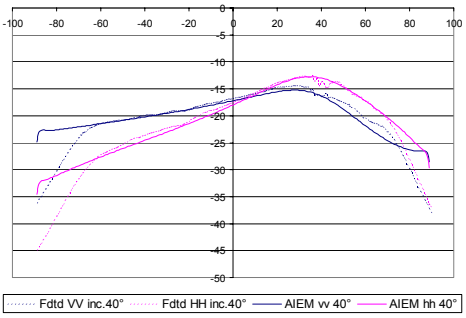

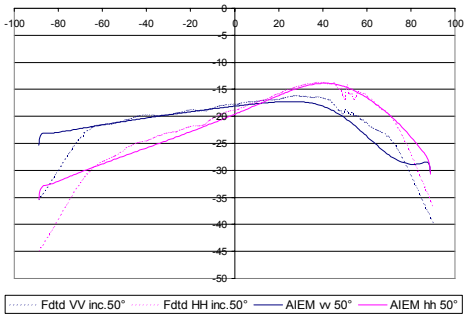

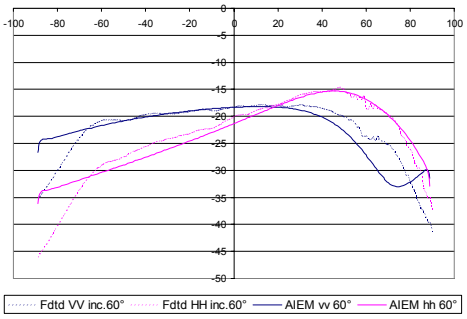

- Land L ks=0.12 kl=2.96 eps=27+j4

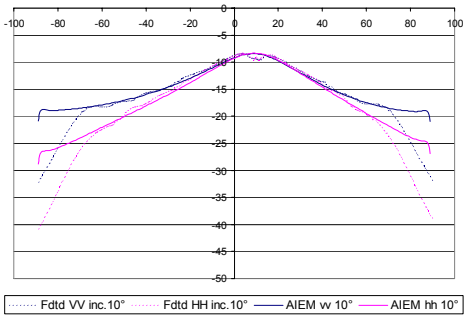

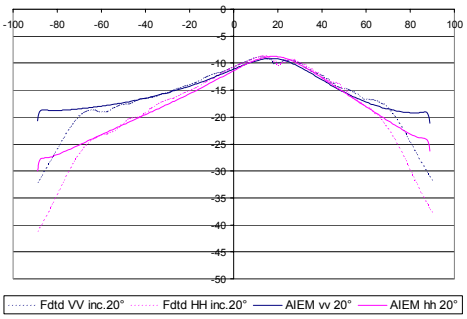

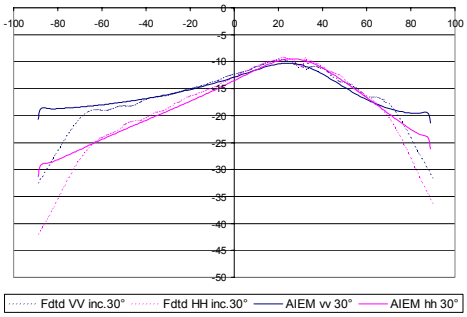

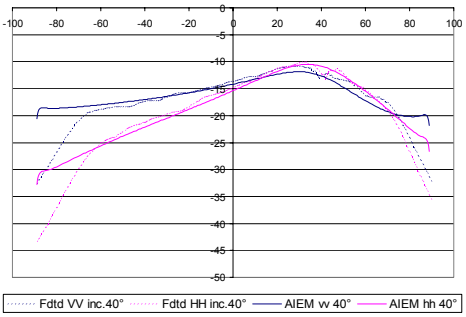

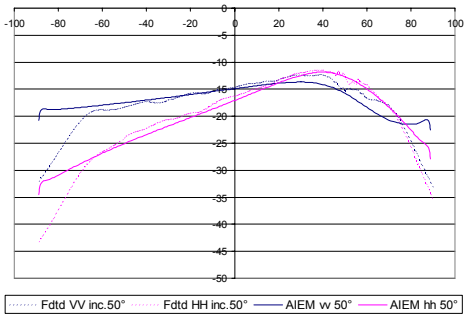

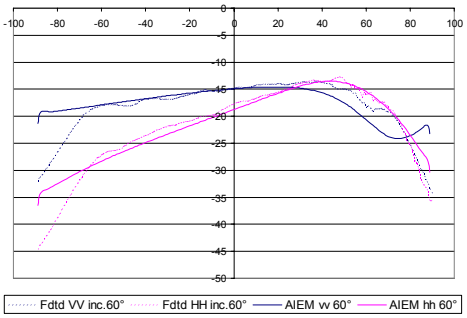

- Land L ks=0.23 kl=1.48 eps=8.5+j1.2

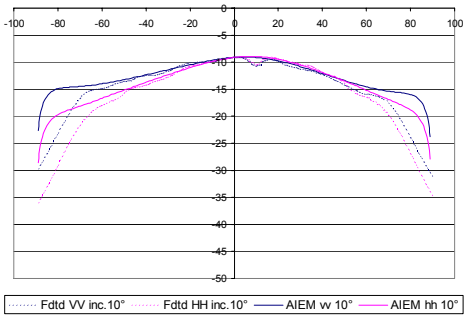

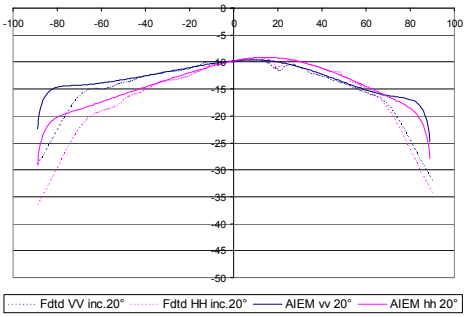

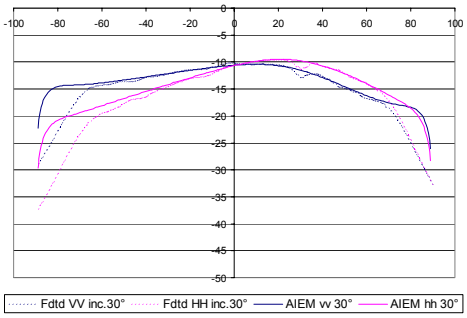

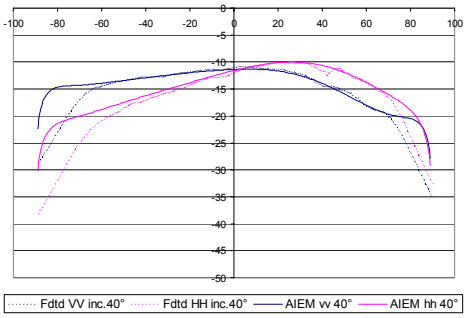

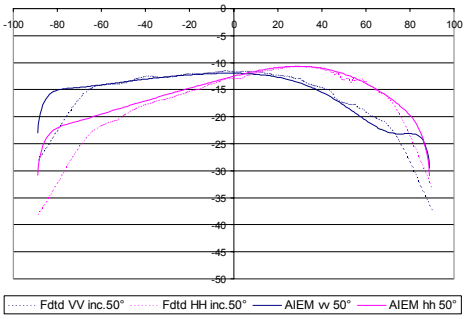

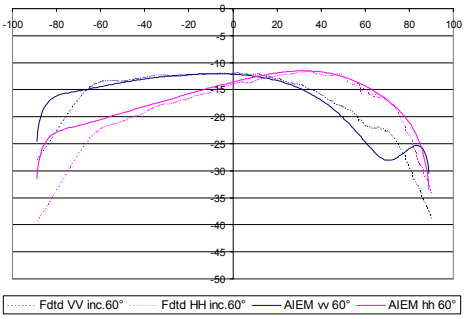

- Land L ks=0.23 kl=1.48 eps=27+j4

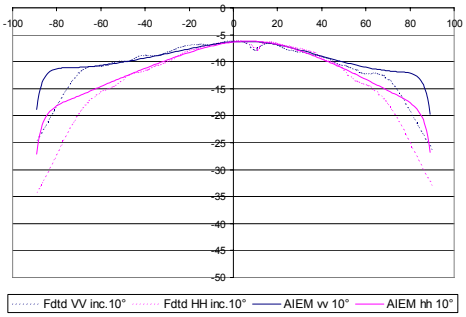

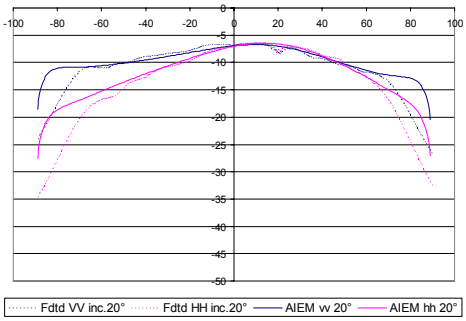

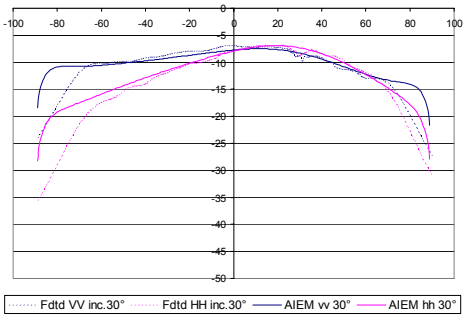

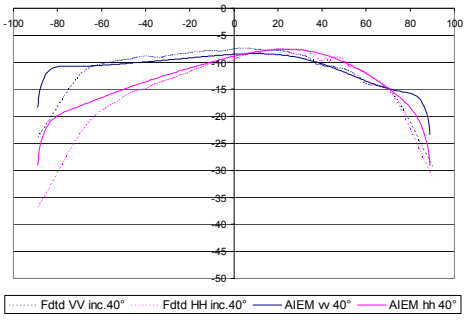

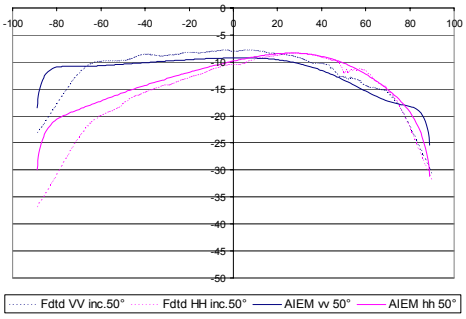

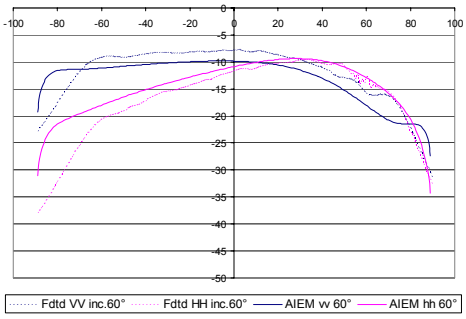

- Land L ks=0.23 kl=2.96 eps=8.5+j1.2

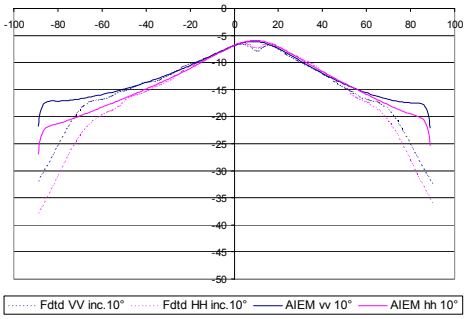

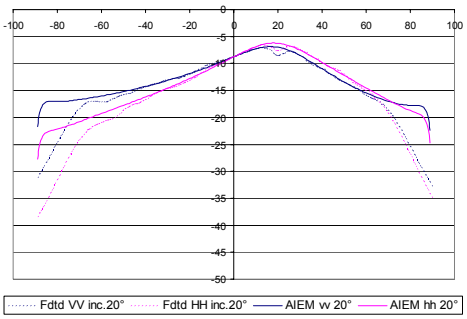

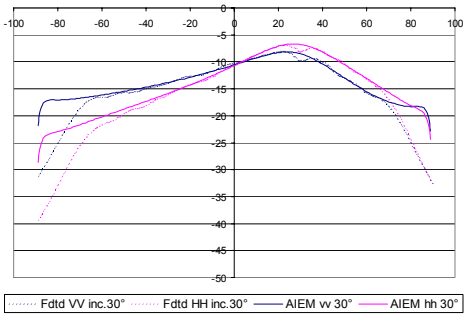

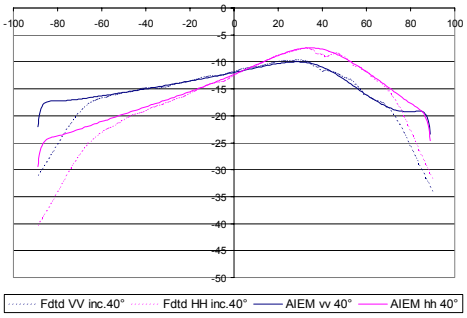

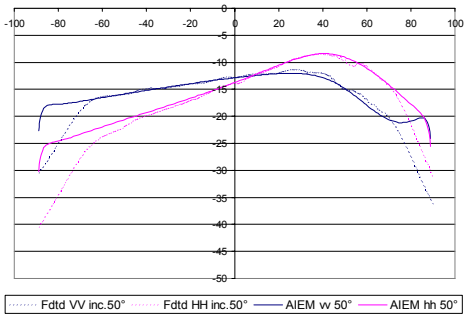

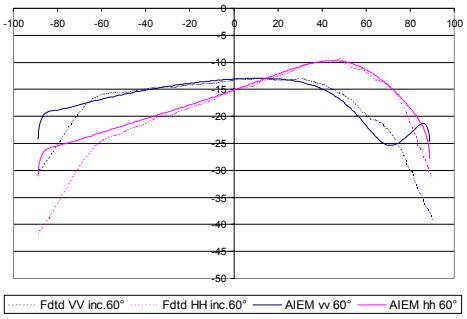

- Land L ks=0.23 kl=2.96 eps=27+j4

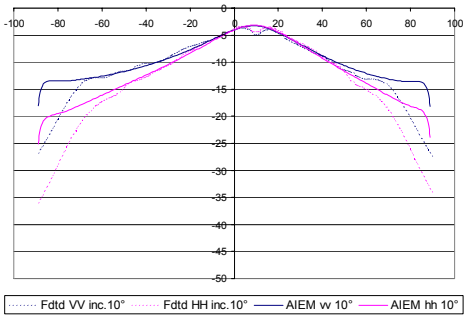

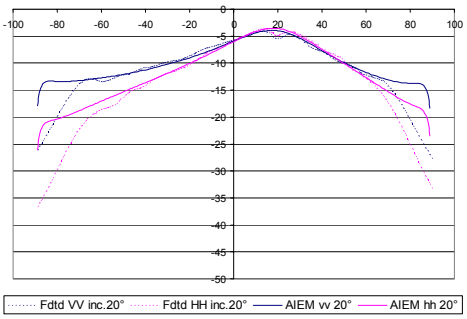

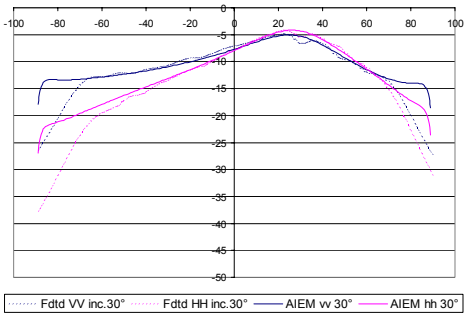

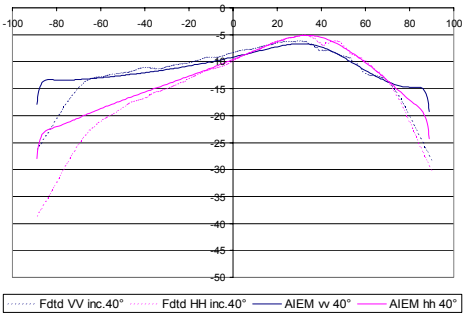

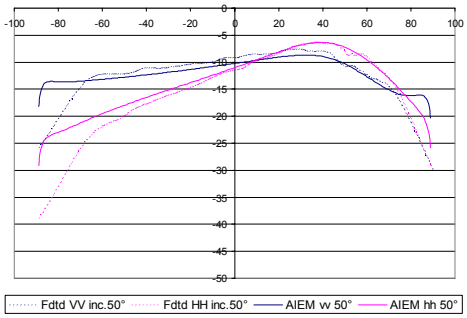

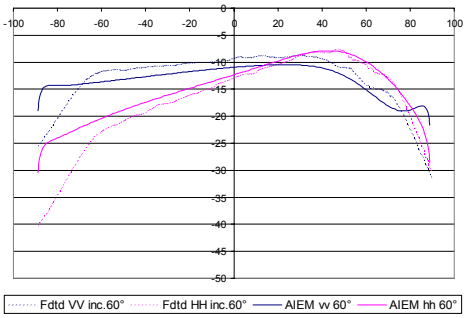

- Land L ks=0.35 kl=1.48 eps=8.5+j1.2

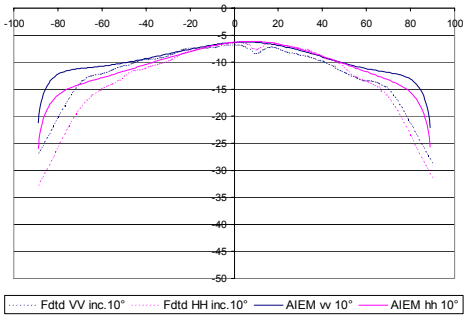

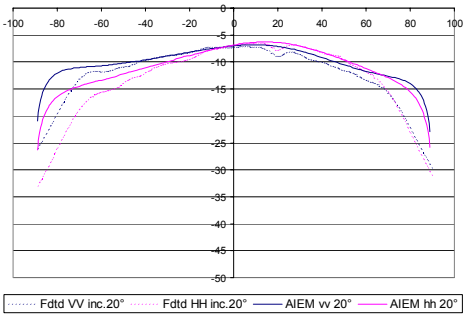

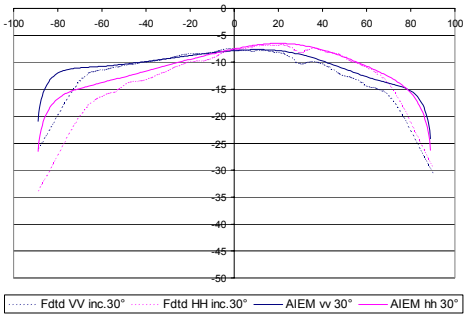

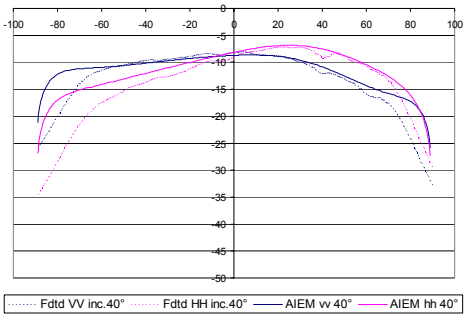

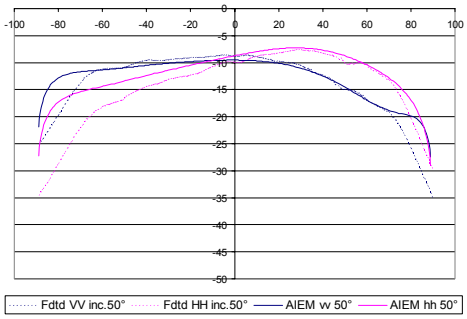

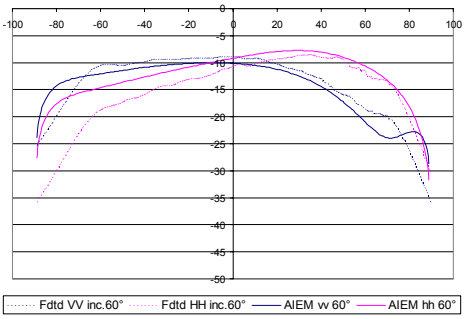

- Land L ks=0.35 kl=1.48 eps=27+j4

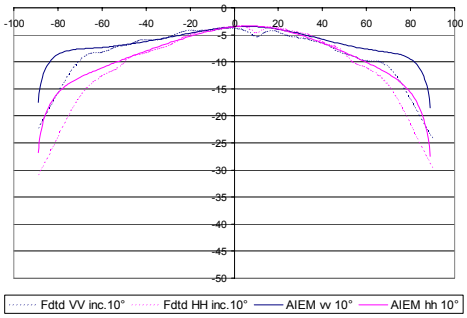

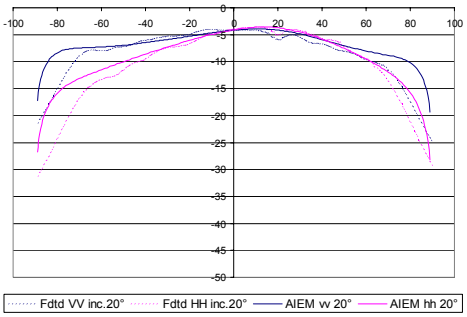

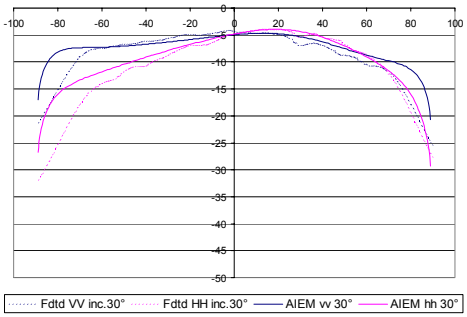

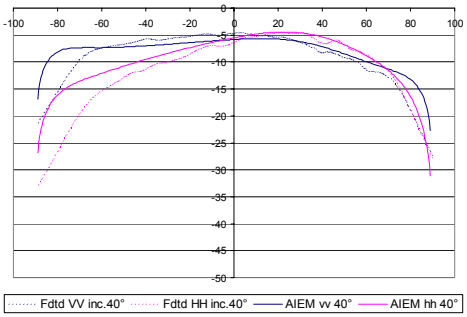

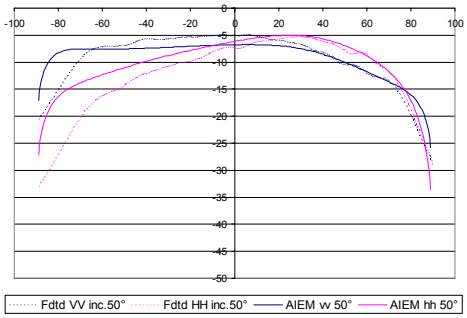

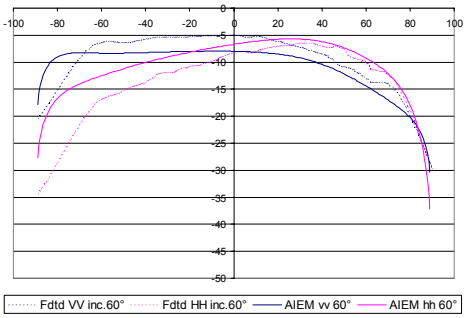

- Land L ks=0.35 kl=2.96 eps=8.5+j1.2

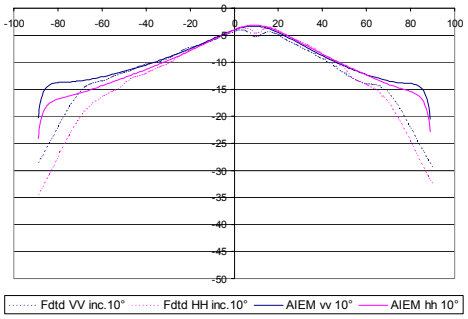

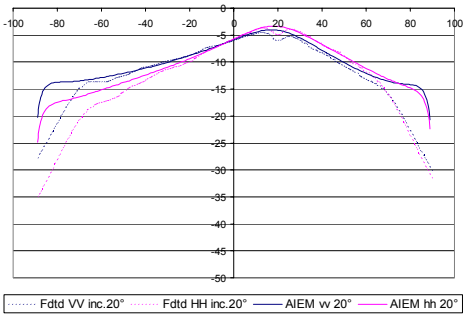

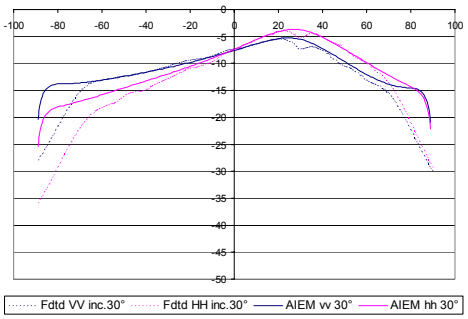

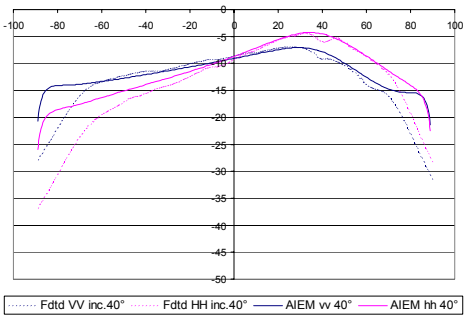

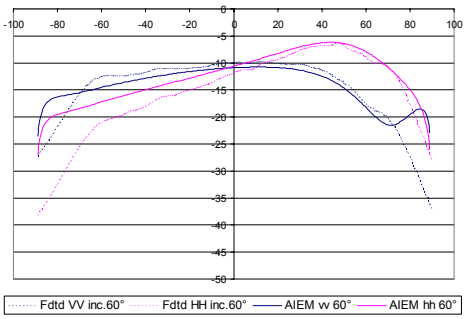

- Land L ks=0.35 kl=2.96 eps=27+j4

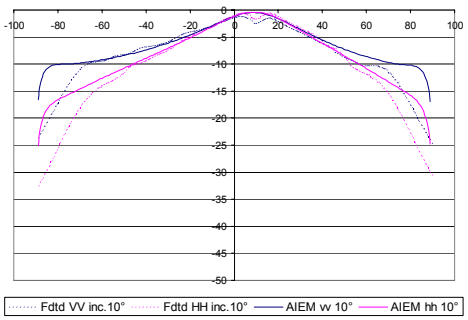

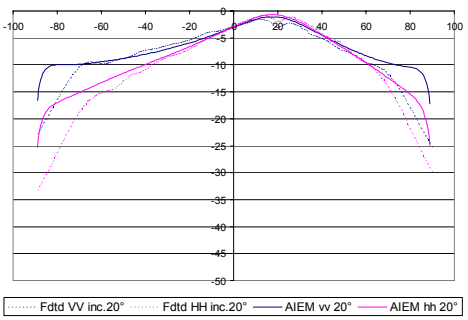

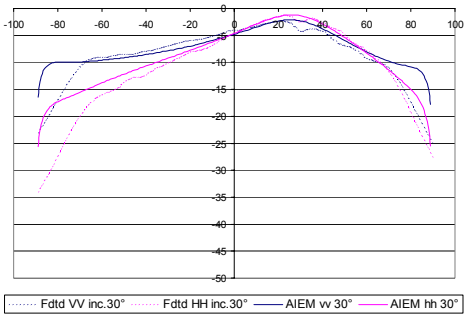

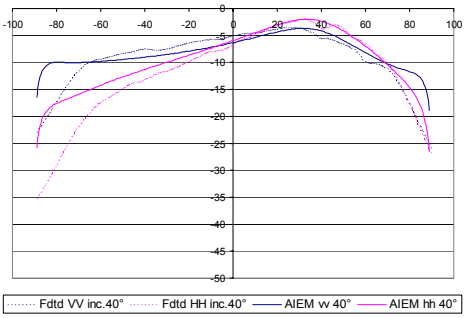

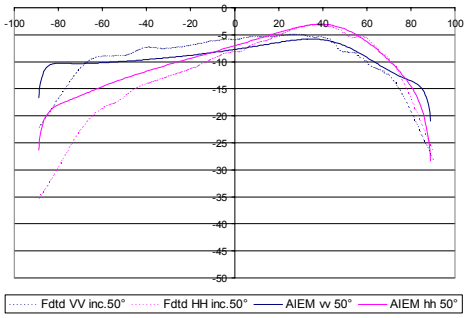

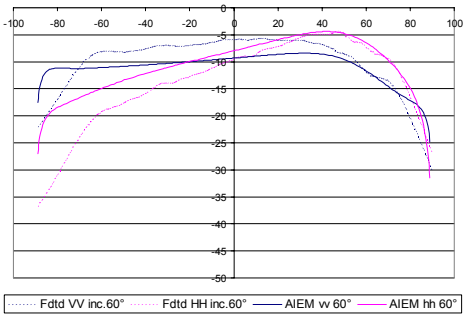

- Land L ks=0.47 kl=1.48 eps=8.5+j1.2

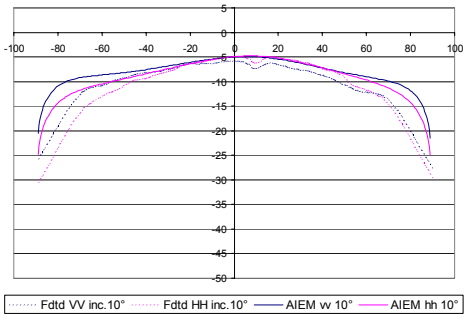

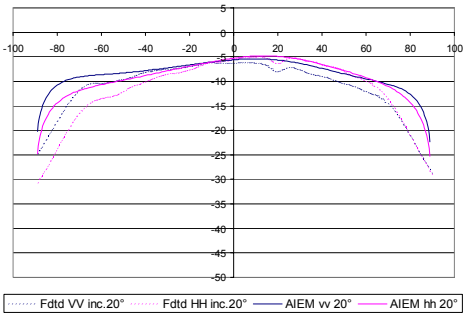

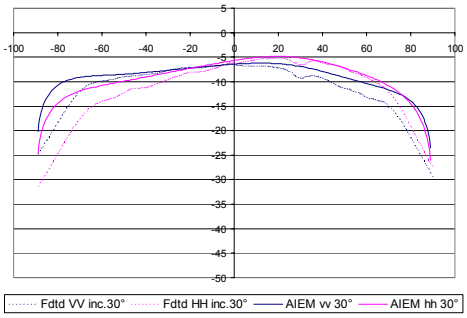

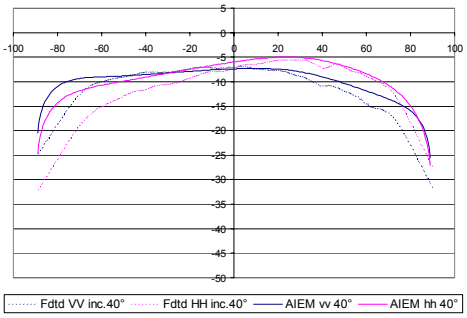

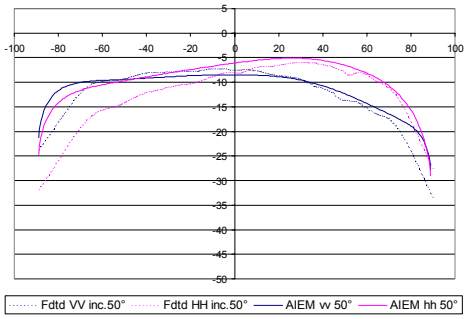

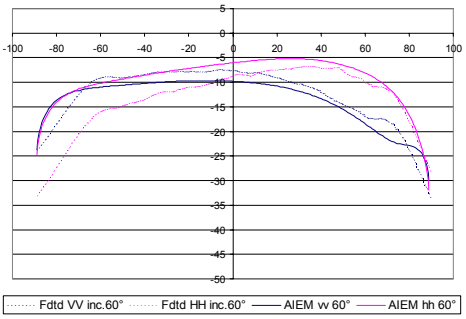

- Land L ks=0.47 kl=1.48 eps=27+j4

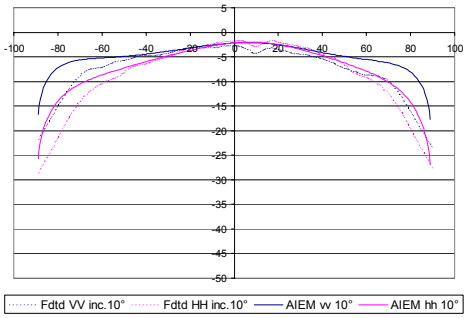

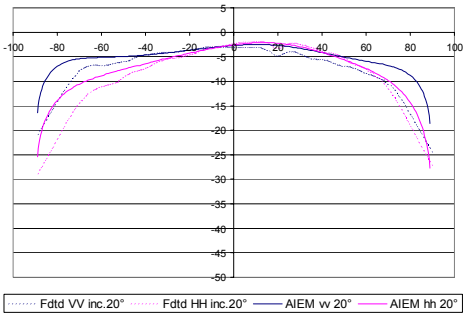

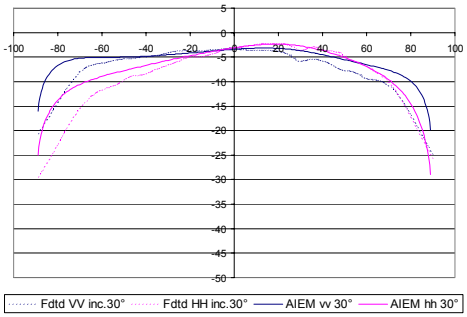

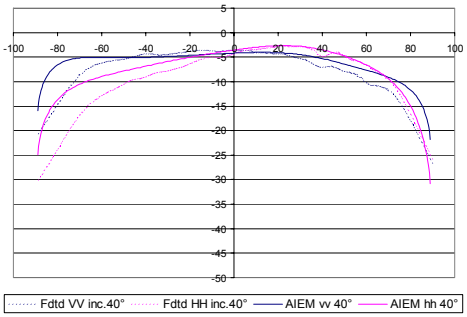

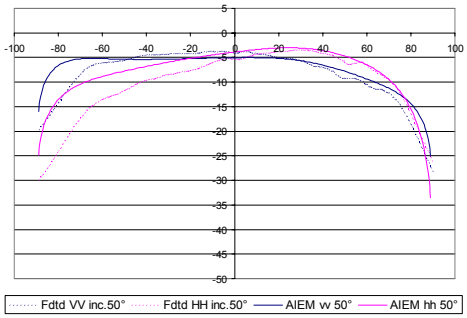

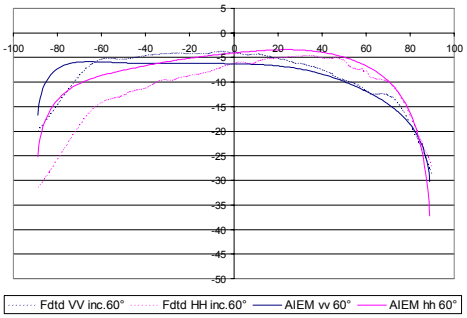

- Land L ks=0.47 kl=2.96 eps=8.5+j1.2

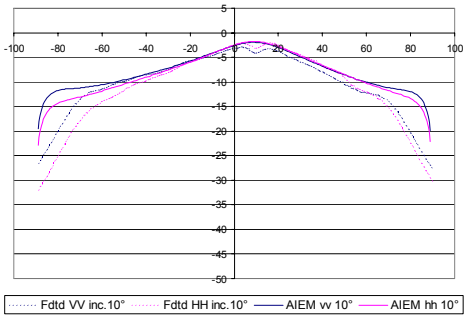

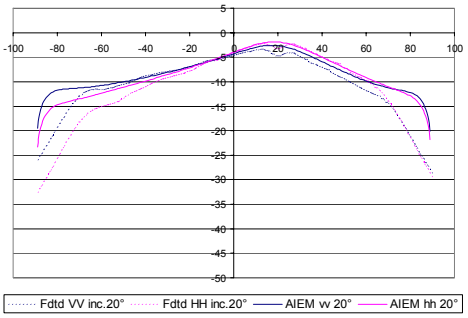

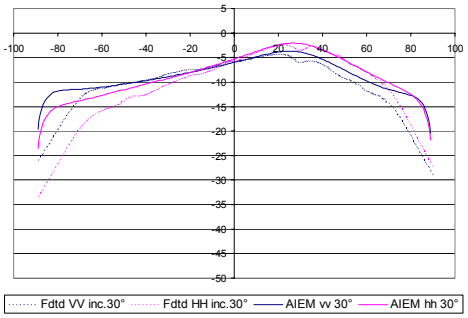

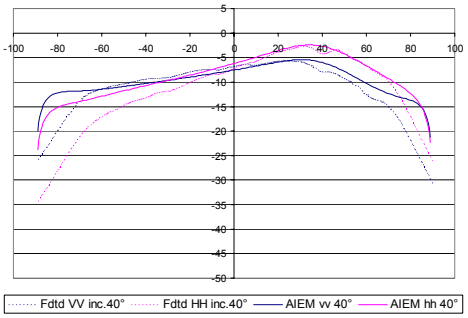

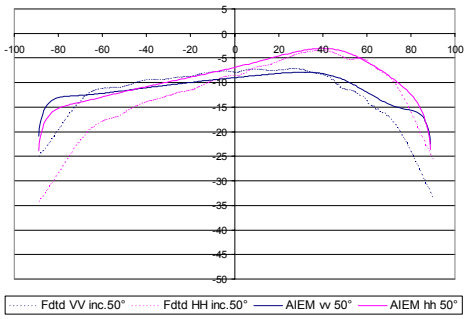

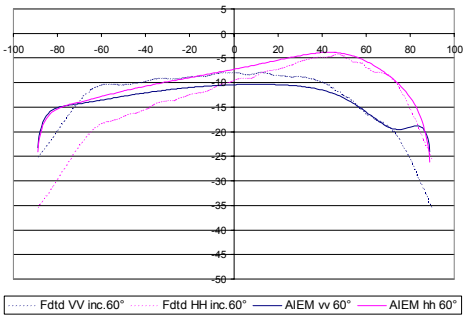

- Land L ks=0.47 kl=2.96 eps=27+j4

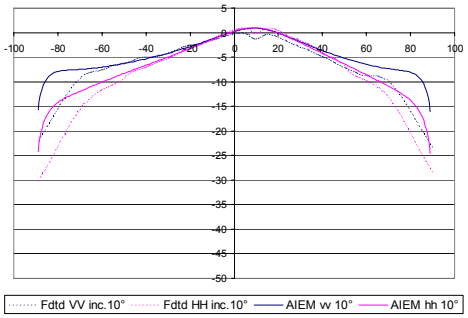

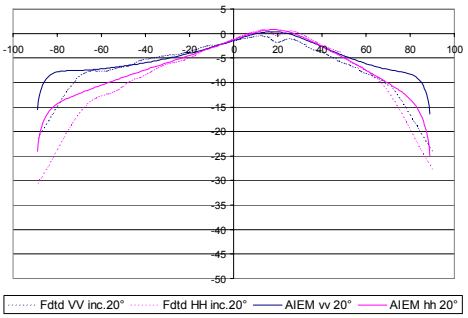

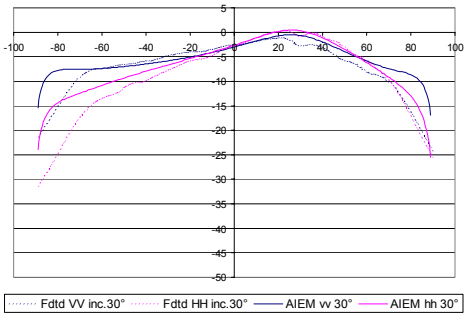

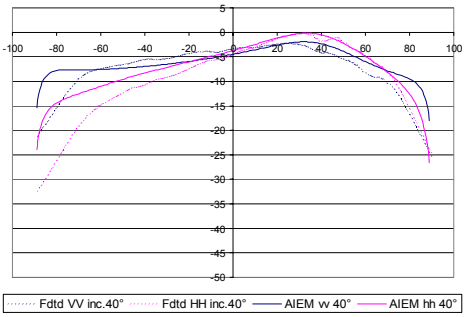

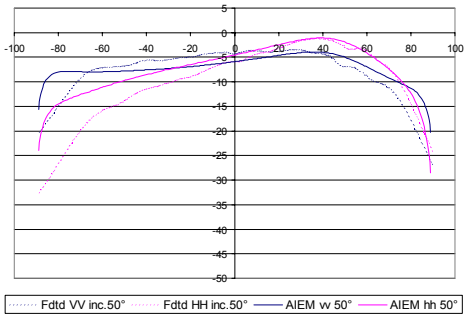

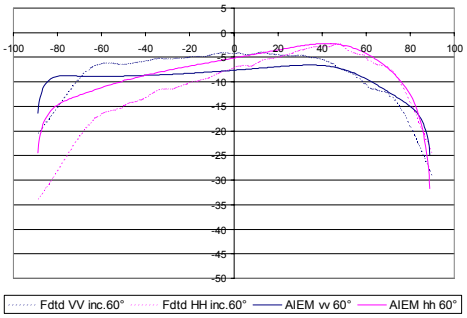

- Land L ks=0.82 kl=1.48 eps=8.5+j1.2

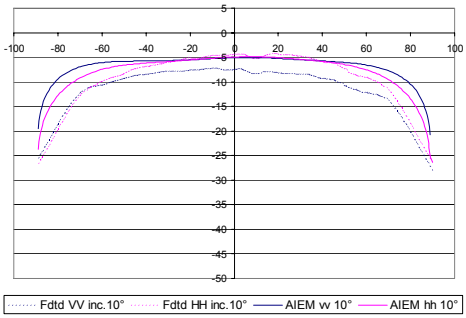

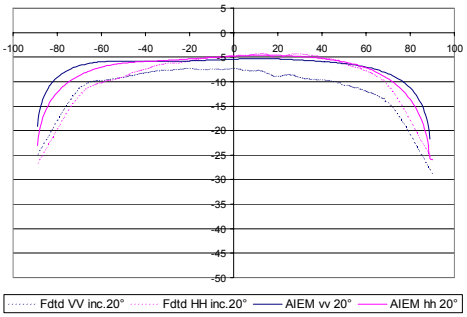

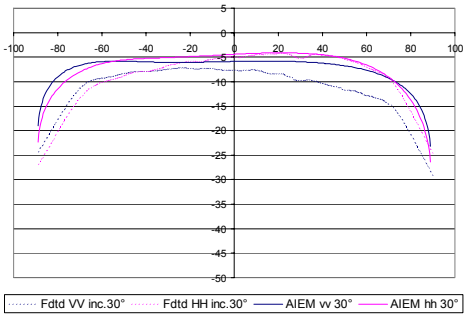

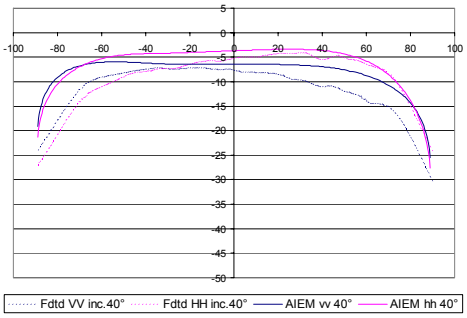

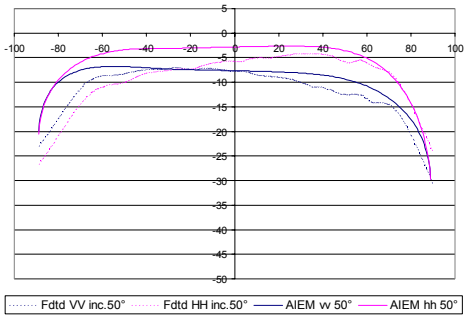

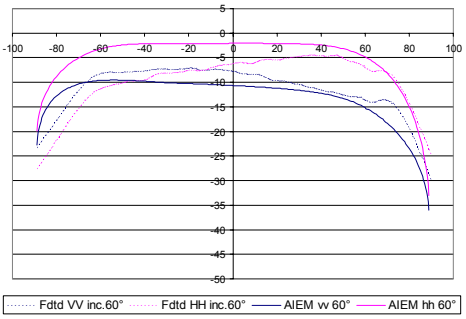

- Land L ks=0. 82 kl=1.48 eps=27+j4

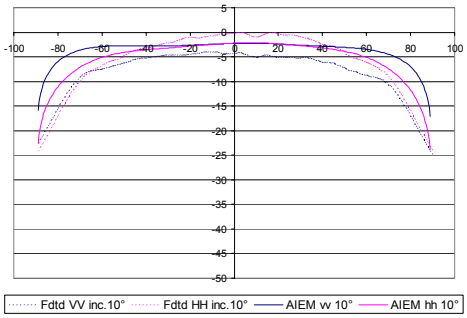

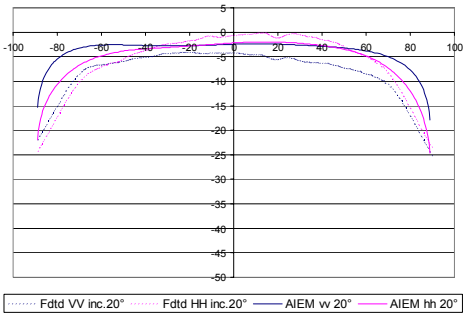

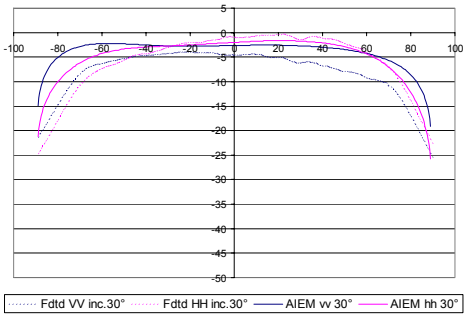

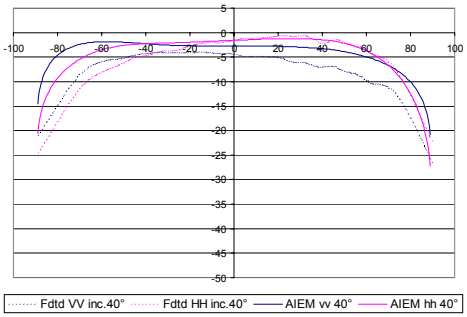

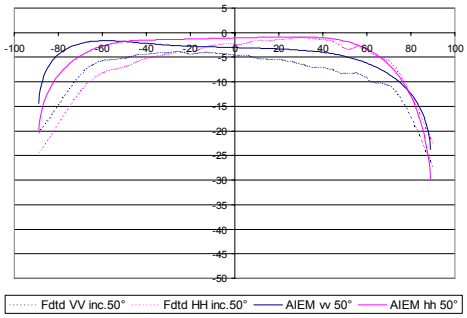

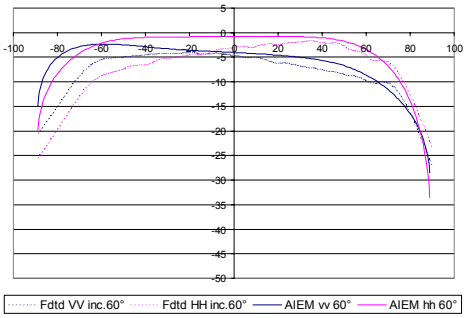

- Land L ks=0. 82 kl=2.96 eps=27+j4

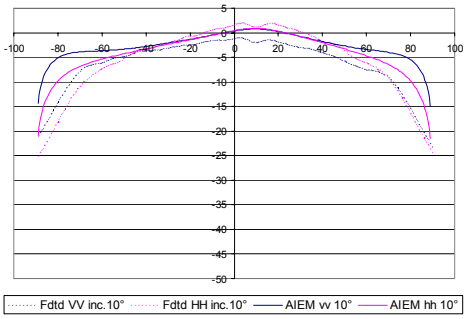

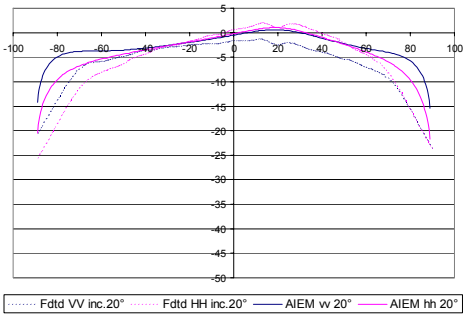

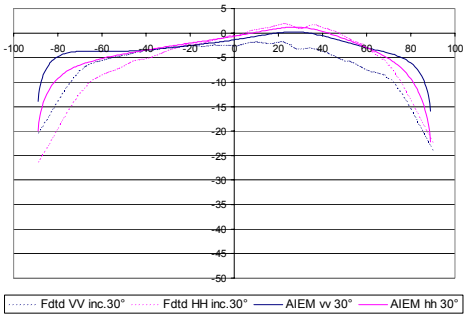

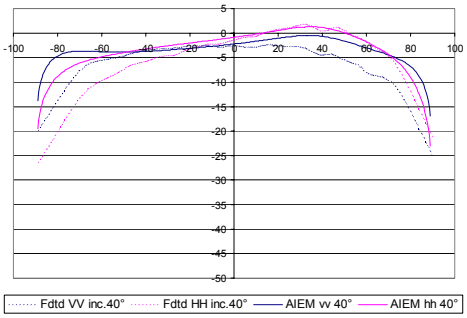

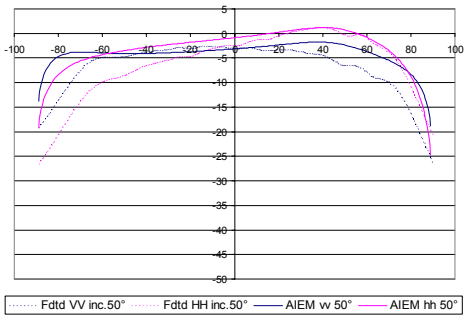

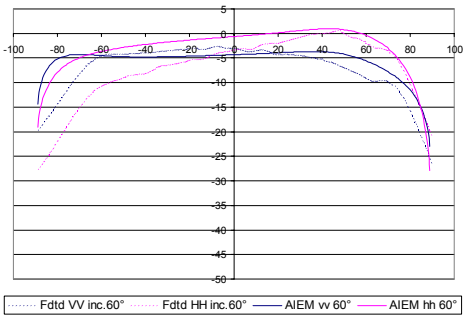

- Land C ks=0.5 kl=6.28 eps=4.06+j0.3

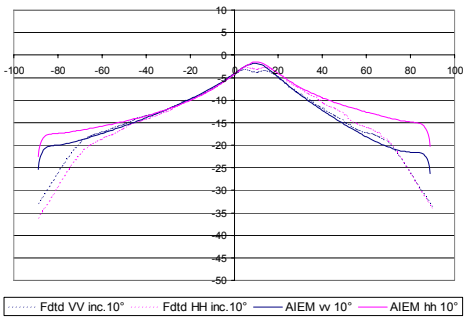

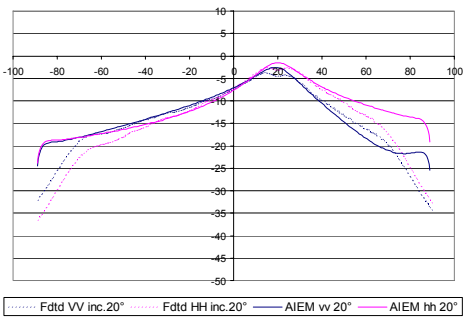

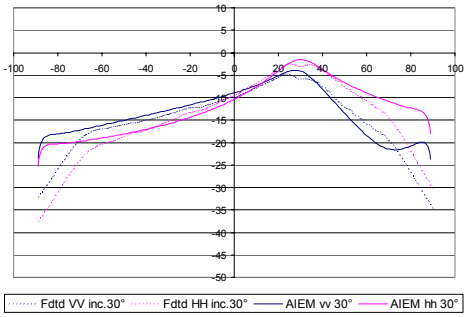

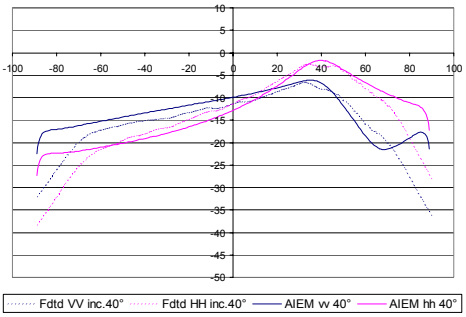

- Land C ks=0.5 kl=6.28 eps=7.0+j0.8

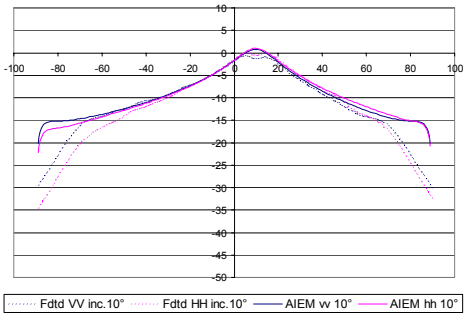

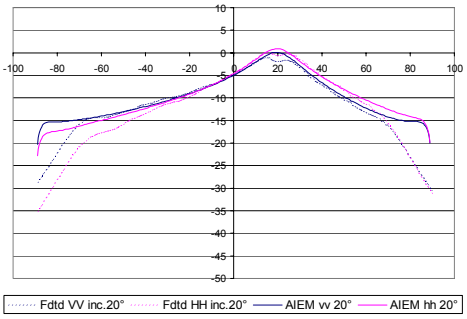

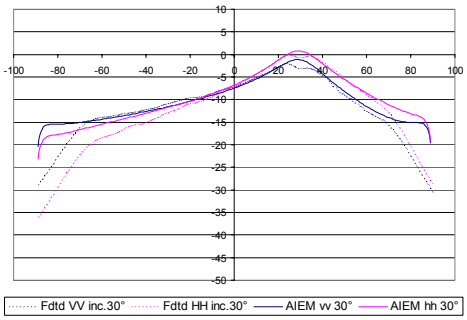

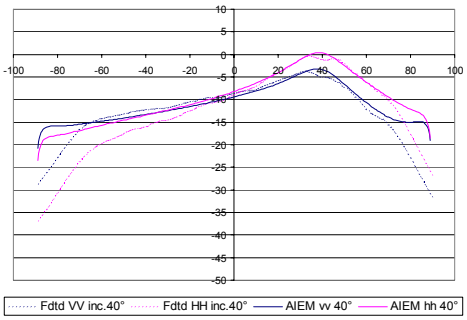

- Land C ks=0.5 kl=6.28 eps=24+j3.19

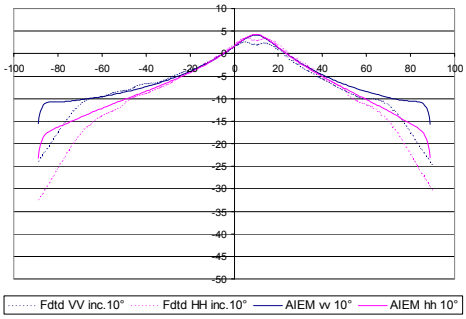

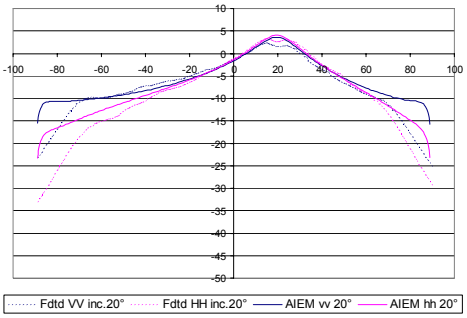

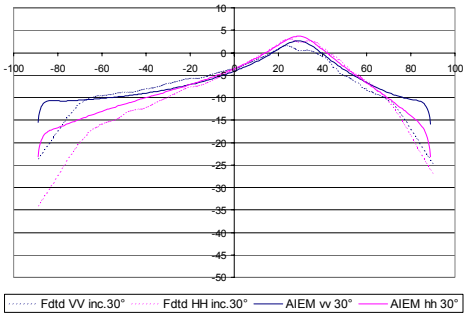

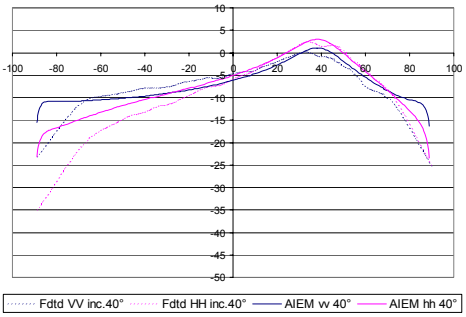

- Land C ks=0.5 kl=12.57 eps=4.06+j0.3

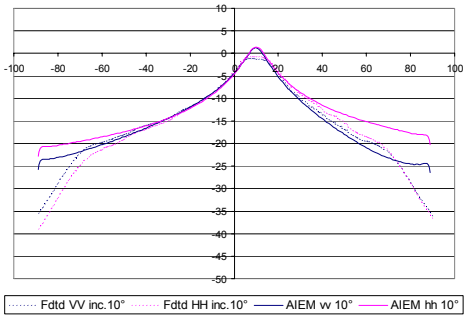

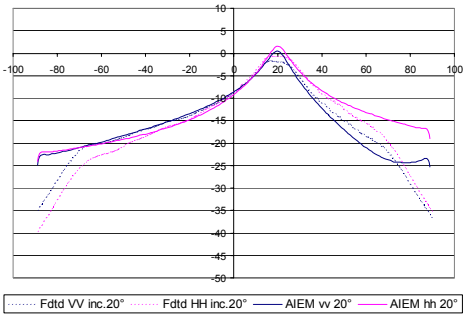

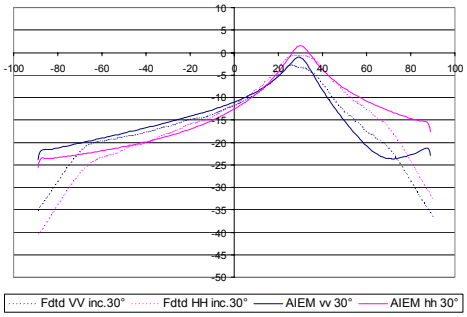

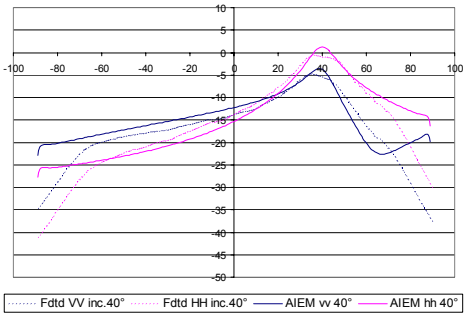

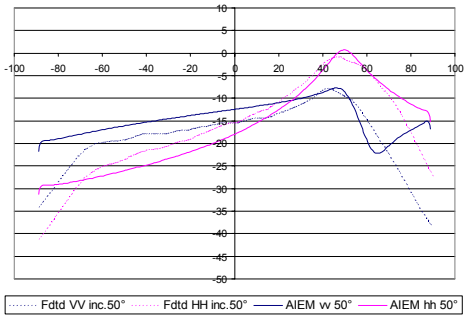

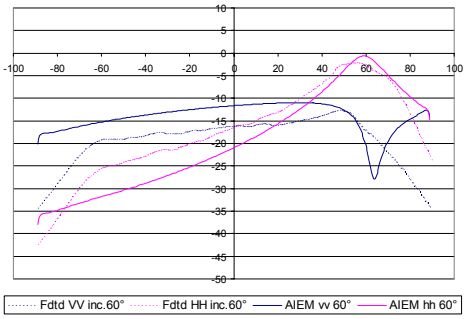

- Land C ks=0.5 kl=12.57 eps=7.0+j0.8

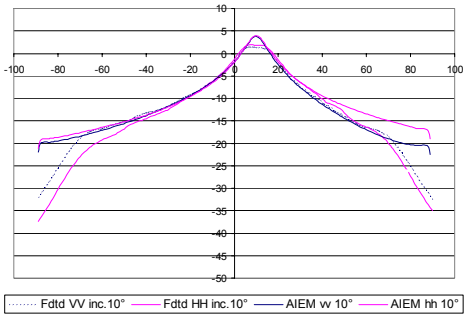

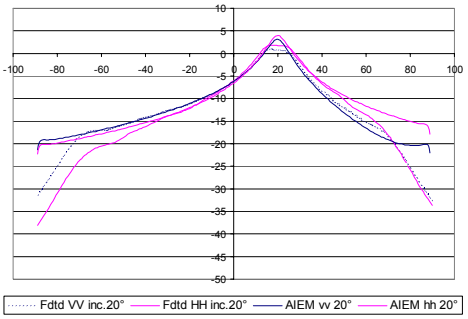

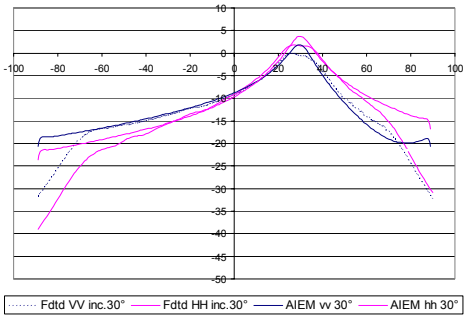

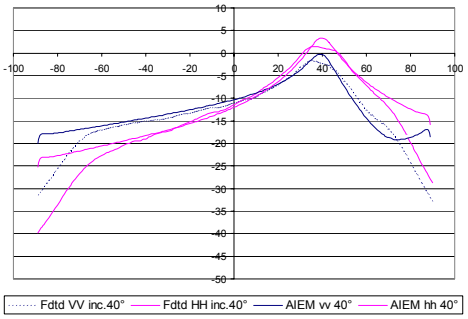

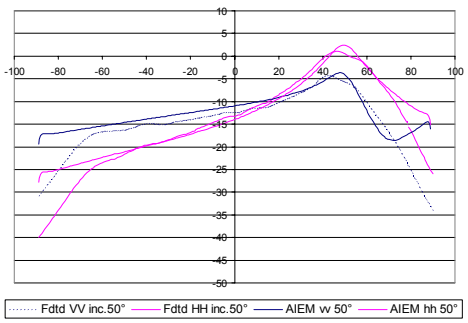

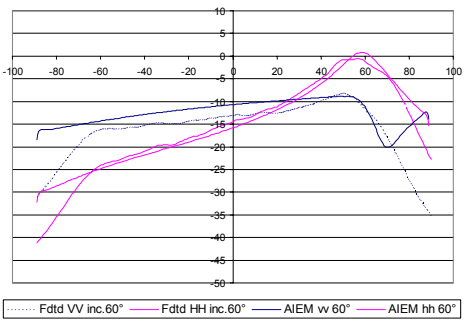

- Land C ks=0.5 kl=12.57 eps=24+j3.19

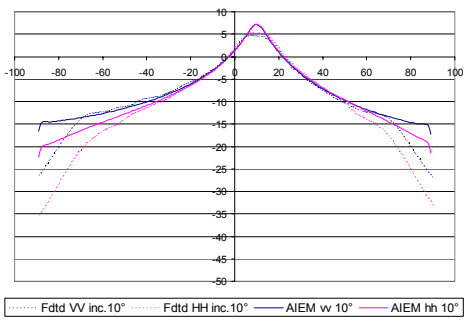

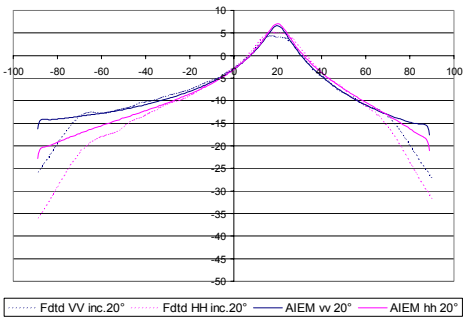

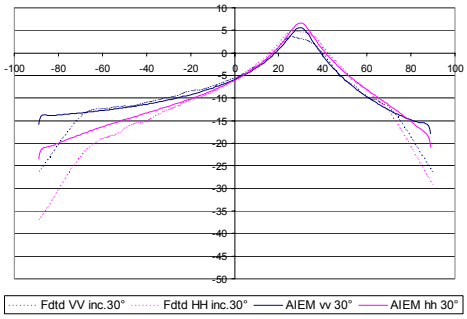

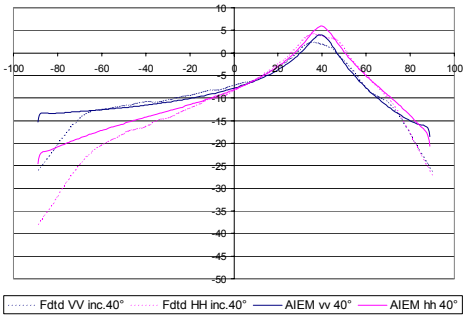

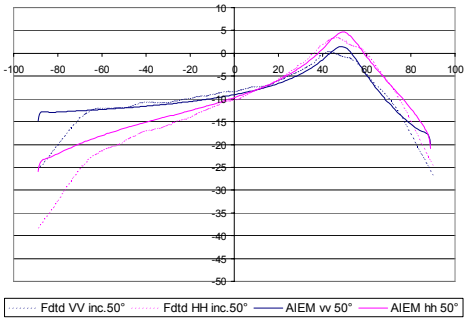

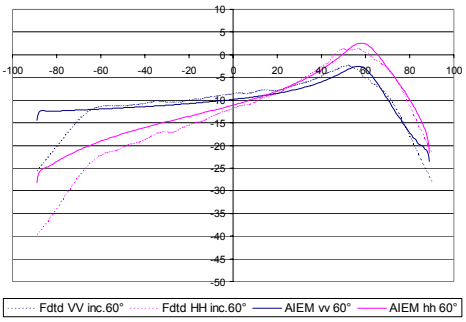

- Land C ks=1.0 kl=6.28 eps=4.06+j0.3

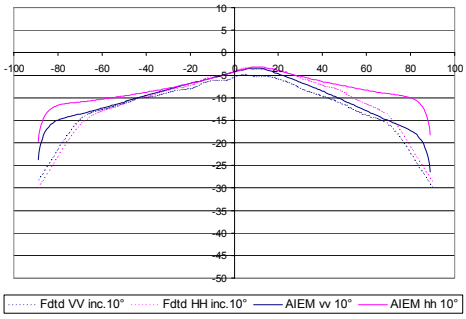

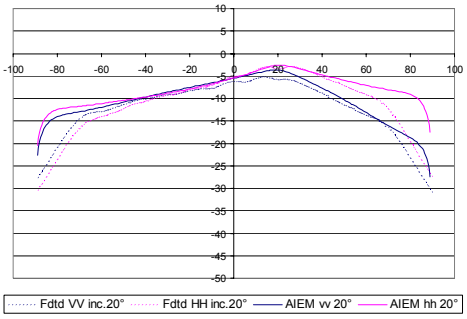

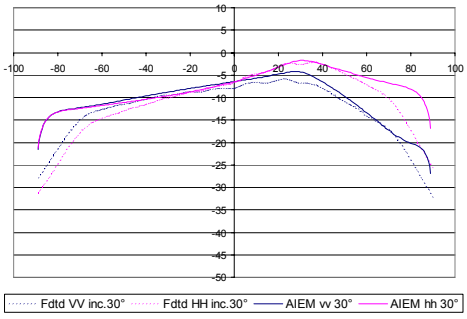

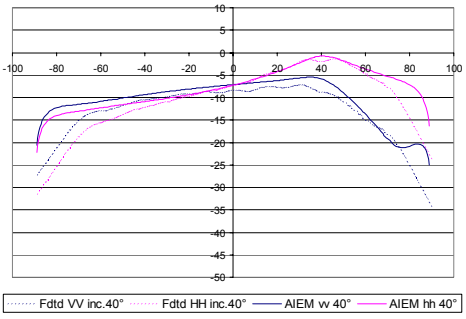

- Land C ks=1.0 kl=6.28 eps=7.0+j0.8
-

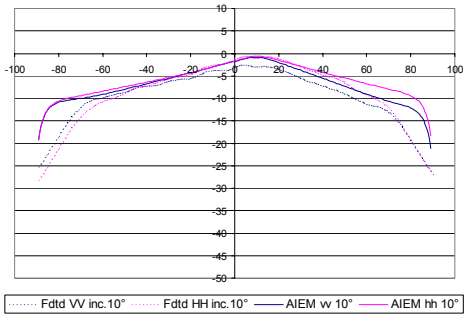

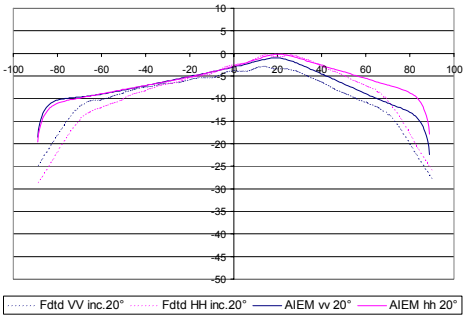

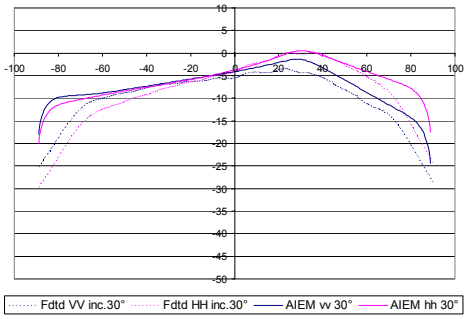

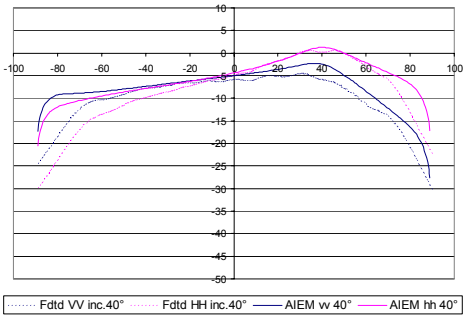

- Land C ks=1.0 kl=6.28 eps=24+j3.19

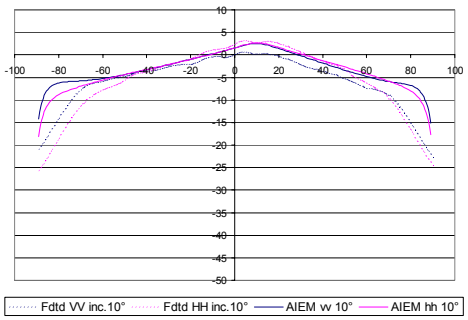

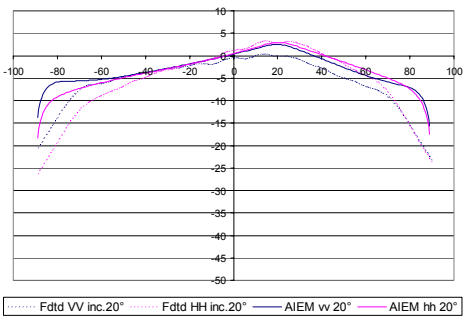

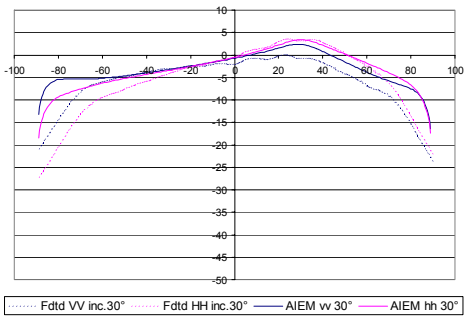

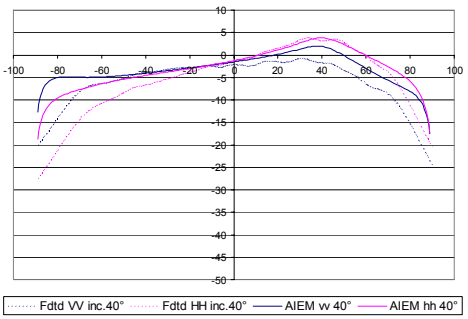

- Land C ks=1.0 kl=12.57 eps=4.06+j0.3

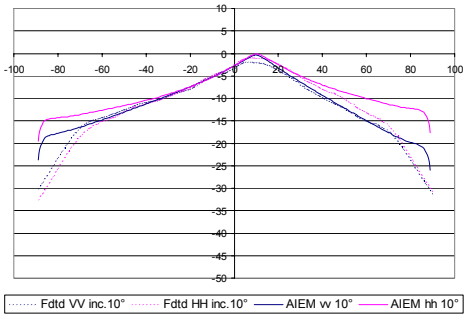

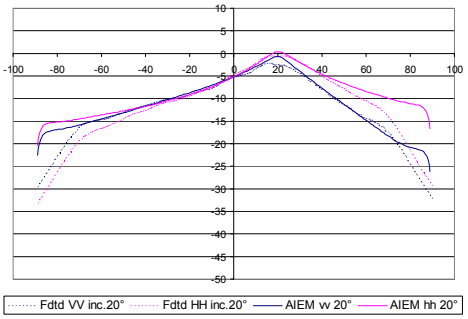

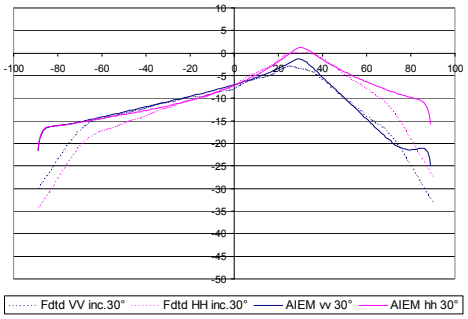

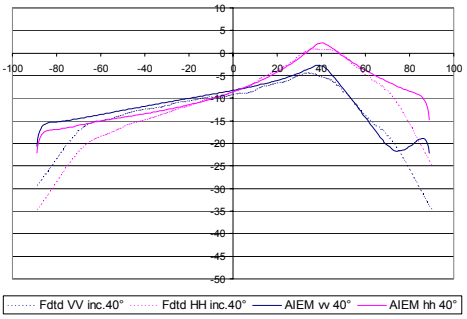

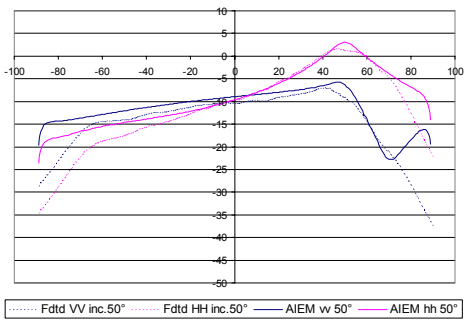

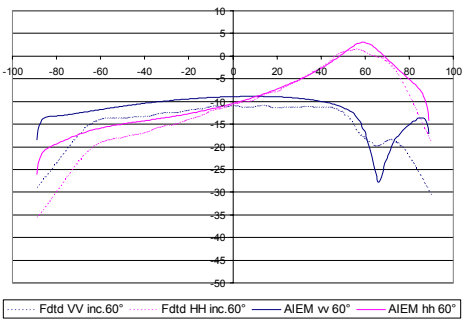

- Land C ks=1.0 kl=12.57 eps=7.0+j0.8

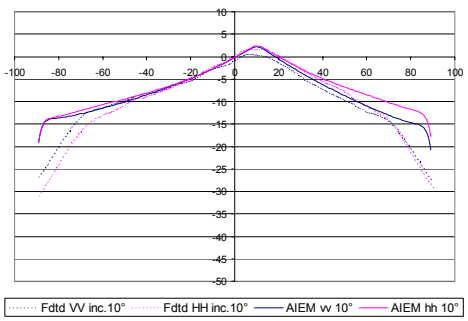

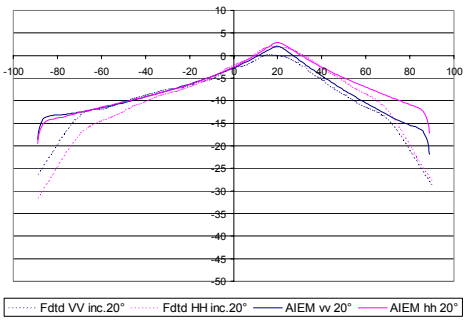

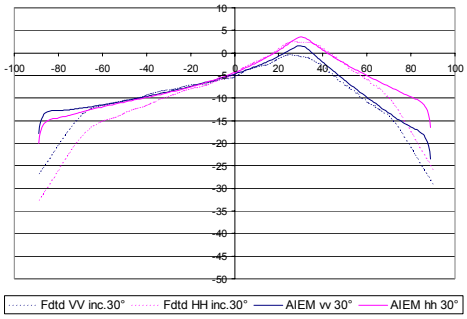

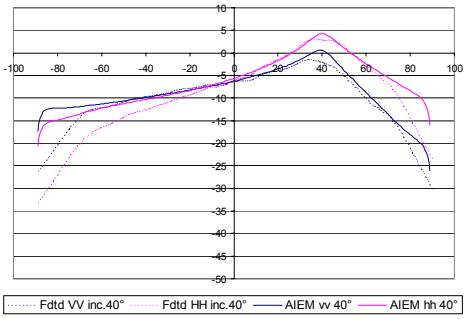

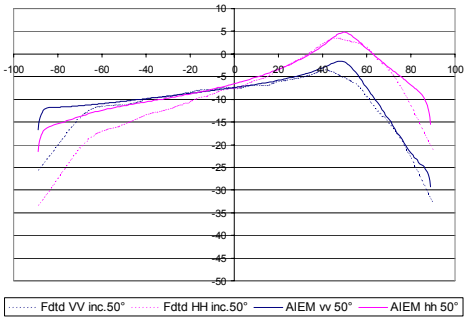

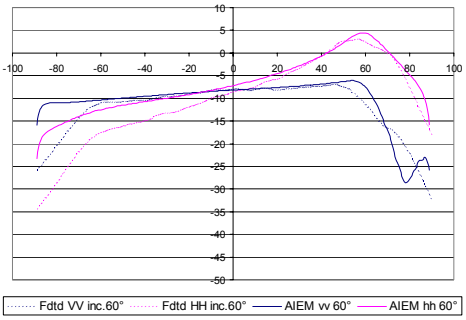

- Land C ks=1.0 kl=12.57 eps=24+j3.19

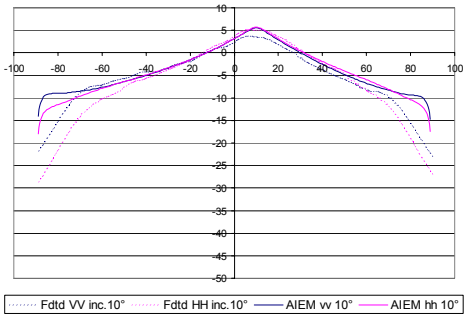

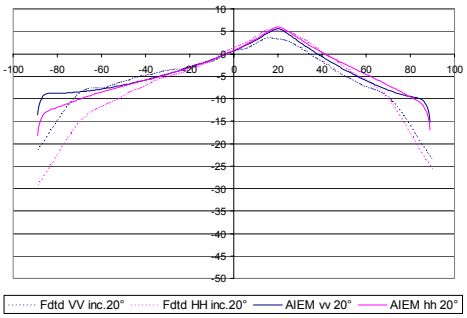

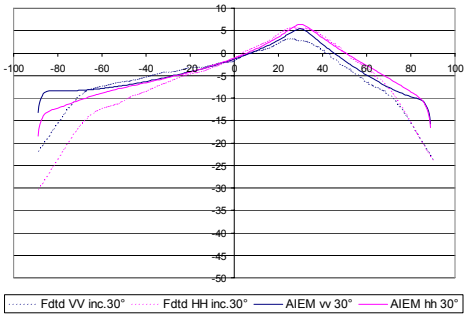

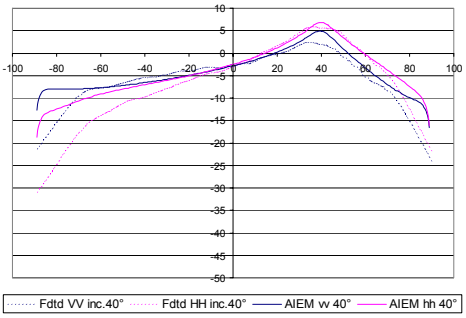

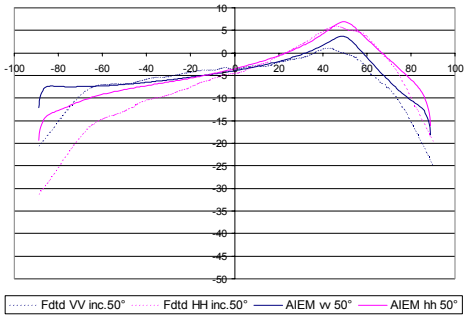

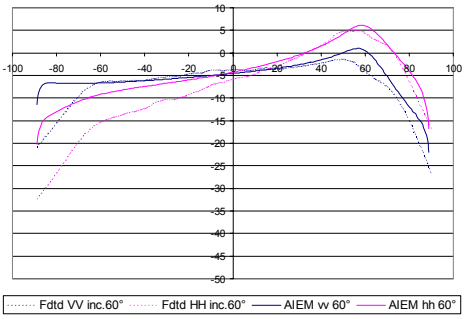

- Land C ks=1.5 kl=6.28 eps=4.06+j0.3

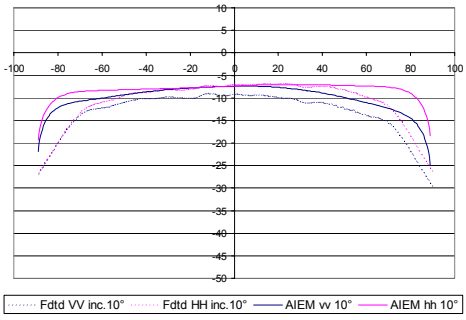

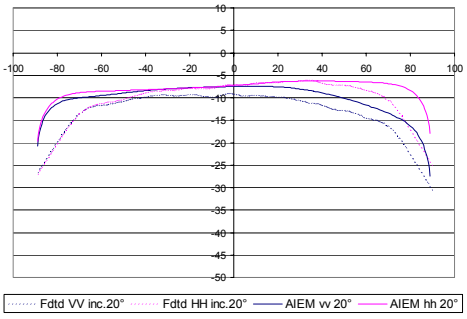

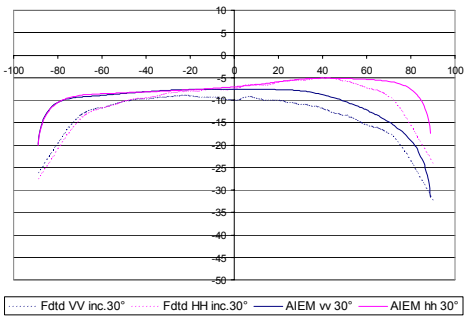

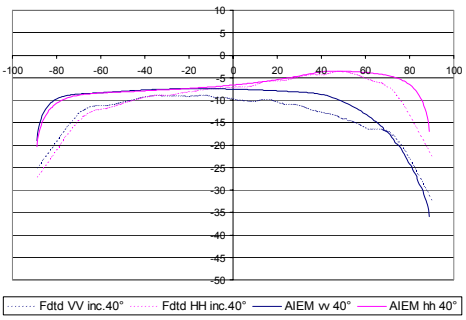

- Land C ks=1.5 kl=6.28 eps=7.0+j0.8

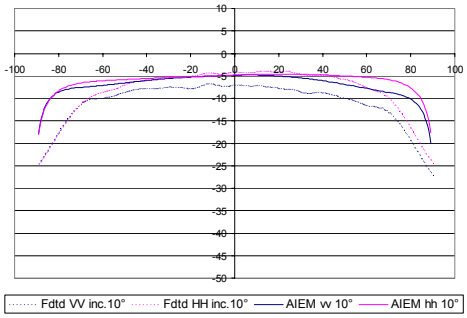

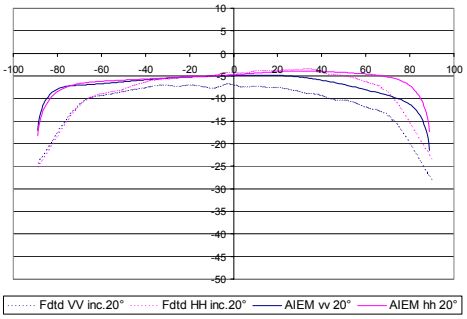

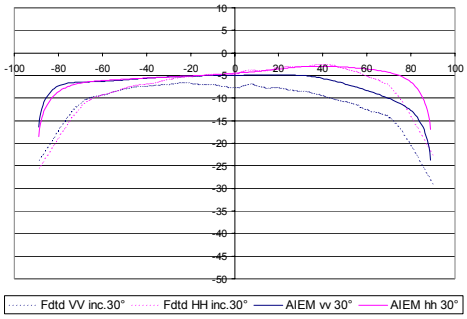

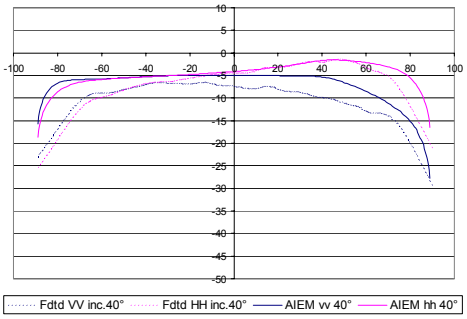

- Land C ks=1.5 kl=6.28 eps=24+j3.19

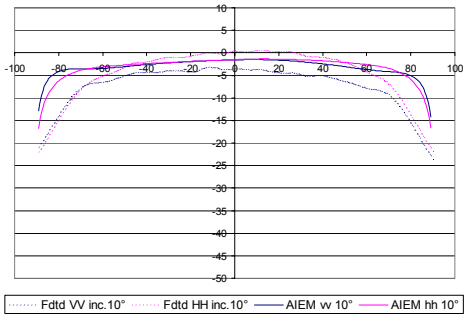

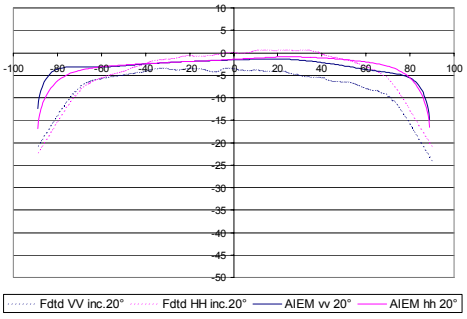

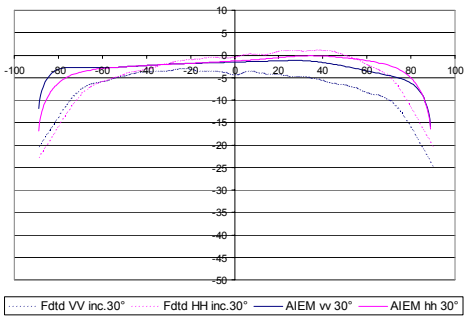

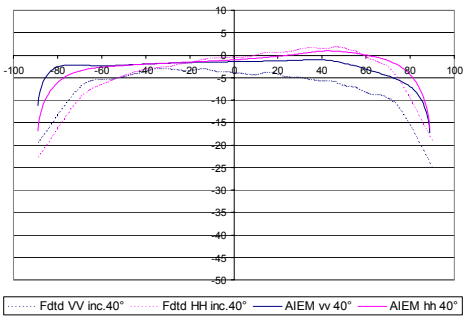

- Land C ks=1.5 kl=12.57 eps=4.06+j0.3

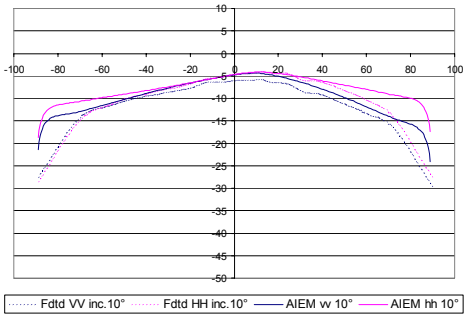

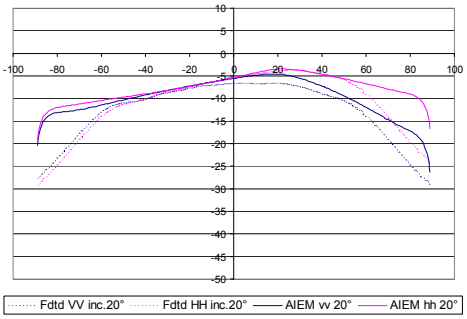

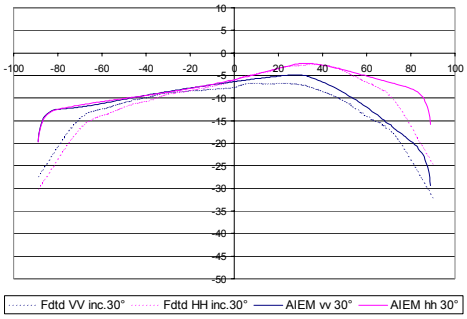

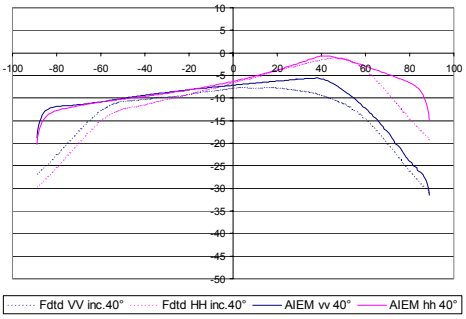

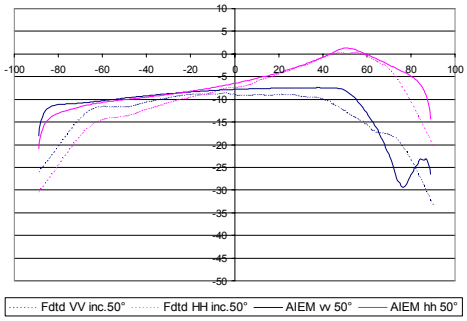

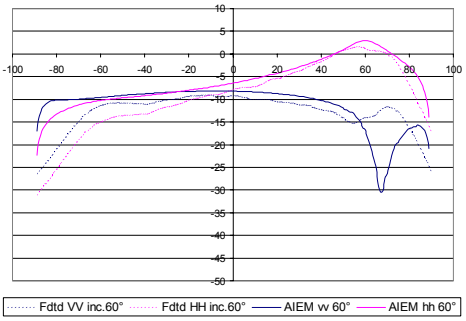

- Land C ks=1.5 kl=12.57 eps=7.0+j0.8

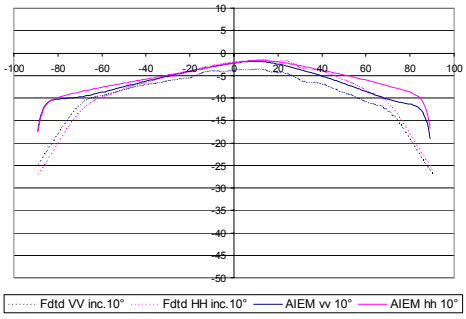

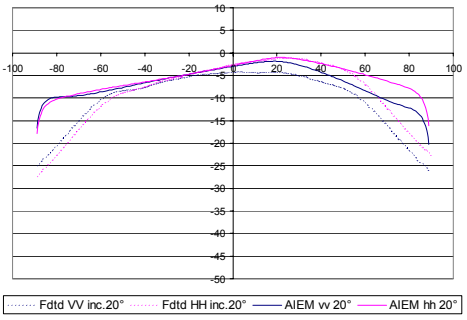

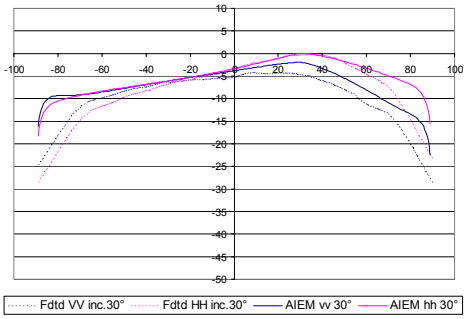

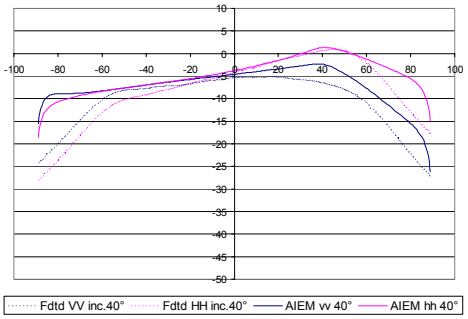

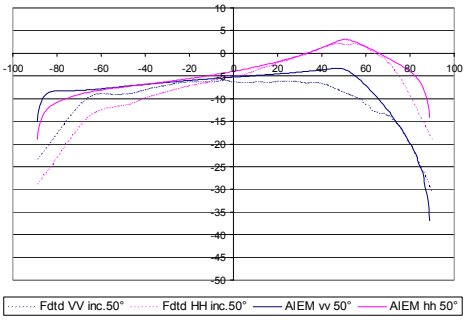

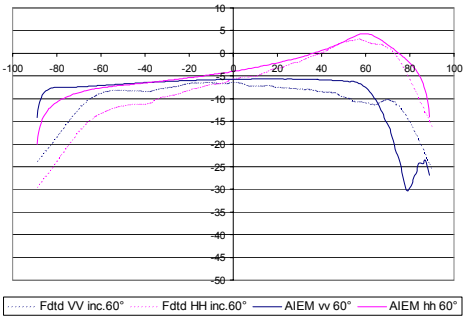

- Land C ks=1.5 kl=12.57 eps=24+j3.19

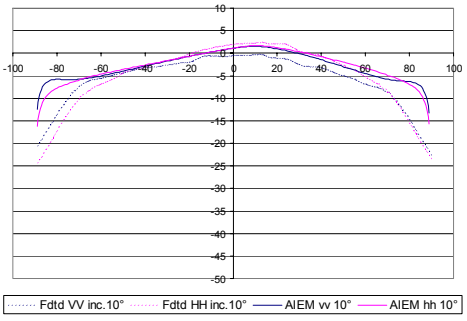

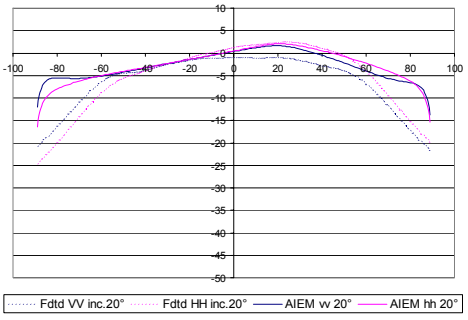

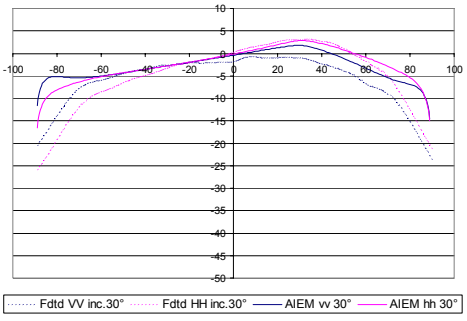

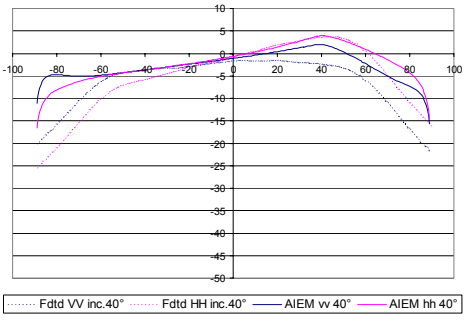

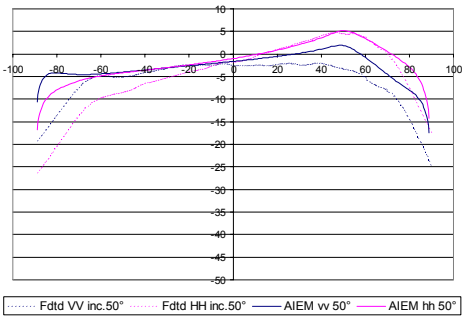

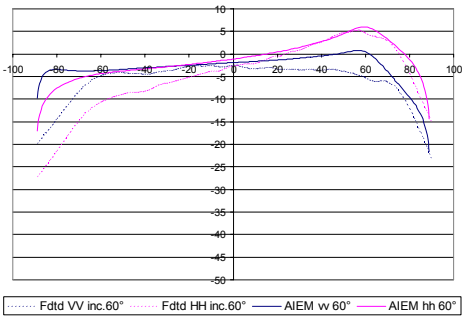

- Land C ks=2.0 kl=6.28 eps=4.06+j0.3

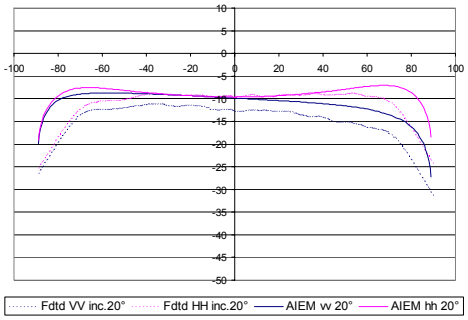

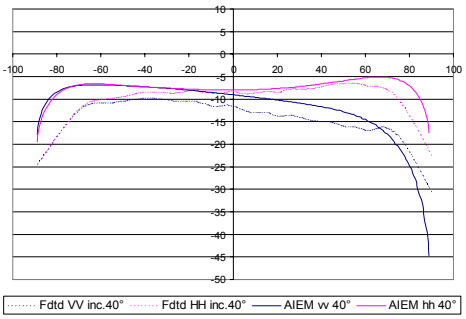

- Land C ks=2.0 kl=6.28 eps=7.0+j0.8

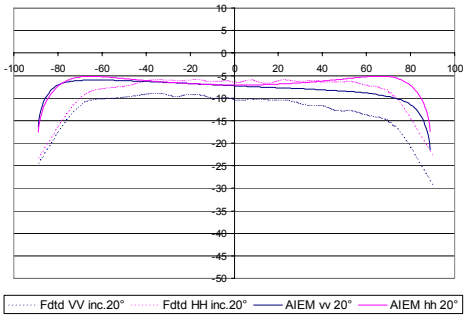

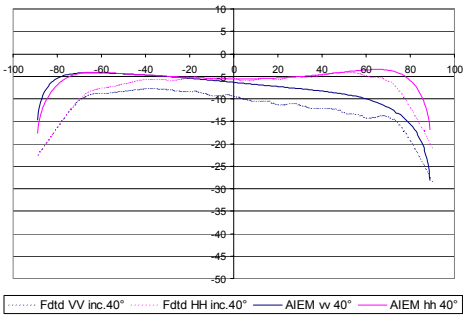

- Land C ks=2.0 kl=6.28 eps=24+j3.19

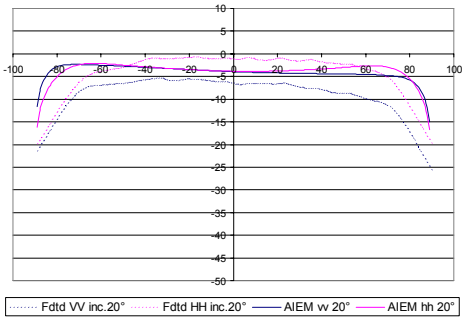

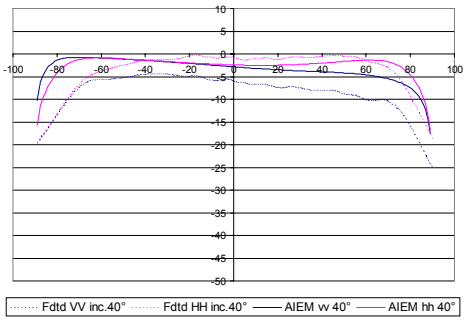

- Land C ks=2.0 kl=12.57 eps=4.06+j0.3

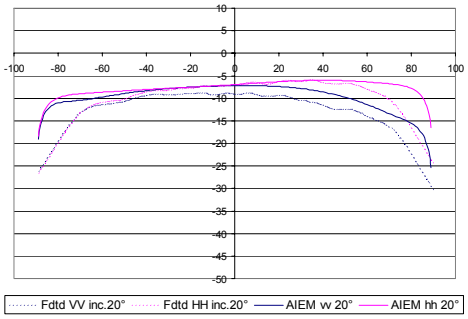

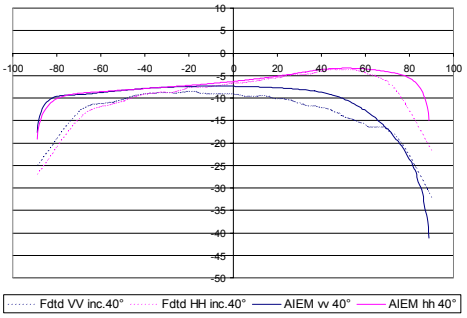

- Land C ks=2.0 kl=12.57 eps=7.0+j0.8

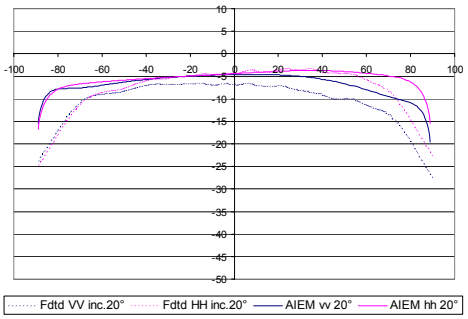

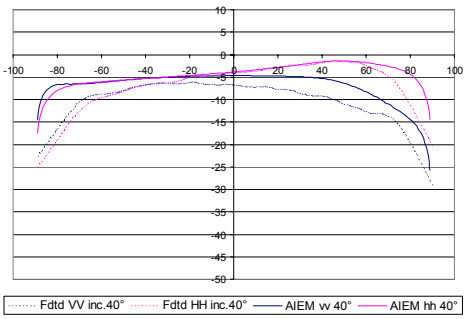

- Land C ks=2.0 kl=12.57 eps=24+j3.19

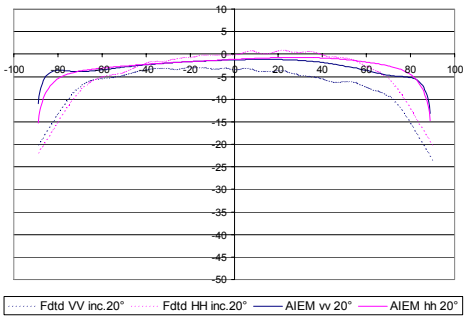

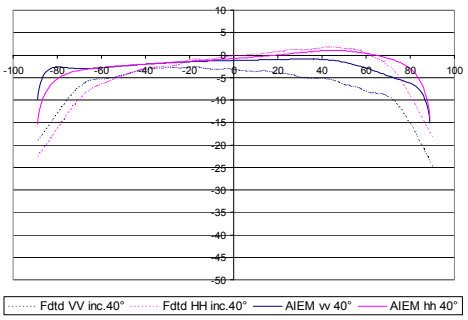

- Land C ks=3.5 kl=6.28 eps=4.06+j0.3

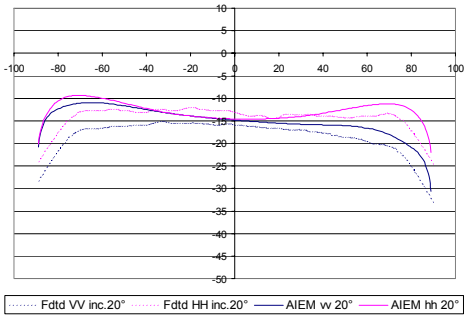

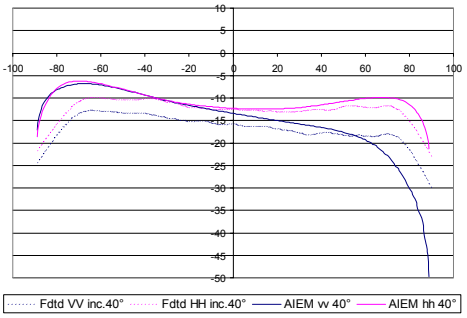

- Land C ks=3.5 kl=6.28 eps=7.0+j0.8

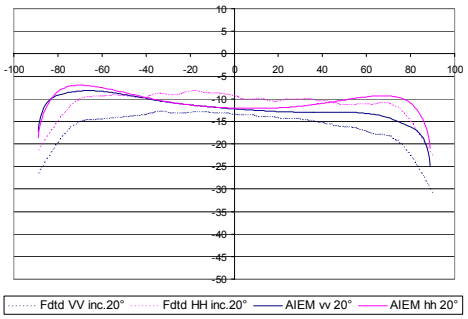

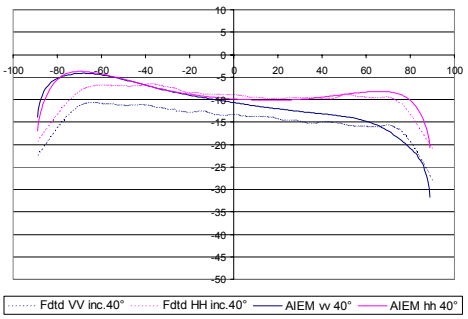

- Land C ks=3.5 kl=6.28 eps=24+j3.19

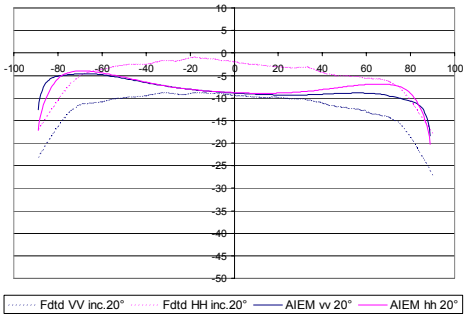

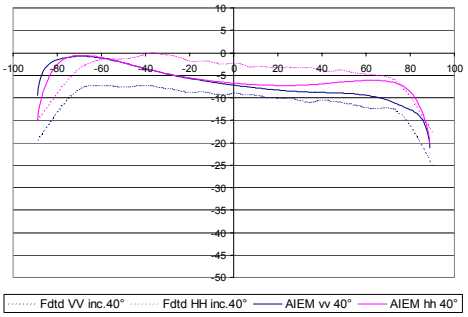

- Land C ks=3.5 kl=12.57 eps=4.06+j0.3

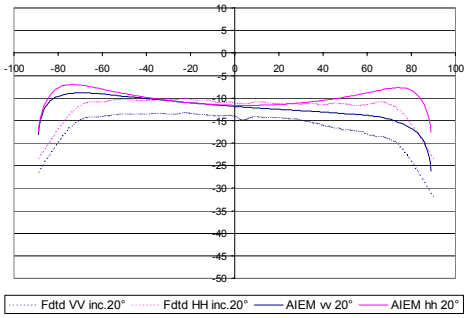

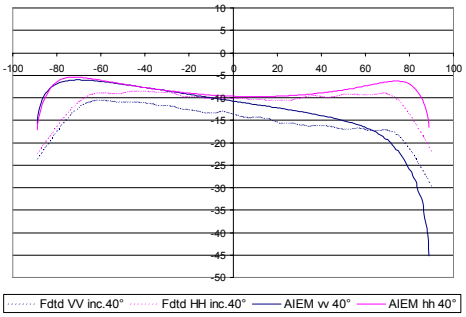

- Land C ks=3.5 kl=12.57 eps=7.0+j0.8

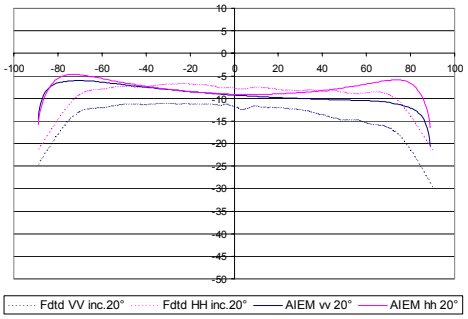

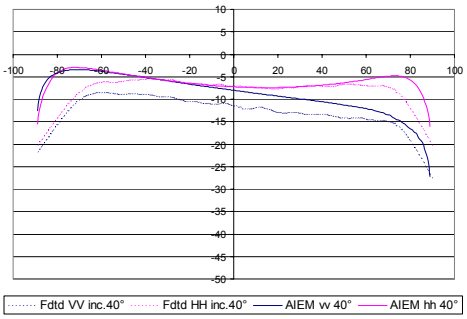

- Land C ks=3.5 kl=12.57 eps=24+j3.19

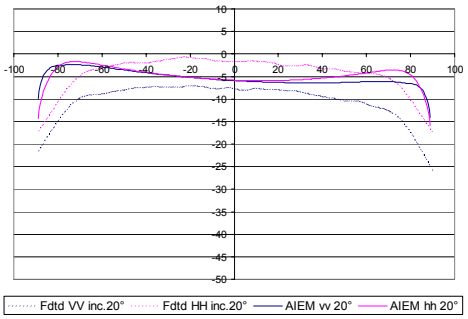

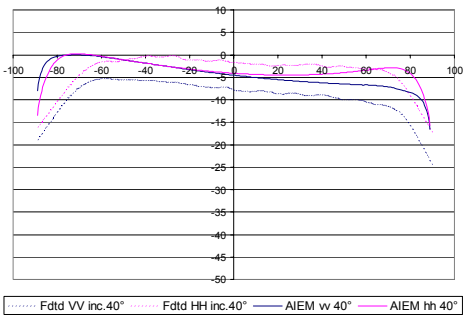

- Land C ks=4.0 kl=6.28 eps=4.06+j0.3

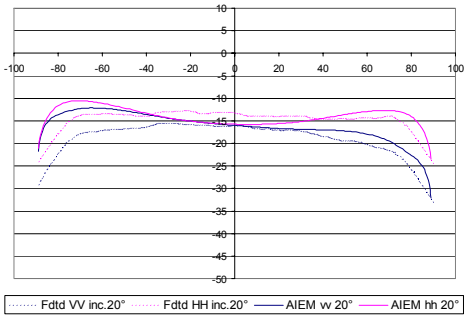

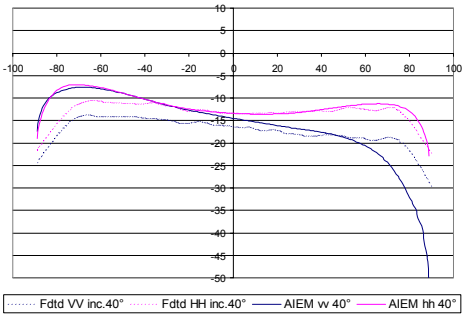

- Land C ks=4.0 kl=6.28 eps=7.0+j0.8

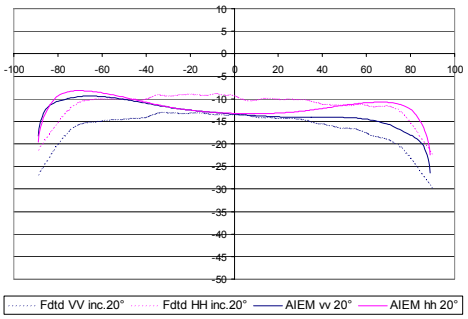

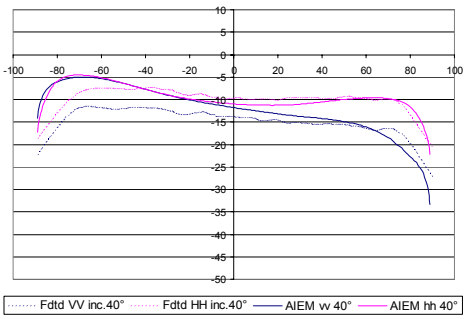

- Land C ks=4.0 kl=6.28 eps=24+j3.19

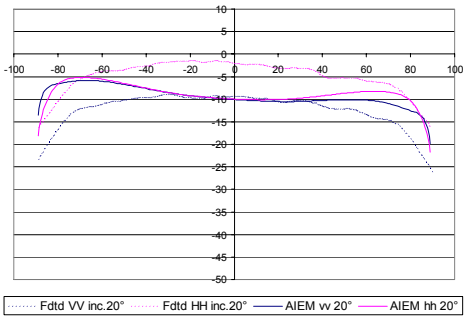

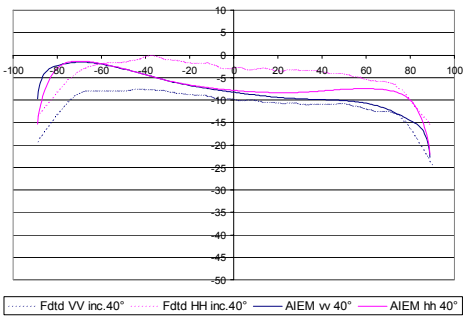

- Land C ks=4.0 kl=12.57 eps=4.06+j0.3

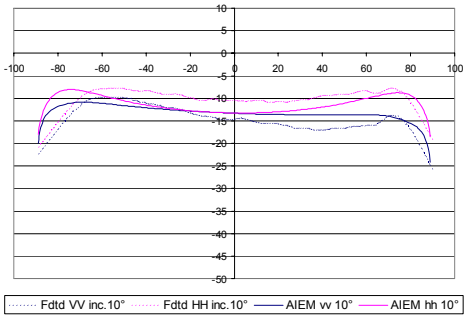

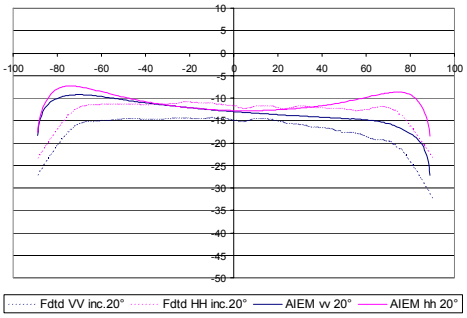

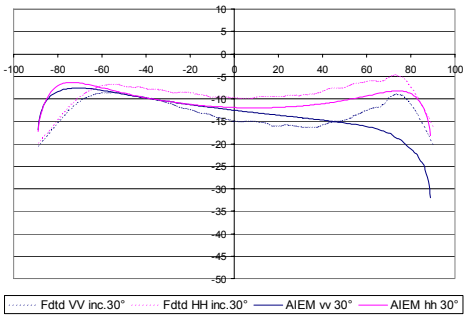

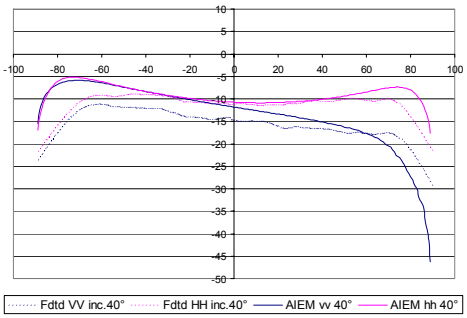

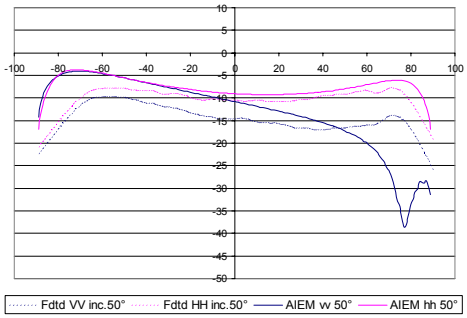

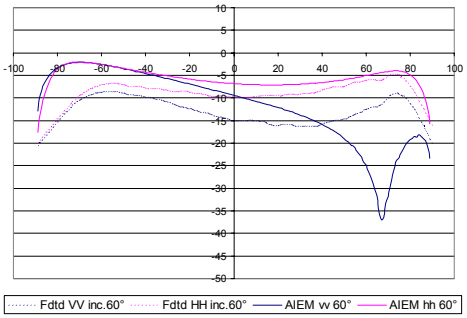

- Land C ks=4.0 kl=12.57 eps=7.0+j0.8

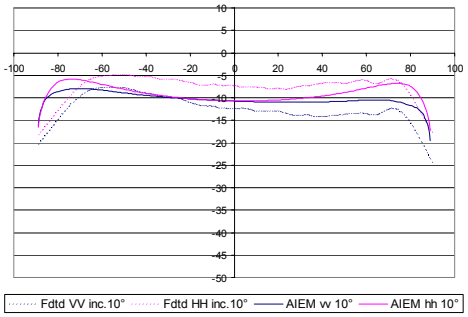

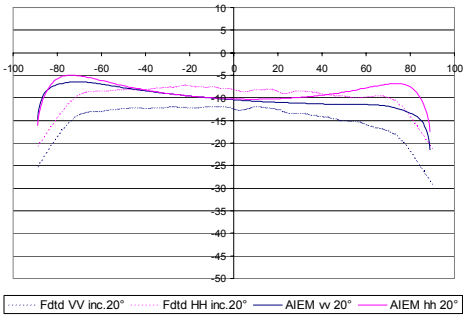

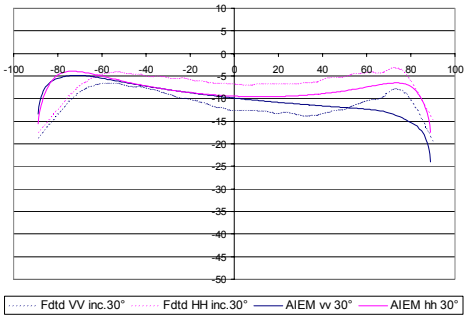

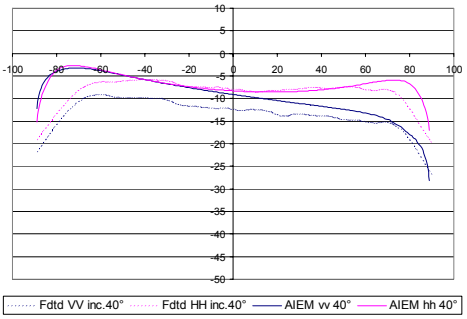

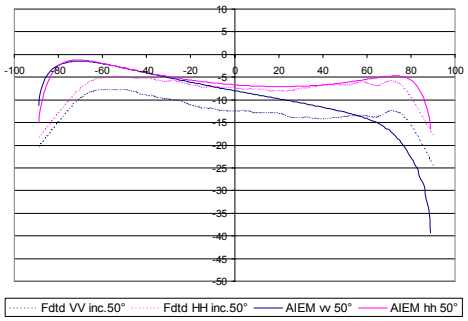

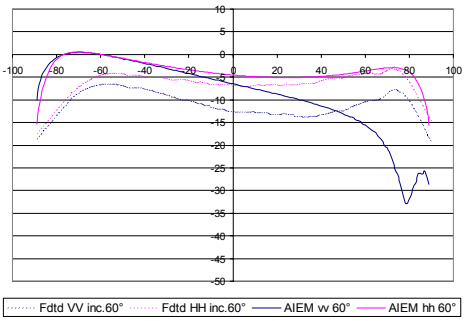

- Land C ks=4.0 kl=12.57 eps=24+j3.19

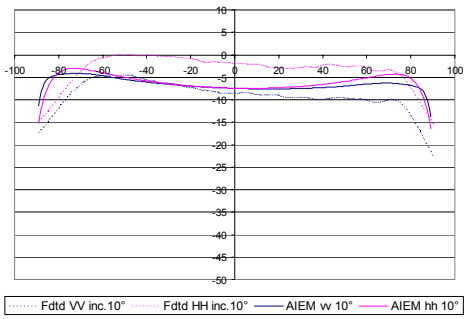

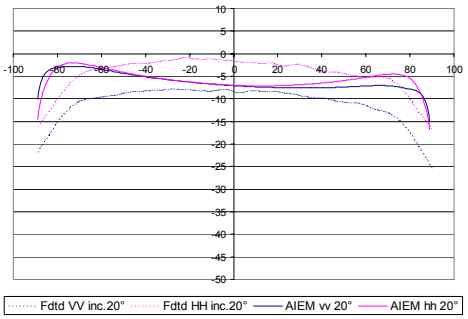

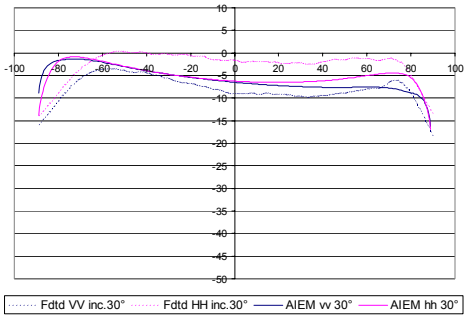

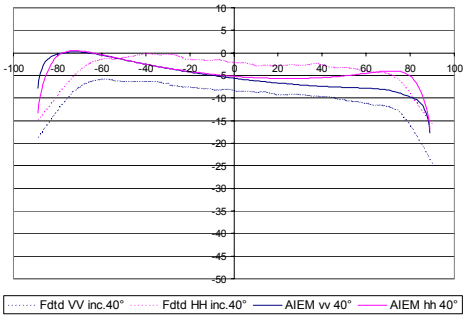

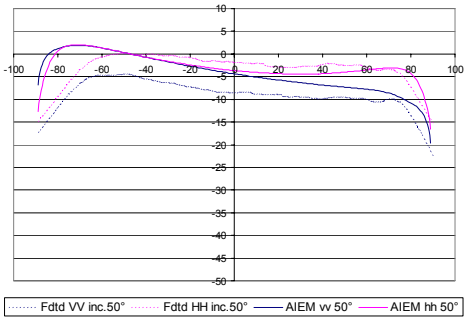

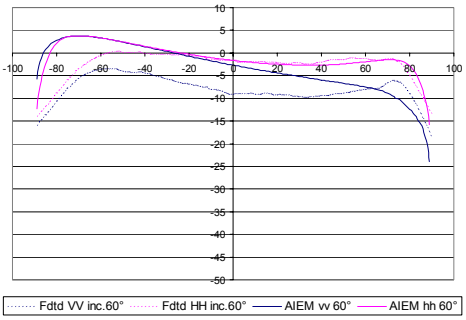

Gaussian correlated surfaces

- Land L ks=0.12 kl=5.48 eps=5+j0.6

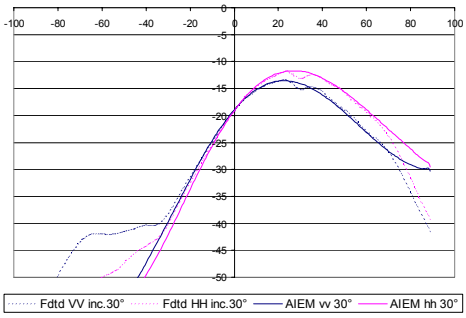

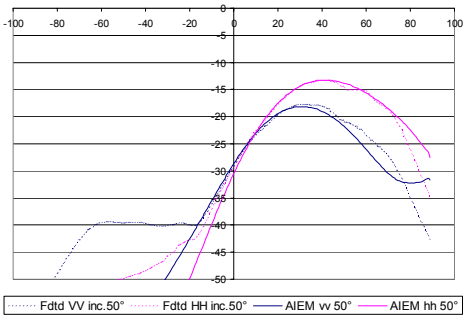

- Land L ks=0.12 kl=5.48 eps=24+j3.19
-

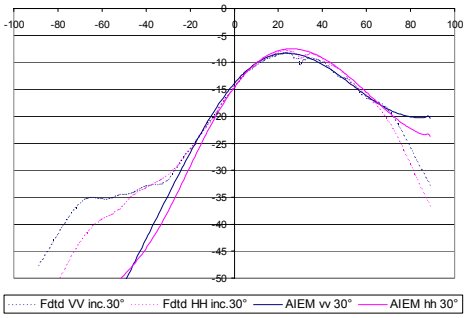

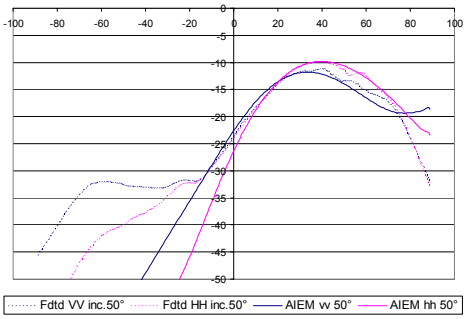

- Land C ks=2.0 kl=12.57 eps=4.06+j0.3

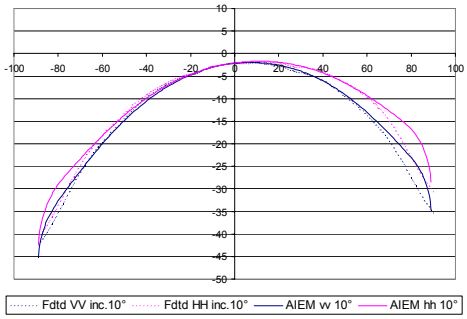

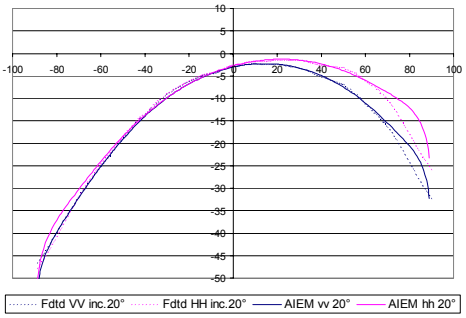

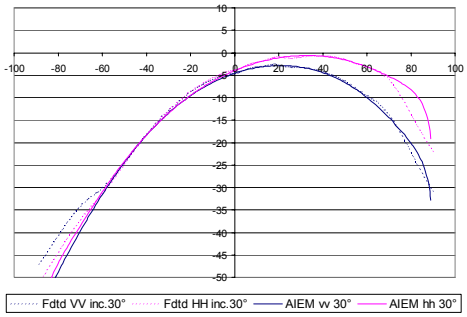

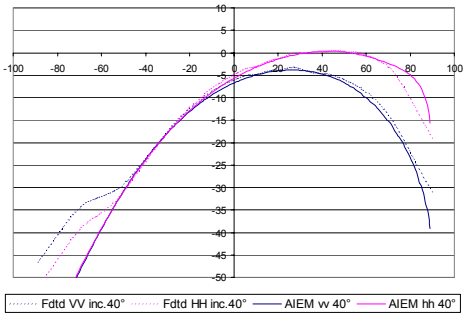

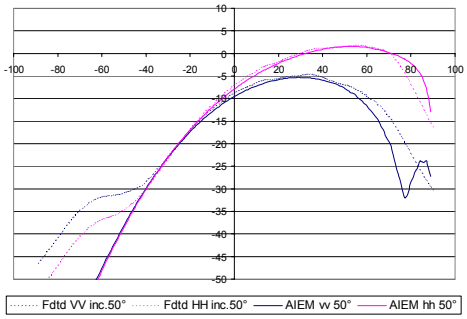

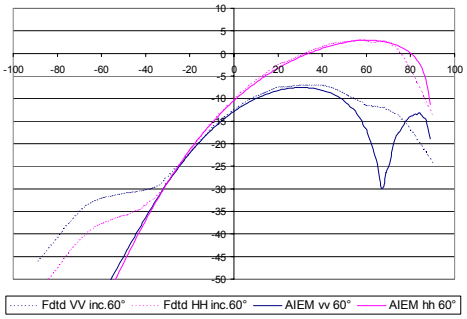

- Land C ks=2.0 kl=12.57 eps=7+j0.8

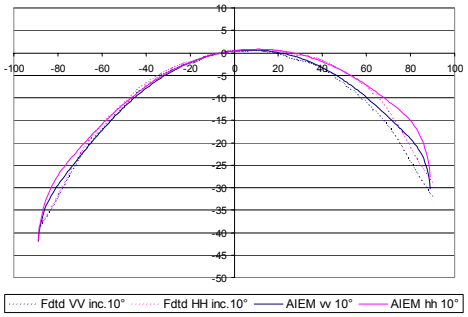

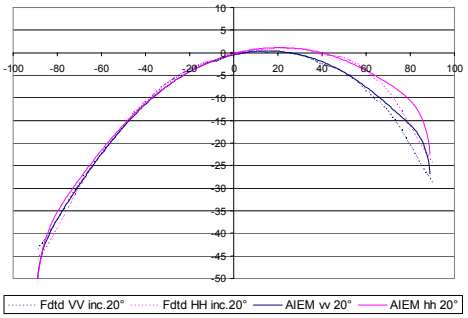

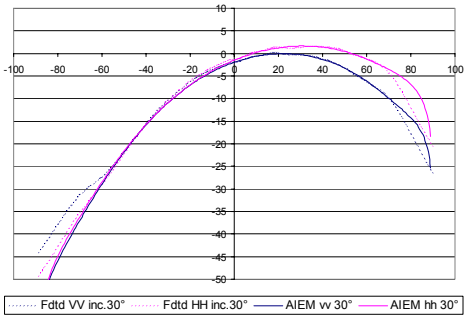

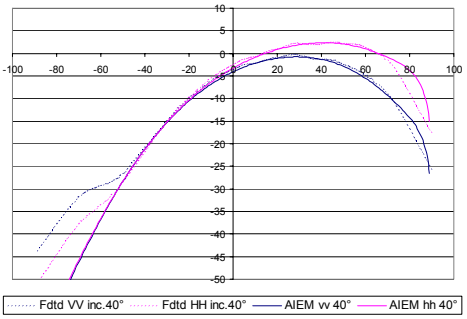

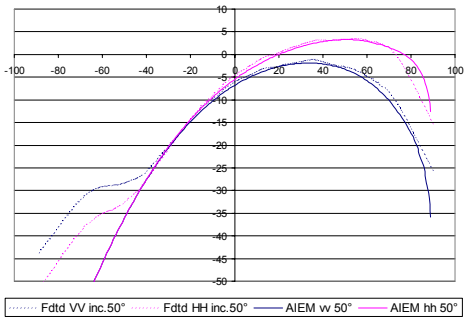

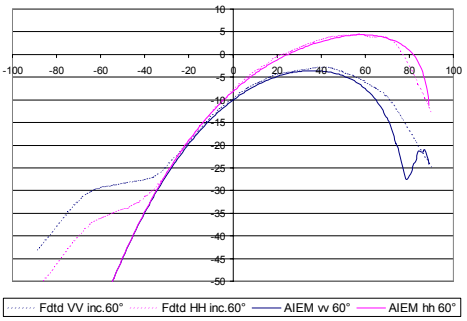

- Land C ks=2.0 kl=12.57 eps=24+j3.19

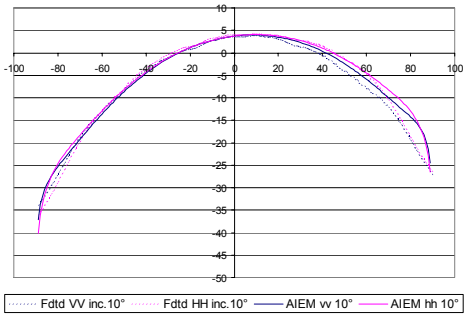

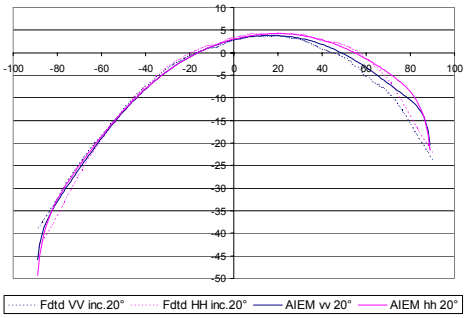

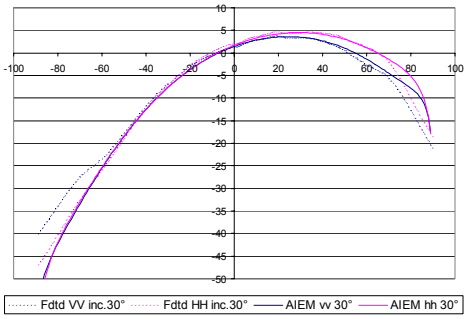

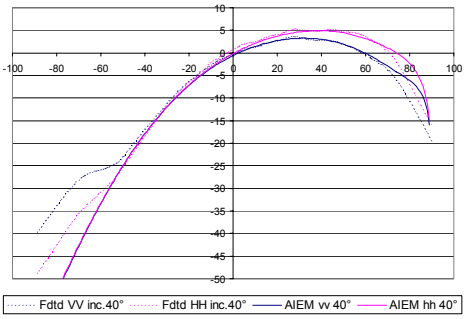

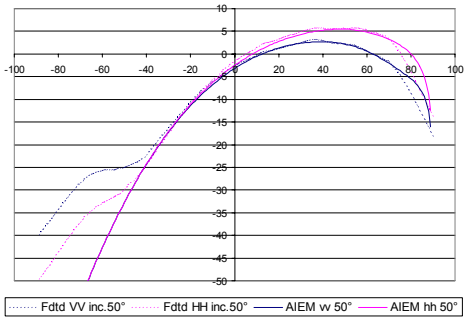

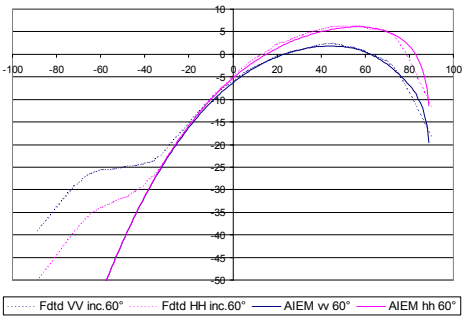

- Land C ks=3.5 kl=12.57 eps=4.06+j0.3

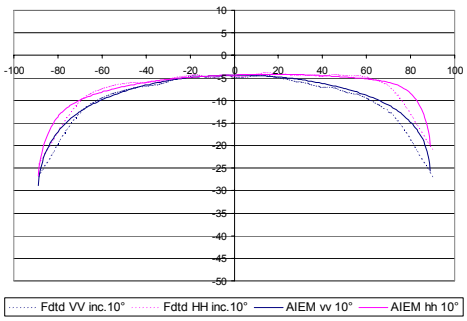

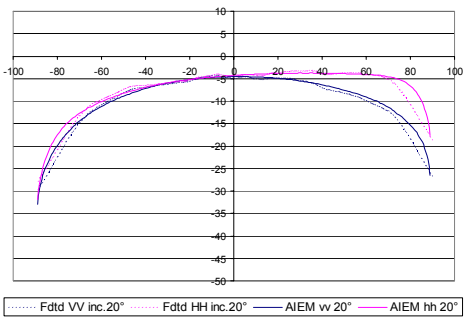

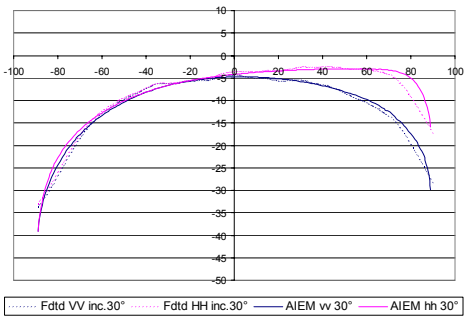

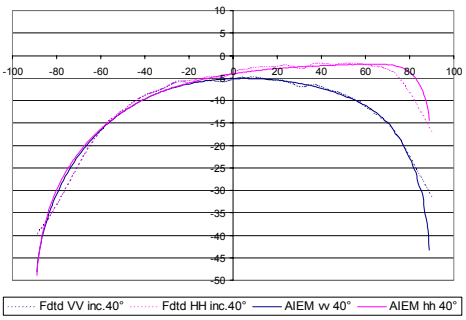

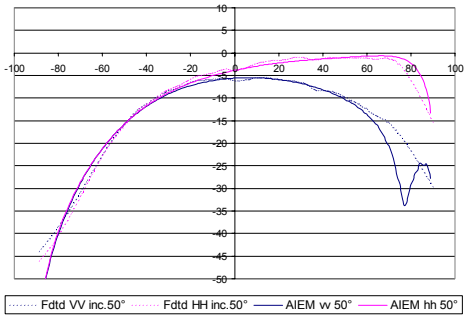

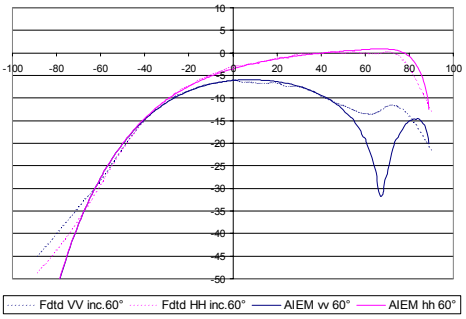

- Land C ks=3.5 kl=12.57 eps=7+j0.8

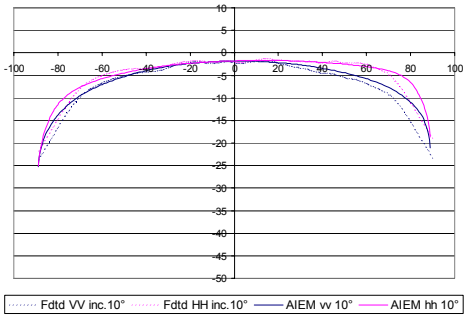

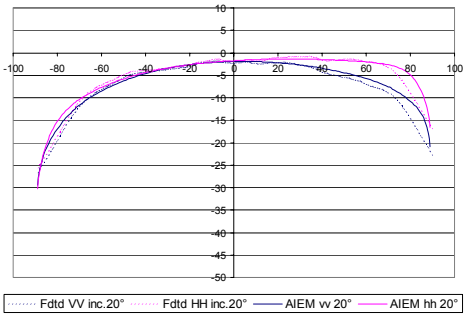

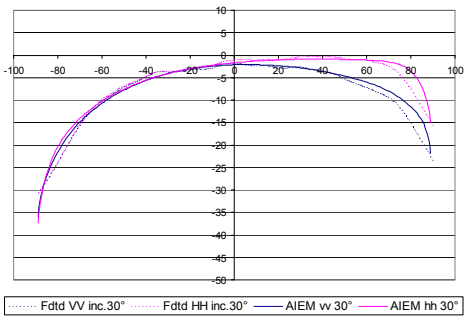

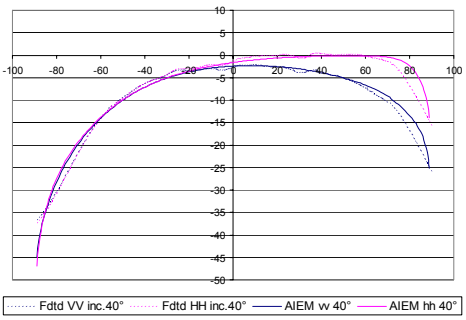

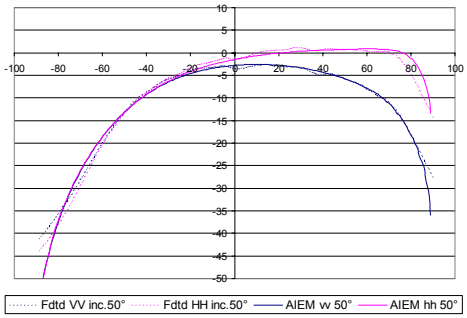

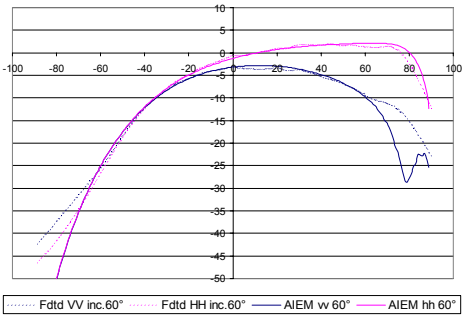

- Land C ks=3.5 kl=12.57 eps=24+j3.19

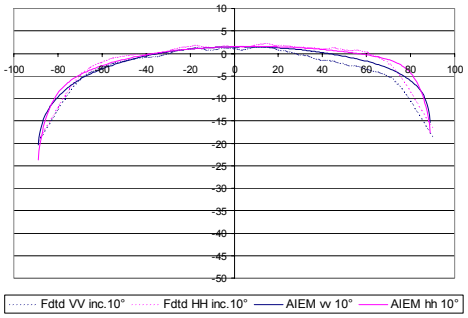

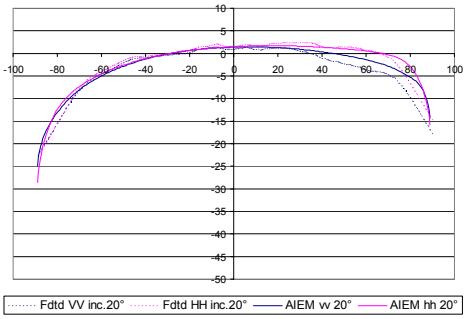

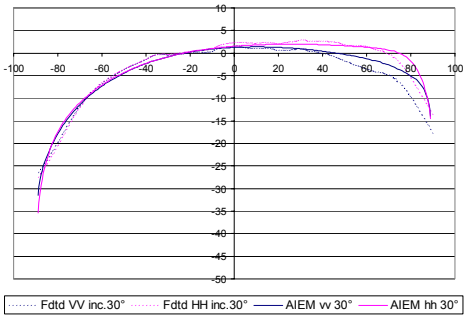

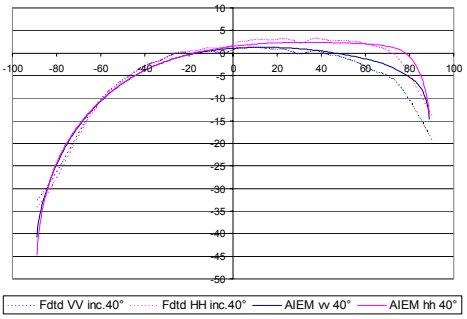

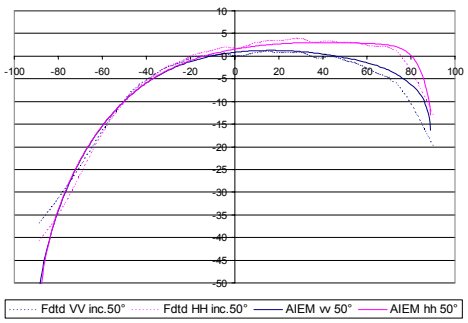

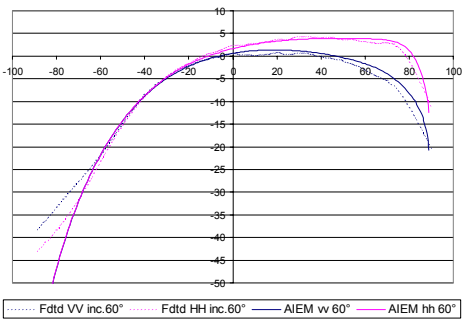

Appendix 2: The permittivity of a dense medium computed by the SFT

The Strong Fluctuation Theory is a method used to solve the wave equation in the case of propagation in an inhomogeneous dense medium. The fundamental concept of the SFT is to describe the random medium as continuous with random fluctuation of the permittivity. Usually, the theory describing the propagation of electromagnetic waves in a heterogeneous medium is developed under two basic assumptions:

- the fractional volume occupied by the scatterers is small
- the dielectric fluctuations in the medium are very small (Born approximation).

These two assumptions failed when applied to some natural media: for instance in the case of wet snow because the fractional volume can reach the 40% and the permittivity of the liquid water can be tent times the one of the background. The previous assumptions are made to disregard the singularity of the Green's dyadic function in the waves equation. Indeed, the Green's function has a singularity for $\underline{r} \to \underline{r}'$ which means that, inside the random medium, the observation and source points can coincide (i.e. the particles act like radiation source).

It is worth reminding that, in a random medium, the e.m. fields strongly fluctuate from point to point due to the scattering among the particles, and thus it is mandatory to apply a statistical average. The obtained equation is called the "Dyson equation" which has infinite terms. If the Dyson equation is directly approximated, the resulting formula holds only for tenuous media and leads to the Weak Fluctuation Theory. A more extensive description of the Strong Fluctuation Theory can be found in [1]-[3].

Considering a continuous medium (Fig. 53) in which the permittivity $\varepsilon(\underline{r})$ is allowed to fluctuate. It can be seen as a host medium (ε_h) which includes spherical particles whose characteristics are: permittivity ε_p and radius a_p, p=1,..,n. In the case of wet snow there are two types of inclusions, i.e. ice and water spheres.

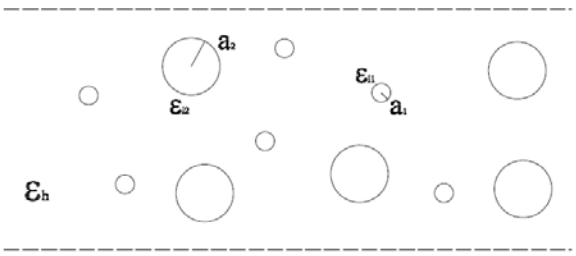

Fig. 53 - The structure of the random medium

The fractional volume occupied by the scatterers is f_p and the one of the host medium is $f_h = 1 - \sum_{i=1}^{n} f_p$. The equation for a wave travelling in such medium is

$$\underline{\nabla} \times \underline{\nabla} \times \underline{E}(\underline{r}) - k_0^2 \frac{\varepsilon(\underline{r})}{\varepsilon_0} \underline{E}(\underline{r}) = 0 \tag{214}$$

where $k_0 = \omega \sqrt{\varepsilon_0 \mu_0}$.

To understand the strong fluctuation theory is better to analyze before the weak one.

The Weak Fluctuation Theory

From an electromagnetic point of view, a random medium is characterized by its permittivity and permeability. Since it is improbable to find ferromagnetic material in remote sensing of natural media, the permeability is supposed to be $\mu = \mu_0$. A common assumption to represent the dielectric constant is to express it as a sum of a constant and a fluctuating parts [3],[4]

$$\begin{aligned} &\varepsilon(\underline{r}) = \varepsilon_m + \varepsilon_f(\underline{r}) \\ &\varepsilon_m = \left\langle \varepsilon(\underline{r}) \right\rangle \\ &\left\langle \varepsilon_f(\underline{r}) \right\rangle = 0 \\ &\left\langle \varepsilon_f(\underline{r}) \varepsilon_f(\underline{r}') \right\rangle = \delta \, \varepsilon_m^2 \, R(\underline{r} - \underline{r}') \end{aligned} \tag{215}$$

where δ and *R* are respectively the normalized variance and the correlation function of the fluctuations.

The wave equation for the random medium can be written as

$$\underline{\nabla} \times \underline{\nabla} \times \underline{E}(\underline{r}) - \omega^2 \mu \varepsilon_m \underline{E}(\underline{r}) = \omega^2 \mu \, \varepsilon_f(\underline{r}) \, \underline{E}(\underline{r}) \tag{216}$$

Neglecting the singularity of the Green's function, the solution of (216) is

$$\underline{E}(\underline{r}) = \underline{E}_0(\underline{r}) + k_0^2 \int PV \, \underline{\underline{G}}(\underline{r}, \underline{r}') \, \varepsilon_f(\underline{r}') \, \underline{E}(\underline{r}') \, dr' \tag{217}$$

The (217) is a Neumann form solution and cannot be solved in a closed form. To obtain the first moment of the electric fields, the bi-local approximation is commonly used and it is valid under the assumption

$$|\delta| << 1 \tag{218}$$

which means that the fluctuation of the permittivity must be weak. To overcome this constrain it is useful to decompose the permittivity in a different way.

The Strong Fluctuation Theory

The WFT is based on two assumptions:

- the singularity of the dyadic Green's function is disregarded
- the two parts of the permittivity are the average and a difference function

These statements lead to a solution with a narrow validity range. To overcome such limitations it is useful to decompose the random permittivity in a different way. Instead of $\varepsilon_m = \langle \varepsilon(\underline{r}) \rangle$ it is better to use an auxiliary permittivity ε_g which will differ from the final ε_{eff} only for a small quantity depending on the particles dimension. Such little quantity will vanish if the grain size will become much smaller than the wavelength. Thus, the new expression of the random permittivity is

$$\varepsilon(\underline{r}) = \varepsilon_g + \varepsilon'_f(\underline{r}) \tag{219}$$

where ε_g is the auxiliary permittivity which is valid in the low-frequency limit (where the e.m. interactions between two particles are negligible) and $\varepsilon'_f(\underline{r})$ is the random fluctuation. ε_g will be obtained later.

By using this decomposition, the wave equation could be written as

$$\underline{\nabla} \times \underline{\nabla} \times \underline{E} - k_0^2 \frac{\varepsilon_g}{\varepsilon_0} \underline{E} = k_0^2 \left(\frac{\varepsilon(\underline{r}) - \varepsilon_g}{\varepsilon_0} \right) \underline{E} \tag{220}$$

Indicating with $\underline{\underline{G}}_g(\underline{r}, \underline{r}')$ the dyadic Green's function which satisfy the waves equation with $k_g = \omega \sqrt{\varepsilon_g \mu_0}$:

$$\underline{\nabla} \times \underline{\nabla} \times \underline{\underline{G}}_g(\underline{r}, \underline{r}') - k_g^2 \underline{\underline{G}}_g(\underline{r}, \underline{r}') = \underline{\underline{I}}\, \delta(\underline{r} - \underline{r}') \tag{221}$$

It should be noted that both $\underline{\underline{G}}_g(\underline{r}, \underline{r}')$ and ε_g are deterministic quantities chosen to approximate the random medium in the very low-frequency limit.

The solution of the equation (220) for the electric field is

$$\underline{E}(\underline{r}) = \underline{E}_0(\underline{r}) + k_0^2 \int \underline{\underline{G}}_g(\underline{r}, \underline{r}') \frac{\varepsilon(\underline{r}') - \varepsilon_g}{\varepsilon_0} \underline{E}(\underline{r}')\, dr' \tag{222}$$

where $\underline{E}_0(\underline{r})$ is the incident wave and $G_g(\underline{r}, \underline{r}')$ is the DGF for a medium with permittivity ε_g.

To solve the (222) the exclusion volume must be chosen to coincide with the shape of the correlation function of the permittivity fluctuations. Because it has been

supposed the scatterers to be spherical, this will be also the shape of the exclusion volume [3].

The dyadic Green's function is expressed by

$$\underline{\underline{G}}_g(\underline{r},\underline{r}') = PV\ \underline{\underline{G}}_g(\underline{r},\underline{r}') + \frac{1}{3k_g^2}\underline{\underline{I}}\ \delta(\underline{r}-\underline{r}') \tag{223}$$

where *PV* stands for "Principal Value". The solution (222) can be rewritten as

$$\begin{aligned}\underline{E}(\underline{r}) &= \underline{E}_0(\underline{r}) + k_0^2 \int PV\ \underline{\underline{G}}_g(\underline{r},\underline{r}')\frac{\varepsilon(\underline{r}')-\varepsilon_g}{\varepsilon_0}\underline{E}(\underline{r}')\,d\underline{r}' \\ &\quad -k_0^2\int \frac{\delta(\underline{r}-\underline{r}')}{3k_g^2}\frac{\varepsilon(\underline{r}')-\varepsilon_g}{\varepsilon_0}\underline{E}(\underline{r}')\,d\underline{r}' = \\ &= \underline{E}_0(\underline{r}) + k_0^2 \int PV\ \underline{\underline{G}}_g(\underline{r},\underline{r}')\frac{\varepsilon(\underline{r}')-\varepsilon_g}{\varepsilon_0}\underline{E}(\underline{r}')\,d\underline{r}' - \frac{k_0^2}{3k_g^2}\frac{\varepsilon(\underline{r})-\varepsilon_g}{\varepsilon_0}\underline{E}(\underline{r}) = \\ &= \underline{E}_0(\underline{r}) + k_0^2 \int PV\ \underline{\underline{G}}_g(\underline{r},\underline{r}')\frac{\varepsilon(\underline{r}')-\varepsilon_g}{\varepsilon_0}\underline{E}(\underline{r}')\,d\underline{r}' - \frac{\varepsilon(\underline{r})-\varepsilon_g}{3\,\varepsilon_0}\underline{E}(\underline{r})\end{aligned} \tag{224}$$

from which

$$\left[1-\frac{\varepsilon(\underline{r})-\varepsilon_g}{3\,\varepsilon_0}\right]\underline{E}(\underline{r}) = \underline{E}_0(\underline{r}) + k_0^2 \int PV\ \underline{\underline{G}}_g(\underline{r},\underline{r}')\frac{\varepsilon(\underline{r}')-\varepsilon_g}{\varepsilon_0}\underline{E}(\underline{r}')\,d\underline{r}' \tag{225}$$

Rearranging the previous expression it can be obtained

$$\left[\frac{\varepsilon(\underline{r})+2\,\varepsilon_g}{3\,\varepsilon_g}\right]\underline{E}(\underline{r}) = \underline{E}_0(\underline{r}) + k_0^2 \int PV\ \underline{\underline{G}}_g(\underline{r},\underline{r}')\,3\frac{\varepsilon_g}{\varepsilon_0}\frac{\varepsilon(\underline{r}')-\varepsilon_g}{\varepsilon(\underline{r}')+2\varepsilon_g}\frac{\varepsilon(\underline{r}')+2\varepsilon_g}{3\varepsilon_g}\underline{E}(\underline{r}')\,d\underline{r}' \tag{226}$$

by operating the following substitutions

$$\underline{F}(\underline{r}) = \left[\frac{\varepsilon(\underline{r})+2\varepsilon_g}{3\varepsilon_g}\right]\underline{E}(\underline{r}) \qquad \xi(\underline{r}) = 3\frac{\varepsilon_g}{\varepsilon_0}\frac{\varepsilon(\underline{r})-\varepsilon_g}{\varepsilon(\underline{r})+2\varepsilon_g} \tag{227}$$

the solution (225) can be written as

$$F(\underline{r}) = E_0(\underline{r}) + k_0^2 \int PV\ \underline{\underline{G}}_g(\underline{r},\underline{r}')\ \xi_f(\underline{r}')\ \underline{F}(\underline{r}')\ dr' \tag{228}$$

which is an equation without singularity similar to (217). The previous equation can be interpreted like if the source $\omega^2\mu\varepsilon_f(\underline{r})\,\underline{E}(\underline{r})$ in the medium with permittivity ε_m become the source $\xi(\underline{r})\underline{F}(\underline{r})$ in the medium ε_g.

Relationship between $\underline{F}$ and $\underline{E}$

The relationship between $\underline{F}$ and $\underline{E}$ can be understood from the electrostatic. Let us consider dipolar particles in vacuum. By indicating with E_l the local electric field acting on a particle (sum of the external field and the ones radiated by all the other particles) and with E the spatially and temporally averaged electric field in a point of the space (which is the sum of the incidence electric field and the ones generated by all the dipoles). From the Lorentz equation it can be written

$$\underline{E}_l = \underline{E} + \frac{\underline{P}}{3\,\varepsilon_0} = \underline{E} + \frac{\varepsilon_0\,\chi\,\underline{E}}{3\,\varepsilon_0} = \underline{E} + \frac{(\varepsilon_r - 1)}{3\,\varepsilon_0}\underline{E}_l = \frac{\varepsilon + 2\,\varepsilon_0}{3\,\varepsilon_0}\underline{E} \tag{229}$$

which is similar to (227). Thus it is possible to make a comparison and see $\underline{F(r)}$ as the local fields exciting the random inclusions (by considering the permittivity fluctuations as dipoles) and $E(r)$ as the macroscopic fields (Fig. 54) .

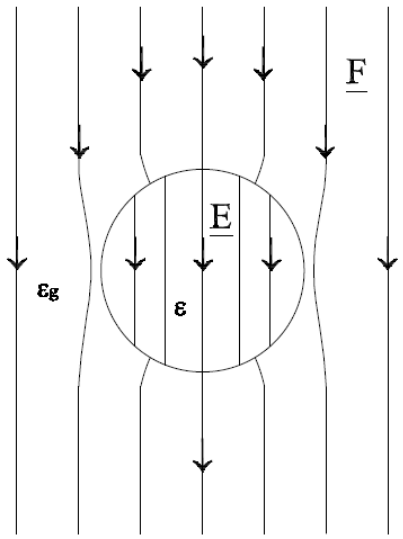

Fig. 54 - Electrostatic fields for a dielectric sphere

Moreover it is possible to give insight also to $\xi(\underline{r})$. In the electrostatic case the polarizability $\underline{P}$ of a particle is

$$\underline{P} = \varepsilon_0\,\chi\,\underline{E} = \varepsilon_0(\varepsilon_r - 1)\underline{E} \;= (\varepsilon - \varepsilon_0)\frac{3\,\varepsilon_0}{\varepsilon + 2\,\varepsilon_0}\underline{E}_l = 3\,\varepsilon_0\frac{\varepsilon - \varepsilon_0}{\varepsilon + 2\,\varepsilon_0}\underline{E}_l \tag{230}$$

Thus, considering the random medium

$$\underline{P}' = 3\,\varepsilon_0 \frac{\varepsilon(\underline{r}) - \varepsilon_g}{\varepsilon(\underline{r}) + 2\,\varepsilon_g} \underline{F}(\underline{r}) = 3\,\varepsilon_g \frac{\varepsilon_0}{\varepsilon_g} \frac{\varepsilon(\underline{r}) - \varepsilon_g}{\varepsilon(\underline{r}) + 2\,\varepsilon_g} \underline{F}(\underline{r}) = \varepsilon_g\ \xi(\underline{r})\ \underline{F}(\underline{r}) \qquad (231)$$

By this way it is possible to see $\xi(\underline{r})$ like the equivalent electrical susceptibility of the dipoles in the medium ε_g. Thus, by using the transformation $\varepsilon \leftrightarrow \xi$ the scattering problem in a medium with permittivity $\varepsilon(\underline{r})$ is become the problem of the scattering from dipoles in the medium ε_g.

Computation of the equivalent permittivity ε_{eff}

By applying the bi-local approximation to *F(r)* it has

$$\left\langle \underline{F}(\underline{r}) \right\rangle = \underline{E}_0(\underline{r}) + k_0^2 \int\int PV\ \underline{\underline{G}}_g(\underline{r},\underline{r}')\ \underline{\underline{\xi}}_{eff}(\underline{r}',\underline{r}'')\ \left\langle \underline{F}(\underline{r}') \right\rangle \quad d\underline{r}'\, d\underline{r}'' \qquad (232)$$

where

$$\underline{\underline{\xi}}_{eff}(\underline{r}',\underline{r}'') = k_0^2\ PV\ \underline{\underline{G}}_g(\underline{r}',\underline{r}'')\ \ R_\xi(|\underline{r}' - \underline{r}''|) \qquad (233)$$

and

$$R_\xi(|\underline{r}' - \underline{r}''|) = \left\langle \xi(\underline{r}')\, \xi(\underline{r}'') \right\rangle \qquad (234)$$

If the average of *F(r)* is computed directly from (228) it has

$$\left\langle \underline{F}(\underline{r}) \right\rangle = \underline{E}_0(\underline{r}) + k_0^2 \int PV\ \underline{\underline{G}}_g(\underline{r},\underline{r}') \left\langle \underline{\underline{\xi}}(\underline{r}')\ \underline{F}(\underline{r}') \right\rangle d\underline{r}' \qquad (235)$$

which compared with (232) gives

$$\left\langle \underline{\underline{\xi}}(\underline{r})\ \underline{F}(\underline{r}) \right\rangle = \int\ \underline{\underline{\xi}}_{eff}(\underline{r} - \underline{r}')\ \left\langle \underline{F}(\underline{r}') \right\rangle d\underline{r}' \qquad (236)$$

The electrical displacement vector *D* is defined as

$$\underline{D} = \varepsilon\ \underline{E} \qquad (237)$$

Thus, by the same way as (236), the spatial average of *D* is

$$\left\langle \underline{D}(\underline{r}) \right\rangle = \left\langle \varepsilon(\underline{r})\ \underline{E}(\underline{r}) \right\rangle \overset{\Delta}{=} \int\ \underline{\underline{\varepsilon}}_{eff}(\underline{r} - \underline{r}')\ \left\langle \underline{E}(\underline{r}') \right\rangle d\underline{r}' \qquad (238)$$

where ε_{eff} if the effective permittivity. To obtain the explicit expression of ε_{eff} is convenient to switch to the transformed domain. For instance

$$\underline{\underline{\varepsilon}}_{eff}(\underline{k}) = \int\ \underline{\underline{\varepsilon}}_{eff}(\underline{r})\ e^{-j\,\underline{k}\cdot\underline{r}}\ d\underline{r} \qquad (239)$$

the same operation must be carried out also on ξ, *D*, *E*, *F*. From the electrostatic

$$\underline{D} = \underline{P} + \varepsilon_0\ \underline{E} \qquad (240)$$

thus it is possible to write

$$
\begin{array}{rcl}
\underline{D}(\underline{r}) & = & \varepsilon_0\ \xi(\underline{r})\ \underline{F}(\underline{r}) + \varepsilon_g\ \underline{E}(\underline{r}) \\
& \downarrow & \\
\left\langle \underline{D}(\underline{r}) \right\rangle & = & \varepsilon_0\ \left\langle \xi(\underline{r})\ \underline{F}(\underline{r}) \right\rangle + \varepsilon_g\ \left\langle \underline{E}(\underline{r}) \right\rangle \\
& \downarrow \Im & \\
\left\langle \underline{D}(\underline{k}) \right\rangle & = & \varepsilon_0\ \underline{\underline{\xi}}_{eff}(\underline{k})\ \left\langle \underline{F}(\underline{k}) \right\rangle + \varepsilon_g\ \left\langle \underline{E}(\underline{k}) \right\rangle
\end{array}
\tag{241}
$$

By using (227) it has

$$
\begin{array}{rcl}
\left\langle \underline{F}(\underline{r}) \right\rangle & = & \dfrac{1}{3\ \varepsilon_g} \left\langle \varepsilon(\underline{r})\ \underline{F}(\underline{r}) \right\rangle + \dfrac{2}{3} \left\langle \underline{E}(\underline{r}) \right\rangle = \\
& & = \dfrac{1}{3\ \varepsilon_g} \left\langle \underline{D}(\underline{r}) \right\rangle + \dfrac{2}{3} \left\langle \underline{E}(\underline{r}) \right\rangle
\end{array}
\tag{242}
$$

The (241) can be written as

$$
\left\langle \underline{D}(\underline{k}) \right\rangle = \frac{\varepsilon_0}{3\ \varepsilon_g}\ \underline{\underline{\xi}}_{eff}(\underline{k})\ \left\langle \underline{D}(\underline{k}) \right\rangle + \frac{2}{3}\ \varepsilon_0\ \underline{\underline{\xi}}_{eff}(\underline{k})\ \left\langle \underline{E}(\underline{k}) \right\rangle + \varepsilon_g\ \left\langle \underline{E}(\underline{k}) \right\rangle
\tag{243}
$$

and by grouping the properly terms it has

$$
\begin{array}{l}
\left[\underline{\underline{I}} - \dfrac{\varepsilon_0}{3\ \varepsilon_g}\ \underline{\underline{\xi}}_{eff}(\underline{k}) \right] \left\langle \underline{D}(\underline{k}) \right\rangle = \left[\dfrac{2}{3}\ \varepsilon_0\ \underline{\underline{\xi}}_{eff}(\underline{k}) + \varepsilon_g\ \underline{\underline{I}} \right] \left\langle \underline{E}(\underline{k}) \right\rangle = \\
\qquad = \varepsilon_g \left[\underline{\underline{I}} - \dfrac{\varepsilon_0}{3\ \varepsilon_g}\ \underline{\underline{\xi}}_{eff}(\underline{k}) \right] \left\langle \underline{E}(\underline{k}) \right\rangle + \varepsilon_g\ \underline{\underline{\xi}}_{eff}(\underline{k})\ \left\langle \underline{E}(\underline{k}) \right\rangle
\end{array}
\tag{244}
$$

By applying the Fourier transform to (238)

$$
\begin{array}{rcl}
\left\langle \underline{D}(\underline{r}) \right\rangle & = & \int\ \underline{\underline{\varepsilon}}_{eff}(\underline{r} - \underline{r}')\ \left\langle \underline{E}(\underline{r}') \right\rangle\ d\,\underline{r}' \\
& \downarrow \Im & \\
\left\langle \underline{D}(\underline{k}) \right\rangle & = & \underline{\underline{\varepsilon}}_{eff}(\underline{k})\ \left\langle \underline{E}(\underline{k}) \right\rangle
\end{array}
\tag{245}
$$

and from (244)-(245) it has

$$
\begin{array}{rcl}
\underline{\underline{\varepsilon}}_{eff}(\underline{k}) & = & \varepsilon_g\ \underline{\underline{I}} + \varepsilon_0 \left[\underline{\underline{I}} - \dfrac{\varepsilon_0}{3\ \varepsilon_g} \underline{\underline{\xi}}_{eff}(\underline{k}) \right]^{-1} \underline{\underline{\xi}}_{eff}(\underline{k}) \\
& \downarrow \Im^{-1} & \\
\underline{\underline{\varepsilon}}_{eff}(\underline{r}) & = & \varepsilon_g\ \underline{\underline{I}} + \varepsilon_0\ \Im^{-1} \left\{ \left[\underline{\underline{I}} - \dfrac{\varepsilon_0}{3\ \varepsilon_g} \underline{\underline{\xi}}_{eff}(\underline{k}) \right]^{-1} \underline{\underline{\xi}}_{eff}(\underline{k}) \right\}
\end{array}
\tag{246}
$$

This is the analytical expression of $\underline{\underline{\varepsilon}}_{eff}$ and the correction term which must be added to ε_g to account for the coherent scattering effects between the particles can be clearly seen.

In order to apply the bi-local approximation, the following condition must be verified

$$\left|\underline{\underline{\xi}}_{eff}(\underline{k})\right| << 1 \tag{247}$$

hence the (246) become

$$\underline{\underline{\varepsilon}}_{eff}(\underline{k}) \cong \varepsilon_g \, \underline{\underline{I}} + \varepsilon_0 \, \underline{\underline{\xi}}_{eff}(\underline{k}) \tag{248}$$

For relatively low frequency, the spatial dispersion of ξ can be neglected and it has

$$\underline{\underline{\xi}}_{eff}(\underline{k}) \cong \underline{\underline{\xi}}_{eff}(0) = \int \underline{\underline{\xi}}_{eff}(\underline{r}) \, d\underline{r} \quad \stackrel{\Delta}{=} \quad \underline{\underline{\xi}}^{0}_{eff} \tag{249}$$

and

$$\underline{\underline{\varepsilon}}_{eff} = \varepsilon_g \, \underline{\underline{I}} + \varepsilon_0 \, \underline{\underline{\xi}}^{0}_{eff} \tag{250}$$

To obtain a useful expression of $\underline{\underline{\varepsilon}}_{eff}$, the quantity $\underline{\underline{\xi}}^{0}_{eff}$ must be calculated. By using the (249) and some properties of the Green's function for spherical exclusion volumes it has

$$\begin{aligned} \underline{\underline{\xi}}^{0}_{eff} &= \int \underline{\underline{\xi}}_{eff}(\underline{r}) \, d\underline{r} = k_0^2 \varepsilon_0 \int PV \, \underline{\underline{G}}_g(\underline{r}) \, R_\xi(|\underline{r}|) \, d\underline{r} = \\ &= \int r^2 \, [PV \; G_1(r) \, \underline{\underline{I}} + PV \; G_2(r) \, \hat{r}\hat{r}] \, R_\xi(r) \, d\underline{r} \end{aligned} \tag{251}$$

Because

$$\int_{4\pi} \hat{r}\hat{r} \, d\Omega = \frac{4}{3}\pi \, \underline{\underline{I}} \tag{252}$$

it can be written

$$\begin{aligned} \underline{\underline{\xi}}^{0}_{eff} &= 4\pi \underline{\underline{I}} \int_0^\infty r^2 \, [PV \; G_1(r) \, \underline{\underline{I}} + PV \; G_2(r) \, \hat{r}\hat{r}] \, R_\xi(r) \, d\underline{r} = \ldots \\ \ldots &= \frac{2}{3} \underline{\underline{I}} \int_0^\infty r \, e^{j k_g r} \, R_\xi(r) \, dr \cong \frac{2}{3} \underline{\underline{I}} \int_0^\infty r \, (1 + j k_g r) \, R_\xi(r) \, dr \end{aligned} \tag{253}$$

Now it is possible to have an explicit expression for $\underline{\underline{\varepsilon}}_{eff}$

$$
\begin{aligned}
\underline{\underline{\varepsilon}}_{eff} &= \varepsilon_g \underline{\underline{I}} + \varepsilon_0 \, \underline{\underline{\xi}}^0_{eff} \\
&\downarrow \\
\underline{\underline{\varepsilon}}_{eff} &= \varepsilon_g \underline{\underline{I}} + k_0^2 \varepsilon_0 \int_0^\infty PV \; \underline{\underline{G}}_g(\underline{r}) \; R_\xi(|\underline{r}|) \; dr \\
&\downarrow \\
\underline{\underline{\varepsilon}}_{eff} &= \varepsilon_g \underline{\underline{I}} + k_0^2 \varepsilon_0 \frac{2}{3} \underline{\underline{I}} \int_0^\infty r \, (1 + j k_g r) \; R_\xi(r) \; dr \\
&\downarrow \\
\underline{\underline{\varepsilon}}_{eff} &= \varepsilon_g \underline{\underline{I}} + k_0^2 \varepsilon_0 \frac{2}{3} \underline{\underline{I}} \int_0^\infty r \; R_\xi(r) \; dr + j k_g k_0^2 \varepsilon_0 \frac{2}{3} \underline{\underline{I}} \int_0^\infty r^2 R_\xi(r) \; dr
\end{aligned}
\tag{254}
$$

Since $\underline{\underline{\varepsilon}}_{eff}$ is a diagonal matrix with identical elements ($\underline{\underline{\varepsilon}}_{eff} = \varepsilon^x_{eff} \, \hat{x}\hat{x} + \varepsilon^y_{eff} \, \hat{y}\hat{y} + \varepsilon^z_{eff} \, \hat{z}\hat{z}$, $\varepsilon^x_{eff} = \varepsilon^y_{eff} = \varepsilon^z_{eff} = \varepsilon_{eff}$) it is possible to consider only a single component

$$
\varepsilon_{eff} \approx \varepsilon_g + k_0^2 \varepsilon_0 \frac{2}{3} \int_0^\infty r \; R_\xi(r) \; dr + j k_g k_0^2 \varepsilon_0 \frac{2}{3} \int_0^\infty r^2 R_\xi(r) \; dr \tag{255}
$$

Usually the first integral of the previous equation can be neglected with respect to ε_g , hence

$$
\varepsilon_{eff} \approx \varepsilon_g + j k_g k_0^2 \varepsilon_0 \frac{2}{3} \int_0^\infty r^2 R_\xi(r) \; dr \tag{256}
$$

This is the expression of the effective permittivity of a random medium according to the Strong Fluctuation Theory.

When the SFT is used to compute the permittivity of a mixture of two constituents (one specie of spherical scatterers embedded in air) the only parameters needed are the permittivity of the two media ε_s and ε_b, the fractional volume and the radius of the scatterers f_s and a respectively. The correlation function $R_\xi(r)$ is expressed by [1]

$$
R_\xi(r) = \begin{cases} \left\langle \xi^2 \right\rangle & 0 \le r \le a \\ 0 & otherwise \end{cases} \tag{257}
$$

and equation (256) becomes

$$
\varepsilon_{eff} \approx \varepsilon_g + j \, \varepsilon_g \, k_g^3 \, a^3 \left(f_s r_s^2 + f_b r_b^2 \right) \tag{258}
$$

$$r_s = \frac{\varepsilon_s - \varepsilon_g}{\varepsilon_s + 2\varepsilon_g} \qquad r_b = \frac{\varepsilon_b - \varepsilon_g}{\varepsilon_b + 2\varepsilon_g} \tag{259}$$

Indeed, for a three components mixture (two species of inclusions in the host medium) it has

$$R_\xi(r) = \begin{cases} \left\langle \xi^2 \right\rangle & 0 \le r \le a_1 \\ \xi_{s2}^2 \; f_{s2} \left(1 + f_{s2}\right) & a_1 \le r \le a_2 \\ 0 & otherwise \end{cases} \tag{260}$$

hence

$$\varepsilon_{eff} \approx \varepsilon_g + j\, k_g \, k_0^2 \, \varepsilon_0 \, 2 \left(\frac{\varepsilon_g}{\varepsilon_0} \right)^2 \left\{ \left(f_{s1} r_{s1}^2 + f_{s2} r_{s2}^2 + f_b r_b^2 \right) a_1^3 + r_{s2}^2 \; f_{s2} \left(1 + f_{s2}\right) \left(a_2^3 - a_1^3 \right) \right\} \tag{261}$$

where

$$r_{s1} = \frac{\varepsilon_{s1} - \varepsilon_g}{\varepsilon_{s1} + 2\varepsilon_g} \qquad r_{s2} = \frac{\varepsilon_{s2} - \varepsilon_g}{\varepsilon_{s2} + 2\varepsilon_g} \qquad r_b = \frac{\varepsilon_b - \varepsilon_g}{\varepsilon_b + 2\varepsilon_g} \tag{262}$$

Computation of the auxiliary permittivity ε_g

The auxiliary permittivity holds in the "very low-frequency" limit, when the scattering between the particles in the random medium can be neglected, i.e.

$$\left\langle \xi(\underline{r}) \right\rangle = 0 \tag{263}$$

Supposing the medium be composed by a dielectric mixture made up by n components, each one with permittivity ε_p and fractional volume f_p, p=1,..,n . If the scatterers are uniformly distributed we have

$$\Pr\left[\varepsilon(\underline{r}) = \varepsilon_p\right] = f_p \qquad p = 1..n \tag{264}$$

and

$$\sum_{p=1}^{n} f_p = 1 \tag{265}$$

Hence, the spatial average (263) can be written as

$$\sum_{p=1}^{n} \frac{\varepsilon_p - \varepsilon_g}{\varepsilon_p + 2\varepsilon_g} f_p = 1 \tag{266}$$

The previous equation is the “Polder-Van Santen” mixing formula, originally derived for inhomogeneous medium with dipoles [5], thus the result is consistent with the very low-frequency approximation of ε_g .

By solving the (266) it is possible to obtain the value of the auxiliary permittivity ε_g .

[1] Tsang L. and J.A. Kong, "**Scattering of electromagnetic waves – Advanced topics**", John Wiley and Sons, New York, 2001

[2] Jin, Y.Q., “**Electromagnetic scattering models for quantitative remote sensing**”, World Scientific, Singapore, 1993

[3] Tsang L. and J.A. Kong, “Scattering of electromagnetic waves from random media with strong permittivity fluctuations”, *Radio Science*, 1981, Vol. 16, no. 3, pp. 303-320

[4] Tsang L., J.A. Kong and R.W. Newton, “Application of Strong Fluctuation Random Medium Theory to Scattering of Electromagnetic Waves from a Half-Space of Dielectric Mixture”, *IEEE Transactions on Antennas and Propagation*, Vol. 30, no. 2, 1982, pp. 292-302

[5] Sihvola A., “**Electromagnetic mixing formulas and applications**”, *The Institution of Electrical Engineers*, 1999

PAPERS LIST

Papers

- Macelloni G., S. Paloscia, P. Pampaloni, M. Brogioni, R. Ranzi and A. Crepaz, "Monitoring of melting refreezing cycles of snow with microwave radiometers: the Microwave Alpine Snow Melting Experiment (MASMEx 2002-2003)", *IEEE Transaction On Geoscience and Remote Sensing*, Vol.43, no.11, pp. 2431 – 2442, Nov. 2005
- G.Macelloni, P.Pampaloni, M.Brogioni, E.Santi, A.Cagnati, M.Drinkwater, "*DOMEX 2004: an experimental campaign at dome-C Antarctica for the calibration of space-borne low-frequency microwave radiometers*", IEEE Trans. On Geoscience and Remote Sensing, Vol.44, no.10, pp. 2642 – 2653, Ott. 2006
- G.Macelloni, M.Brogioni, P.Pampaloni, A.Cagnati, *"Multi-frequency Microwave Emission from the East Antarctic Plateau:Temporal and Spatial Variability "*, IEEE Trans. On Geoscience and Remote Sensing, Vol.45, no.7-1, pp. 2029 – 2039, Jul. 2007
- Macelloni G., A. Cagnati, M. Brogioni, P. Pampaloni and M. Drinkwater, "*Low-frequency microwave emission of the Antarctic plateau: DOMEX 04 an experimental campaign for the calibration of space-borne radiometers*", Terra Antarctica reports, Vol.14, 2008
- Pierdicca N., L. Pulvirenti, F. Ticconi, M. Brogioni, "*Radar bistatic configurations for soil moisture retrieval: a simulation study"*, submitted to IEEE Trans. On Geoscience and Remote Sensing
- Brogioni, M., S. Pettinato, G. Macelloni, S. Paloscia, P. Pampaloni, F. Ticconi, N. Pierdicca; *"Sensitivity of Bistatic Scattering to Soil Moisture and Surface Roughness of Bare Soils",* submitted to International Journal of Remote Sensing
- Macelloni G., P. Pampaloni and M. Brogioni, "*Preparation of an experimental campaign in Antarctica for the calibration of low frequency space-borne radiometers*", Rivista Italiana di Telerilevamento, n°35, 2006, pp. 91-102

Proceedings and conferences

- Pampaloni P., M. Brogioni, G. Macelloni, S. Paloscia and R. Ranzi, "Multifrequency microwave radiometry of the snow-melting cycle and the retrieval of snow water equivalent", Progress in Electromagnetics Research Symposium (PIERS) 2005, Hangzhou, 2005

- Macelloni G., P. Pampaloni , M. Brogioni, A. Cagnati and M. Drinkwater, “DOMEX 2004: an experimental campaign at Dome-C Antartica for the calibration of space-born low-frequency microwave radiometers”, URSI Commission F Symposium, JRC Ispra, 2005
- P. Pampaloni, Brogioni M., G. Macelloni, and E.Santi, “On the contribution of the surface layers to microwave emission from snow: the case of Antarctica Plateau at Dome C”, Proc. Proceedings of IEEE Geoscience and Remote Sensing Symposium, IGARSS 2005, Seul, Corea, CD-Rom, ISBN 0-7803-9051-2.
- G.Macelloni, P.Pampaloni, M.Brogioni, E.Santi, A.Cagnati, M.Drinkwater, “DOMEX 2004: an experimental campaign at dome-C Antarctica for the calibration of space-borne low-frequency microwave radiometers”, Proceedings of IEEE Geoscience and Remote Sensing Symposium, IGARSS 2005, Seul, Corea, CD-Rom, ISBN 0-7803-9051-2.
- Macelloni G., A. Cagnati, M. Brogioni, P. Pampaloni and M. Drinkwater, “Low-frequency microwave emission of the Antarctic plateau: DOMEX 04 an experimental campaign for the calibration of space-borne radiometers”, 5° Convegno Nazionale Di Glaciologia Antartica - CONGA 5,Milano, Ottobre 2005
- P.Pampaloni, G.Macelloni, M.Brogioni, “An Experimental Campaign in Antarctica for the Calibration of Low-frequency Space-borne Radiometers”. Proceedings of IEEE Geoscience and Remote Sensing Symposium, IGARSS 2006, Denver, Colorado, CD-Rom, ISBN 0-7803-9510-7
- P.Pampaloni, M.Brogioni, G.Macelloni, S.Paloscia, S.Pettinato, E.Santi, “Monitoring Snow Cover Characteristics with Multifrequency Active and Passive Microwave Sensors”. Proceedings of IEEE Geoscience and Remote Sensing Symposium, IGARSS 2006, Denver, Colorado, CD-Rom, ISBN 0-7803-9510-7P.Pampaloni, G.Macelloni, M.Brogioni, “Temporal and Spatial Variability of Multi-frequency Microwave Emission of the East Antarctica Plateau”, Proceedings of IEEE Geoscience and Remote Sensing Symposium, IGARSS 2006, Denver, Colorado, CD-Rom, ISBN 0-7803-9510-7
- F.Ticconi, N.Pierdicca, L.Pulvirenti, M.Brogioni, “A Theoretical Study of the Sensitivity of Spaceborne Bistatic Microwave Systems to Geophysical Parameters of Land Surfaces”, Proceedings of IEEE Geoscience and Remote Sensing Symposium, IGARSS 2006, Denver, Colorado, CD-Rom, ISBN 0-7803-9510-7
- M. Brogioni, G. Macelloni, S. Paloscia, P. Pampaloni, S. Pettinato, E. Santi, “Estimating Snow water equivalent from satellite passive and active sensors”, Proceedings of IEEE Geoscience and Remote Sensing Symposium, IGARSS 2006, Denver, Colorado, CD-Rom, ISBN 0-7803-9510-7
- Macelloni, G., M. Brogioni, P.Pampaloni, E. Santi, “Multifrequency Microwave Emission from the Antarctic Plateau”. San Juan de Puerto Rico, Microrad 2006

- F.Ticconi, N.Pierdicca, L.Pulvirenti, M.Brogioni, “Studio della sensibilita’ di un sistema bistatico ai parametri geofisici del suolo”. Genova, XVI Riunione Nazionale di Elettromagnetismo, 2006
- Macelloni G., Brogioni M., Pampaloni P., Cagnati A., “Low-frequency microwave emission from the Antarctic Plateau: an experimental campaign at Dome-C Antartica”, Torino, XCII Congresso nazionale della Società Italiana di Fisica, 2006
- Brogioni M., Macelloni G., Paloscia S., Pampaloni P., Pettinato S., Santi E., “Global-scale monitoring of land hydrological parameters by using microwave multifrequency satellite radiometers”, Torino, XCII nazionale Congresso della Società Italiana di Fisica, 2006, invited paper
- Brogioni M., Paloscia S., Macelloni G., Pampaloni P., Pettinato S., Santi E., “High-resolution mapping of soil moisture and snow cover with satellite Synthetic Aperture Radar”, Torino, XCII Congresso nazionale della Società Italiana di Fisica, 2006
- Macelloni G., M. Brogioni, P. Pampaloni, E. Santi, “Multifrequency Microwave Emission from the Antarctic Plateau”, Microrad’06, 9th Specialist Meeting on Microwave Radiometry and Remote Sensing of the Environment, San Juan, Puerto Rico (invited paper)
- Brogioni M., G. Macelloni, S. Paloscia, P. Pampaloni, S. Pettinato, F. Ticconi, “ Bistatic Scattering from Bare Soils: Sensitivity to Soil Moisture and Surface Roughness”, Proceedings of IEEE Geoscience and Remote Sensing Symposium, IGARSS 2007, Barcellona
- Brogioni M., G. Macelloni, S. Paloscia, P. Pampaloni, S. Pettinato , E. Santi, S. Zecchetto, **“***Monitoring Snow Cover in Alpine Regions with Multi-Frequency Microwave Sensors”* , Proceedings of IEEE Geoscience and Remote Sensing Symposium, IGARSS 2007, Barcellona
- Macelloni G., M. Brogioni, S. Vey, *“Calibration of a Ground Based Radiometer for a One-Year Experiment in Antarctica : A Contribution to SMOS Calibration”,* Proceedings of IEEE Geoscience and Remote Sensing Symposium, IGARSS 2007, Barcellona
- Macelloni G., M. Brogioni, E. Santi, ***“****Retrieval from AMSR-E data of the snow temperature profile at Dome-C Antarctica Giovanni Macelloni****”*** *,* Proceedings of IEEE Geoscience and Remote Sensing Symposium, IGARSS 2007, Barcellona

Reports

- “Final Report”, Technical support for the deployment of an L-Band radiometer at Concordia Station, ESA contract n.18060/04/NL/CB

- “State of the Art on Bistatic Microwave Measurements for Earth Observation”, Use of Bi-Static Microwave Measurements for Earth Observation, ESA contract n. ESTEC 19173/05/NL/GLC
- “Microwave interaction bistatic models: development and validation”, Use of Bi-Static Microwave Measurements for Earth Observation, ESA contract n. ESTEC 19173/05/NL/GLC
- “Preliminary sensitivity analysis of bistatic interaction models”, Use of Bi-Static Microwave Measurements for Earth Observation, ESA contract n. ESTEC 19173/05/NL/GLC
- “System performance analysis”, Use of Bi-Static Microwave Measurements for Earth Observation, ESA contract n. ESTEC 19173/05/NL/GLC
- “Final report”, Use of Bi-Static Microwave Measurements for Earth Observation, ESA contract n. ESTEC 19173/05/NL/GLC

Posters

- Macelloni G., M. Brogioni, E.Santi, *“Retrieval of snow temperature profile from AMSR-E data at Dome-C Antarctica” ,* Proceedings of IEEE Geoscience and Remote Sensing Symposium, IGARSS 2007, Barcellona